Glucose-induced activation of Tas1R3 disrupts calcium signaling and macrophage functionality

Dissertation

zur

Erlangung des Doktorgrades (Dr. rer. Nat.)

der

Mathematisch-Naturwissenschaftlichen Fakultät

der

Rheinischen Friedrich-Wilhelms-Universität Bonn

vorgelegt von

Laura Schlautmann

aus Hilden

Bonn, Januar 2025

Angefertigt mit Genehmigung der Mathematisch-Naturwissenschaftlichen Fakultät

der Rheinischen Friedrich-Wilhelms-Universität Bonn

Gutachter/Betreuer: Prof. Dr. Sven Burgdorf

Gutachterin: Prof. Dr. Irmgard Förster

Tag der Promotion: 15.05.2025

Erscheinungsjahr: 2025

Table of contents

Eidesstaatliche Erklärung

Hiermit erkläre ich, dass ich die vorliegende Dissertation selbstständig verfasst habe. Es wurden keine anderen als die angegebenen Quellen und Hilfsmittel benutzt sowie Zitate kenntlich gemacht.

Die Experimente, die in dieser Dissertation beschrieben sind, wurden von mir selber designed und durchgeführt. Ausgenommen davon sind die folgenden Experimente:

- Die STED Mikroskopie sowie vorherige Generierung von ‘membrane sheets‘ wurde von Daniel Burgdorf unter Betreuung von Sara C. Schmidt und Thorsten Lang durchgeführt.
- *In situ* Migrationsassays sowie die entsprechende Bildanalyse wurden von Shaunak Ghosh und Eva Kiermaier durchgeführt.

Bonn, den

_____

Laura Schlautmann

List of Abbreviations

°C	Degree Celsius
µ	Micro
2-APB	2-aminoethoxydiphenyl borate
2D	Two dimensional
2-DG	2-Deoxyglucose
3D	Three dimensional
AC	Adenylyl cyclase
ADP	Adenosine diphosphate
ALN	Another-Regulin
AM	Cell-permeable acetoxymethyl (AM) ester of fluorescent calcium indicators
AP-1	Activator protein-1
ASC	Apoptosis associated speck-like protein
ATF	Activating transcription factor
ATP	Adenosine triphosphate
AUC	Area under the Curve
BIM	Bisindolylmaleimide
BiP	Binding Immunoglobulin Protein
BMDMs	Bone marrow-derived macrophages
BMI	Body Mass Index
BSA	Bovine serum albumin
c	Centi
Ca^{2+}	Calcium
$CaCl_2$	Calcium chloride
CaMKII	Ca^{2+}/calmodulin-dependent protein kinase II
cAMP	Cyclic adenosine monophosphate
CaSR	Calcium-sensing receptor
Ca_V	Voltage-gated Ca^{2+} channel
C-CL	Chemokine C-C motif ligand
CD	Cluster of differentiation
CD	Control diet
CO_2	Carbon dioxide
CRAC	Ca^{2+} release-activated Ca^{2+} channel
DAG	Diacylglycerol
DCs	Dendritic cells
DMEM	Dulbecco's Modified Eagle Medium
DNA	Deoxyribonucleic acid

Dworf	Dwarf open reading frame
ECM	Extracellular matrix
EDTA	Ethylenediaminetetraacetic acid
eIF	Eukaryotic Initiation Factor
ELISA	Enzyme-linked immunosorbent assay
ELN	Endoregulin
ER	Endoplasmic Reticulum
FBS	Fetal bovine serum
FcγR	Fc-gamma receptor
FITC	Fluorescein isothiocyanate
FMI	Forward Migration Index
G protein	Guanine-nucleotide binding protein
GEF	Guanine exchange factor
Glu	Glucose
GM-CSF	Granulocyte-macrophage colony-stimulating factor
gMFI	Geometric Mean Fluorescence Intensity
GPCR	G protein coupled receptor
GRK	GPCR kinase
GTP/GDP	Guanosine tri/diphosphate
h	Hours/hour
H_2SO_4	Sulfuric acid
HbA1c	Glycated hemoglobin
HBSS	Hank's Balanced Salt Solution
HDL	High Density Lipoprotein
HFD	High fat diet
HOMA	Homeostasis Model Assessment
IFN-γ	Interferon-gamma
IL	Interleukin
IMDM	Iscove's Modified Dulbecco's Medium
int	Intermediate
IP_3	Inositol triphosphate
IP_3R	IP_3 receptor
IRE1	Inositol-requiring enzyme 1
IRS	Insulin receptor substrate
IκB	Inhibitor of NF-κB
JNK	Jun N-terminal kinase
K^+	Potassium
L	Litre

LPMs	Large peritoneal macrophages
LPS	Lipopolysaccharide
Ly6c	Lymphocyte antigen 6 family C
M	Molar (mol/L)
MAPK	Mitogen-activated protein kinase
M-CSF	Macrophage colony-stimulating factor
MFI	Mean Fluorescence Intensity
MHC I/II	Major histocompatibility complex class I/II
min	Minutes
MLN	Myoregulin
mTOR	Mammalian Target of Rapamycin
n	Nano
Na^+	Sodium
NAD^+	Oxidized form of NADH
NADH	Nicotinamide-Adenine-Dinucleotide
NCX/NCKX	Potassium-dependent/-independent sodium-calcium exchanger
NFAT	Nuclear factor of activated T cells
NF-κB	Nuclear factor of κB
norm.	Normalized
OD	Optical Density
p	Pico
P2X/P2Y	Purinergic receptors
PBMCs	Peripheral Blood Mononuclear Cells
PBS	Phosphate buffered saline
PCMA	Plasma membrane Ca^{2+} ATPase
PEP	Phosphoenol pyruvate
PERK	Protein kinase R-like ER-kinase
PFA	Paraformaldehyde
PI3K	Phosphoinositide-3-kinase
PIP_2	Phosphatidylinositol 4,5-bisphosphate
PKA	Protein kinase A
PLC	Phospholipase C
PLL	Poly-L-lysine
PLN	Phospholamban
PMA	Phorbol-12-myristat-13-acetate
PP1	Protein phosphatase 1
RNA	Ribonucleic acid
RPMI	Roswell Park Memorial Institute

RT	Room temperature
RTPCR	Reverse Transcriptase Polymerase Chain Reaction
RyR	Ryanodine receptor
s	Seconds
S1P	Sphingosine-1-phosphate
SDS	Sodium dodecyl sulfate
SDS-PAGE	SDS polyacrylamide gel electrophoresis
SEM	Standard error of the mean
Ser	Serine
SERCA	Sarcoplasmic/endoplasmic reticulum calcium ATPase
siRNA	Small interfering RNA
SLN	Sarcolipin
SOCE	Store-operated calcium entry
SPMs	Small peritoneal macrophages
SSC	Side scatter
STIM	Stromal interaction molecule
Suc	Sucralose
Tas1R3	Taste receptor type 1 member 3
TLR	Toll-like receptor
TMB	3,3',5,5'-teramethylbenzidine
TNF	Tumor necrosis factor
TRP	Transient receptor potential
TRPC	Transient receptor potential canonical
UPR	Unfolded protein response
w/	With
w/o	Without
XBP	X-box binding protein
α	Alpha
β	Beta
γ	Gamma
Δ	Difference

List of Figures

List of Tables

1. Abstract

The incidence of *diabetes mellitus* has risen alarmingly in recent years, becoming one of the leading causes of death worldwide. The disease is characterized by hyperglycemia, increased blood glucose levels, and is often accompanied by secondary diseases, including cardiovascular diseases, atherosclerosis and kidney failure. Moreover, diabetes has been linked to metaflammation, a chronic low-grade inflammation. One of the important immune cell types implicated in the onset of metaflammation and also diabetes are macrophages. These cells serve as key immune sentinels, playing an essential role in maintaining tissue homeostasis and mediating responses to microenvironmental changes.

This thesis investigated how hyperglycemia influences the activation and functionality of murine and human macrophages, with a particular focus on calcium (Ca^{2+}) signaling.

We demonstrated that elevated glucose concentrations promote the secretion of pro-inflammatory cytokines, such as TNF and IL-1β, which is mediated via mTOR and NF-κB signaling. Furthermore, we showed that hyperglycemia leads to the depletion of Ca^{2+} from intracellular stores, such as the endoplasmic reticulum (ER), and consequently impaired Ca^{2+} signaling. We identified that macrophages sense glucose via the taste receptor Tas1R3 and delineated the downstream signaling mechanism. Glucose-mediated activation of Tas1R3 induces the release of Ca^{2+} from the ER via activation of the inositol triphosphate (IP_3) receptor and inhibition of the sarco-/endoplasmic reticulum Ca^{2+} ATPase (SERCA). We revealed that the Tas1R3 signaling cascade involves the phospholipase C-mediated generation of IP_3 and the modulation of phospholamban, a potent modulator of SERCA, via PLC/PKC/PP1 signaling. Accordingly, by simultaneously promoting Ca^{2+} release from the ER and inhibiting Ca^{2+} reuptake, glucose induced an initial increase in cytosolic Ca^{2+} concentrations, followed by a loss of Ca^{2+} and depletion of Ca^{2+} stores over time.

The intensity of glucose-induced Ca^{2+} signaling correlated with Tas1R3 expression across different cell subsets of murine and human cohorts. Moreover, we observed a strong negative correlation between blood glucose concentrations and the Ca^{2+} signaling intensity in human $CD14^+$ monocytes and murine peritoneal macrophages, further highlighting that elevated glucose concentrations substantially influence Ca^{2+} signaling in macrophages within a physiological context.

Finally, we demonstrated that hyperglycemia-induced disruption of Ca^{2+} homeostasis impairs macrophage functionality. Specifically, glucose-mediated depletion of Ca^{2+} from its stores induced ER stress and inhibited MHC I-restricted antigen presentation. In addition, elevated glucose concentrations disrupted chemokine-mediated Ca^{2+} signaling, thereby impairing cellular migration.

In summary, these data revealed that hyperglycemic macrophages are primed towards a pro-inflammatory cytokine profile and exhibit impaired Ca^{2+} homeostasis, which further compromises Ca^{2+}-dependent cellular functions. Strikingly, our findings reveal a novel role of Tas1R3 in macrophages and provide new insights into the understanding and molecular mechanisms underlying immune dysfunction in the context of diabetes.

2. Introduction

2.1. Diabetes mellitus

In recent decades, there has been a notable increase in the number of deaths associated with non-communicable diseases, which now account for approximately 75% of deaths globally. Along with cancer, cardiovascular disease, and chronic respiratory disease, diabetes is one of the leading causes of premature death worldwide. [2,3]

Diabetes mellitus encompasses several metabolic disorders, mainly characterized by hyperglycemia, an elevated blood glucose level [4]. The prevalence of diabetes is rising every year and is expected to reach a prevalence of over 12% by 2045 (Figure 1) [1].

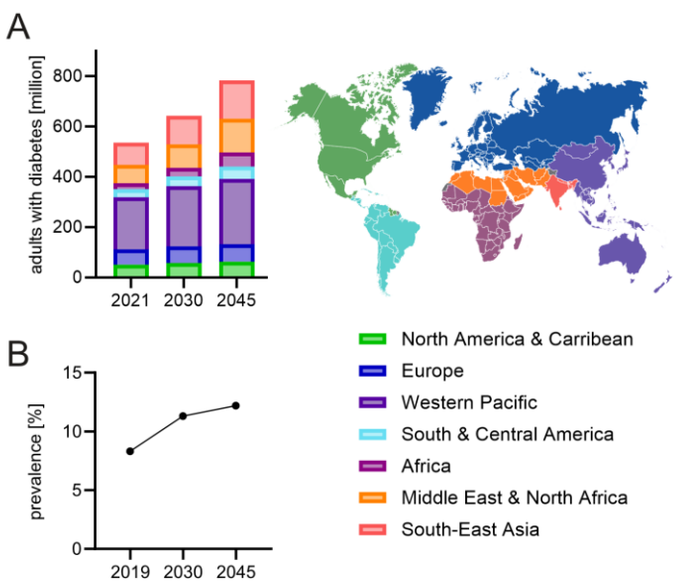

Figure 1 - Global prevalence and cases of diabetes
Estimated numbers of adults (20-79 years) with diabetes per region (**A**) and globally as relative prevalence normalized to the expected world population for the respective years (**B**). Data are estimations derived from IDF Diabetes Atlas [1].

A key aspect of diabetes involves the regulation of blood glucose levels, a process primarily controlled by the function of pancreatic beta cells. The functionality of these cells and the mechanisms underlying their dysfunction is central to the disease. In a healthy situation, beta cells within the pancreas secrete insulin following nutrient uptake due to increased blood glucose levels sensed by beta cells [5]. The secreted insulin then binds to the insulin receptor on the surface of cells across various tissues in the body and activates signaling that mediates the insertion of glucose transporters into the cell membrane. In addition to glucose transport, activation of insulin receptor signaling promotes glycogen and protein synthesis and inhibits gluconeogenesis. [6]

The classification of *diabetes mellitus* depends on the underlying cause of impaired regulation of blood glucose levels, resulting in defined subtypes of the disease. Type 1 diabetes, also referred to as juvenile diabetes, is caused by a lack of insulin due to the destruction of beta cells in the pancreas. In contrast, in type 2 diabetes, the body's cells become resistant to the binding of insulin. Consequently, glucose levels do not decline efficiently resulting in increased fasting blood glucose levels. Following an initial compensatory period of increased insulin secretion by beta cells, type 2 diabetes is characterized by a reduction of insulin levels at later stages due to beta cell dysfunction [7,8].

As defined by the American Diabetes Association and the World Health Organization, individuals are diagnosed with diabetes when their fasting blood glucose levels exceed 7 mM, whereas blood glucose levels below 5.5 mM are considered healthy. Furthermore, additional laboratory parameters, such as the oral glucose tolerance test and glycated hemoglobin (HBA1c), are employed for classification: In an oral glucose tolerance test, patients ingest 75 g of glucose and their blood glucose levels are subsequently determined over a two-hour period. In contrast to healthy subjects, not only the fasting blood glucose level but especially the glucose level after glucose ingestion increases and does not decline efficiently (Figure 2) [9]. Glucose levels between 7.8 and 11 mM two hours after glucose intake are considered prediabetic, whereas two-hour blood glucose levels above 11 mM are considered diabetic. Furthermore, individuals with HbA1c levels between 5.7% and 6.4% or above 6.5% are considered prediabetic or diabetic, respectively. This is a measure of the proportion of glycated hemoglobin and refers to an individual's blood glucose levels over the preceding two to three months. [10–12]

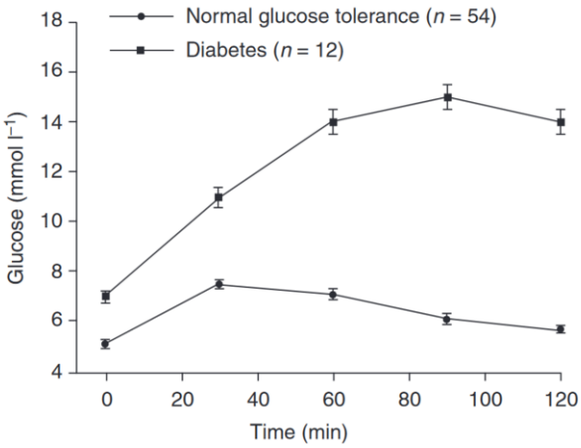

Figure 2 - Glucose tolerance test as diagnostic criterium for diabetes
Blood glucose levels are monitored for 2 h after intake of 75 g glucose. Screening test to diagnose diabetes. Modified from Ahrén et al. [2].

Diabetes mellitus is associated with an elevated risk of developing a variety of health complications including stroke, blindness, heart attack, kidney failure, and amputation [13,14]. These comorbidities, rather than the hyperglycemia itself, are the primary cause of mortality in individuals with diabetes. Furthermore, sustained elevated blood glucose levels are linked to increased levels of inflammatory mediators and inflammatory immune cell phenotypes that contribute to chronic inflammation [15]. This chronic, low-grade inflammation, also referred to as metaflammation, has been further described to play a crucial role in the development and onset of diabetes, particularly in obese individuals [13,16]. Accordingly, the pathophysiological changes observed in diabetes and metaflammation exert a reciprocal influence, thereby exacerbating the respective disease. A critical role in the development and onset of diabetic complications has been attributed to macrophages in particular, which will be elaborated in greater detail in the following chapter. [17–19]

2.1.1. Regulation of glucose levels by insulin

The regulation of blood glucose levels is mainly achieved through the precise control of two pancreatic peptide hormones. While insulin functions to reduce blood glucose levels, glucagon mediates an increase in blood glucose levels by promoting gluconeogenesis and glycogenolysis. Postprandially, various peptides, such as the glucagon-like peptide, are involved in the reduction of glucagon levels while simultaneously increasing insulin secretion and further improving insulin sensitivity. [20,21]

Upon hyperglycemia, glucose is transported into the beta cells located in the pancreatic islets and metabolized, leading to the generation of adenosine triphosphate (ATP). Subsequently, ATP-dependent potassium channels are closed resulting in cellular depolarization and opening of voltage-dependent calcium channels, facilitating the exocytosis of insulin-containing vesicles. [22]

Upon binding to the insulin receptor and activation of downstream signaling, insulin stimulates the cellular glucose uptake by increasing membrane insertion of glucose transporters (GLUT), which regulates the cellular glucose uptake, and further influences the cellular metabolism. Insulin exerts an inhibitory effect on glycogenolysis, lipolysis, proteolysis, and hepatic gluconeogenesis. Additionally, insulin plays a regulatory role in cell proliferation and supports glycogen synthesis in the liver and muscles. The insulin-mediated signaling cascade is initiated by autophosphorylation of the receptor and subsequent recruitment and phosphorylation of several substrates, including the insulin-receptor substrates (IRS) 1 to 4. IRS phosphorylation results in the activation of the phosphoinositide-3-kinase(PI3K)-Akt pathway, which is responsible for mediating the aforementioned metabolic effects. [23–26]

2.2. Macrophages as key regulators of inflammation and homeostasis

2.2.1. Macrophage development and function

Humans and other organisms are equipped with an immune system enabling them to defend against potentially harmful pathogens and danger signals. With its ability to discriminate between self and non-self, the immune system is crucial for protecting an organism and ensuring the organism's integrity. The immune system can be divided into innate and adaptive immunity: While the innate response is a rapid but non-specific response to immune triggers, the adaptive immune response is a specific response that involves the activation of a cell-mediated response and facilitates immune memory. [27]

Mononuclear phagocytes, which comprise dendritic cells, monocytes and macrophages, are critical immune cells that play a pivotal role in both innate and adaptive immunity. Due to their immunomodulatory function, macrophages are often referred to as immune sentinels [28]. Macrophages are not only involved in maintaining tissue homeostasis but also respond to changes in the microenvironment. These cells have been described as gatekeepers for the balance between

inflammation and homeostasis. Accordingly, macrophages fulfill a wide range of functions and can be found in virtually every tissue.

Tissue-resident macrophages, which are long-lived and bear a self-renewing capacity, typically originate from the yolk sac or fetal liver during embryogenesis. Additionally, macrophages differentiate from monocytes derived from hematopoietic stem cells in the bone marrow, which circulate in the blood and lymphatics in a homeostatic state [29,30]. Monocyte-derived macrophages replenish tissue-resident macrophages upon high demand or in tissues with high turnover. Furthermore, this short-lived subset is recruited during inflammation and is also involved in resolving inflammation, tissue repair as well as wound healing [30–32].

Their phagocytic activity enables the engulfment and degradation of extracellular material, thereby clearing cellular debris and pathogens. Furthermore, macrophages secrete soluble mediators, including growth factors, cytokines and antimicrobial peptides, which are relevant for the first line of defense against pathogens, as well as for the initiation of inflammation and for the recruitment of other immune cells. [29,33] To fulfill their function, macrophages are capable of migrating within the tissue under homeostatic conditions and responding to external stimuli, such as chemokine gradients [34,35]. Cytoskeletal remodeling during cell migration and in response to migratory stimuli is strongly dependent on intracellular calcium signaling [36,37]. Since calcium is one of the main parameters elaborated in this thesis, calcium signaling will be discussed in more detail in chapter 2.3.

In vitro differentiation of murine bone marrow cells or human monocytes is widely used to study macrophage biology and function, facilitating the dissection of the broad spectrum of macrophages existing *in vivo.* The differentiation of murine bone marrow cells with either granulocyte-macrophage colony-stimulating factor (GM-CSF) or macrophage colony-stimulating factor (M-CSF) gives rise to macrophages with a predominantly pro-inflammatory or anti-inflammatory profile, respectively [38]. In humans, *in vitro* methods for studying macrophages mainly rely on the differentiation of monocytes isolated from human blood. In contrast to mice, Sanders et al. have demonstrated that both differentiation with M-CSF and GM-CSF gives rise to a macrophage population that exhibits similarities to inflammatory macrophages *in vivo* [39].

2.2.2. Macrophage activation

Previously, macrophages were frequently categorized according to two polarization states, either as pro-inflammatory 'M1' or anti-inflammatory 'M2' macrophages. Pro-inflammatory macrophages are involved in the recruitment and the activation of leukocytes, the activation of the endothelium, and most notably the modulation of the adaptive immune system. Anti-inflammatory macrophages possess functions that facilitate the resolution of inflammation and wound healing by producing anti-inflammatory mediators, induction of remodeling of extracellular matrix and clearance of dead cells. [31,40] Nevertheless, contemporary research has revealed that macrophages give rise to a broad spectrum of cells classified based on their function, with M1 and M2 representing the extremes. This high plasticity enables macrophages to exert their wide variety of functions ranging from inflammation to resolution of infection and relevance during homeostasis [38,41,42]. The *in vitro* culture and differentiation of macrophages using a combination of lipopolysaccharide (LPS) and interferon-gamma (IFN-γ) or with interleukin-4 (IL-4) largely recapitulates the described and oversimplified M1/M2 macrophage dichotomy. In this model, M1 macrophages are characterized by the secretion of pro-inflammatory cytokines, such as tumor necrosis factor (TNF) and IL-6, while M2 macrophages are defined by the release of anti-inflammatory cytokines, including IL-10, and enhanced immunosuppressive function. [41–43] In general, immune stimuli recognized by pattern recognition receptors on the surface of macrophages, such as LPS recognition by Toll-like receptor 4 (TLR4), induce signaling cascades leading to metabolic and transcriptional reprogramming to fulfill their stimulus-dependent function [41,44]. This cellular reprogramming involves metabolic changes, such as a switch to increased glycolysis in inflammatory macrophages to meet the high energy demand as well as transcriptional changes, including upregulation of cytokines and various receptors.

Upon stimulation with LPS, the transcription of pro-inflammatory cytokines, including TNF, IL-6 and pro-IL-1β, and the induction of the inflammasome complex are mainly driven by the translocation of nuclear factor of κB (NF-κB) into the nucleus. At steady state, the classical NF-κB complex, consisting of the two subunits p65 and p50, resides inactive in the cytosol. TLR4 activation by LPS results in a cellular signaling cascade, that activates the IκB kinase complex, which mediates the phosphorylation and degradation of the inhibitor of κB and subsequent phosphorylation of NF-κB allowing its nuclear localization. In addition, LPS stimulation is associated with the induction of type I interferons. [45,46]

2.2.3. Characterization of mouse and human macrophages

A broad spectrum of macrophages and monocytes possessing tissue- and environment-specific functions have been described in both mice and humans. [28,30]

In the blood, monocytes account for 10-20% of total peripheral blood mononuclear cells (PBMCs), whereas 70-90% are lymphocytes, including T cells and B cells [47]. The subset of circulating blood monocytes can be further classified based on their expression of Ly6C or CD14 in mice and humans, respectively. Monocytes that express Ly6C or CD14 are referred to as classical monocytes, which are derived from stem cells in the bone marrow. These cells possess pro-inflammatory functions and are distinguished by augmented phagocytic activity and the expression of chemotactic receptors. During inflammation, classical monocytes are recruited into the tissue to replenish the tissue macrophages and are critical for initiating an immune response. In contrast, $Ly6C^-$ or $CD14^{low}$ non-classical monocytes, which differentiate from classical monocytes, exert a protective role by promoting tissue repair, modulating immune responses and patrolling through the vasculature. In a homeostatic situation, non-classical monocytes contribute to the replenishment of tissue-resident macrophages. Tissue-resident macrophages can adapt to specific tissue environments and exhibit remarkable plasticity. Accordingly, distinct subsets arise depending on their location and the physiological state of the tissue. [30,42,48]

Within the peritoneal cavity, large numbers of macrophages contribute to the immune surveillance of the abdominal cavity and the surrounding tissues. In mice, these macrophages are characterized by high expression of CD11b and are further classified into two subtypes: large peritoneal macrophages (LPMs) and small peritoneal macrophages (SPMs). At steady state, embryonic-derived LPMs with self-renewal capacity account for approximately 90% of all peritoneal macrophages. [49,50] Murine LPMs express high levels of the macrophage marker F4/80 as well as co-stimulatory molecules and receptors to respond to pathogens and are critical for maintaining a homeostatic state [49,50]. In the context of inflammation, the highly phagocytic LPMs decrease in number and provide a pivotal contribution to the immunological defense through their migration to damaged tissue [51]. Opposingly, the subset of SPMs strongly increases upon inflammation. This short-lived subset is characterized by low expression of F4/80, but high levels of major histocompatibility complex class II (MHC II) and is derived from circulating monocytes [49,50]. Together with their inflammatory monocytic precursors, SPMs critically contribute to the induction of the immune response due to their phagocytic activity against bacteria and their capacity to activate a $CD4^+$ T cell response [52]. Due to the ease of accessibility and enhanced stability of murine peritoneal macrophages in comparison to macrophages from other sources [53,54], these cells are frequently utilized to investigate the biology of resident macrophages in naïve mice or of elicited macrophages in mice, wherein a mild inflammatory response has been induced by thioglycolate injection [53,55]. Like the murine peritoneal macrophage subtypes, human peritoneal macrophages play critical roles in immune surveillance and tissue repair and distinct subsets contributing to both inflammatory and

anti-inflammatory responses have been described. However, in contrast to the classification of murine peritoneal macrophages, human peritoneal macrophages are mainly categorized by their origin as well as functional and phenotypic markers, such as CD14, CD16 and CD163, reflecting their greater plasticity and functional diversity. [56,57]

2.2.4. Macrophages in diabetes

In addition to responding to immune triggers, macrophages also sense microenvironmental signals, including changes caused by dietary habits and obese conditions, which result in phenotypic changes in these cells [58]. There is considerable evidence suggesting that macrophages may play a pivotal role in both the development and onset of diabetes, as well as in increased risk for associated complications [59–61].

During the development of diabetes, macrophages have been described to contribute to both the induction of insulin resistance and beta cell dysfunction [18,62]. In the context of obesity and metaflammation, macrophages undergo a phenotypic switch to a pro-inflammatory state and infiltrate into adipose tissue and insulin-target organs, including the liver and skeletal muscle. Subsequently, increased levels of various macrophage-derived pro-inflammatory cytokines mediate insulin resistance. TNF and IL-1β signaling has been demonstrated to result in increased serine phosphorylation of IRS through the activation of NF-κB and c-Jun-amino terminal kinase (JNK) signaling pathways. Serine phosphorylation of IRS prevents its tyrosine phosphorylation, which is required for the insulin receptor signaling response, thereby mediating insulin resistance. [18] Furthermore, cytokine-mediated activation of NF-κB and activator protein-1 (AP-1) has been shown to promote the expression of inflammatory genes, thereby aggravating insulin resistance. Accordingly, TNF blockade strongly ameliorates insulin resistance in obese rats [63]. In addition to TNF and IL-1β, IL-6 signaling has been shown to result in proteasomal degradation of IRS, thereby mediating insulin resistance [64]. These data are further supported by the development of insulin resistance in non-obese mice that received an acute IL-6 infusion [65].

Although the precise mechanisms are not fully understood yet, beta cell dysfunction has been attributed to several macrophage-dependent processes. Despite the secretion of inflammatory mediators, direct cell-cell interactions have also been identified as a contributing factor in the destruction of beta cells and the reduction of glucose-induced insulin secretion [62]. It has been shown that the extent of beta cell destruction correlates with the accumulation of pro-inflammatory macrophages [66]. Accordingly, the depletion of islet macrophages has been demonstrated to strongly increase glucose-stimulated insulin secretion in mice treated with a high-fat diet [67]. Recently, Zhang *et al.* revealed that macrophage-derived microRNA miR-155 impairs insulin biosynthesis and glucose-stimulated insulin secretion in beta cells of diabetic mice [68]. Overall, these findings highlight that macrophages play a critical role in beta cell dysfunction and contribute to altered insulin regulation and pathophysiology in diabetes.

Several immune complications associated with diabetes are related to phenotypic alterations in hyperglycemic macrophages, which are characterized by their paradoxical functions in the context of diabetes (Figure 3). On the one hand, hyperglycemic macrophages exhibit a pro-inflammatory profile characterized by elevated secretion of pro-inflammatory cytokines. Thus, macrophages contribute to the progression of metaflammation and the pathogenesis of diabetic complications, including nephropathy, atherosclerosis and retinopathy [17,69]. On the other hand, impaired immunity and increased susceptibility to bacterial infections have been linked to functional changes in macrophages of patients with diabetes. Hyperglycemic macrophages show diminished phagocytic and anti-bactericidal activity [15,69]. Additionally, impaired wound healing and chronic tissue inflammation result from increased infiltration of pro-inflammatory macrophages and a further delayed transition to repairing macrophages [70,71]. Diabetes results in reduced adhesion capacity of macrophages and impaired chemotaxis and leukocyte recruitment upon infection, thereby attenuating the immune response [72,73]. Despite the described associations, the exact mechanisms responsible for the functional differences in diabetic macrophages remain largely unknown or poorly understood.

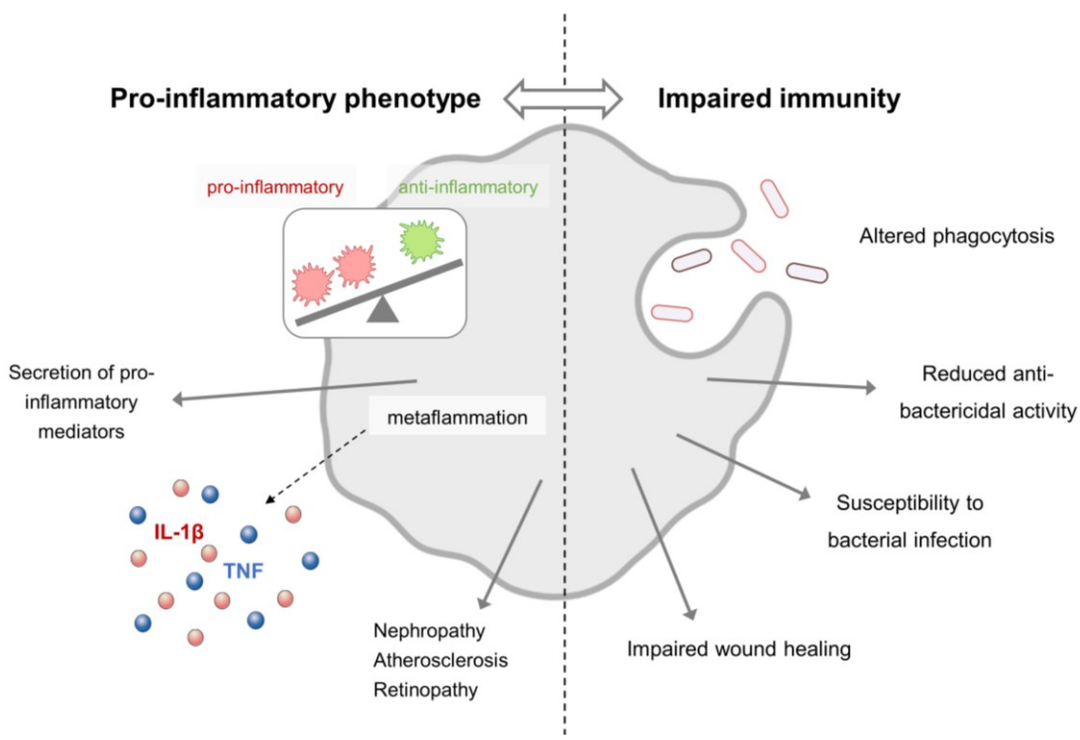

Figure 3 – Macrophage paradox in diabetes
A shift towards a pro-inflammatory profile characterizes diabetic macrophages. The increased secretion of pro-inflammatory cytokines and mediators contributes to metaflammation, a chronic low-grade inflammation, as well as various diabetic complications. Contrary, diabetic macrophages contribute to impaired immunity observed in diabetic patients. [15,69,71] Created using Servier Medical Arts [74].

2.3. Relevance of calcium as signaling molecule

2.3.1. Ca^{2+} signaling in macrophages

Calcium (Ca^{2+}) serves as a second messenger, participating in a multitude of intracellular signaling pathways. Accordingly, Ca^{2+} is indispensable for cellular functions during homeostasis, as well as in response to external stimulation, such as inflammation. Under homeostatic conditions, cytosolic Ca^{2+} concentrations are low (100 nM), whereas Ca^{2+} concentrations are 10,000-fold higher in the extracellular space as well as in intracellular Ca^{2+} stores, such as the endoplasmic reticulum (ER) [75]. In response to stimulation, calcium ions are released from intracellular stores or enter the cell through the plasma membrane. The majority of Ca^{2+} signaling occurs in response to external stimuli, including changes in pH, temperature and osmolarity, as well as the binding of soluble factors, such as chemokines, microbial products and growth factors. [76–78]

It has been demonstrated that perturbations in Ca^{2+} dynamics are associated with the development and aggravation of various diseases, including metabolic disorders, neurodegenerative diseases and cancer. Accordingly, Ca^{2+} signaling and its involvement in disease pathologies as well as potential therapeutic approaches have been and continue to be the subject of numerous research papers and studies [79–83].

2.3.1.1. Mechanisms of Ca^{2+} signaling: channels and responses

The elevation of cytosolic Ca^{2+} concentrations can be mediated by the activation of a wide range of cation-transporting channels that facilitate the influx of Ca^{2+} across the plasma membrane. In addition, the activation of various receptors triggers intracellular signaling cascades, which orchestrate the release of Ca^{2+} from the ER and enhance Ca^{2+} influx from the extracellular space (Figure 4). The signaling cascades resulting from receptor stimulation typically involve phospholipase C (PLC)-dependent generation of inositol triphosphate (IP_3) and subsequent release of Ca^{2+} via activation of the IP_3 receptor (IP_3R) in the ER. [84,85] The decrease of Ca^{2+} concentrations in the ER is sensed by stromal interaction molecules (STIM) located in the ER membrane. The subsequent aggregation of STIM1 and the formation of ER-plasma membrane contact sites results in the activation of the store-operated Ca^{2+} entry (SOCE) mechanism. SOCE is mediated by the activation of Ca^{2+} release-activated Ca^{2+} (CRAC) channels, which are composed of ORAI proteins. Based on this dynamic interplay, Ca^{2+} release from the ER induces Ca^{2+} transport across the plasma membrane and vice versa, resulting in a bidirectional amplification of Ca^{2+} signaling. [86,87]

In addition to the IP_3R, macrophages express low levels of an isoform of the ryanodine receptor (RyR), which is a Ca^{2+}-sensitive receptor that is also activated via physical coupling to L-type voltage-gated Ca^{2+} channels (Ca_v) [85,88]. Ca_v channels, which are primarily associated with excitable cells, have been implicated in macrophage responses to infection and shown to be responsive to extracts of necrotic cells [85,86].

Depending on the receptor, different isoforms of PLC are activated upon stimulation. PLCγ is the target of enzyme-linked receptors containing a Src homology domain. Activation of these receptors is initiated by several mechanisms, including the crosslinking of Fc-gamma receptors (FcγR) by immunoglobulin-containing immune complexes, the activation of C-type lectin receptors by binding of carbohydrate structures and the engagement of TLR4. The activation of G protein-coupled receptors (GPCRs), including chemokine receptors, purinergic P2Y receptors and the calcium-sensing receptor (CaSR), has been demonstrated to mediate PLCβ activation (Figure 4). [84,89,90]

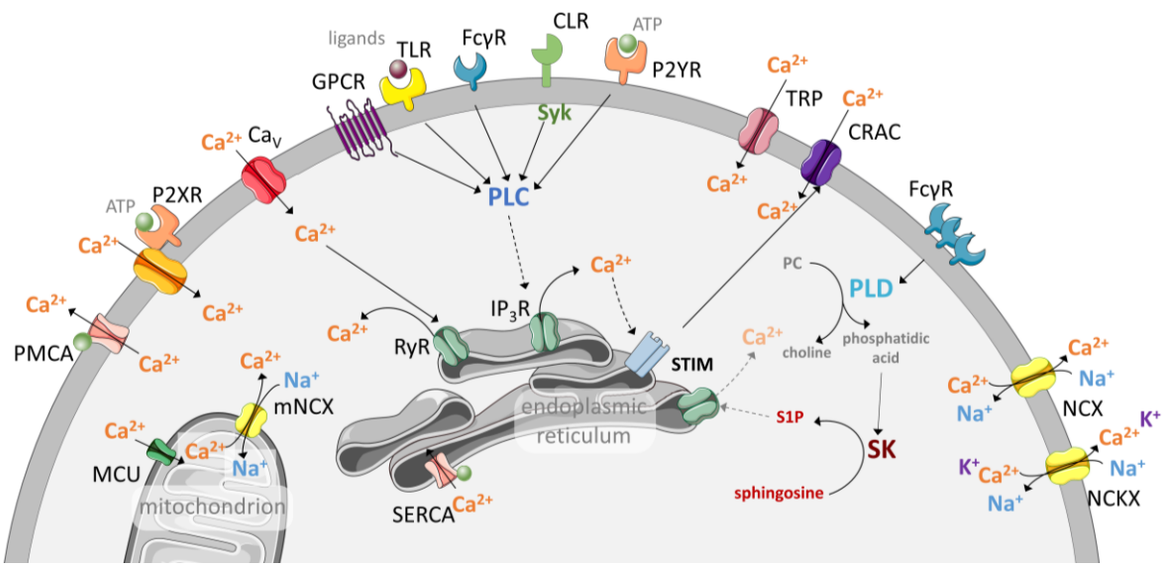

Figure 4 – Calcium channels in macrophages
Activation of receptors coupled to signal transduction pathways or activation of Ca^{2+} channels results in an increase of cytosolic Ca^{2+} concentrations via influx from the extracellular space or release from internal stores. Amplification of Ca^{2+} release from the ER via activation of store-operated Ca^{2+} entry by STIM-dependent activation of CRAC channels. Ca^{2+} further enters the cell via membrane-potential-dependent Ca_V channels, P2X receptors as well as TRP channels. Ca^{2+} levels are decreased by Ca^{2+} transport into the endoplasmic reticulum by SERCA or into mitochondria via the MCU as well as by export through the plasma membrane via PCMA and Na^+-Ca^{2+} antiporter. *Abbreviations: ATP, adenosine triphosphate; Ca^{2+}, calcium CLR; C type lectin receptor; CRAC, Ca^{2+}-release activated Ca^{2+} channels; GPCR, G protein-coupled receptor; IP_3, inositol triphosphate; (m)NCX, (mitochondrial) Na^+-Ca^{2+} exchanger; MCU, mitochondrial Ca^{2+} uniporter; PC, phosphatidylcholine; PL, phospholipase; PMCA, plasma membrane Ca^{2+} pump; P2XR/P2YR, purinergic receptors; R, receptor; RyR, ryanodine receptor; SERCA, sarcoplasmic/endoplasmic reticulum Ca^{2+} ATPase; SK, sphingosine kinase; STIM, stromal interaction molecule; S1P, sphingosine-1-phosphate; TLR, Toll-like receptor; TRP, transient receptor potential*. [84–86] Created using Servier Medical Arts [74].

The crosslinking of the FcγR further induces a signaling cascade resulting in sphingosine-1-phosphate (S1P)-dependent release of Ca^{2+} from the ER. However, the precise mechanism by which this occurs remains unclear. [68,91]

In contrast to G protein-coupled P2Y receptors, purinergic P2X receptors are ligand-gated ion channels activated by ATP. In macrophages, the mRNA expression of different subtypes has been described. However, thus far, a functional role during inflammatory responses of macrophages has only been ascribed to P2X4 and P2X7 receptors. [86,92,93] Another group of ion channels that are permeable to calcium ions are transient receptor potential (TRP) channels, a family of non-selective cation channels. TRP channels respond to various biochemical and physical stimuli, including

changes in temperature, pH and osmolarity, mechanical forces but also inflammatory molecules. [94,95] Further, TRP channels are positively regulated by mediators of the PLC pathway [95,96].

Restoring of Ca^{2+} concentrations following stimulation as well as maintenance of low cytosolic Ca^{2+} concentrations under homeostatic conditions is achieved by the activity of various Ca^{2+} transporters (Figure 4). The sarcoplasmic/endoplasmic reticulum Ca^{2+} ATPase (SERCA) and the plasma membrane Ca^{2+} ATPase (PMCA) pump Ca^{2+} from the cytosol into the ER or to the extracellular space, respectively. In addition, potassium (K^+)-dependent and K^+-independent sodium (Na^+)-calcium exchangers (NCKX, NCX) facilitate the export of Ca^{2+} across the plasma membrane. [85,97] High cytosolic Ca^{2+} concentrations further result in conformational changes and the activation of the mitochondrial Ca^{2+} uniporter (MCU), which contributes to the decrease the cytosolic Ca^{2+} concentrations through the uptake of Ca^{2+} into the mitochondrial matrix [97,98]. Abnormal Ca^{2+} concentrations within the mitochondrial matrix are prevented by the export of Ca^{2+} through the mitochondrial Na^+-Ca^{2+} exchanger (mNCX) [99].

2.3.1.2. Endoplasmic reticulum as Ca^{2+} store and regulator of Ca^{2+} homeostasis

The endoplasmic reticulum (ER) is the most important Ca^{2+} store within the cell, reaching Ca^{2+} concentrations in the mM range. Within the ER, Ca^{2+}-binding proteins help to regulate free Ca^{2+} levels and thereby contribute to the maintenance of Ca^{2+} homeostasis at steady state. In addition to the Ca^{2+} release upon cellular stimulation, Ca^{2+} is leaking from the ER already at steady state. A large number of channels contribute to this Ca^{2+} leak, although their precise roles remain to be fully elucidated. It has been shown that the two classical Ca^{2+} release channels (RyR and IP_3R) are capable of releasing Ca^{2+} in the absence of ligand binding at low cytosolic Ca^{2+} concentrations (below 1 µM). The phosphorylation of the RyR was observed to enhance the Ca^{2+} release by destabilizing the channel. Similarly, hyperphosphorylation of the IP_3R or its proteolytic cleavage uncoupling the channel domain of the IP_3R have been described to result in increased Ca^{2+} leak from the ER. [100,101] Several studies have shown that the Ca^{2+} release activity of the IP_3R after ligand binding can be also regulated and is modulated in different ways. Serine phosphorylation of the IP_3R by protein kinase A (PKA) sensitizes the receptor's affinity for binding of IP_3, thereby enhancing its opening probability [102]. Other proteins, such as PLCβ and adenylyl cyclase 6, have been demonstrated to augment IP_3R activity by enhancing the delivery of IP_3 to the receptor [103]. In addition, Zeng *et al.* revealed that Gβγ results in IP_3R activation and Ca^{2+} release in an IP_3-independent manner [104]. Conversely, IP_3R is inhibited by Ca^{2+}-dependent proteins, such as calmodulin and calcineurin, which may function as a negative feedback mechanism following IP_3R activation [103,105].

In order to counteract the constant Ca^{2+} leak and Ca^{2+} release in response to stimulation, SERCA pumps Ca^{2+} against its chemical gradient into the ER lumen using energy from ATP hydrolysis [100,101]. In several studies, the specific and irreversible SERCA inhibitor thapsigargin has been used to induce a Ca^{2+} depletion from the ER and to investigate the Ca^{2+} leak into the cytosol and amplification via SOCE [106]. It has been shown that SERCA activity is modulated by a number of micropeptides, including phospholamban (PLN), sarcolipin (SLN), dwarf open reading frame (Dworf), myoregulin (MLN), endoregulin (ELN) and another-regulin (ALN). These micropeptides have been described to bind to the same groove. [107,108] In contrast to all other regulins, Dworf, which is expressed in cardiac muscle, has been identified as the only molecule so far that results in stimulation of SERCA [108,109]. It has been demonstrated that while MLN and SLN are expressed in skeletal muscle cells, PLN is mainly restricted to cardiac muscle cells and ELN is detected in epithelial and endothelial cells. In contrast, ALN has been described as a ubiquitously expressed SERCA modulator.[107,108] While SLN and ALN have been shown to decrease SERCA activity, PLN mainly interferes with the calcium sensitivity [108,110,111]. Generally, inhibitory functions of all regulins have been described to depend on their phosphorylation status, since they inhibit SERCA only in their dephosphorylated state [108]. It has been shown that PLN, which is - due to its role in cardiac contractility - the most extensively studied micropeptide, may undergo phosphorylation by multiple kinases, whereas protein phosphatase 1 leads to its dephosphorylation and hence sustains the inhibitory effect of PLN on SERCA [108,110]. Furthermore, elevated cytoplasmic Ca^{2+} concentrations have been shown to diminish PLN-mediated inhibition of SERCA [112], while enhancing the affinity of the SERCA activator Dworf [113].

2.3.1.3. Signaling pathways activated downstream of G protein-coupled receptors

GPCRs include a broad range of receptors that respond to a wide range of stimuli. P2Y receptors, which are involved in the induction of inflammatory cytokines and anti-viral responses, are activated by binding of different nucleotides [114]. Both P2Y2 and P2Y11 have been demonstrated to be activated by ATP and contribute to chemotaxis induced by ATP, which is released by apoptotic cells [115]. Furthermore, a positive feedback loop involving ATP secretion and subsequent P2Y2 activation has been revealed in the context of C5a-dictated migration of peritoneal macrophages [116].

The calcium-sensing receptors (CaSR) are GPCRs that are activated in response to sensing elevations of extracellular Ca^{2+} concentrations [117]. The increase in cytosolic Ca^{2+} concentrations upon activation of CaSR is not only mediated by Ca^{2+} release from the ER via the IP_3R but also relies on interaction with TRP channels [118,119]. Moreover, the activation of CaSR has been demonstrated to play a role in the chemotaxis and the recruitment of macrophages to sites of infection and injury, where elevated Ca^{2+} concentrations are detectable [120].

Chemokine sensing by G protein-coupled chemokine receptors plays a putative role in shaping macrophage-mediated immune responses, contributing to a range of processes, including cytokine secretion, macrophage recruitment and polarization. [121,122]

Upon activation, GPCRs interact with three main regulatory proteins, namely the guanine nucleotide-binding (G) proteins, G protein-coupled receptor kinases (GRK) and β-arrestins. G protein-mediated signaling results in the activation of enzymes that are critically required for various physiological changes and cellular responses, which will be described in greater detail below. [123] Conversely, GRK and β-arrestin are implicated in the termination of GPCR signaling. [124,125]

G proteins are heterotrimeric proteins composed of an alpha (Gα), beta (Gβ) and gamma (Gγ) subunit. Upon activation, guanosine diphosphate (GDP) bound to the Gα protein is exchanged for guanosine triphosphate (GTP), and a dimer of Gβ and Gγ (Gβγ) dissociates from the G protein complex. [123] By interacting with the GDP-bound Gα subunit, Gβγ possesses an inhibitory function on the G protein complex. Additionally, Gβγ is involved in the modulation of the activity of various proteins. Gβγ exerts its effects through protein-protein interactions, resulting in the activation of the phosphoinositide-3-kinase (PI3K) and phospholipase C β (PLCβ) and in the modulation of adenylyl cyclase (activation of AC2,4,7 and inhibition of AC1,5) [123,126,127]. PI3K and subsequent activation of the serine/threonine kinase Akt constitute a signaling pathway involved in cell survival, whereby pro-apoptotic signals are downregulated. Downstream effectors of Akt include inhibition of the pro-apoptotic transcription factor Foxo1/3, as well as the activation of NF-κB and mammalian target of Rapamycin (mTOR) supporting protein synthesis. [123]

The Gα subunits can be classified into four distinct groups: $G\alpha_s$, $G\alpha_i$, $G\alpha_q$ and $G\alpha_{12/13}$ [128]. It has been proposed that selectivity to Gα proteins depends on structural variations mainly within the C terminus governing the binding ability to one or several G proteins [129,130]. While the signaling of chemokine receptors, including CCR2 and CCR7, activates $G\alpha_i$, CaSR has been linked to both $G\alpha_i$ and $G\alpha_q$ activation [131–133]. The signaling of purinergic GPCRs is more diverse and can be grouped into $G\alpha_q$ (such as P2Y2) as well as $G\alpha_i$-coupled (such as P2Y11) receptors, which often further couple to one or more other Gα subunits [134].

The main targets of the $G\alpha_s$ subunit are adenylyl cyclases (ACs) resulting in the generation of cAMP, which activates PKA. PKA phosphorylates a variety of downstream effectors, thereby modulating their activity. One such effector is the cAMP-responsive element-binding protein (CREB), a cellular transcription factor that supports cellular proliferation and immune regulation. [123,135] In contrast, $G\alpha_i$ has been demonstrated to inhibit ACs resulting in the reduction in cAMP levels [128]. $G_{12/13}$ signaling primarily results in Rho guanine exchange factor (RhoGEF)-mediated activation of Rho, which regulates the actin cytoskeleton [136,137]. Activation of $G\alpha_q$ is primarily known to induce the activation of PLCβ [123,137]. Generally, the various Gα subunits as well as Gβγ have all been described to be involved in the induction of various mitogen-activated protein kinase (MAPK) pathways, which modulate the activity of transcription factors influencing cell proliferation and survival as well as regulating actin dynamics and chemotaxis [131,138,139].

PLCβ, activated by $G\alpha_q$ and Gβγ signaling, catalyzes the conversion of phosphatidylinositol 4,5-bisphosphate (PIP_2) to IP_3 and diacylglycerol (DAG) (Figure 5). IP_3 induces the activation of the IP_3R, which then mediates the release of Ca^{2+} from the ER. [97,140] The corresponding increase in cytosolic Ca^{2+} concentrations is further amplified via SOCE (see 2.3.1.1). DAG, on the other hand, has been shown to activate the protein kinase C (PKC), which mediates the phosphorylation of the protein phosphatase 1 (PP1) inhibitor I-1 [141,142]. PKC-mediated phosphorylation of I-1 reduces its affinity for PP1, thereby increasing PP1 activity [142,143]. Subsequently, PP1 induces the dephosphorylation and activation of the inhibitory function of the SERCA inhibitor PLN. [142,144] Inhibition of SERCA attenuates the Ca^{2+} transport into the ER, which further increases cytosolic Ca^{2+} concentrations [142,145].

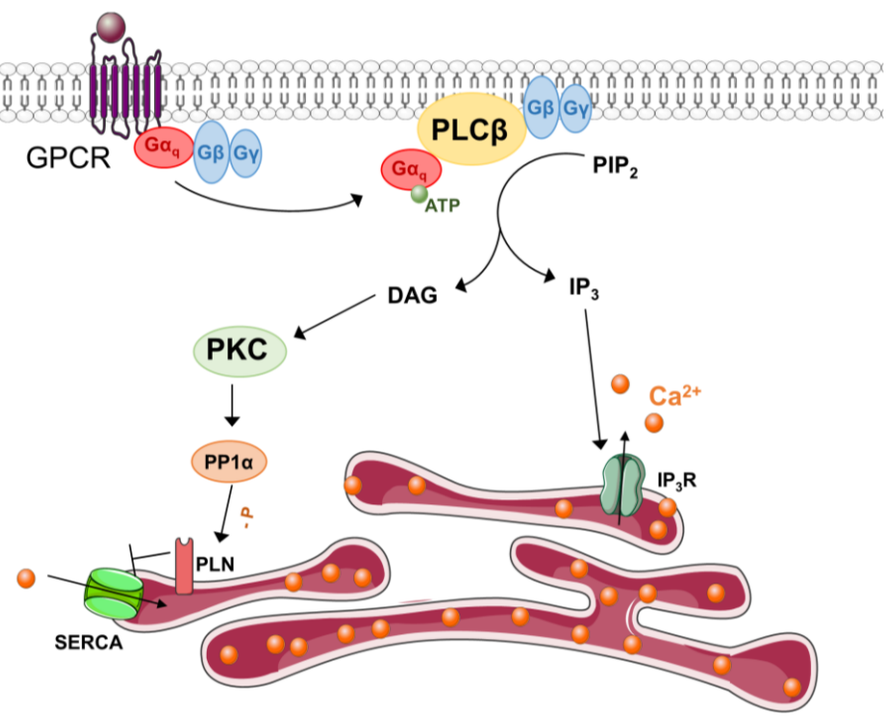

Figure 5 – GPCR-mediated PLCβ signaling
GPCR activation results in Ca^{2+} release from the ER by activation of the IP_3R and inhibition of SERCA. Following GPCR activation, $G\alpha_q$ or Gβγ activate PLCβ, which converts PIP_2 to DAG and IP_3. IP_3 opens its respective Ca^{2+}-transporting receptor in the ER. DAG mediates the inhibition of Ca^{2+} transport into the ER by increasing the inhibitory activity of the SERCA modulator PLN via PKC and PP1 signaling. *Abbreviations: Ca^{2+}, calcium; DAG, diacylglycerol; GPCR, G protein-coupled receptor; $IP_3(R)$, inositol triphosphate receptor; P, phosphate/phosphorylation; PIP_2, phosphatidylinositol 4,5-bisphosphate; PKC, protein kinase C; PLCβ, phospholipase C beta; PLN, phospholamban; PP1, protein phosphatase 1; SERCA, sarcoplasmic/endoplasmic reticulum ATPase.* [140,142] Created using Servier Medical Arts [74].

2.3.2. Calcium-dependent functions in mononuclear phagocytes

As a second messenger, Ca^{2+} is involved in a wide range of signal transduction pathways indispensable for cellular functions. In addition to the importance of Ca^{2+} in cell type-independent processes, including post-transcriptional processing and protein folding (see chapter 2.3.2.2), Ca^{2+} is essential for several immune cell- and macrophage-specific functions (Figure 6). [85,101,146]

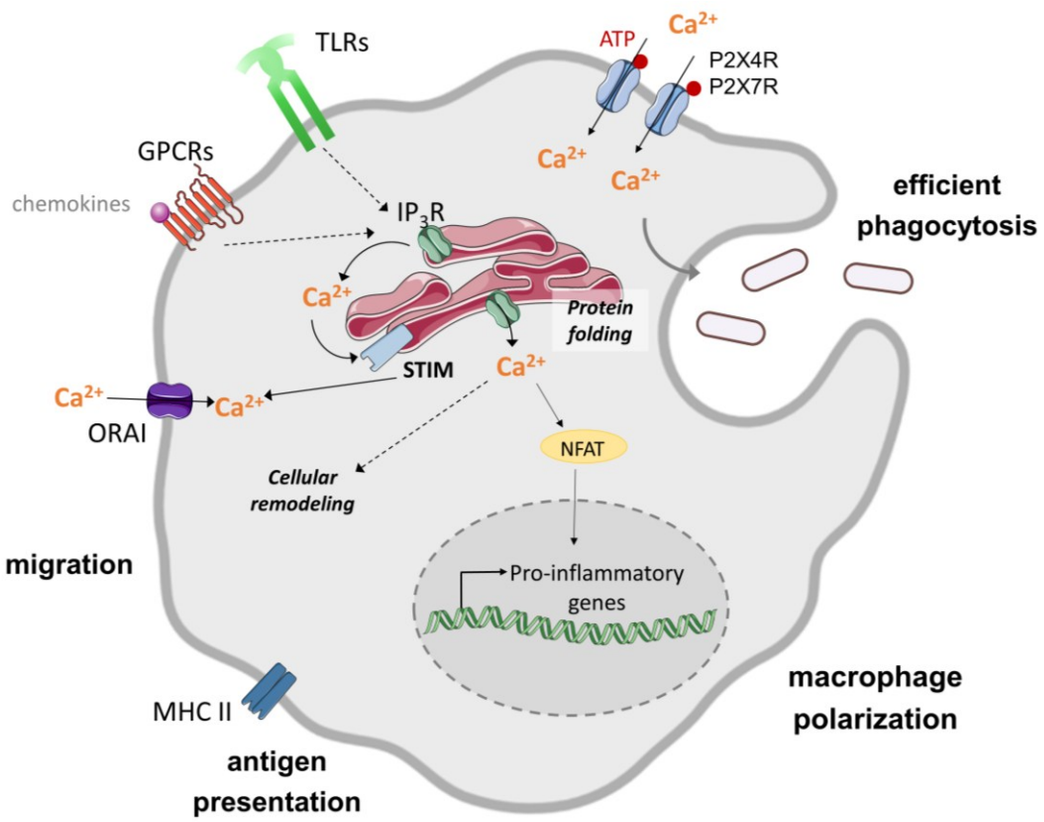

Figure 6 – Calcium is crucial for macrophage function
Calcium (Ca^{2+}) is involved in various cellular processes and therefore essential for macrophage function, including migration, antigen presentation via MHC II, phagocytosis as well as macrophage polarization. Chaperones involved in protein folding, proteins involved in cytoskeletal remodeling and activation of transcription factors further rely on Ca^{2+} as cofactor. [85,146–148]. Created using Servier Medical Arts [74].

It has been shown that Ca^{2+} signaling is essential for efficient phagocytosis of pathogens and apoptotic cells [146,148]. In this context, Zumerle *et al.* demonstrated that ATP secreted by macrophages in response to microbial stimuli or derived from damaged and necrotic tissue mediates an increased phagocytic activity in neighboring macrophages through the activation of Ca^{2+} signaling via P2X4 and P2X7 receptors [146]. Furthermore, it has been shown that macrophage polarization strongly depends on Ca^{2+} signaling. While IFN-γ-mediated induction of inflammatory macrophages relies on Ca^{2+} influx via the canonical TRP channel 1 (TRPC1), Ca^{2+} signaling involved in naïve or anti-inflammatory macrophages is mainly dependent on ORAI channels [36,147]. Accordingly, in patients with systemic inflammatory response syndrome, TRPC1 levels in circulating monocytes have been observed to positively correlate with both inflammatory mediators as well as the severity of disease [147].

During the process of cellular migration, Ca^{2+} is not only involved in the propagation of signals in response to migratory stimuli but is also required as a cofactor for various proteins involved in cytoskeletal remodeling, which enables cellular migration (for further details refer to chapter 2.3.2.1) [76,149].

Additionally, it has been demonstrated that Ca^{2+} is involved in the induction of pro-inflammatory cytokine production. For example, the sensing of LPS results in the mobilization of Ca^{2+} via a PLCγ2-dependent mechanism that is independent of TLR4. This process involves the binding of LPS to CD14 and induction of Ca^{2+}-dependent proteins, which in turn enables the nuclear translocation of several transcription factors [150,151]. Moreover, LPS has been demonstrated to result in increased expression of synaptotagmin VII, which is involved in exocytosis required for efficient MHC II presentation as well as efficient phagocytosis [152]. LPS-mediated processes rely on both Ca^{2+} increase from intracellular stores as well as from extracellular stores. Accordingly, inhibition of SOCE with SKF-96365 has been shown to reduce MHC II presentation, secretion of TNF and IL-6 as well as chemokine-mediated migration [153].

As already stated above, cellular activation and Ca^{2+} signaling can result in a Ca^{2+}-dependent increase in gene transcription. An increase in cytosolic Ca^{2+} levels leads to the activation of various Ca^{2+}/Calmodulin-dependent protein kinases and phosphatases, including Ca^{2+}/calmodulin-dependent protein kinase II (CaMKII) and calcineurin, respectively. [154,155] It has been shown that the activation of calcineurin mediates the dephosphorylation of the nuclear factor of activated T cells (NFAT), while the activation of CaMKII mediates the phosphorylation of NF-κB, resulting in the nuclear translocation of both transcription factors and induction of the transcription of pro-inflammatory cytokines [150,156].

2.3.2.1. Cellular migration

Macrophage migration plays a crucial role during both homeostasis and inflammation, as it enables these cells to fulfill their functions at the desired location within the body. Macrophages are capable of migrating on two-dimensional (2D) surfaces, such as endothelial monolayers of blood vessels, or within the extracellular matrix (ECM) within tissues forming a three-dimensional (3D) environment. [34,157]

2D migration of macrophages involves various steps to allow so-called slow rolling, increased adhesion induced by chemokine receptor signaling, crawling and finally para- or transcellular migration of the macrophages, a process that is strongly dependent on adhesion receptors of the selectin and integrin family [34,157,158]. 3D migration can be subdivided into amoeboid and mesenchymal migration. The rather fast amoeboid movement occurs mainly in areas with loose ECM and depends on chemoattractant signaling via GPCRs, which is particularly relevant during inflammation. In contrast, in mesenchymal migration cells attach to the ECM via integrins and degrade the dense ECM resulting in slower movement. [34,159]

Cellular migration towards sites of inflammation or tissue injury as well as within lymphatic vessels is directed by chemokine gradients. Chemotactic migration, which is initiated in response to chemokine stimulation of the respective receptors, involves Ca^{2+}-dependent cellular signaling cascades and cellular remodeling. Since chemokine receptors belong to the family of GPCRs, sensing of changes in chemokine gradients by the respective receptors activates signal transduction pathways that mediate the release of Ca^{2+} from the ER [160]. The chemokine C-C motif ligand 2 (CCL2), also known as monocytic chemotactic protein 1 (MCP-1), is especially involved in the recruitment of immune cells from the blood into the tissue during infection. Its respective receptor, C-C chemokine receptor type 2 (CCR2) has been demonstrated to be particularly expressed by blood monocytes, natural killer cells and memory T lymphocytes [161,162]. Sources of CCL2 include various cell types, such as endothelial cells, epithelial cells and myeloid cells, and its expression is further induced by inflammatory immune mediators [163]. In addition to its chemotactic activity, various studies have described the involvement of CCL2 in integrin-dependent adhesion, phagocytic capacity as well as a potential role in the induction of cytokine secretion and macrophage polarization [163–165]. In contrast to CCL2, the chemokine CCL19 mainly dictates the migration of antigen-presenting cells to secondary lymphoid organs, a crucial step during adaptive immunity induction. CCR7, the receptor for CCL19, has been demonstrated to be not only expressed by naïve and memory T cells and B cells but also by monocytes, macrophages, and, in particular, mature dendritic cells (DCs). [122,166]. Upon immune stimulation and antigen loading, expression of CCR7 is strongly upregulated facilitating increased infiltration into lymphoid organs and subsequent activation of T cells [166,167].

Ca^{2+} plays a fundamental role during the process of migration, as it is involved in both the transduction of external signals and cytoskeletal remodeling. In summary, the actin reorganization and the formation of actin-dependent protrusions at the leading edge are tightly regulated by a range of Ca^{2+}-dependent proteins, including small GTPases and the myosin light chain kinase. Furthermore, both the assembly and the disassembly of focal adhesions are strongly dependent on the fine-tuning of cellular Ca^{2+} concentrations. [76,168]

Accordingly, variations in migratory dynamics can often be attributed to changes in Ca^{2+} signaling. The role of SOCE yet remains open and controversial. Depletion of SOCE has been shown to attenuate chemotactic velocity and thus total distance as well as to further disturb the fine dynamics of the cytoskeleton in the leading edge of macrophages exposed to various chemoattractants [169]. Recently, Fresquez *et al.* revealed that increased infiltration of macrophages observed during inflammation in male mice could be attributed to increased SOCE, which enhanced the migratory capacity of monocytes [170]. Various studies further link TRP channel activity and cellular migration: Capsaicin-mediated activation of TRPV1 has been shown to induce DC migration, while TRPV4 has been implicated to be involved in cytoskeletal remodeling and reorientation [171,172].

2.3.2.2. ER stress and induction of the unfolded protein response

The processes of protein folding within the ER depend on the proper function of various molecules, which require Ca^{2+} as a cofactor: Chaperones, including calnexin, calreticulin and Binding immunoglobulin protein (BiP), assist the process of protein folding, whereas Ca^{2+}-dependent oxidoreductases and protein disulfide isomerases catalyze the formation of disulfide bonds. [101] Consequently, the disruption of Ca^{2+} signaling and the loss of Ca^{2+} from the ER have been linked to the accumulation of misfolded proteins, resulting in ER stress and the activation of the unfolded protein response (UPR). [101,173]

Activation of the UPR in turn promotes the transcription of chaperones and the degradation of misfolded proteins, while concomitantly decreasing the synthesis of new proteins. The activation of the UPR is dependent on three sensor proteins: inositol-requiring enzyme 1 (IRE1), protein kinase R-like ER kinase (PERK) and activating transcription factor 6 (ATF6). These sensory proteins usually reside in an inactive state within the ER membrane. Upon activation, ATF6 translocates to the Golgi apparatus, where it is processed by proteases resulting in the release of the cytosolic domain of ATF6. This ATF6 fragment acts as a transcription factor for the induction of BiP, X-Box binding protein 1 (XBP1) mRNA and various other chaperones. The other two UPR sensors, IRE1 and PERK, dimerize and undergo autophosphorylation upon activation. Subsequently, the phosphorylation of eukaryotic translation initiation factor (eIF) 2α by PERK results in the inhibition of general translation by preventing ribosome assembly. Simultaneously, eIF2α mediates an increase in the translation of specific mRNAs, including ATF4, which acts as a transcription factor for chaperones and antioxidant genes.

Finally, IRE1 phosphorylation leads to the activation of its intrinsic endoribonuclease activity, which mediates the splicing of the XBP1 mRNA (XBP1s). XBP1s then translocates into the nucleus, where it acts as a transcription factor regulating the transcription of UPR target genes (Figure 7). [173–175]

To restore normal ER function, the ER stress-mediated induction of UPR not only contributes to the induction of proteins supporting proper protein folding and reducing the amount of misfolded protein but also involves regulation of the ER Ca^{2+} content [173,176]. Various mechanisms have been described by which ER stress results in reduced IP_3R activity and consequently mediating a reduction in the efflux of Ca^{2+} from the ER [173,176]. IRE1 has been further described to interact with STIM1, which results in the formation of ER-plasma membrane contact sites and subsequently Ca^{2+} influx via SOCE [177].

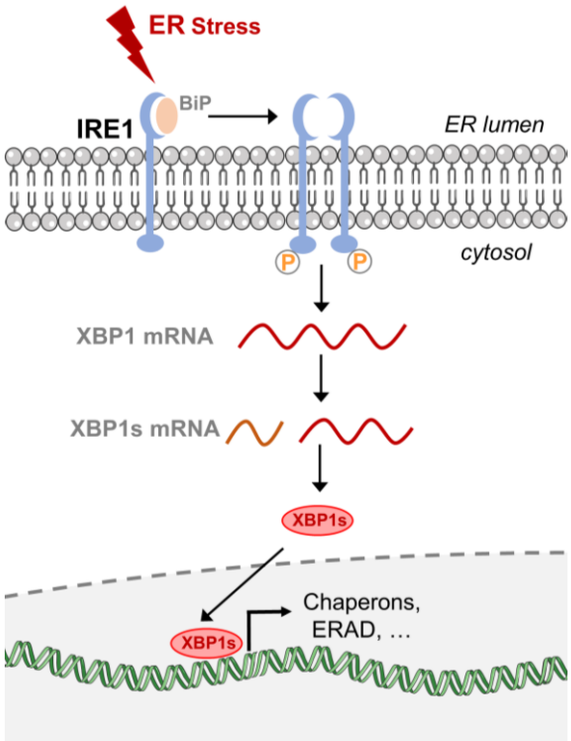

Figure 7 - ER stress sensor IRE1 mediates splicing of XBP1 mRNA
ER stress resulting from disruption of Ca^{2+} homeostasis in the ER and accumulation of misfolded proteins is sensed by IRE1 after dissociation of the chaperone BiP. Autophosphorylation and dimerization of IRE1 activates its endonuclease, which cleaves XBP1s mRNA. Spliced version of XBP1 acts as transcription factor to increase expression of chaperones and ER-associated degradation (ERAD) to increase protein folding capacity and mediate degradation of misfolded proteins. [80] Created using Servier Medical Arts [60].

Experimentally, various agents are used to disrupt ER function, thereby facilitating the study of ER stress-related processes. The majority of ER stressors rely on the accumulation of misfolded proteins, either by directly preventing proper protein folding or by disturbing Ca^{2+} homeostasis and consequently functionality of Ca^{2+}-dependent processes in the ER. The accumulation of misfolded proteins can be induced by treatment with tunicamycin, which prevents N-linked glycosylation [178] or by treatment with dithiothreitol, which disrupts disulfide bonds in proteins [179]. Thapsigargin induces ER stress by inhibiting SERCA, which results in the depletion of ER Ca^{2+} and disruption of Ca^{2+} homeostasis, thereby further contributing to impaired protein folding [180].

2.4. Aim of the thesis

Diabetes, characterized by hyperglycemia, represents a growing global health issue and is linked to chronic inflammation and several health-related complications [16,181]. As key immune sentinels, macrophages are known to contribute to the progression of diabetes and metaflammation [58]. For understanding the immunological phenotypes observed in diabetic patients, it is critical to investigate macrophage biology in the context of hyperglycemia.

Therefore, the aim of this thesis was to investigate the influence of hyperglycemia on macrophage activation and functionality. Specifically, the following research objectives were addressed:

1. **Influence of hyperglycemia on macrophage activation**

   To understand whether and how glucose influences inflammatory responses in macrophages, this thesis aimed to examine the effect of hyperglycemia on pro-inflammatory cytokine secretion by LPS-stimulated macrophages, and the molecules involved in modulating the inflammatory response.

2. **Ca^{2+} signaling in hyperglycemic macrophages**

   The second objective of this thesis was to investigate the effects of hyperglycemia on cellular Ca^{2+} homeostasis, in particular on intracellular Ca^{2+} levels and Ca^{2+} signaling. A key focus should be placed on elucidating the molecular mechanisms potentially involved in these processes under hyperglycemic conditions.

3. **Functional consequences of hyperglycemia on macrophages**

   Given that Ca^{2+} is indispensable for various macrophage functions [36,37,146], the influence of hyperglycemia on Ca^{2+}-related processes in macrophages, including ER stress and cell migration, should be investigated.

Collectively, the results of this thesis are expected to enhance our understanding of immunological changes associated with diabetes and metaflammation, particularly regarding macrophage phenotypes in hyperglycemic conditions.

3. Material and Methods

3.1. Material

3.1.1. Laboratory equipment

Equipment	Company
Balance	440-35A (Kern & Sohn, Balingen, Germany) ML204 (Mettler Toledo, Gießen, Germany)
Centrifuges	5424/5810 (Eppendorf, Hamburg, Germany)
Electrophoresis Equipment	Mini-PROTEAN and Mini Trans-Blot Cell (Bio-Rad Laboratories, München, Germany) Horizontal electrophoresis system Mini-Sub Cell GT (Bio-Rad Laboratories, München, Germany)
Electroporation System	Gene Pulser Xcell (Bio-Rad Laboratories, München, Germany)
ELISA washer	CAPP wash 12 (CAPP, Odense Germany)
Flake ice machine	Scotsman Ice Systems, Hubbard systems, Ipswich, Great Britain
Flow cytometer	BD LSR II Flow Cytometer, BD Symphony A5 (BD Bioscience, Heidelberg, Germany)
Freezer (-20°C)	Liebherr, Biberach, Germany
Freezer (-80°C)	New Brunswick Scientific, New Jersey, USA
Fridge (+4°C)	Bosch, Gerlingen, Germany Liebherr, Biberach, Germany
Heating devices	Water bath (GFL, Burgwedel, Germany) Heating block Thermostat TH21 (HLC BioTech, Bovenden, Germany)
Imaging System	ChemiDoc MP Imaging System (Bio-Rad Laboratories, München, Germany) Odyssey Infrared Imaging System (LI-COR Biosciences, Lincoln, USA)
Incubator, 37°C	Binder, Neckarsulm, Germany
Laboratory glass bottles (100 mL, 250 mL, 500 mL, 1000 mL)	Schott, Mainz, Germany
Measuring cylinder	VWR, Langenfeld, Germany
Micro balance ABJ	Kern & Sohn, Balingen, Germany
Microplate reader	Infinite 200 PRO (Tecan Trading AG, Männedorf, Switzerland)

Equipment	Company
Microscopes	TS100 (Nikon, Tokyo, Japan) IX81 (Olympus, Hamburg, Germany) TI2 (Nikon, Tokyo, Japan) Eclipse TE2000 (Nikon, Tokyo, Japan) LSM FV 1000 (Olympus, Hamburg, Germany) LSM 880 Airyscan (Zeiss, Oberkochen, Germany) Axio (Zeiss, Oberkochen, Germany) 4 channel STED Microscope (Abberior, Göttingen, Germany)
Neubauer counting chamber	Brand, Wertheim, Germany
Pipettes	Multichannel pipettes (50-200 µL), Pipettes (2-20 µL, 20-200 µL, 100-1000 µL), Accu-Jet Pro (Brand, Wertheim, Germany) Pipettes (0.1-25 µL, 1-10 µL) (Mettler-Toledo Rainin, Gießen, Germany)
Scissors, tweezers and gavage needles	Everhards, Meckenheim, Germany
Sonifier	Sonoplus GM2070 (Bandelin, Berlin, Germany)
Spectrophotometer (RNA)	NanoDrop ND-1000 (NanoDrop Products, Wilmington, USA)
Sterile bench,	Laminar Flow BDK, Sonnenbühl, Genkingen, Germany
Vortex shaker	VELP Scientifica, Usmate, Italy

3.1.2. Expendable items

Item	Company
Cannula Sterican (G26 x 1” / ø 0.25 x 40 mm)	Braun, Melsungen, Germany
Cell culture dish (100 x 20 mm, 60 x 20 mm)	Sarstedt, Nümbrecht, Germany
Cell Imaging Plate, 24 well, 10 µm coverglass bottom	Eppendorf, Hamburg, Germany
Cell scraper 25 cm	Sarstedt, Nümbrecht, Germany
Cell strainer EASYstainer™ (40 µm)	Greiner Bio-One, Kremsmünster, Austria
Disposable weighing trays	Carl Roth GmbH, Karlsruhe, Germany
ELISA plate F-Form	Greiner Bio-One, Kremsmünster, Austria
FACS tubes	Sarstedt, Nümbrecht, Germany
Gloves	Semperit Technische Produkte GmbH, Wien, Austria
Microscope slide	Thermo Scientific, Darmstadt, Germany

Item	Company
Multiwell culture plates (24 and 96 wells, flat bottom, treated and Suspension)	Sarstedt, Nümbrecht, Germany
Petri dishes	Sarstedt, Nümbrecht, Germany
Pipette tips	Sarstedt, Nümbrecht, Germany
Reaction tubes (1.5, 2.0 or 5.0 mL)	Eppendorf, Hamburg, Germany
Reaction tubes (15 or 50 mL)	Sarstedt, Nümbrecht, Germany
Serological pipettes (5, 10 or 25 mL)	Greiner, Kremsmünster, Austria
Syringes Inject (5 or 10 mL)	Braun, Melsungen, Germany
Transwell polycarbonate membrane cell culture inserts (pore size 0.5 µm)	Corning, New York, USA

3.1.3. Chemicals and reagents

Chemical or reagent	Company
100 bp DNA ladder	New England Biolabs, Ipswich, USA
2-Aminoethyl diphenylborinate (2-APB); modulator of IP_3-induced Ca^{2+} release	Sigma-Aldrich, Taufkirchen, Germany
2-Deoxyglucose	Carl Roth, Karlsruhe, Germany
4-20% Mini-PROTEAN Precast Protein Gels	Bio-Rad Laboratories, München, Germany
Adensoin-5'-triphosphate disodium salt (ATP)	Carl Roth, Karlsruhe, Germany
Agarose Standard	Carl Roth, Karlsruhe, Germany
Ammonium persulfate (APS)	Sigma-Aldrich, Taufkirchen, Germany
Bay 11-7082; NFκB inhibitor	Sigma-Aldrich, Taufkirchen, Germany
Beta-Glycerolphosphate	Sigma-Aldrich, Taufkirchen, Germany
Beta-Nicotinamide-adenine-dinucleotide, reduced disodium salt (NADH)	Biomol, Hamburg, Germany
Bisindolylmaleimide I; PKC inhibitor	Sigma-Aldrich, Taufkirchen, Germany
Bovine Serum Albumin (BSA)	Sigma-Aldrich, Taufkirchen, Germany
Bromphenolblue	Carl Roth, Karlsruhe, Germany
BSA – bovine serum albumin	Carl Roth, Karlsruhe, Germany
Calcium chloride	Carl Roth, Karlsruhe, Germany
Calcium Indicator, Cal-520 AM	AAT Bioquest, Pleasanton, USA
Calcium Indicator, Fluo-3 AM	Thermo Scientific, Darmstadt, Germany
Calcium Indicator, Fura Red AM	AAT Bioquest, Pleasanton, USA

Chemical or reagent	Company
Calcium ionophore A23187 (Calcimycin)	Sigma-Aldrich, Taufkirchen, Germany
Calyculin A; PP1/PP2A inhibitor	Cayman Chemical, Ann Arbor, Germany
Collagen I, Pure Col	Advanced BioMatrix, Carlsbad, USA
cOmplete Protease inhibitor	Sigma-Aldrich, Taufkirchen, Germany
Cyanine Cy^3 Streptavidin	Jackson ImmunoResearch, Cambridgeshire, UK
DAPI for nucleid acid staining	Sigma-Aldrich, Taufkirchen, Germany
D-Glucose	Carl Roth, Karlsruhe, Germany
D-Glucose (200 g/L)	Gibco, part of Thermo Scientific, Darmstadt, Germany
Dimethylsulfoxide (DMSO)	Carl Roth, Karlsruhe, Germany
DMEM, 4.5 g/L Glucose, w/o Sodium Pyruvate	PAN Biotech, Aidenbach, Germany
DMEM, no Glucose/L-Glutamine/Phenol Red	Thermo Scientific, Darmstadt, Germany
DNA gel stain, Sybr Safe	Thermo Scientific, Darmstadt, Germany
dNTPS	Carl Roth, Karlsruhe, Germany
EDTA – ethylenediaminetetraacetic acid	Carl Roth, Karlsruhe, Germany
ER tracker Blue White DPX	Thermo Scientific, Darmstadt, Germany
Ethanol	Sigma-Aldrich, Taufkirchen, Germany
Ethylene Glycol Tetraacetic Acid (EGTA)	Carl Roth, Karlsruhe, Germany
Ethylenediaminetetraacetic acid (EDTA, Ultrapure 0.5 M, pH 8.0)	Thermo Scientific, Darmstadt, Germany
Fetal Bovine Serum Premium	PAN Biotech, Aidenbach, Germany
Fetal Bovine Serum Standard Quality	GE Healthcare, Illinois, USA
Formaldehyde (3o%, low methanol)	Carl Roth, Karlsruhe, Germany
Geneticin (G418 Sulfate)	Thermo Scientific, Darmstadt, Germany
Glycine	Carl Roth, Karlsruhe, Germany
HBSS, with Calcium/Magnesium	PAN Biotech, Aidenbach, Germany
HBSS, without Calcium/Magnesium	PAN Biotech, Aidenbach, Germany
HEPES (1M, pH 7.0)	Thermo Scientific, Darmstadt, Germany
IMDM, 1 g/L Glucose, w/o L-Glutamine	PAN Biotech, Aidenbach, Germany
IMDM, 4.5 g/L Glucose, w/ L-Glutamine	PAN Biotech, Aidenbach, Germany
Immunoblot PVDF membrane, 0.2 µm pore size	Bio-Rad Laboratories, München, Germany
Intercept (TBS) Blocking Buffer	LI-COR Biosciences, Lincoln, USA
Ionomycin calcium salt from *Streptomyces conglobatus*	Sigma-Aldrich, Taufkirchen, Germany

Chemical or reagent	Company
Kanamycin	Carl Roth, Karlsruhe, Germany
Lactic dehydrogenase, recombinant from *Escherichia coli,* ≥90 U/mg	Sigma-Aldrich, Taufkirchen, Germany
Lactisole	Cayman Chemical, Ann Arbor, Germany
LB Agar/LB Medium (Lennox)	Carl Roth, Karlsruhe, Germany
L-Glutamine (200 mM)	Sigma-Aldrich, Taufkirchen, Germany
Lipofectamine 2000 Transfection Reagent	Thermo Scientific, Darmstadt, Germany
Lipopolysaccharide (LPS) from *Escherichia coli O127:B8*	Sigma-Aldrich, Taufkirchen, Germany
Magnesium chloride	Sigma-Aldrich, Taufkirchen, Germany
Meso-Erythritol	Thermo Scientific Chemicals, Darmstadt, Germany
Methanol	Sigma-Aldrich, Taufkirchen, Germany
Mounting Medium without DAPI	Thermo Scientific, Darmstadt, Germany
Mouse IL-6 recombinant protein, from *Pichia pastoris*	Invitrogen, Darmstadt Germany
Mouse serum	PAN Biotech, Aidenbach, Germany
N,*N*,*N*′,*N*′-tetramethylethylene-diamine (TEMED)	Carl Roth, Karlsruhe, Germany
NeutravidinTM Horseradish Peroxidase Conjugate	Thermo Scientific, Darmstadt, Germany
Nigericin	Thermo Scientific, Darmstadt, Germany
Nigericin	Thermo Scientific, Darmstadt, Germany
Nitrocellulose membrane	GE Healthcare, Düsseldorf, Germany
Odyssey Protein Molecular Weight Marker (10-250 kDa), protein Ladder	LI- COR Biosciences, Lincoln, USA
OptiMEM	Thermo Scientific, Darmstadt, Germany
Pancoll Human; Cell Separation Medium, Density 1.077 g/mL	PAN Biotech, Aidenbach, Germany
Paraformaldehyde (PFA)	Carl Roth, Karlsruhe, Germany
Penicillin-Streptomycin (10,000 U/mL Penicillin, 10 mg/mL Streptomycin)	PAN Biotech, Aidenbach, Germany
Percoll	Sigma-Aldrich, Taufkirchen, Germany
Phalloidin-iFluor 488 Reagent	Abcam, Cambridge, UK
Phorbol 12-myristate 13-acetate (PMA)	Sigma-Aldrich, Taufkirchen, Germany
Phosphate Buffered Saline Dulbecco w/o Ca2+ and Mg+	PAN Biotech, Aidenbach, Germany
Phospho(enol)pyruvic acid monopotassium salt	Sigma-Aldrich, Taufkirchen, Germany

Chemical or reagent	Company
Phusion High-Fidelity DNA Polymerase	New England Biolabs, Ipswich, USA
Pierce 660 nm Protein Assay Reagent	Thermo Scientific, Darmstadt, Germany
Pierce Pre-Diluted Protein Assay Standard: Bovine Serum Albumin	Thermo Scientific, Darmstadt, Germany
Poly-L-lysine	Sigma-Aldrich, Taufkirchen, Germany
Ponceau S Solution	Sigma-Aldrich, Taufkirchen, Germany
Potassium chloride	Sigma-Aldrich, Taufkirchen, Germany
Prolong Gold Antifade Mountant	Thermo Scientific, Darmstadt, Germany
Pyruvate kinase, from *Bacillus stearothermophilus*, 100-300 units/mg	Sigma-Aldrich, Taufkirchen, Germany
Rapamycin	Sigma-Aldrich, Taufkirchen, Germany
Recombinant human macrophage colony-stimulating factor (M-CSF)	Immunotools, Friesoythe, Germany
Recombinant murine CCL2 (MCP-1)	Immunotoools, Friesoythe, Germany
Recombinant murine MIP-3β (CCL19)	Peprotech, Hamburg, Germany
Restriction Enzymes BamHI/XhoI	New England Biolabs, Ipswich, USA
RiboLock Rnase inhibitor	Thermo Scientific, Darmstadt, Germany
Rotiphorese Gel (Acryl amide)	Carl Roth, Karlsruhe, Germany
SDS	Carl Roth, Karlsruhe, Germany
Sodium fluoride	Sigma-Aldrich, Taufkirchen, Germany
Sodium pyrophosphate	Sigma-Aldrich, Taufkirchen, Germany
Sodium Pyruvate	Carl Roth, Karlsruhe, Germany
Sodium Pyruvate	Sigma-Aldrich, Taufkirchen, Germany
Sodium-ortho-vanadate	Sigma-Aldrich, Taufkirchen, Germany
Sucralose	Cayman Chemical, Ann Arbor, Germany
Sucrose	Sigma-Aldrich, Taufkirchen, Germany
Sulfuric acid (H2SO4)	Honeywell Fluka, Wesseling, Germany
Superscript IV Reverse Transcriptase	Thermo Scientific, Darmstadt, Germany
Taq polymerase	New England Biolabs, Ipswich, USA
Thapsigargin	Sigma-Aldrich, Taufkirchen, Germany
TMB One/Plus 2	Kem-En-Tec, Taastrup, Denmark
Tris-Hydrochloride	Carl Roth, Karlsruhe, Germany
Triton-X 100	Carl Roth, Karlsruhe, Germany

Chemical or reagent	Company
Trypan Blue	Sigma-Aldrich, Taufkirchen, Germany
Tween 20	Sigma-Aldrich, Taufkirchen, Germany
U-73122; PLC inhibitor	Cayman Chemical, Ann Arbor, Germany
Zombie Violet Fixable Viability dye	Biolegend, San Diego, USA
β-Mercaptoethanol	Sigma-Aldrich, Taufkirchen, Germany

3.1.4. Solutions and buffers

Solution	Composition
2 mM EDTA/PBS (stored at 4°C)	PBS 0.5 M EDTA (1:250)
4x Laemmli Buffer	40% Glycerol 240 mM Tris/HCl (pH 6.8) 8% SDS 0.04% Bromphenolblue If necessary 5% β-Mercaptoethanol
Cell lysis buffer	50 mM Tris-HCl (pH 7.5) 1 mM EGTA (pH 8.0) 1 mM EDTA (pH 8.0) 10 mM β-glycerolphosphate 50 mM sodium fluoride 5 mM sodium pyrophosphate 1 mM sodium vanadate 0.27 M sucrose 1% Triton-X
Coating buffer	0.1 M $NaHCO_3$, pH 8.2
ELISA blocking buffer	1% BSA in PBS
ELISA wash buffer	0.05% Tween 20 in PBS
HEK medium	DMEM (+ L-Glutamine, 4.5 g/L Glucose, - Sodium Pyruvate) 10% FBS Standard Pen/Strep (100 units/mL Penicillin, 0.1 mg/mL Streptomycin) Sodium Pyruvate (1 mM)
High glucose Medium	IMDM (+ L-Glutamine, 4.5 g/L Glucose) 10% FBS Premium Pen/Strep (100 units/mL Penicillin, 0.1 mg/mL Streptomycin) β-Mercaptoethanol (50 mM)

Solution	Composition
Homogenization Buffer	250 mM sucrose 5 mM HEPES (pH 7.0) 1x protease inhibitor
Low glucose medium	IMDM (1 g/L Glucose, - L-Glutamine) 10% FCS Premium Pen/Strep (100 units/mL Penicillin, 0.1 mg/mL Streptomycin) β-Mercaptoethanol (50 mM) L-Glutamine (2 mM)
Lysis Buffer	50 mM Tris-HCl (pH 7.5) 1 mM EGTA (pH 8.0) 1 mM EDTA (pH 8.0) 10 mM β-glycerolphosphate 50 mM sodium fluoride 5 mM sodium pyrophosphate 1 mM sodium vanadate 0.27 M sucrose 1% Triton-X
Perm/Block Buffer	10% goat serum 0.5% Triton-X 1% FBS Diluted in PBS
PFA (4%, pH 7.4)	4 g PFA 100 mL PBS
Physiological metabolite medium	DMEM (- D-Glucose, - L-Glutamine, - Sodium Pyruvate) 10% FBS Premium Pen/Strep (100 units/mL Penicillin, 0.1 mg/mL Streptomycin) β-Mercaptoethanol (50 mM) L-Glutamine (0.5 mM) Sodium Pyruvate (0.1 mM) 1 g/L (5.5 mM) Glucose
Reaction Buffer	100 mM potassium chloride 10 mM magnesium chloride 20 mM HEPES 10 mM phosphoenolpyruvate 1 mM EGTA 0.5 mM NADH 2 µM calcimycin 15 U/mL pyruvate kinase 15 U/mL lactic dehydrogenase 5 µM calcium chloride

Solution	Composition
SDS Running Buffer	150 mM glycine 25 mM Tris 0.1% SDS
Sonication Buffer (pH 7.2)	120 mM potassium glutamate 20 mM potassium acetate 10 mM EGTA 20 mM HEPES
TBS (pH 7.5)	50 mM Tris, 150 mM NaCl
TBST	0.1% TWEEN®20 in 1x TBS
Towbin Buffer	25 mM Tris 192 mM glycine
Tris-Acetate-EDTA (TAE) Buffer	40 mM Tris-acetate 1 mM EDTA

3.1.5. Kits

Kit	**Company**
Mouse IL-1beta DuoSet ELISA	R&D Systems, Minneapolis, USA
Mouse TNF-alpha DuoSet ELISA	R&D Systems, Minneapolis, USA
Nucleobond Xtra Maxi Kit	Macherey-Nagel, Düren, Germany
Nucleospin Gel and PCR Clean-up Kit	Macherey-Nagel, Düren, Germany
Nucleospin Plasmid Kit	Macherey-Nagel, Düren, Germany
Quick-RNA Miniprep Kit	Zymo Research, Freiburg, Germany

3.1.6. Antibodies

3.1.6.1. ELISA antibodies

All antibodies were prepared at a concentration of 500 µg/mL.

Antigen	**Clone**	**Species**	**Conjugate**	**Company**
anti-IL-6	MP5-20F3	Rat	Purified	eBioscience
anti-IL-6	MP5-32C11	Rat	Biotin	eBioscience

3.1.6.2. Antibodies for flow cytometry

Antibody	Conjugate	Isotype	Dilution	Clone	Company
Anti-human CD14	APC	Mouse	1:300	M5E2	BioLegend
Anti-human CD16	PerCP/Cyanine5.5	Mouse	1:300	3G8	BioLegend
Anti-human CD19	PE	Mouse	1:300	SJ25C1	BioLegend
Anti-human CD3	PE/Cyanine7	Mouse	1:300	UCHT1	BioLegend
Anti-mouse CD11b	PE/Cyanine7	Rat	1:400	M1/70	Invitrogen
Anti-mouse CD45	PerCP/Cyanine5.5	Rat	1:400	30-F11	BioLegend
Anti-mouse F4/80	eFluor660	Rat	1:50	BM8	Invitrogen
Anti-mouse MHC I (H-2Db)	PE	Mouse	1:400	24-14-8	Invitrogen
Anti-mouse MHC II (I-A/I-E)	PE	Rat	1:400	M5/114.15.2	Invitrogen
Anti-Tas1R3	AlexaFluor488	Rabbit	1:100-1:400	-	Biozol

3.1.6.3. Purified antibodies

Antibody	Conjugate	Isotype	Dilution	Clone	Company
Anti-ASC	Purified	Mouse	1:100	2EI-7	Sigma-Aldrich
Anti-Flag	Purified	Mouse	1:1,000	M2	Sigma-Aldrich
Anti-GAPDH	Purified	Mouse	1:30,000	6C5	Sigma-Aldrich
Anti-IP3R	Purified	Rabbit	1:1,000	D53A5	Cell Signaling
Anti-IRE1α	Purified	Rabbit	1:1,000	14C10	Cell Signaling
Anti-mouse LYVE1	Purified	Rat	1:200	ALY7	Invitrogen
Anti-mouse MHC II (I-A/I-E)	Biotin	Rat	1:400	M5/114.15.2	Invitrogen
Anti-NFκB	Purified	Rabbit	1:1,000	D14E12	Cell Signaling
Anti-phopsho- NFκB	Purified	Mouse	1:1,000	E.949.5	Invitrogen
Anti-phospho-IP3R (Ser1756)		Rabbit	1:1,000	-	Cell Signaling
Anti-phospho-IRE1α (Ser724)	Purified	Rabbit	1:1,000	-	Invitrogen
Anti-phospho-PLN	Purified	Rabbit	1:200	-	Cell Signaling
Anti-phospho-PLN	Purified	Rabbit	1:500	-	Sigma-Aldrich
Anti-phospho-PP1α (Thr320)	Purified	Rabbit	1:1,000	-	Cell Signaling
Anti-PLN	Purified	Goat	1:1,000	-	Sigma-Aldrich

Antibody	Conjugate	Isotype	Dilution	Clone	Company
Anti-PP1α	Purified	Rabbit	1:1,000	-	Cell Signaling
Anti-SERA3	Purified	Mouse	1:1,000	PL/IM430	Santa Cruz
Anti-SERCA2	Purified	Rabbit	1:1,000	-	Cell Signaling
Anti-STIM1	Purified	Rabbit	1:200	D88E10	Cell Signaling
Anti-Tubulin	Purified	Mouse	1:1,000	DM1A	Cell Signaling
Anti-Vinculin	Purified	Rabbit	1:1,000	-	Cell Signaling
Anti-Vinculin	Purified	Mouse	1:1,000	h-VIN-1	Sigma-Aldrich
Anti-XBP1s	Purified	Rabbit	1:1,000	E9V3E	Cell Signaling

3.1.6.4. Secondary antibodies

Antibody	Conjugate	Isotype	Dilution	Clone	Company
Anti-goat	IRDye 680RD	Donkey	1:15,000	-	LI-COR
Anti-mouse IgG	AlexaFluor488	Donkey	1:800	-	Thermo Scientific
Anti-mouse/rabbit	IRDye 680RD	Goat	1:15,000	-	LI-COR
Anti-mouse/rabbit	IRDye 800CV	Goat	1:15,000	-	LI-COR
Anti-Rabbit IgG	StarRed	Goat	1:200	-	Abberior
Anti-Rat IgG (H+L)	AlexaFluor488	Donkey	1:400	-	Jackson ImmunoResearch

3.1.7. PCR Primer sequences

Target		Sequence (5' to 3')
GAPDH [182]	Forward	ACCATCTTCCAGGAGCGAGA
	Reverse	GGGCCATCCACAGTCTTCTG
PLN	Forward BamHI	GCGCGCGGATCCATGGAAAAAGTGCAATACCTCACTCG
	Reverse XhoI	GATCGACTCGAGTCACAGAAGCATCACAATGATGCAG
Primer Oligo(dT)		AAAAAAAAAAAAAAAAAA
XBP-1 [182]	Forward	GGTCTGCTGAGTCCGCAGCA
	Reverse	AAGGGAGGCTGGTAAGGAAC

3.1.8. Small interfering RNAs (siRNAs)

Target	Company	Identification
AllStars Negative control siRNA	Qiagen	Cat#1027281
Stealth siRNA targeting sequence – murine Tas1R3 #1	Thermo Scientific	Cat#MSS234755
Stealth siRNA targeting sequence – murine Tas1R3 #2	Thermo Fisher	Cat#MSS234756
Stealth siRNA targeting sequence – murine Tas1R3 #3	Thermo Fisher	Cat#MSS234757

3.1.9. Vectors

Name	Resistance	Origine
Plasmid pCMV-Tag2B	Kanamycin	Strategene

3.1.10. Animals for research

Strain	Description
C57BL/6	Wild type mice (WT)
C57BL/6J Tas1R3$^{-/-}$	Mice lacking the taste receptor Tas1R3, kindly provided by H. Wang, Monell Chemical Senses Center, Philadelphia

3.1.11. Cell lines and bacteria

Cell line/Bacteria	Description
DH5α, *Escherichia coli*	Chemically competent bacteria
HEK293T	Human Embryonic Kidney cell line
J558L GM-CSF producing line	Murine myeloma cell line (BALB/c), transduced with murine GM-CSF sequence

3.1.12. Software

Tool	Company
Affinity Designer	Serif, Nottingham, UK
Chemotaxis and Migration plug-in in ImageJ	Ibidi, Gräfelfing, Germany
Citavi	Citavi, Wädenswil Schweiz
Excel/Word, Office Standard 2019	Microsoft, Redmond, USA
FACS Diva	BD, Franklin Lakes, USA
FlowJo	TreeStar, Ashland, USA
ImageJ	ImageJ, U.S. Institues of Health, Bethesda, USA

Tool	Company
Manual Tracking plug-in in Image J	National Insitute of Health, Bethesda, USA
NanoDropTM ND-1000	Peqlab, Erlangen, Germany
Prism, Version 10	GraphPad, La Jola, USA
R, Version 4.3.1	R foundation for Statistical Computing, Vienna, Austria
Servier Medical ART	Les Labortoires Servier, Neuilly-sur-Seine, France
TECAN Plate reader software i-control 1.10	Tecan, Männedorf, Switzerland

3.2. Methods

3.2.1. Experimental models and human study details

3.2.1.1. Housing of mice and experimental design

Wild type mice were held under specific pathogen-free conditions in the Genetic Resource Center of the LIMES Institute, Bonn. If not indicated otherwise, experiments were performed with 8–12-week-old mice and mice were sacrificed by cervical dislocation or euthanization with CO_2.
Bones from the hind legs of Tas1R3$^{-/-}$ mice were kindly provided by H. Wang (Philadelphia) and shipped in PBS on ice.

All procedures were conducted in accordance with the guidelines from Directive 2010/63/EU of the European Parliament and were approved by the local institutional animal care committee (Landesamt für Natur, Umwelt und Verbraucherschutz (LANUV), North Rhine Westphalia).

To assess the influence of long-term obesity on macrophages, mice from a mouse maternal obesity model (as described in Mass *et al.* [183]) were used. Female 5–6-week-old mice were put on a control diet (CD, sniff E15748-047) or high-fat diet (HFD, sniff E15742-347). At the age of 50-60 weeks, mice were euthanized with CO_2. Peritoneal macrophages were then isolated as described in 3.2.2.3. In addition, peritoneal macrophages from aged mice (age between 48 and 65 weeks) were investigated in this thesis.

Blood glucose concentrations were determined using an Accu-Chek Instant blood glucose measuring device, with a blood drop obtained from the tail shortly after euthanization.

3.2.1.2. Collection of human samples

Healthy individuals as well as patients with prediabetes and/or metabolic syndrome were recruited as part of a study at the University of Bonn. This study complied with all relevant ethical regulations and was conducted in accordance with the principles of the Declaration of Helsinki and its subsequent amendments, approved by the ethics committee of the Medical Faculty, University of Bonn. Written informed consent was obtained from all the participants prior to their involvement in the study. Sample collection and physical examinations were carried out on a total of four study days. The participants were assigned to the different study days (10 to 12 participants per day) based on data collected from a query (BMI, age, gender). On every study day, venous blood samples (36 mL) were drawn in EDTA-containing cuvettes from every individual between 7:30 a.m. and 10:00 a.m. after overnight fasting for a minimum of 12 hours. In addition, anthropometric measurements, including body weight, waist circumference, and blood pressure, were determined. The blood was used for isolation of peripheral blood mononuclear cells (PBMCs) (as described in 3.2.2.4.) as well as clinical characterization by the central laboratory at the University Hospital Bonn.

For the generation of monocyte-derived macrophages, buffy coats from healthy donors were obtained from the University Hospital Bonn after approval from the local ethics committee. In addition, fresh blood was obtained from healthy volunteers after written informed consent.

3.2.2. Cell isolation and cell cultivation procedures

All cells were cultured at 37°C with 5% CO_2 and a relative humidity of 90%. The procedures were performed under sterile conditions. Adherent cells were detached with 2 mM EDTA in PBS for 5 to 10 min at 37°C. If not indicated otherwise, cells were centrifuged at 300 x g for 5 min.

To resemble a more physiological environment, cells were deprived of excessive amounts of nutrients and cultured in a medium containing physiological concentrations of glucose (5.5 mM), pyruvate (0.1 mM) and glutamine (0.5 mM) by exchanging the medium 24 h prior to the start of the experiment.

3.2.2.1. Production of GM-CSF-containing supernatant

The supernatant containing Granulocyte/Macrophage Colony-Stimulating Factor (GM-CSF) was produced using transgenic J558 cells capable of secreting GM-CSF into its supernatant.

J558 cells were initially thawed and then subjected to selection using Geneticin (1 mg/mL) for a duration of one week. Following this, the cells were expanded and finally plated at a density of $0.5*10^6$/mL in high glucose medium. After four days, the supernatant was collected, centrifuged and sterile filtered with a BottleTop filter (0.2 µm). The GM-CSF concentration was determined by ELISA and the sterile supernatant was stored in aliquots at -20°C.

3.2.2.2. Generation of GM-CSF-grown bone marrow-derived macrophages

To isolate bone marrow cells, tibiae and femurs were dissected and the surrounding tissue and muscles were removed. Bones were opened under sterile conditions and flushed out with PBS using a 10 mL syringe with a cannula (26G). Cells were separated and filtered through a 40 µm cell strainer.

Bone marrow cells were plated in 12 mL medium with GM-CSF-containing supernatant (final concentration of 25 ng/mL) onto three 10 cm petri dishes. Unless indicated otherwise, glucose was adjusted to concentrations comparable to those found in mammalian plasma (5.5 mM), while glutamine (2 mM) and sodium pyruvate (1 mM) were provided at elevated concentrations in the medium used for differentiation, ensuring sufficient nutrient availability required for proliferation and differentiation. Cells were split in a 1:2 ratio (six 10 cm or twenty 3 cm dishes) at day three of cultivation. At day six, the medium was replaced by a medium containing physiological concentrations of glucose (5.5 mM), glutamine (0.5 mM) and sodium pyruvate (0.1 mM). In this thesis, the murine bone marrow cells differentiated with GM-CSF are referred to as bone marrow-derived macrophages (BMDMs).

After 24 h, additional glucose (final concentration 11 mM), sucralose (1 mM) or the glucose analog 2-deoxyglucose (2-DG, 5.5 mM) were added for 4 h, 24 h or 48 h. If indicated, inhibitors were added simultaneously with sugars: 2-APB (100 µM, 24 h), Bay11-7082 (30 µM, 24 h), BIM (1 µM, 4 h), Calyculin A (10 nM, 4 h), Rapamycin (10 nM, 24 h), PMA (100 nM, 24 h), U73122 (0.2 µM, 48 h), thapsigargin (500 nM for 4 h or 3 µM for 3 h).

3.2.2.3. Isolation of murine peritoneal macrophages

In order to isolate peritoneal macrophages, the body surface of euthanized mice was disinfected and the skin was carefully opened without damaging the peritoneum. The peritoneal cavity was then filled with 5 mL of 2 mM EDTA in PBS and 5 mL of air by peritoneal injection using a 10 mL syringe and a 26G needle (0.45 mm diameter). Subsequently, peritoneal cells were detached and dissolved in the solution through gentle massage and shaking of the mouse's body. The peritoneal cells were then isolated by aspirating the solution using the syringe.

The isolated peritoneal cells were either utilized directly for analysis by flow cytometry or peritoneal macrophages were cultivated for two days. For the cultivation process, the cells were plated ($1*10^6$ per well in 12 well, $5*10^4$ per well in 96 well plate) and allowed to settle down for 2 h. Then, the medium containing non-adherent cells was removed and fresh medium with either physiological (5.5 mM) or elevated (11 mM) glucose concentrations was added to the cells. The medium was exchanged after 24 h and then incubated for additional 24 h.

3.2.2.4. Isolation of human peripheral blood mononuclear cells (PBMCs)

Human PBMCs were isolated by density gradient centrifugation with Pancoll (density 1.077 g/mL). In detail, 9 mL of fresh blood collected in EDTA-containing cuvettes or approximately 15 mL of blood from a buffy coat were transferred into 50 mL canonical tubes. The volume was filled up to 35 mL by addition of PBS. The PBS-blood layer was underlayered with 14 mL Pancoll using a 10 mL pipette. Tubes were then centrifuged at 610 x g for 30 min at room temperature (acceleration 4, break 1). The PBMC layer was carefully collected using a 10 mL pipette and transferred to a new 50 mL canonical tube. The tubes were filled up with ice-cold PBS to a final volume of 50 mL and centrifuged at 610 x g for 10 min at 4°C. The resulting cell pellets were resuspended in another 50 mL of ice-cold PBS and centrifuged at 200 x g for 10 min at 4°C to remove platelets. Afterwards, the PBMCs were either directly stained for analysis by flow cytometry or further processed for the isolation of monocytes (see 3.2.2.5).

3.2.2.5. Isolation of human monocytes and generation of human M-CSF-derived macrophages

In order to further separate lymphocytes and monocytes, the monocyte fraction was isolated using a hyper-osmotic density gradient centrifugation (48.5% Percoll in 0.16 M sodium chloride solution). Initially, 10 mL of hyper-osmotic solution was added to a 15 mL canonical tube. Subsequently, the isolated PBMCs resuspended in RPMI 1640 (150-200*10^6 cells in 3 mL) were slowly added on top. The tubes were centrifuged at 580 x g for 15 min at room temperature (acceleration 4, break 1) and monocytes were isolated from the interphase layer. Following a washing step with ice-cold PBS (centrifugation 350 x g, 10 min, 4°C), 2*10^6 cells were plated into 6-well plates. After incubation for 2 h, the medium was exchanged to remove cellular debris and non-adherent cells.

Human monocytes were differentiated into macrophages with 100 µg/mL M-CSF. After cultivation for three days (low glucose medium), the medium was exchanged for an M-CSF-supplemented medium containing physiological amounts of glucose (5.5 mM), glutamine (0.5 mM) and pyruvate (0.1 mM). After 24 h, glucose (final concentration 11 mM) was added to the culture. Human macrophages were used for experiments after incubation for additional 48 h.

The successful differentiation of human monocytes with M-CSF into macrophages was confirmed by analyzing the surface expression of CD14, CD163 and CD206 via flow cytometry. In line with the literature [184–186], the monocyte-derived macrophages could be characterized as $CD14^+$ cells with clear expression of CD206 and CD163 (Figure 8).

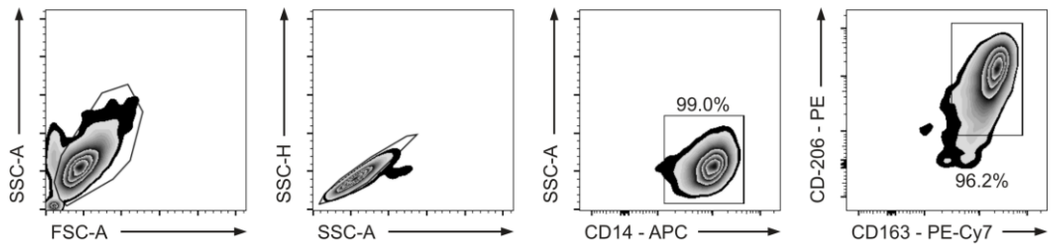

Figure 8 – Phenotypic characterization of human monocyte-derived macrophages
Human monocytes isolated from fresh blood were differentiated with M-CSF for six days. Expression of typical surface markers was analyzed by flow cytometry. Gating strategy to validate expression of surface markers (CD14, CD163, CD206) in M-CSF-derived macrophages gated for single cells.

3.2.2.6. Cultivation of HEK cells

Human embryonic kidney (HEK) cells were cultured on cell culture dishes. For splitting, $0{,}4*10^6$ cells for three days or $1*10^6$ cells for two days were plated on 10 cm dishes.

3.2.3. Flow cytometry

3.2.3.1. Surface staining

Cells were transferred into FACS tubes and washed with 2 mL of PBS by centrifugation at 300 x g for 5 min. The supernatant was discarded and cells were resuspended in the staining master mix. The master mix contained desired antibodies (diluted as described in 3.1.6.2) and mouse serum (1:100) to reduce unspecific binding of the antibodies, diluted in PBS. The staining was incubated for 20 min at room temperature in the dark. For staining of Tas1R3, CCR2 and CCR7, cells were incubated for 30 min at 37°C. After washing with 2 mL of ice-cold PBS, cells were resuspended in 100 µL of PBS and samples were analyzed on a BD LSR II Cytometer.

3.2.3.2. Ca^{2+} analyses by flow cytometry

To analyze cellular Ca^{2+} levels or Ca^{2+} signaling in response to various stimuli, cells were stained with Ca^{2+}-sensitive dyes. To enable the cellular uptake, the dyes were used in their acetoxymethyl (AM) ester form. Upon binding of Ca^{2+}, single-wavelength Ca^{2+} indicators, such as Cal-520 and Fluo-3, exhibit an increase in their fluorescence intensity, whereas ratiometric indicators, such as Fura Red, display an absorption shift.

For the staining procedure, cells were transferred to FACS tubes and washed with HBSS with (1.26 mM) or without Ca^{2+} by centrifugation at 300 x g (murine cells) or 350 x g (human cells) for 5 min. After discarding the supernatant, cells were stained with Fluo-3 AM (1 µg/mL), Cal-520 AM (5 µM) or Fura Red (5 µM) for 30 min at room temperature in the dark. After washing, cells were resuspended in the required HBSS and Ca^{2+} levels were monitored by flow cytometry using a BD LSR II or BD Symphony A5 flow cytometer. Excitation of Fluo-3 AM and Cal-520 AM was achieved with a Blue Laser (561 nm) and emission was recorded using a 525 nm filter with 50 nm bandwidth. For Fura Red, changes in Ca^{2+} concentrations were obtained from the ratio of increasing

signals monitored with the Violet Laser over decreasing signals monitored with the Yellow-Green laser. For the Violet Laser (405 nM) emission was recorded with a 677 nm filter with 20 nm bandwidth and for the Yellow-Green Laser (561 nm) emission was recorded with a 670 nm filter with 30 nm bandwidth.

For the measurement, cells were diluted in HBSS to reach an event rate of at least 300 events/s. After recording of the baseline, Ca^{2+} signals in response to addition of various stimuli were monitored: 2-DG (22 mM), ATP (100 µM), calcium chloride ($CaCl_2$, 1 or 2 mM), CCL2 (14.5 nM), CCL19 (500 ng/mL), meso-erythritol (5 mM), glucose (22 mM), ionomycin (1 µg/mL), sodium pyruvate (11 mM), sucralose (5 mM), thapsigargin (1 µM).
To analyze the effect of disrupting cellular signaling cascades, cells were pre-incubated with various inhibitors 10 min prior to the analysis of the Ca^{2+} response to glucose: 2-APB (100 µM), BIM (5 µM), Calyculin A (100 nM), lactisole (5 mM), U73122 (5 µM).

For the analyses of *ex vivo* peritoneal macrophages, cells were stained with a LiveDead stain and antibodies against CD45, CD11b, F4/80 and MHC II simultaneously to Cal-520 AM. This enables gating of $CD45^+$ alive singlet immune cells and subsequent discrimination of small ($CD11b^+$ $MHC\ II^+$) and large ($CD11b^+$ $F4/80^+$) peritoneal macrophages. For i*n vitro* cultured peritoneal macrophages, expression of CD11b was verified in addition to staining with Cal-520 AM.
Human PBMC subsets were stained with Cal-520 AM, a Live Dead stain as well as antibodies against CD3, CD14, CD16 and CD19. Human monocyte-derived macrophages were stained with antibodies against CD14, CD163 and CD206.

The data were analyzed using the FlowJo software as well as GraphPad Prism. After gating of the cells, changes in Ca^{2+} levels were evaluated using the Kinetics platform in GraphPad Prism. From this, a time series with values of (geometric) Mean Fluorescence Intensity ((g)MFI) for every second of the measurement can be exported. Additionally, the creation of time ranges enables the determination of various summary parameters, including the Area under the Curve (AUC) for each time frame (dt). The intensity of Ca^{2+} signaling was calculated from the difference (Δ) of the AUC normalized to one second (AUC/s) from the period before and after stimulation (Figure 9). To depict Ca^{2+} levels over time from all independent experiments in one curve, data were pooled in GraphPad Prism and visualized using the smoothing function by averaging neighboring values on each size. Curves of Ca^{2+} concentrations were normalized for samples containing peritoneal macrophages due to high variations between the

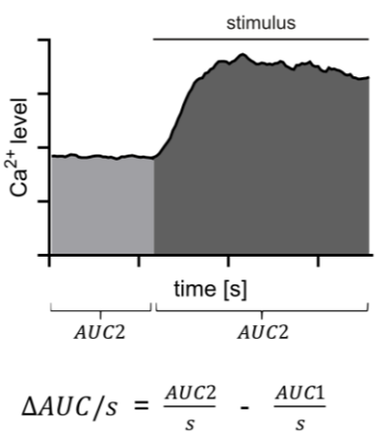

Figure 9 - Calculation of intensity of Ca^{2+} signaling
Intensity of Ca^{2+} signaling was determined as difference (Δ) of the Area under the curve (AUC) normalized to one second between the stimulated and baseline range.

experiments, as well as for inhibitor analyses to allow easier comparison. For this purpose, the mean of each baseline was calculated and then the ratio of each individual value and the respective mean was determined.

3.2.4. Cell-biological methods

3.2.4.1. Transfection of HEK cells

For transfection, $0.6*10^6$ HEK293T cells were plated on 6 cm culture dishes and incubated overnight. The following day, the medium was replaced with a medium without antibiotics and incubated for 1 h. Then, 8.5 µg of plasmid DNA and 10.5 µL Lipofectamine 2000 were separately mixed with Opti-MEM (each 145 µL) and incubated for 5 min at room temperature. Both mixtures were combined and incubated for another 20 min at room temperature and then added to the HEK cells. After 4 h incubation at 37°C and 5% CO_2 medium was replaced with Opti-MEM and incubated for two days.

3.2.4.2. siRNA-mediated downregulation of Tas1R3

RNA interference was used to downregulate the expression of Tas1R3. For this purpose, small interfering RNA (siRNA) was introduced into the cells by electroporation using a Gene Pulser Xcell Electroporator (Bio-Rad).

On day six of culture, BMDMs were harvested, washed with Opti-MEM and resuspended in Opti-MEM at a concentration of $44.4*10^6$ cells/mL. Subsequently, BMDMs ($4*10^6$) were added to 5 µg of siRNA at the bottom of a 4 mm cuvette and incubated for exactly 3 min. Two square pulses of 1000 V were applied for 0.5 ms with a time interval of 5 s. Cells were then immediately plated afterwards in high glucose medium. Four hours after electroporation, the medium was changed to physiological concentrations of glutamine (0.5 mM), glucose (5.5 mM) and sodium pyruvate (0.1 mM). Cells were analyzed after incubation for another two days.

3.2.4.3. Cytokine secretion assays

To determine cytokine secretion, BMDMs were harvested and $5*10^4$ cells were plated in a 96-well plate and allowed to adhere for 1 h at 37°C and 5% CO_2. Peritoneal macrophages were used without harvesting and re-plating. The cells were then stimulated with 50 and 100 ng/mL (BMDMs) or only 100 ng/mL (peritoneal macrophages) LPS for 3 h. For secretion of IL-1β, LPS-stimulated cells were treated with 10 µM nigericin for an additional hour. Secretion of TNF, IL-6 and IL-1β was assessed in the supernatants by ELISA.

3.2.4.4. Enzyme-linked Immunosorbent Assay (ELISA)

Sandwich-ELISA assays were performed to quantify the levels of different cytokines in the supernatant of stimulated cells. The secretion of TNF and IL-1β were determined using the DuoSet ELISA Kits from R&D Systems, whereas the secretion of IL-6 was determined using antibodies from EbioScience. Samples from BMDMs were diluted 1:3, 1:6 and 1:8 in medium for TNF, IL-6 and IL-1β, respectively. Samples from peritoneal macrophages were used undiluted.

DuoSet ELISA kits from R&D Systems were used according to manufacturer's instructions unless indicated otherwise. In contrast to the manufacturer's instructions, only 50 µL of antibody solutions, reagents and samples were added to each well. TMB Plus2 solution was used as substrate for the horseradish peroxidase. Conversion of the TMB substrate into a blue chromogenic dye was stopped by the addition of 50 µL of 0.2M H_2SO_4 and optical density was determined at 450 nm.

For IL-6, ELISA plates were coated with 50 µL of purified antibody diluted 1:1000 (0.5 µg/mL) in Coating buffer (incubation overnight at 4°C). The plates were washed three times with ELISA wash buffer between each step. The wells were then blocked with 150 µL of blocking buffer for 1 h at room temperature. Afterwards, 50 µL of samples and the standard as well as a negative control were added to the wells and incubated for 2 h at room temperature. The standard covered a range from 0.24 ng/mL to 250 ng/mL and was diluted in blocking buffer. Next, 50 µL of Neutravidin Horseradish Peroxidase Conjugate diluted 1:1000 in PBS (working concentration 1 µg/mL) were incubated 30 min at room temperature. For detection, 50 µL of TMB One Substrate was added and the reaction was stopped by adding 50 µL of 0.2M H_2SO_4. The optical density was determined at 450 nm and the cytokine concentration was calculated using GraphPad Prism by reference to the standard curve.

3.2.5. General molecular-biological methods

3.2.5.1. RNA isolation and cDNA synthesis

After incubation with 2-DG (5.5 mM) or thapsigargin (500 nM) for 4 h, up to 10^7 BMDMs were lysed in 300 µL of RNA Lysis Buffer (Zymo) and stored at -80°C. RNA was isolated using the Quick-RNA Miniprep Kit according to the manufacturer's instructions including DNase I treatment. The RNA concentrations were determined via Nanodrop and the samples were used directly or stored at -80°C until cDNA synthesis.

As first step of cDNA synthesis, 5 µg of RNA diluted in nuclease-free water were incubated with 50 µM Oligo(dT) primer and a dNTP mix for 5 min at 65°C for primer annealing. After a cooldown step to 4°C and incubation on ice for at least 1 min, 7 µL of the master mix (0.1 M DTT, 2 units/µL RiboLock, 10 units/µL SuperScript IV reverse transcriptase, diluted in SSIV buffer) was added to each tube. RNA was transcribed into cDNA by incubation at 52°C for 10 min and the reaction was stopped by inactivation of the reverse transcriptase at 80°C for 10 min. The cDNA was used directly or stored at -20°C until further use.

3.2.5.2. Polymerase chain reaction (PCR) and analysis by agarose gel electrophoresis

The cDNA was amplified by a polymerase chain reaction using primers for XBP1 [182], GAPDH [182] or PLN. To minimize mutations in cDNA, a proof-reading polymerase with high speed was used for cloning. Otherwise, cDNA was amplified using a OneTaq Polymerase.

For the OneTaq Polymerase, 23 µL of the master mix (Table 1) were added to 2 µL of each cDNA and the PCR was performed according to the protocol depicted in Table 2 in a thermocycler.

The PCR products were separated by electrophoresis in a 2-3% agarose gel poured in TAE buffer with SYBR safe (1:15,000) and visualized under UV light. The expected sizes of the PCR fragments were 256 bp (XBP1), 230 bp (spliced XBP1), 350 bp (GAPDH) or 183 bp (PLN).

Table 1 – Master mix for cDNA synthesis

Reagent	Amount for one approach
H_2O	16.38 µL
OneTaq Standard Puffer	5 µL
10 mM dNTP Mix	0.5 µL
10 µM Forward Primer	0.5 µL
10 µM Reverse Primer	0.5 µL
One Taq	0.125 µL

Table 2 – Program for cDNA synthesis

Temperature	Incubation time	
95°C	5 min	
95°C 58°C 72°C	1 min 30 s 30 s	34x
72°C	5 min	

For cloning, the cDNA was amplified with a Phusion High-Fidelity DNA polymerase according to the manufacturer's instructions. Primers were annealed at 53°C for 30 s and amplification contained 30 cycles. The PCR products were separated by agarose gel electrophoresis and the part of the gel containing the desired DNA fragments was sliced out. The DNA was purified in accordance with the manufacturer's instructions using the NucleoSpin Gel and PCR Clean-up Kit.

3.2.5.3. Cloning

Murine PLN was cloned into a pCMV-Tag2B plasmid for analysis in transfected HEK cells. The pCMV-Tag2B plasmid contains a Kanamycin resistance and enables tagging of proteins with an N-terminal Flag-Epitope. The PLN was amplified from cDNA (as described in 3.2.5.2) using primers that introduce BamHI and XhoI cutting sites.

The pCMV plasmid and purified PLN cDNA were digested with the restriction enzymes for 15 min at 37°C diluted in rCutSmart Buffer and the DNA was then purified using the NucleoSpin Gel and PCR Clean-up Kit. A T4 DNA ligase was used for ligation of 5' phosphates and 3' hydroxy ends of the DNA fragments. The reaction was incubated for 2 h at room temperature. Afterwards, competent DH5α bacteria (100 µL), which were thawed on ice, were mixed with 10 µL of ligated DNA. Following a 30 min incubation on ice, the bacteria were heated to 42°C for 90 s and then cooled down on ice for 1 min. Antibiotic-free LB Medium (1 mL) was added and incubated for 45 min at 37°C with shaking at 300 rounds/min. Thereafter, the bacteria were plated on LB agar plates containing Kanamycin (100 µg/mL) and incubated overnight at 37°C.

To confirm successful cloning, selected colonies were picked and amplified in 3 mL of LB medium (with 100 µg/mL Kanamycin) at 37°C overnight. Plasmid DNA was isolated from 1.5 mL of the culture using the Nucleospin Plasmid Kit and resuspended in 30 µL of water. The purified plasmid DNA was then digested with XhoI and BamHI as described above and separated by agarose gel electrophoresis. In addition, the correct insertion of PLN was verified by sequencing of the plasmid DNA by Eurofins Genomics.

Positive clones were further amplified in 300 mL of LB medium. The DNA was isolated using the NucleoBond Xtra Maxi Kit and the DNA concentration was determined via measurement at the NanoDrop.

3.2.6. Microscopy

3.2.6.1. Microscopic analysis of Ca^{2+} dyes

The cellular distribution of Ca^{2+} sensors used for flow cytometric analyses was assessed by confocal microscopy. Harvested BMDMs (180.000 cells) were plated into glass-bottom 24-well plates and allowed to adhere for 1 h at 37°C. After washing with HBSS containing calcium (w/ Ca^{2+}), cells were stained with Cal-520 AM (0.5 µM) or Fluo-3 AM (0.1 µg/mL) and the ER tracker Blue White DPX (200 nM) diluted in HBSS w/ Ca^{2+}. After incubation for 30 min at 37°C and washing, microscopic images were acquired using an Olympus LSM FV 1000 microscope with a 60x objective.

3.2.6.2. Microscopic analysis of Ca^{2+} signaling

In addition to flow cytometric analysis, Ca^{2+} signaling in response to ionomycin (1 µg/mL) as well as glucose (22 mM) was further monitored through live cell imaging.

Harvested BMDMs were plated on cover slips (diameter 25 mm, 125,000 cells/0.5 mL per cover slip) or into 24-well glass bottom plates (180,000 cells/well) and allowed to adhere for 1 h at 37°C. The cells were then carefully washed with HBSS w/ Ca^{2+} and then stained with Cal-520 AM (5 µM) diluted in HBSS w/ Ca^{2+} for 30 min at 37°C in the dark. The staining solution was removed and cells were again carefully washed with HBSS w/ Ca^{2+}.

For ionomycin-induced Ca^{2+} signaling, the cover slips were sealed in a custom-made circular holder and 500 µL HBSS w/ Ca^{2+} was added. Images of cells were acquired using a TS1000 microscope at a 60x magnification at a rate of one image per second. After acquiring the baseline Ca^{2+} levels for 30 s, 500 µL of HBSS w/ Ca^{2+} containing ionomycin (2x concentrated, final concentration 1 µg/mL) was added and images were acquired for another 60 s. Each condition was acquired in three technical replicates.

For glucose-induced Ca^{2+} signaling, cells were imaged in the glass bottom plates at a Nikon TI2 microscope equipped with a stationary incubation chamber. Images were acquired at a 40x magnification for 60 s and glucose (22 mM) was added after 30 s.

Image analysis was performed using ImageJ. To compare the ionomycin-induced Ca^{2+} signaling between BMDMs treated with elevated (11 mM) and physiological (5.5 mM) glucose concentrations, the fluorescence intensity of four randomly chosen cells per image was determined and the background was subtracted. Fluorescence intensities were then normalized to the baseline before addition of the stimulus and depicted over time as pooled data using the smoothing function of GraphPad Prism. The intensity of the Ca^{2+} signaling was further determined by averaging the Mean Fluorescence Intensity (MFI) after baseline subtraction. Due to bleaching, the mean was only calculated from the first 30 s after addition of ionomycin.

3.2.6.3. Quantification of cellular ASC specks

BMDMs were exposed to elevated glucose concentrations (11 vs 5.5 mM) for 48 h. Afterwards, $3*10^5$ cells were plated into 24-well glass bottom imaging plates. Cells were allowed to adhere for 45 min at 37°C and 5% CO_2 and then stimulated with 200 ng/mL LPS. After 2 h of incubation, ASC specking was induced by addition of nigericin (10 µM) for one additional hour. The medium was removed and the cells were fixed in 4% formaldehyde in PBS for 30 min at 37°C. Cells were gently washed twice with PBS and then permeabilized and simultaneously blocked for 30 min at 37°C in Perm/Block Buffer. The primary antibody against ASC (10 µg/mL, diluted in Perm/Block buffer) was incubated overnight at 4°C. The following day, the wells were gently washed three times with Perm/Block buffer and then incubated with the secondary donkey anti-mouse AlexaFluor488-coupled antibody (2.5 µg/mL, diluted in Perm/Block buffer) for 1 h at room temperature. After repeated washing, the nuclei were stained with DAPI (1 µg/mL in PBS) for 10 min at room

temperature. The wells were washed three times with PBS and the last PBS was left in the wells. Images were acquired using a Zeiss Axio microscope with a 40x objective and analyzed using ImageJ.

3.2.6.4. STED microscopy of STIM aggregates

Microscopy of membrane sheets by STED microscopy allows the evaluation of STIM1 aggregation near the plasma membrane that occurs due to the formation of ER and plasma membrane contact sites. These experiments were primarily conducted by Daniel Burgdorf under the supervision of Thorsten Lang.

Ethanol-cleaned cover slips (diameter 25 mm) were coated with poly-L-lysine (PLL, 100 µg/mL) for 30 min at room temperature, dried overnight and sterilized with UV light. Harvested BMDMs ($0.3*10^6$ in 500 µL) were plated onto the PLL-coated cover slips and allowed to adhere for 1 h at 37°C with 5% CO_2. The medium was removed and the cells were stimulated with elevated glucose concentrations (11 mM), 2-deoxyglucose (5.5 mM), or thapsigargin (3 µM) as a positive control for 3 h at 37°C. Afterwards, membrane sheets were generated. For this purpose, cells were washed once with ice-cold PBS and then placed into a dish containing ice-cold sonication buffer. To generate the membrane sheets, one ultrasound pulse of 100 ms was applied using a Sonoplus sonifier (Bandelin). Membrane sheets were then fixed in 4% PFA in PBS for 20 min at room temperature. Subsequently, PFA reactivity was quenched with 50 mM NH_3Cl in PBS for 15 min and cells were permeabilized in 0.2% Triton-X for 1 min. After washing with PBS, samples were blocked with 3% BSA in PBS and stained with the primary antibody (α-STIM1, diluted 1:200 in blocking buffer) for 1 h at room temperature. The secondary antibody solution (α-rabbit IgG StarRed, diluted 1:200 in blocking buffer) further containing Phalloidin488 (1:1000) was incubated for 1 h at room temperature, as well. Between every incubation step, the samples were washed three times with PBS for 5 min. Finally, samples were embedded in ProLong Gold Antifade Mountant onto microscopy slides, sealed with nail polish and stored at 4°C until imaging.

The membrane sheets were imaged by confocal and STED microscopy using a four-channel STED microscope (Abberior) in combination with an Olympus IX-83 confocal microscope equipped with a UplanSApo 100x objective (Olympus). Membrane sheets were selected by confocal microscopy of the stained F-actin, which was analyzed by excitation at 488 nm and detection of emission with a 510 nm filter with 20 nm bandwidth. STIM1 staining was then assessed by STED microscopy determining the StarRed signal using a 640 nm laser for excitation and a 685 nm filter with 70 nm bandwidth to record emission. Depletion of the respective signals was achieved by pulsing with a 775 nm STED laser. The pinhole was set to 1 AU and the pixel size was set to 25 nm.

In addition to STIM1, ORAI staining was simultaneously assessed as Atto594 signal. Atto594 is excited using a 561 nm laser and emission is recorded with a 605 nm filter with 50 nm bandwidth. Since both STED signals are determined simultaneously and Atto594 causes weak signals within the StarRed measurements, StarRed signals were corrected for cross-excitation using ImageJ as described before [187]. In brief, Atto594 signals were multiplied with the factor 0.5 and then signals were subtracted from StarRed signals excluding the determination of false positive STIM1 signals.

Also, further image analysis was performed using custom-made macros in ImageJ [187]. Briefly, after reducing pixel noise by smoothing the images with a Gaussian Blur filter ($\sigma = 0.5$), regions of interest (ROIs) for the background and foreground were selected. The maxima were determined within the ROI with the 'find maxima' function. A threshold was set to 5 arbitrary units to exclude detection of false maxima resulting from background signal. In addition, the area of the region of interest was calculated. The density of maxima (maxima/µm^2) was calculated as the ratio of the number of all detected maxima to the size of the selected ROI.

3.2.7. Migration assays

3.2.7.1. Transwell and 3D collagen assays

The migratory behavior of BMDMs towards CCL19 was assessed via transwell and 3D collagen assays following the methodology described by Quast *et al.* [188]. BMDMs were treated with elevated glucose concentrations (11 mM) for 48 h. Thereafter, the cells were additionally stimulated with 200 ng/mL LPS with a simultaneous exchange of half of the media. After overnight incubation, the cells were harvested and resuspended in physiological metabolite medium containing only 0.5% FBS.

In transwell assays, 700 µL of medium was added to the lower chamber and 2*10^5 cells in 300 µL were plated in the upper compartment of the inserts with a polycarbonate membrane with a pore size of 5 µm. After incubation for 1 h at 37°C, the inserts were transferred into wells containing medium with 200 ng/mL CCL19 in the lower compartments. Chemotactic migration was assessed by counting the transmigrated cells to the lower compartment after incubation for 3 h at 37°C with 5% CO_2.

Transmigrated cells were calculated using the following formula:

$$Transmigrated\ cells\ [\%] = \frac{cells\ counted\ within\ a\ big\ square\ \ *.\frac{10^4}{mL}\ \ *.0.7\ mL}{2 * 10^5}$$

For 3D collagen assays, BMDMs (final concentration $1.3*10^6$ cells/mL) were slowly mixed with ice-cold collagen solution (Collagen I with 0.7% Sodium Bicarbonate and 1x MEM) and filled into custom-made chemotaxis chambers. The collagen was allowed to polymerize for 1 h at 37°C. Medium containing 1000 ng/mL CCL19 was added on top of the gels and the chambers were sealed with heated wax. Cellular migration was monitored by automated bright-field microscopy, acquiring images every 5 min for 3 h at 37°C in a humidified environment. For this purpose, a TE Eclipse microscope (Nikon) with a 10x phase-contrast objective equipped with a heating device was used. For every experiment, 80 individual cells per condition were tracked using the manual tracking plug-in from ImageJ. Calculation of forward migration index, velocity, accumulated and Euclidian distance, as well as visualization of migratory path was performed using the chemotaxis and migration tool from ImageJ. The y-directed forward migration index (yFMI) is a measure to determine the chemotactic direction towards the chemotactic source. The yFMI is calculated as the ratio of the movement into the direction of the chemotactic source and the accumulated distance of the cell path [189]. Cells with a velocity below 0.1 µm/min were excluded in the analysis.

3.2.7.2. In situ migration

In situ migration was assessed in explanted ear sheets as described previously [190,191]. The experiments were performed by Shaunak Ghosh and Eva Kiermaier. Ears from 5-week-old C57BL/6 JRcc mice were cut off and separated into dorsal and ventral sheets using forceps. The ventral ear sheets were then placed upside down into physiological metabolite medium containing 5.5 or 11 mM of glucose and incubated at 37°C with 5% CO_2 for 24 h or 48 h. For ear sheets incubated for 48 h, the medium was replaced with fresh medium after 24 h.

Subsequently, the ear sheets were fixed in 4% PFA in PBS overnight and permeabilized in 0.2% Triton-X in PBS for 20 min. Following this, the sheets were blocked in 1% BSA in PBS for 1 h at room temperature and then incubated overnight at room temperature with primary antibodies against LYVE-1 (1:200) and MHC II (1:400, biotin-conjugated) diluted in blocking solution. Afterwards, secondary antibodies (1:400, anti-rat Alexafluor-488 and Streptavidin-Cy3) were incubated for 1 h at room temperature. Between every step, the ear sheets were washed three times in PBS for 10 min. The samples were mounted on microscopy slides with the ventral side towards a protecting cover slip in mounting medium without DAPI and stored at 4°C in the dark until analysis. The ear sheets were analyzed by confocal microscopy using a Zeiss LSM880 microscope equipped with an Airy scan module. Maximum intensity projection was performed of acquired Z stack images and the distance between cells and lymphatic vessels was quantified using a custom-made Matlab script [191].

3.2.8. Biochemical methods

3.2.8.1. Generation of cell lysates

To analyze proteins via Western blot, whole cell lysates were generated. For this purpose, cells were harvested, in 15 mL reaction tubes and centrifuged at 300 x g for 5 min. Cells were washed with 1 mL of ice-cold PBS and transferred into 1.5 mL reaction tubes. After centrifugation, cells were lysed in cell lysis buffer supplemented with protease inhibitor ($8*10^6$ cells/100 µL) by freezing at -20°C. On the day of further analysis, the samples were thawed and centrifuged at 16,000 x g for 5 min at 4°C to remove cellular debris. The supernatant was then transferred into a new reaction tube, mixed with Laemmli buffer containing β-Mercaptoethanol and heated for 5 min at 95°C.

3.2.8.2. SDS-Polyacrylamide gel electrophoresis (SDS-PAGE)

To separate proteins by molecular weight, the cell lysates were loaded onto sodium dodecyl sulfate (SDS) polyacrylamide gels. Depending on the size of the proteins to be separated, 10% to 12% resolving gels were used. For analysis of phospholamban, the proteins were separated using a 4-20% gradient gel.

The electrophoresis was performed using the MiniProtean system from Bio-Rad according to manufacturer's instructions. Separation of proteins was performed at 30 mA per gel.

3.2.8.3. Western Blot

After separation of proteins by gel electrophoresis, proteins were transferred to a membrane by Western blotting using the Mini Trans-Blot system from Bio-Rad. Except for the analysis of phospholamban, proteins were transferred onto nitrocellulose membranes by wet blotting for 60 min at 350 mA. For phospholamban, proteins were transferred onto a methanol-equilibrated PVDF membrane (0.2 µm pore size) by blotting for 30 min at 80 V in Towbin buffer with additional 20% methanol. To confirm the equal transfer and allow easier horizontal cutting, the membranes were stained with Ponceau S staining solution.

After destaining in water, the membranes were blocked in Intercept blocking buffers for 1 h at room temperature. The membranes were stained with primary antibodies diluted in Intercept blocking buffer with 0.2% Tween by overnight incubation on a rocker at 4°C. Secondary antibodies (diluted 1:15,000 in Intercept blocking buffer with 0.2% Tween) were stained for 1 h at room temperature. Between every staining step, membranes were washed three times in TBST by incubation on a rocker for at least 5 min. Infrared-chemiluminescence was detected by the ChemiDoc Imaging System. Protein levels were quantified with ImageStudioLite and ImageJ.

3.2.8.4. SERCA activity assay

SERCA activity was determined using an indirect enzyme-linked spectrophotometric assay adapted from Gehrig et al [192]. In brief, ATP hydrolysis by cellular ATPases is coupled to nicotinamide adenine dinucleotide (NADH) oxidation by various enzyme conversions. Adenosine diphosphate (ADP) is converted back to ATP by the pyruvate kinase with simultaneous conversion of phosphoenolpyruvate (PEP) to pyruvate. Lactate dehydrogenase reduces PEP to lactate leading to oxidation of NADH. NADH and NAD^+ both have an absorption maximum at 260 nm. Since NADH has a specific second absorption maximum at 340 nm, oxidation of NADH can be indirectly determined as a decrease in optical density at 340 nm (Figure 10).

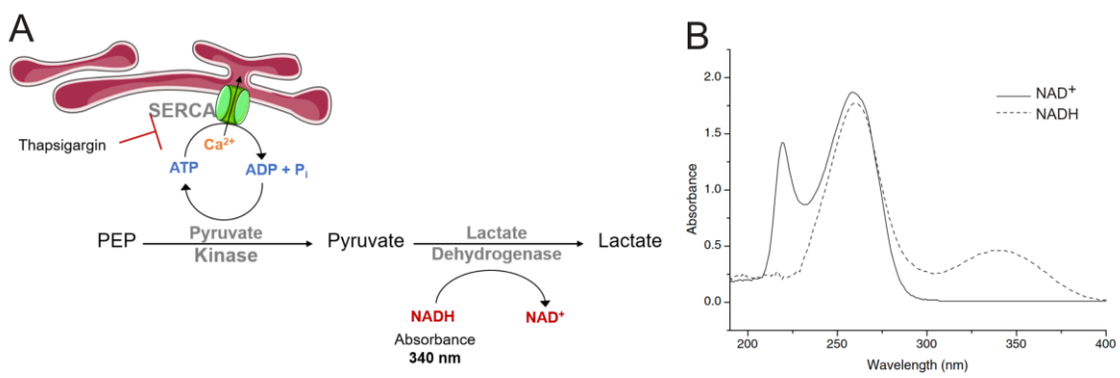

Figure 10 – Determination of SERCA activity with NADH-coupled assay
(**A**) ATP hydrolysis can be indirectly measured in an enzyme-coupled spectrophotometric assay. Pyruvate kinase generates ATP upon conversion of phosphoenolpyruvate (PEP) to pyruvate, which is further converted to lactate by the lactate dehydrogenase simultaneously oxidizing NADH. (**B**) Absorption spectra of NAD^+ and NADH. Modified from Ruyck *et al.* [193]. *Abbreviations: ATP, adenosine triphosphate; ADP, adenosine diphosphate; Ca^{2+}, calcium; NAD^+/NADH, nicotinamide adenine dinucleotide; PEP, phosphoenolpyruvate SERCA, sarcoplasmic endoplasmic reticulum calcium ATPase.*

For the assay, BMDMs were lysed in homogenization buffer for 5 min on ice. After centrifugation for 5 min at 13,000 x g, the supernatant was transferred into a new reaction tube. The protein concentration of each sample was determined using the Pierce 660 nm Protein Assay Reagent. For this purpose, 10 µL of each sample as well as 10 µL of Protein Assay Standard (BSA) were transferred into a 96-well plate. Then, 150 µL of Protein Assay Reagent were added on top and incubated for 1 min on a rocker in the dark. After further incubation for 5 min in the dark, the optical density (OD) was determined at 660 nm. The protein amount of the samples was then calculated from interpolation of the standard curve and samples were diluted in Homogenization Buffer to a final protein concentration of 600 µg/mL.

The reaction buffer was prepared on ice and mixed with each sample (final protein concentration 30 µg/mL) and 5 µM $CaCl_2$ in the absence or presence of 10 µM thapsigargin. The plates were placed into the microplate reader, which had been prewarmed to 37°C. The baseline OD at 340 nm was recorded for 3 min with 30 s intervals. Then, 5 mM ATP was added to each sample and the OD was monitored for further 20 min at 37°C with 30 s intervals. The OD of each sample was normalized to the mean of the baseline before the addition of ATP. The specific SERCA ATPase activity was

determined as the difference between the total cellular ATPase activity and the ATPase activity in the presence of the SERCA inhibitor thapsigargin.

3.2.9. Statistical analysis

GraphPad Prism, R and Excel were used for the creation of diagrams and for statistical analysis. The results were depicted as mean ± standard error of the mean (SEM). Significances, as noted in the figure legend, were calculated using paired and unpaired Student's t-test, calculation of confidence intervals, One-way ANOVA corrected for multiple comparisons by the Tukey or Dunnett method, Two-Way ANOVA corrected for multiple comparisons by the Šidák or Tukey method and Mann-Whitney test. Correlation analysis was performed using simple linear regression or Pearson correlation. Statistical significance is indicated as * $p<0.05$, ** $p<0.01$, *** $p<0.001$.

4. Results

Usually, cell culture media contain excessive, non-physiological amounts of various carbohydrates, including amino acids, glucose, glutamine and pyruvate. These serve as sources for carbon and energy production, thereby supporting optimal cell proliferation and differentiation. To resemble a more physiological microenvironment similar to mammalian plasma, a cell cultivation protocol using nutrient-deprived media has been established. Media used for differentiation of murine bone marrow-derived or human monocyte-derived macrophages in this study typically contained physiological concentrations of glucose (5.5 mM) although still elevated concentrations of glutamine (2 mM) and sodium pyruvate (1 mM). One day prior to the start of the experiment, the medium was exchanged for a medium containing physiological concentrations of glucose (5.5 mM), glutamine (0.5 mM) and sodium pyruvate (0.1 mM).

4.1. Hyperglycemia increases pro-inflammatory cytokine secretion through signaling via mTOR and NF-κB

In response to innate immune triggers, such as LPS, macrophages produce and secrete pro-inflammatory cytokines, including TNF and IL-6. Additionally, the secretion of IL-1β can be induced by the activation of LPS-primed macrophages with an additional immune stimulus, such as induction of potassium efflux by nigericin. During this activation step, caspase activation is mediated after inflammasome assembly, a process in which ASC adaptor proteins link the inflammasome sensors to the pro-caspase. [194] To assess the impact of elevated glucose concentrations on cytokine secretion, the production of the aforementioned cytokines under hyperglycemic conditions was determined by ELISA.

Incubation with elevated glucose concentrations (11 mM vs 5.5 mM) for 48 h resulted in a significant increase in TNF and IL-6 secretion by LPS-stimulated BMDMs (Figure 11A). Similarly, TNF secretion was also increased in glucose-treated peritoneal macrophages (Figure 11B).

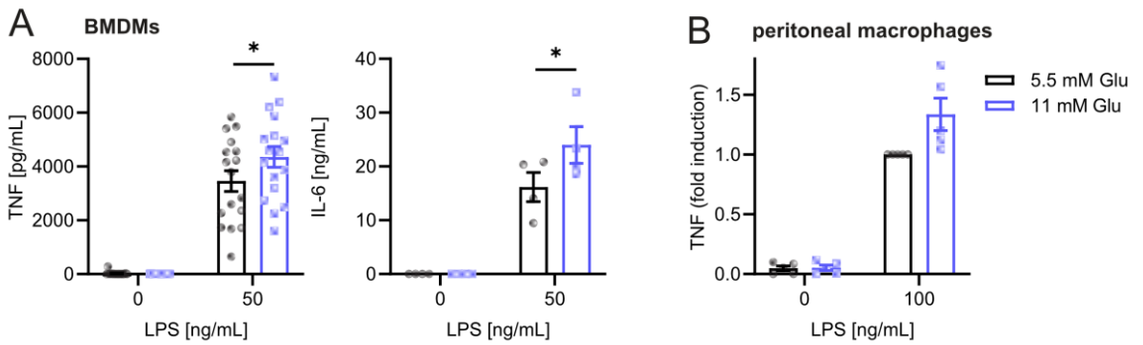

Figure 11 – Elevated glucose concentrations enhance the secretion of pro-inflammatory cytokines
BMDMs (**A**) and peritoneal macrophages (**B**) were treated with elevated glucose concentrations for 48 h. Production of pro-inflammatory cytokines (IL-6, TNF) in response to LPS (3 h) was assessed in the supernatants by ELISA (n = 17 for A (TNF), n = 4 for A (IL-6) and in B)). For peritoneal macrophages, data were normalized to cytokine levels in untreated cells. Data are shown as mean ± SEM; significance was determined by Two-Way ANOVA corrected for multiple comparisons by the Šídák method (* $p<0.05$). *Abbreviations: BMDMs, bone marrow-derived macrophages; Glu, glucose; IL-6, Interleukin-6; LPS, Lipopolysaccharide; TNF, tumor necrosis factor.*

Furthermore, the secretion of IL-1β and the formation of ASC specks were determined to assess how hyperglycemia influences the activation of the NOD-like receptor family pyrin domain containing 3 (NLRP3) inflammasome in macrophages. While IL-1β was undetectable in BMDMs stimulated with LPS alone, IL-1β secretion was detectable in response to stimulation with LPS and nigericin. A tendency towards increased IL-1β secretion was observed in macrophages treated with elevated glucose concentrations (Figure 12A). Additionally, elevated glucose concentrations were associated with an increase in the number of cells forming ASC specks (Figure 12B and C).

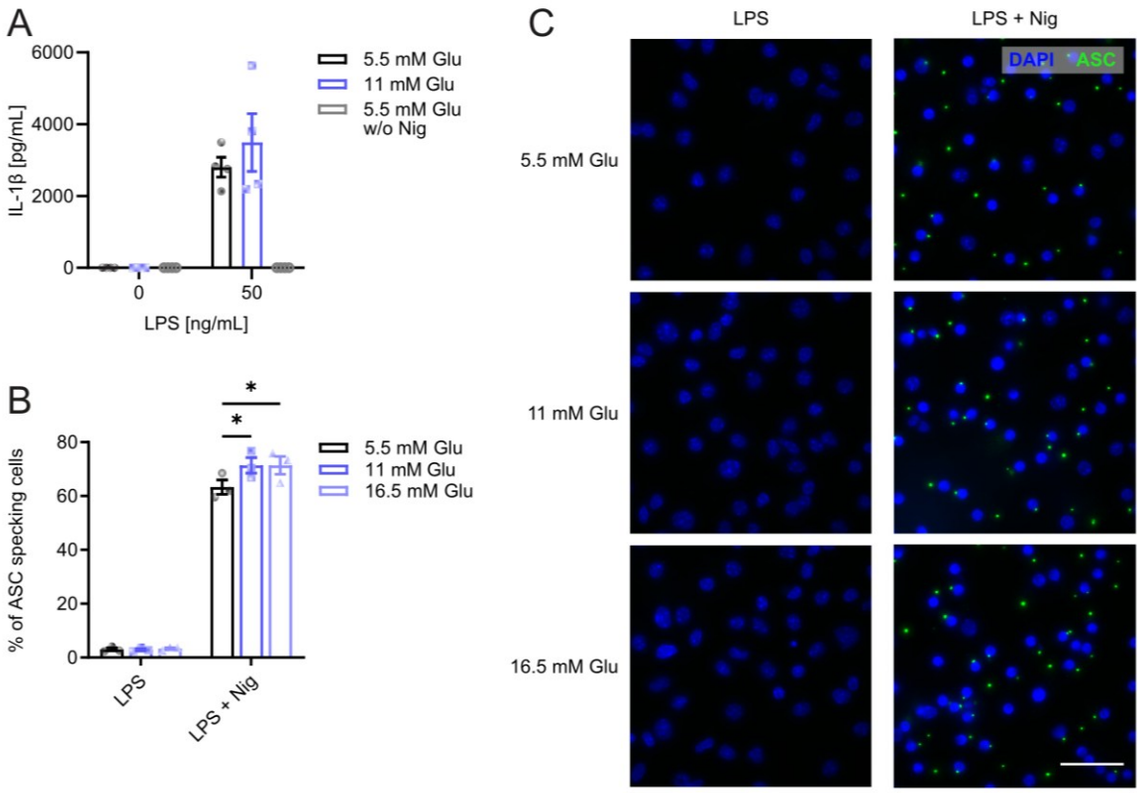

Figure 12 – Increased inflammasome activation in hyperglycemic macrophages
Glucose-treated BMDMs (48 h) were stimulated with LPS (50 ng/mL) for 3 h followed by nigericin (10 µm) for 1 h. (**A**) Secretion of IL-1β was assessed by ELISA (n = 4). (**B** and **C**) Formation of ASC specks was monitored by epifluorescence microscopy (n = 3). (**B**) Determination of the proportion of ASC specking cells. (**C**) Exemplary Z projections of immunofluorescent staining shown as merged pictures (DAPI = blue, ASC specks = green). The scale bar is equivalent to 40 µm. Data are shown as mean ± SEM; significance was determined by Two-Way ANOVA corrected for multiple comparisons by the Tukey method (* $p<0.05$). *Abbreviations: ASC, Apoptosis-associated speck-like protein containing CARD; BMDMs, bone marrow-derived macrophages; Glu, glucose; IL-1β, Interleukin-1beta; LPS, Lipopolysaccharide; Nig, nigericin; w/o, without.*

The previous data demonstrated that hyperglycemia increases the secretion of pro-inflammatory cytokines in LPS-stimulated macrophages. To elucidate the underlying mechanisms by which hyperglycemia mediates the observed effects, signaling molecules implicated in the induction of pro-inflammatory cytokines were analyzed. In order to assess whether the observed changes in LPS-stimulated macrophages at hyperglycemia were due to alterations in NF-κB activity, the phosphorylation of the NF-κB subunit p65 was monitored in glucose-treated BMDMs. Upon its activation, NF-κB is phosphorylated and translocated to the nucleus, where it functions as a transcription factor regulating the expression of inflammatory genes, including the upregulation of TNF. As depicted in Figure 13A, elevated glucose concentrations increased the phosphorylation of p65, pointing out that NF-κB activation is involved in increased cytokine secretion observed in hyperglycemic macrophages.

It has been observed that increased glucose levels activate mTOR [195], which mediates the degradation of IκB and subsequent phosphorylation of NF-κB [195,196]. To further explore the involvement of the described mTOR-NF-κB axis, BMDMs were incubated with the mTOR inhibitor Rapamycin simultaneously to treatment with elevated glucose concentrations. Indeed, addition of Rapamycin reverted both the increased phosphorylation of p65 (Figure 13B) and the elevated secretion of TNF (Figure 13C) by hyperglycemic BMDMs.

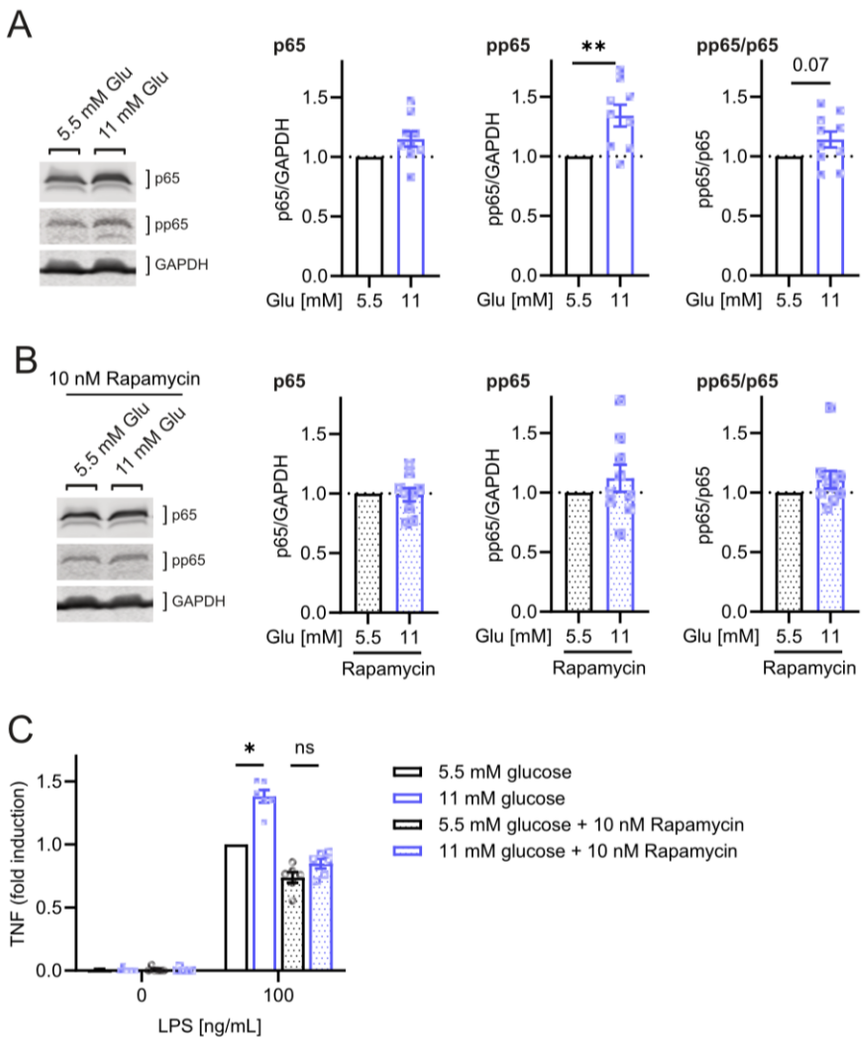

Figure 13 – Glucose-mediated increase in TNF secretion is mediated via NF-κB in a mTOR-dependent manner
BMDMs were simultaneously treated with elevated glucose concentrations and the mTOR inhibitor Rapamycin (10 nM) for 24 h. (**A** and **B**) Phosphorylation and expression of p65 were assessed in whole cell lysates by Western blot. GAPDH was used as a loading control. Exemplary blots from one out of nine independent experiments and relative expression levels normalized to untreated cells (n = 9). (**C**) Secretion of TNF after stimulation with LPS for 3 h was assessed by ELISA and normalized to untreated LPS-primed BMDMs (n = 5). Data are shown as mean ± SEM; significance was determined by the calculation of confidence intervals (* $p<0.05$, ** $p<0.01$). *Abbreviations: BMDMs, bone marrow-derived macrophages; Glu, glucose; ns, not significant.*

Taken together, the secretion of pro-inflammatory cytokines was increased in hyperglycemic macrophages. This increase could be attributed to a glucose-mediated activation of mTOR resulting in increased phosphorylation and activation of the pro-inflammatory transcription factor NF-κB.

4.2. Hyperglycemia impairs intracellular Ca^{2+} homeostasis

4.2.1. Hyperglycemia reduces cellular Ca^{2+} levels and impairs Ca^{2+} signaling

Ca^{2+} serves as a second messenger, participating in various cellular signaling pathways and being indispensable for macrophage functionality. Moreover, dysregulation of Ca^{2+} homeostasis has been documented in the context of diabetes and elevated glucose concentrations [197–200]. Accordingly, we next wanted to investigate whether hyperglycemia influences the Ca^{2+} homeostasis in macrophages.

Different Ca^{2+}-sensitive dyes have been established, allowing the monitoring of cellular Ca^{2+} concentrations by microscopy or flow cytometry. One of the longest and most commonly used green dyes for staining cellular Ca^{2+} is Fluo-3, which exhibits a 100-fold increase in fluorescence intensity upon Ca^{2+} binding [201]. Although this indicator is often designated as a cytosolic Ca^{2+} indicator, it has been reported that the dye might stain ER and mitochondrial Ca^{2+}, as well, suggesting that Fluo-3 rather stains the whole cellular Ca^{2+} [202]. In comparison to Fluo-3, the newer dye Cal-520 is characterized by an increased affinity to Ca^{2+}, resulting in a more pronounced increase in the fluorescence intensity upon Ca^{2+} binding (300-fold). Cal-520 has been further optimized to more specifically only stain cytosolic Ca^{2+}, thereby improving signal-to-noise ratios [203,204].

To evaluate the loading properties and assess the cellular distribution of Ca^{2+} staining using different Ca^{2+}-sensitive dyes in macrophages, BMDMs were loaded with Fluo-3 AM or Cal-520 AM in the presence of an ER tracker, and analyzed by confocal microscopy. Cal-520 AM uniformly stained the cytosolic Ca^{2+} (Figure 14A). In contrast, baseline Ca^{2+} signals in Fluo-3 AM-stained cells were not evenly distributed. Notably, in addition to weak signals in the cytosol, Fluo-3 AM signals strongly overlapped with the staining for the ER (Figure 14B), reflecting markedly higher Ca^{2+} concentrations in the ER compared to the cytosol [75]. Accordingly, these observations confirm that Fluo-3 AM may be used as an indicator for the whole cellular Ca^{2+}, including the ER.

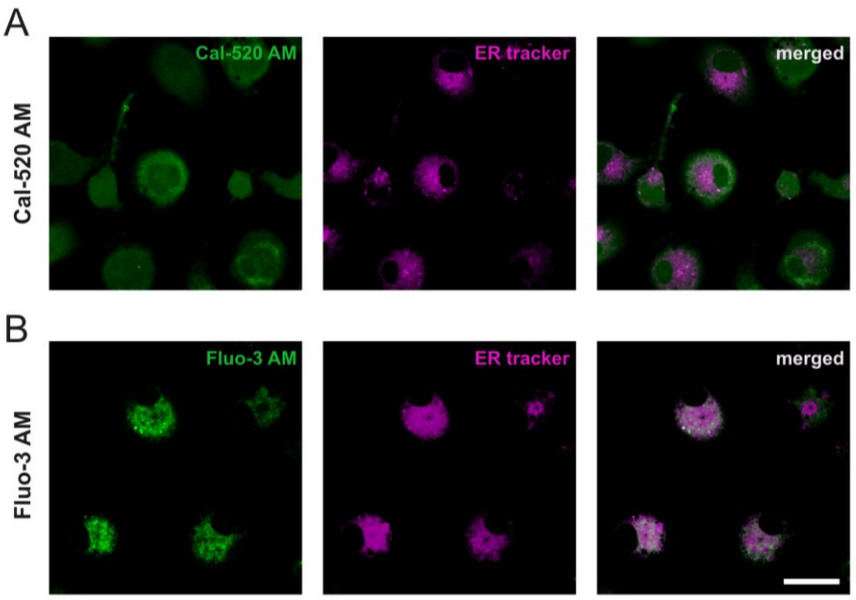

Figure 14 – Staining of BMDMs with Ca^{2+}-sensitive dyes
BMDMs were plated onto wells of glass-bottom plates and stained with the ER tracker Blue White DPX as well as a Ca^{2+}-sensitive dye, either Cal-520 AM (**A**) or Fluo-3 AM (**B**). Images were acquired by confocal microscopy. The scale bar is equivalent to 20 µm.

To thoroughly investigate how hyperglycemia affects cellular Ca^{2+} homeostasis, cellular Ca^{2+} concentrations were monitored over time following the addition of glucose. Fluo-3 AM staining was used to determine total intracellular Ca^{2+} concentrations. A slight increase in Fluo-3 AM intensity was observed after treatment with elevated glucose (11 mM) for one to two hours (Figure 15A). Strikingly, Ca^{2+} concentrations after 4 h of elevated glucose concentrations approached the levels observed in BMDMs in medium with physiological glucose concentrations. Thereafter, increased glucose concentrations led to a gradual decrease in the intracellular Ca^{2+}, stagnating after 18 h (Figure 15A). Reduced cellular and slightly reduced cytosolic Ca^{2+} concentrations were also observed after treatment of BMDMs with elevated glucose concentrations for a longer period of time (48 h) using the Ca^{2+} indicator Fluo-3 AM as well as Cal-520 AM (Figure 15B and C), demonstrating that hyperglycemia leads to a depletion of cellular Ca^{2+}.

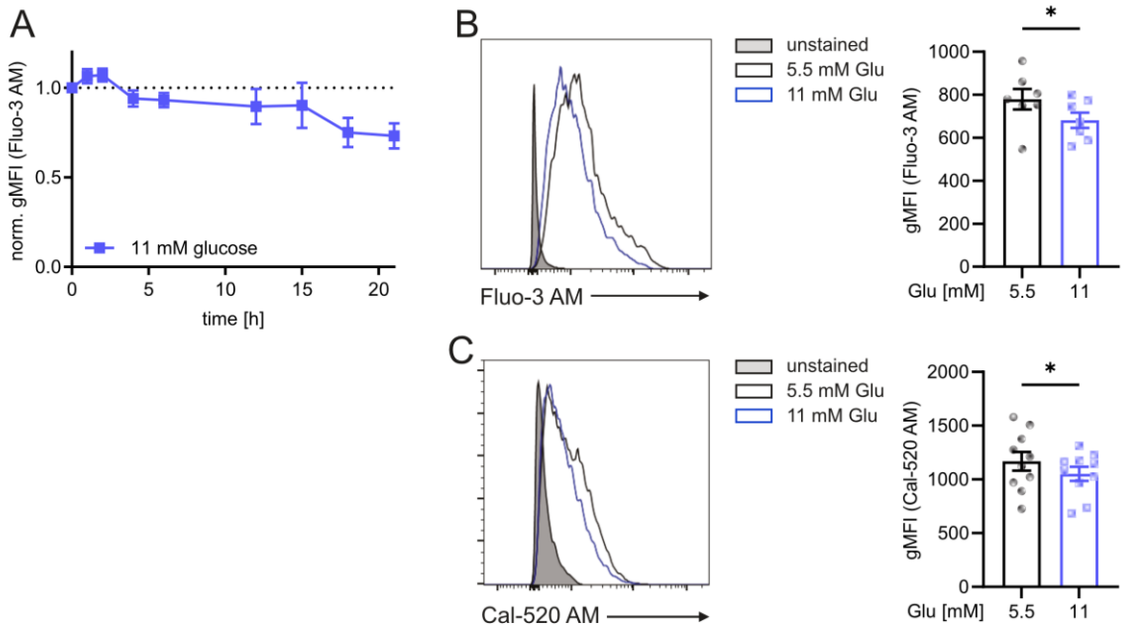

Figure 15 – Glucose reduces intracellular Ca^{2+} levels
Flow cytometric analysis of cellular Ca^{2+} levels. (**A**) BMDMs were reversibly treated with additional glucose (11 mM) for indicated periods of time and stained with Fluo-3 AM (n = 3). The gMFI was normalized to untreated BMDMs (5.5 mM glucose). (**B** and **C**) Representative histograms and gMFI in BMDMS stained with Fluo-3 AM (**B**) or Cal-520 AM (**C**). BMDMs were previously treated with glucose for 48 h (n = 7 for B, n = 10 for C). Data are shown as mean ± SEM; significance was determined by paired Student's t-test (* $p<0.05$). *Abbreviations: BMDMs, bone marrow-derived macrophages; Glu, glucose; gMFI, geometric Mean Fluorescence Intensity; norm., normalized.*

To further investigate whether glucose-mediated reduction of cellular Ca^{2+} levels also influences Ca^{2+} signaling in macrophages, changes in cytosolic Ca^{2+} concentrations in response to various stimuli were assessed. One of the stimuli used for these experiments was the ionophore ionomycin, which raises intracellular Ca^{2+} concentrations by acting as a carrier, enabling the transport of Ca^{2+} across cellular membranes independently of Ca^{2+} channels [205]. Microscopic analysis revealed a marked reduction in Ca^{2+} mobilization in response to ionomycin in glucose-treated BMDMs (Figure 16A).

In addition to microscopy, a flow cytometry-based protocol to monitor Ca^{2+} signaling was established. Compared to microscopic analysis, analysis of Ca^{2+} signaling by flow cytometry allows the monitoring of changes in cytosolic Ca^{2+} concentrations with high cell numbers and temporal resolution combined with fast and simple data analysis. Consistent with the findings obtained by microscopy, the flow cytometric analysis also demonstrated a decrease in ionomycin-induced Ca^{2+} mobilization in glucose-treated BMDMs (Figure 16B). Furthermore, a similar reduction in ionomycin-induced Ca^{2+} influx into the cytosol was observed in peritoneal macrophages treated with elevated glucose concentrations (Figure 17A). For this purpose, peritoneal cells were cultivated for two days, and peritoneal macrophages were selected based on their expression of CD11b and F4/80 (Figure 17B).

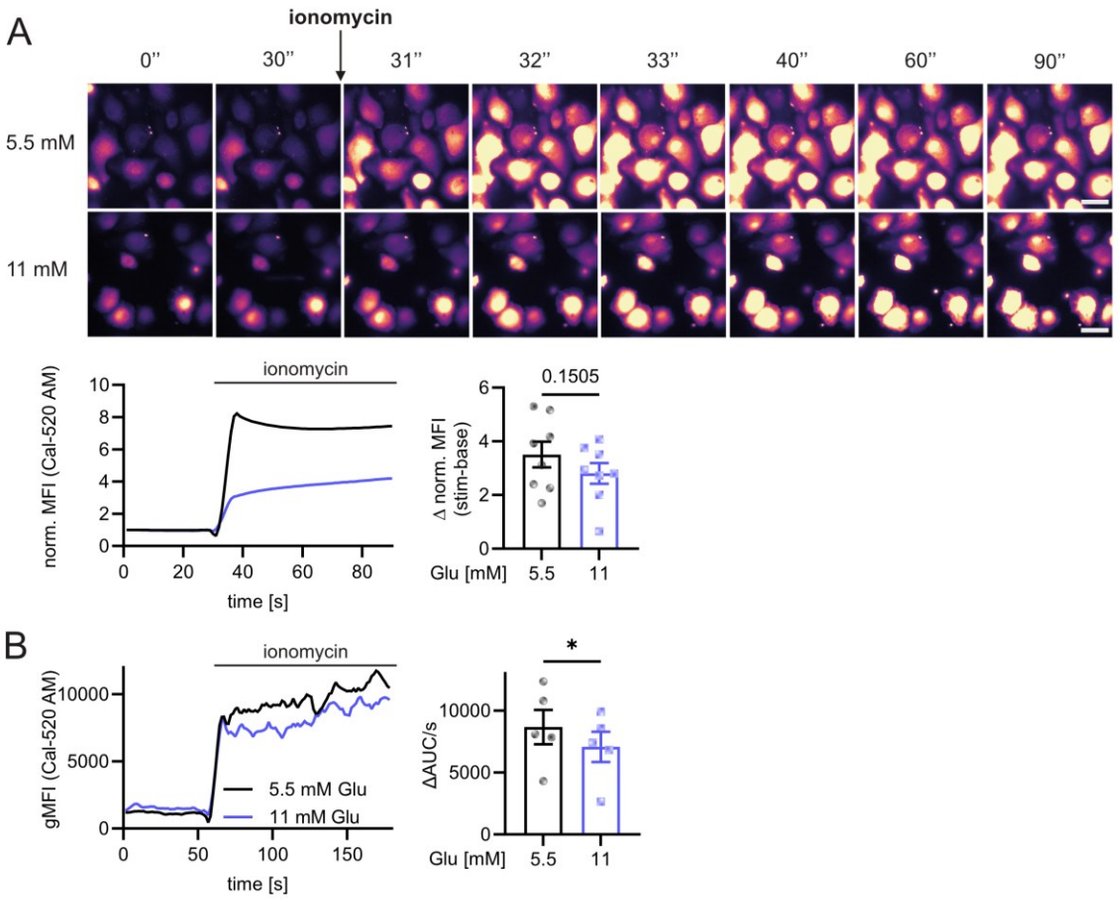

Figure 16 – Ionomycin-induced Ca^{2+} signaling is reduced in glucose-treated BMDMs
Ca^{2+} mobilization in response to ionomycin (1 µg/mL) was monitored in BMDMs treated with indicated glucose concentrations for 48 h and stained with Cal-520 AM. (**A**) Live cell imaging; representative images from one out of eight independent experiments; the scale bar is equivalent to 30 µm. Mean Fluorescence Intensity was determined from four cells per image and plotted normalized to the baseline against the time. The intensity of Ca^{2+} signaling was calculated as the difference of the MFI of the baseline and the MFI of the first 30 s after addition of ionomycin. (**B**) Flow cytometric analysis; intensity of Ca^{2+} signals depicted as the difference of the area under the curve normalized to one second before and after addition of the stimulus (n = 5). Ca^{2+} curves are represented as pooled data from the same independent experiments as depicted in the bar graph. Data are shown as mean ± SEM; significance was determined by paired Student's t-test (* $p<0.01$). *Abbreviations: AUC, area under the curve; BMDMs, bone marrow-derived macrophages; Δ, difference; Glu, glucose; gMFI, geometric Mean Fluorescence Intensity; norm., normalized; '', seconds.*

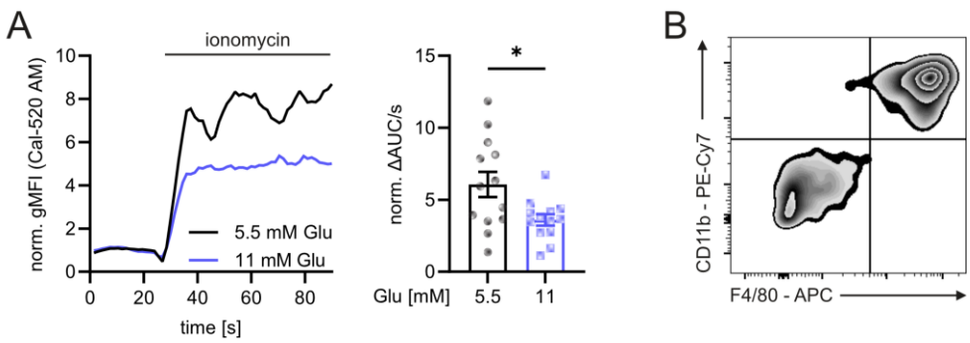

Figure 17 – Ionomycin-induced Ca^{2+} signaling is reduced in glucose-treated peritoneal macrophages
Flow cytometric analysis of Ca^{2+} mobilization in response to ionomycin (1 µg/mL) in glucose-treated (48 h) peritoneal macrophages stained with Cal-520 AM. (**A**) Intensity of Ca^{2+} signaling is depicted as the difference of the area under the curve normalized to one second before and after addition of the stimulus. Ca^{2+} signaling curve is represented as pooled data from the same independent experiments as depicted in the bar graph normalized to each baseline (n = 13). (**B**) Gating strategy to select peritoneal macrophages ($CD11b^+$ $F4/80^+$). Data are shown as mean ± SEM; significance was determined by paired Student's t-test (* $p<0.05$). *Abbreviations: AUC, area under the curve; Δ, difference; Glu, glucose; gMFI, geometric Mean Fluorescence Intensity; norm., normalized.*

Ionomycin elicits the maximal possible cellular Ca^{2+} response without specifically activating signaling cascades that mediate Ca^{2+} influx into the cytosol. Accordingly, to investigate the influence of hyperglycemia on specific cellular Ca^{2+} signaling pathways, Ca^{2+} responses to extracellular calcium chloride ($CaCl_2$), ATP and thapsigargin were also evaluated. Furthermore, to assess Ca^{2+} signaling in macrophages derived from various sources, BMDMs, as well as other human and murine macrophage cultures, were utilized. The addition of ATP results in the activation of the P2X and P2Y receptors, which are ligand-gated ion channels and GPCRs, respectively (see 2.3.1). Furthermore, Ca^{2+} influx into the cytosol can be induced in response to the sensing of elevated extracellular Ca^{2+} via CaSR as well as the inhibition of SERCA and, consequently, reduced reuptake of Ca^{2+} into the ER by thapsigargin.

Ca^{2+} signaling induced by extracellular $CaCl_2$ was significantly reduced in glucose-treated BMDMs (Figure 18A) as well as peritoneal macrophages (Figure 18B). Similarly, the increase of cytosolic Ca^{2+} concentrations in response to the addition of ATP was strongly reduced in glucose-treated BMDMs (Figure 18C) as well as human monocyte-derived macrophages (Figure 18D). Additionally, treatment with elevated glucose concentrations for 48 h further reduced thapsigargin-induced Ca^{2+} signaling (Figure 18E).

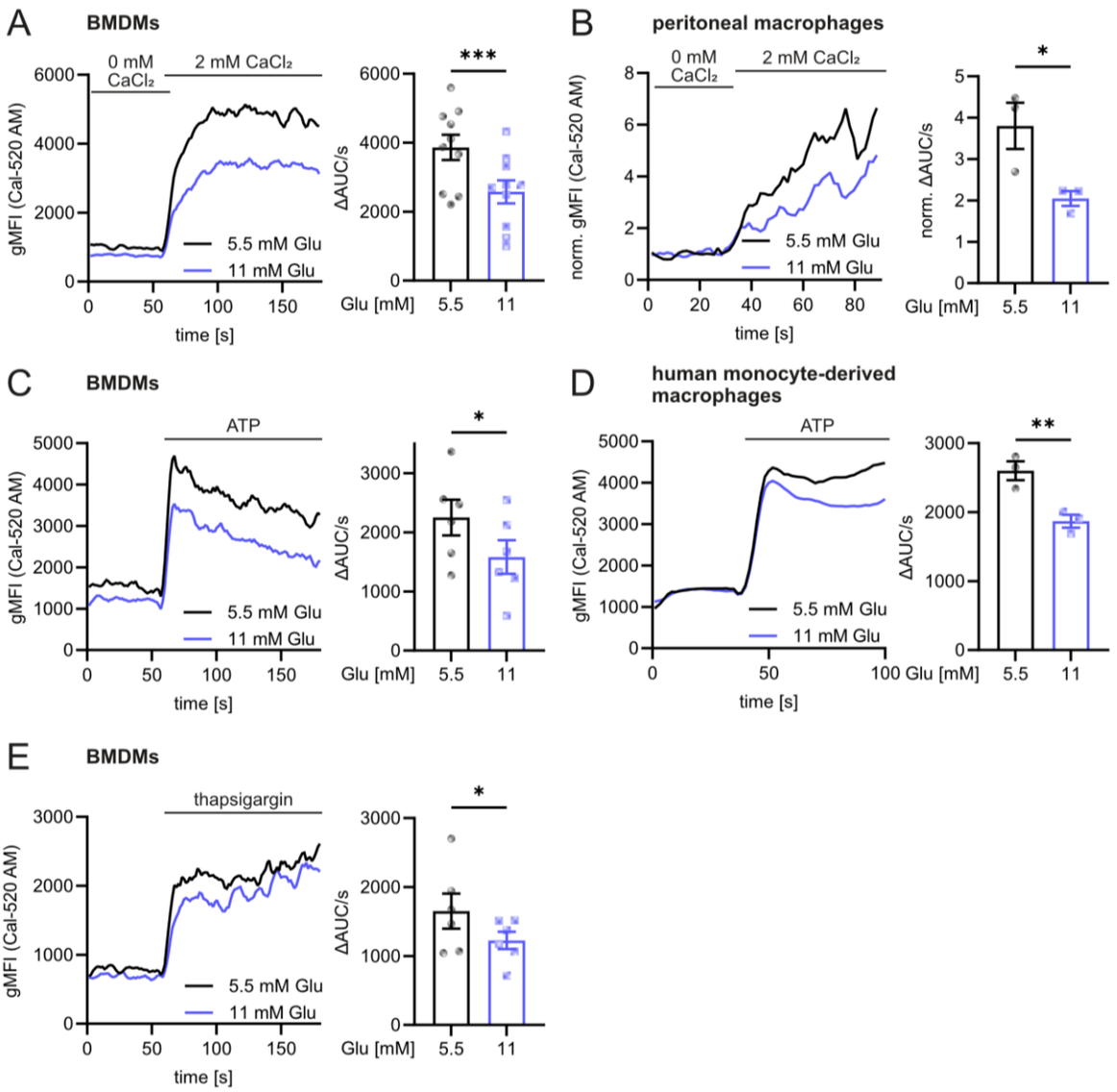

Figure 18 – Ca^{2+} signaling elicited by ATP, extracellular $CaCl_2$ and thapsigargin is reduced after treatment with enhanced glucose concentrations

BMDMs (**A, C, E**), peritoneal macrophages (**B**) and human monocyte-derived macrophages (**D**) were treated with additional glucose for 48 h and stained with Cal-520 AM. Cellular Ca^{2+} concentrations in response to 2 mM extracellular $CaCl_2$ (**A, B**), 100 µM ATP (**C, D**) or 1 µM thapsigargin (**E**) were monitored by flow cytometry. Changes in geometric Mean Fluorescence Intensity are shown over time as curve – for peritoneal macrophages normalized to each baseline. Intensity of Ca^{2+} signaling is depicted as the difference of the area under the curve normalized to one second before and after addition of the stimulus. Ca^{2+} signaling curves are represented as pooled data from the same independent experiments as depicted in the bar graph (n = 10 for A, n = 6 for C and E, n = 3 for B and D). Data are shown as mean ± SEM; significance was determined by paired Student's t-test (* $p<0.5$, ** $p<0.01$, *** $p<0.001$). *Abbreviations: AUC, area under the Curve; BMDMs, bone marrow-derived macrophages; Δ, difference; Glu, glucose gMFI, geometric Mean Fluorescence Intensity; norm., normalized.*

Single-wavelength Ca^{2+} indicators, such as Cal-520, provide high fluorescence yields, thereby offering increased sensitivity and enabling the detection of subtle changes in Ca^{2+} levels with high precision. However, these dyes are more sensitive to variations in dye loading and experimental conditions. To exclude a potential influence of inconsistent dye loading on observed differences in Ca^{2+} signaling under hyperglycemia, the reduction of Ca^{2+} signaling caused by glucose was further validated in BMDMs stained with the ratiometric dye Fura Red (Figure 19), for which the measurement is less sensitive to variations in intracellular dye concentration. As observed in Cal-520 AM-stained cells, reduced Ca^{2+} signaling was also evident in hyperglycemic BMDMs stained with Fura Red. Together, the previous data clearly demonstrate that hyperglycemia disrupts Ca^{2+} signaling in macrophages.

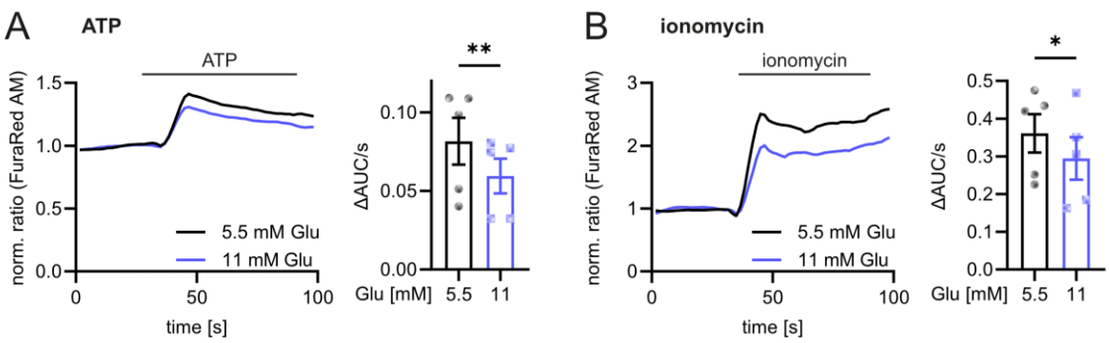

Figure 19 – Ca^{2+} signaling in hyperglycemic macrophages using a ratiometric dye
Ca^{2+} signaling in response to 100 µM ATP (**A**) and 1 µg/mL ionomycin (**B**) in glucose-treated BMDMs stained with Fura Red AM and analyzed by flow cytometry using the BV650 and PE-Cy5 channel. The Fura Red signal was calculated as ratio between BV650 and PE-Cy5. Intensity of Ca^{2+} signaling was calculated as the difference of the area under the curve normalized to one second before and after addition of the stimulus. Ca^{2+} signaling curves are represented as pooled data from the same independent experiments as depicted in the bar graph; Ca^{2+} signaling curves were normalized to each baseline before addition of stimulus (n = 5). Data are shown as mean ± SEM, significance was determined by paired Student's t-test (*$p<0.05$). *Abbreviations: AUC, area under the curve; BMDMs, bone marrow-derived macrophages; Δ, difference; Glu, glucose.*

4.2.2. Impairment of Ca^{2+} signaling by glucose is independent of mTOR and NF-κB

As described in 4.1, glucose enhances the secretion of pro-inflammatory cytokines via activation of the mTOR/NF-κB axis. To assess whether mTOR plays a role in the disruption of Ca^{2+} signaling mediated by glucose, BMDMs were treated with additional glucose and simultaneously the mTOR inhibitor Rapamycin for 24 h. Similar to changes observed after 48 h of additional glucose (Figure 16), glucose treatment for 24 h reduced ionomycin-evoked Ca^{2+} signaling. This effect persisted even after treatment with Rapamycin (Figure 20), suggesting that mTOR is not involved in glucose-mediated reduction of Ca^{2+} signaling.

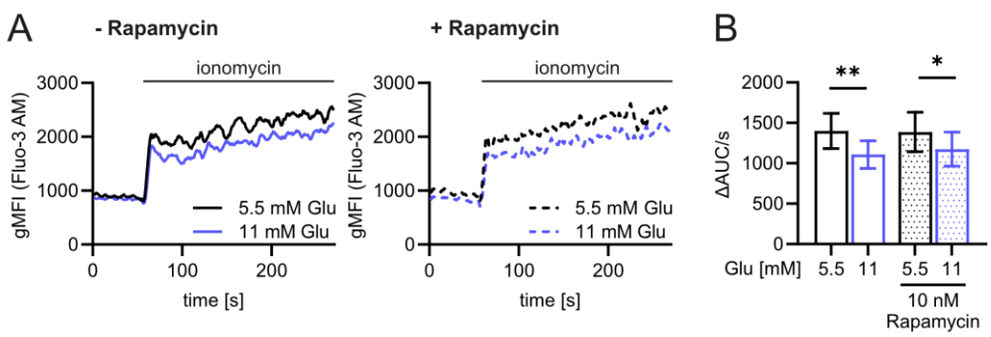

Figure 20 – Reduction of Ca^{2+} signaling by glucose is independent of mTOR
BMDMs were treated with indicated glucose concentrations in the presence or absence of mTOR inhibitor Rapamycin (10 nM) for 24 h and stained with Fluo-3 AM. Ionomycin (1 µg/mL)-induced cellular Ca^{2+} response was monitored by flow cytometry. (**A**) Changes in geometric Mean Fluorescence Intensity over time. (**B**) Intensity of Ca^{2+} signaling is depicted as the difference of the area under the curve normalized to one second before and after addition of the stimulus. Ca^{2+} signaling curves are represented as pooled data from the same independent experiments as depicted in the bar graph (n = 11). Data are shown as mean ± SEM; significance was determined by Two-Way ANOVA corrected for multiple comparisons by the Tukey method (* $p<0.05$, ** $p<0.01$). *Abbreviations: AUC, area under the curve; BMDMs, bone marrow-derived macrophages; Δ, difference; Glu, glucose; gMFI, geometric Mean Fluorescence Intensity; norm., normalized.*

To further investigate the involvement of NF-κB in the decrease of Ca^{2+} signaling observed after treatment with glucose, changes in Ca^{2+} levels in response to ionomycin were monitored in BMDMs treated with the NF-κB inhibitor Bay 11-7082 in combination with glucose. This inhibitor prevents the phosphorylation and thus the degradation of IκB, keeping NF-κB inactive in the cytosol (Figure 21A) [206]. To ensure that the inhibitory effect of Bay 11-7082 lasted for 24 h, LPS-induced TNF secretion, initiated by translocation of NF-κB into the nucleus, was monitored in BMDMs treated with Bay 11-7082. As shown in Figure 21B, Bay 11-7082 strongly reduced TNF secretion over 24 h. Similar to Rapamycin, inhibition of NF-κB with Bay 11-7082 did not affect glucose-mediated reduction of Ca^{2+} signaling (Figure 21C and D).

In conclusion, these data show that, in contrast to cytokine secretion, the reduction in Ca^{2+} signaling observed in hyperglycemic macrophages is independent of mTOR and NF-κB.

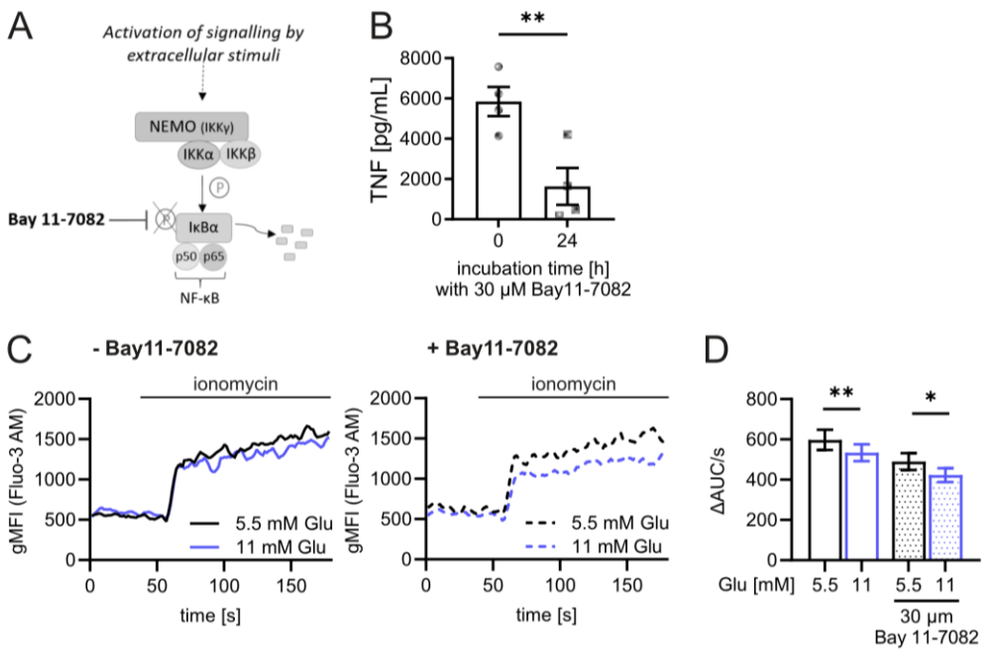

Figure 21 – NF-κB is not involved in impaired Ca^{2+} signaling in response to elevated glucose concentrations
(**A**) Bay 11-7082 inhibits activation and thus nuclear translocation of NFκB by preventing phosphorylation of IκB. (**B**) Treatment of BMDMs with 30 µM Bay 11-7082 for 24 h and subsequent stimulation with 100 ng/mL LPS for 3 h. TNF production was determined in supernatants by ELISA (n = 5). (**C** and **D**) BMDMs were treated with indicated glucose concentrations in the presence or absence of Bay 11-7082 (30 µM) for 24 h and stained with Fluo-3 AM. Ionomycin (1 µg/mL)-induced cellular Ca^{2+} response was monitored by flow cytometry. (**C**) Changes in geometric Mean Fluorescence Intensity over time. (**D**) Intensity of Ca^{2+} signaling is depicted as the difference of the area under the curve normalized to one second before and after addition of the stimulus. Ca^{2+} signaling curves are represented as pooled data from the same independent experiments as depicted in the bar graph (n = 7). Data are shown as mean ± SEM; significance was determined by paired Student's t-test (B) or Two-Way ANOVA corrected for multiple comparisons by the Tukey method (D) (* $p<0.05$, ** $p<0.01$). *Abbreviations: AUC, area under the curve; BMDMs, bone marrow-derived macrophages; Δ, difference; Glu, glucose; gMFI, geometric Mean Fluorescence Intensity; norm., normalized.*

4.2.3. Glucose-mediated changes on cellular Ca^{2+} homeostasis persist after glucose deprivation

As described in the previous sections (4.2.1, 4.2.2), exposure of BMDMs to elevated glucose concentrations for 24 h or 48 h significantly reduced the Ca^{2+} response to various stimuli. To further investigate whether the impairment of cellular Ca^{2+} signaling caused by elevated glucose concentrations persists after switching again to physiological glucose concentrations, the Ca^{2+} response to thapsigargin and extracellular $CaCl_2$ was assessed after changing the medium back to a physiological metabolite medium containing 5.5 mM glucose.

Remarkably, the Ca^{2+} response was reduced in BMDMs previously treated with elevated glucose concentrations for 48 h up to 11 days after switching to medium with physiological glucose concentrations (Figure 22). Five days after the medium change (day 14 of culture), the cells displayed an overall decreased response to the addition of thapsigargin and extracellular $CaCl_2$, recognizable by a reduced increase of the fluorescence intensity after stimulation and a corresponding reduced

difference of the area under the curve before and after stimulation. These data indicate that glucose-mediated alterations in the cellular Ca^{2+} response remained for several days after withdrawal of the additional glucose.

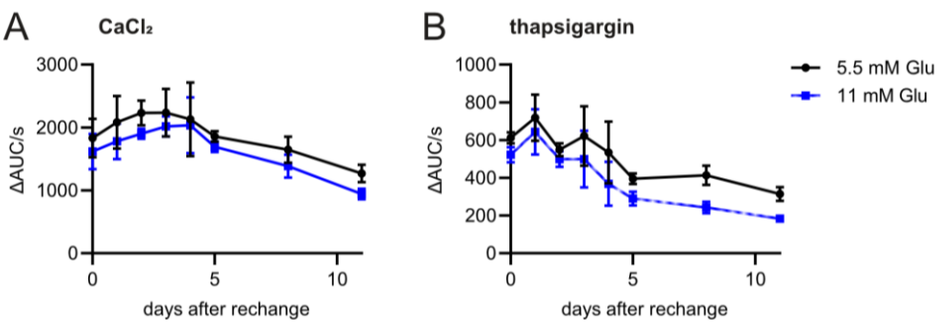

Figure 22 – Glucose-mediated reduction in Ca^{2+} signaling remains several days after switch to medium with physiological concentrations of glucose
BMDMs were treated with additional glucose for 48 h. Afterwards, the medium was switched to a medium containing physiological concentrations of glucose (5.5 mM) and half of the medium was exchanged every other day. Ca^{2+} signaling in response to 2 mM extracellular $CaCl_2$ (**A**) or 1 µM thapsigargin (**B**) was assessed by flow cytometry in Cal-520 AM-stained cells at indicated time points after the switch. Intensity of Ca^{2+} signaling was calculated as difference of the area under the curve normalized to one second before and after addition of the stimulus. Data are shown as mean ± SEM; pooled data from 4 independent experiments. *Abbreviations: AUC, area under the curve; BMDMs, bone marrow-derived macrophages; Δ, difference; Glu, glucose.*

4.2.4. Glucose impairs cellular Ca^{2+} homeostasis at the ER

Cellular Ca^{2+} responses leading to an increase in cytosolic Ca^{2+} concentrations can be induced through various interdependent pathways that also influence each other. Depending on the stimulus, Ca^{2+} is released from intracellular Ca^{2+} stores, such as the ER, or Ca^{2+} enters the cell from the extracellular space via ion channels in the plasma membrane. To distinguish whether elevated glucose concentrations rather influence Ca^{2+} influxes at the level of the plasma membrane or the ER, the cascade mediating intracellular Ca^{2+} signaling was interrupted by the addition of inhibitors along with the elevation of glucose concentrations. The intensity of the Ca^{2+} response was then determined by flow cytometry.

As PLC is known to play a critical role in the regulation of Ca^{2+} signaling in response to various stimuli (as described in 2.3.1), activation of PLC was prevented by U73122. Inhibition of PLC by U73122 reversed the glucose-mediated reduction of Ca^{2+} signaling induced by addition of extracellular $CaCl_2$ (Figure 23A), indicating that glucose does not influence Ca^{2+} responses at the level of the plasma membrane, but rather inside the cell involving PLC-mediated induction of Ca^{2+} release from the ER.

In order to gain deeper insights into the influence of glucose on the Ca^{2+} signaling inside the cell, Ca^{2+} signaling in response to extracellular Ca^{2+} was further examined in BMDMs treated with glucose in the presence or absence of the IP_3R inhibitor 2-APB. Similar to the inhibition of PLC,

glucose-mediated impairment of Ca^{2+} signaling was abolished by the addition of the IP_3R inhibitor 2-APB (Figure 23B), suggesting that hyperglycemia impairs Ca^{2+} signaling mainly at the ER.

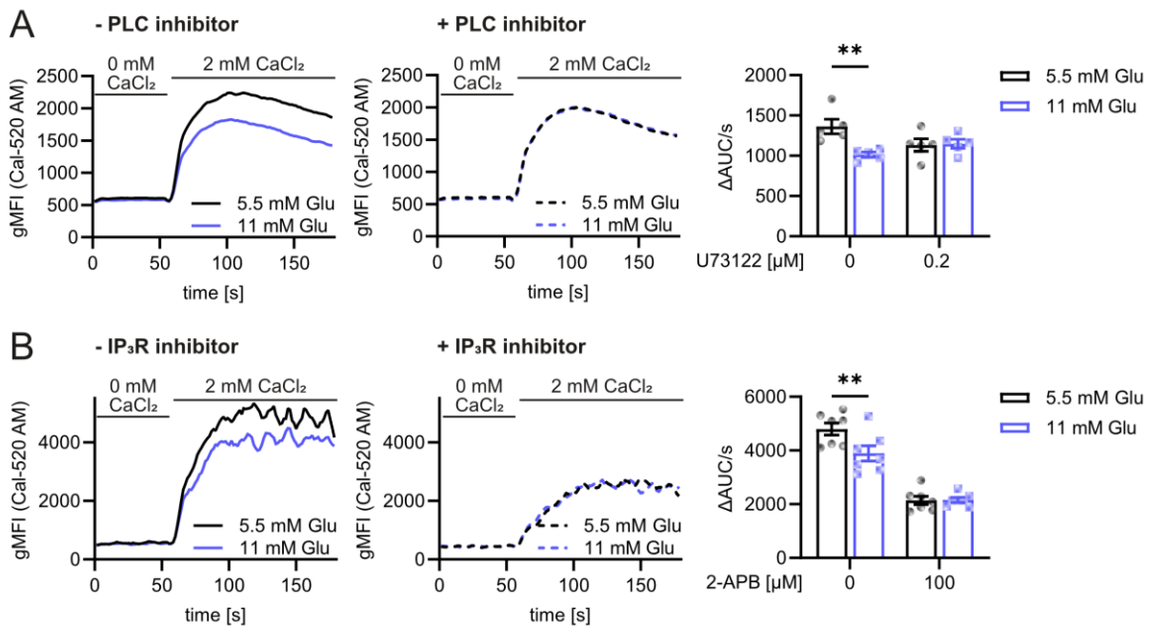

Figure 23 – Glucose-mediated reduction in Ca^{2+} signaling is overcome by inhibition of PLC and IP_3R
(**A**) BMDMs were treated with elevated glucose concentrations in the presence or absence of the PLC inhibitor U73122 (0.2 µM) for 48 h. Ca^{2+} signaling in response to 2 mM extracellular $CaCl_2$ was analyzed in Cal-520 AM-stained cells by flow cytometry. The intensity of Ca^{2+} signaling was calculated as difference of the area under the curve normalized to one second before and after addition of the stimulus. (**B**) As in (A) but treatment with elevated glucose concentrations in the presence or absence of the IP_3R inhibitor 2-APB (100 µM) for 24 h. Ca^{2+} signaling curves are represented as pooled data from the same independent experiments as depicted in the bar graph (n = 5 for A, n = 7 for B). Data are shown as mean ± SEM; significance was determined by Two-Way ANOVA corrected for multiple comparisons by the Šidák method (** $p<0.01$). *Abbreviations: AUC, area under the curve; BMDMs, bone marrow-derived macrophages; Δ, difference; Glu, glucose; gMFI, geometric Mean Fluorescence Intensity; IP_3R, inositol triphosphate receptor; PLC, phospholipase C; 2-APB, 2-aminoethoxydiphenyl borate.*

At steady state, Ca^{2+} is constantly leaking from the ER, and is transported back by SERCA. Inhibition of SERCA with thapsigargin increases cytosolic Ca^{2+} concentrations by disrupting this balance [207], which is further amplified by SOCE. Analyzing thapsigargin-induced Ca^{2+} signaling in a Ca^{2+}-deprived solution enables the measurement of the Ca^{2+} release from the ER without activating Ca^{2+} influx from the plasma membrane. Strikingly, Ca^{2+} release from the ER was also significantly reduced in glucose-treated BMDMs (Figure 24A) and human monocyte-derived macrophages (Figure 24B) in the absence of extracellular Ca^{2+}. The reduction of thapsigargin-induced Ca^{2+} signaling by glucose in the absence of extracellular Ca^{2+} was further validated in BMDMs stained with the ratiometric dye Fura Red (Figure 24C), demonstrating that glucose indeed modulates Ca^{2+} homeostasis at the level of the ER.

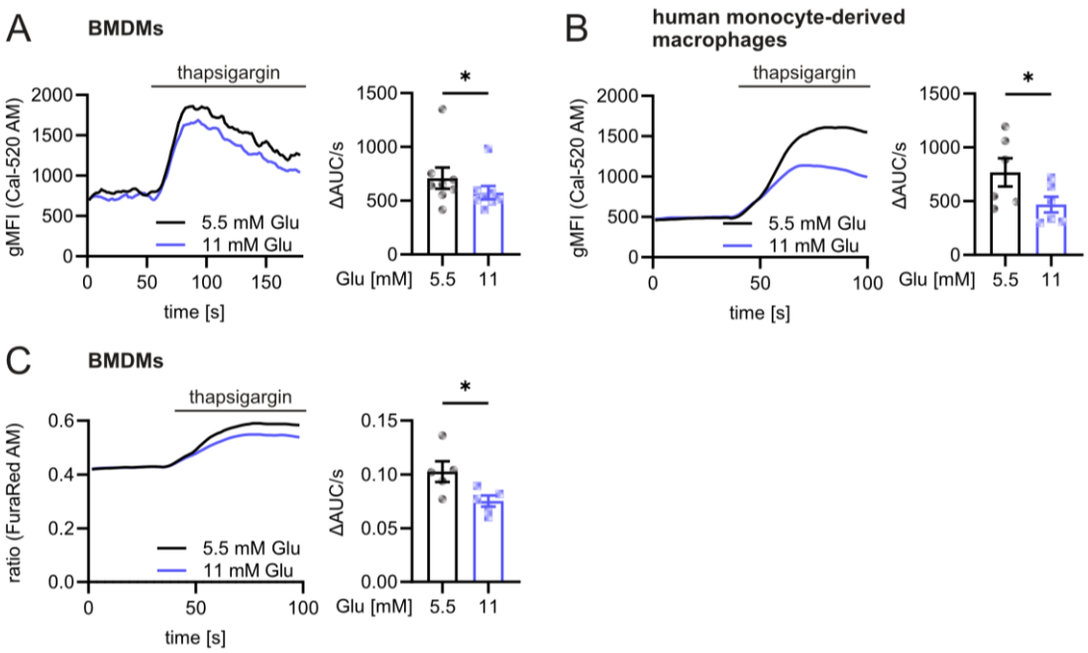

Figure 24 – Ca^{2+} signaling in response to thapsigargin is reduced by glucose in the absence of extracellular Ca^{2+}
Ca^{2+} signaling in response to 1 µM thapsigargin in glucose-treated BMDMs (**A** and **C**) as well as human monocyte-derived macrophages (**B**) in the absence of extracellular Ca^{2+}. Cells were stained with Cal-520 AM (**A, B**) or Fura Red AM (**C**) and analyzed by flow cytometry using the FITC channel or the BV650 and PE-Cy5 channel, respectively. For Fura Red fluorescence was calculated as ratio between BV650 and PE-Cy5. Intensity of Ca^{2+} signaling was calculated as the difference of the area under the curve normalized to one second before and after addition of the stimulus. Ca^{2+} signaling curves are represented as pooled data from the same independent experiments as depicted in the bar graph (n = 8 for A, n = 5 for B and C). Data are shown as mean ± SEM; significance was determined by paired Student's t-test (*p<0.05). *Abbreviations: AUC, area under the curve; BMDMs, bone marrow-derived macrophages; Δ, difference; Glu, glucose; gMFI, geometric Mean Fluorescence Intensity.*

4.3. Glucose-induced changes in cellular Ca^{2+} levels are mediated by signaling via the taste receptor Tas1R3

4.3.1. Glucose itself induces Ca^{2+} signaling

As previously shown in this thesis, enhanced glucose concentrations strongly impair Ca^{2+} signaling and further decrease intracellular Ca^{2+} stores within hours (4.2). These data indicate that glucose might directly influence cellular Ca^{2+} homeostasis. To test whether glucose mediates immediate changes in Ca^{2+} concentrations, Ca^{2+} influx into the cytosol was monitored in response to the addition of glucose (22 mM) as stimulus. Strikingly, a clear increase in cytosolic Ca^{2+} levels was observed within the first seconds after the addition of glucose by fluorescence microscopy acquiring one image per second (Figure 25A). Similarly, immediately after the addition of glucose an influx of Ca^{2+} into the cytosol was observed by flow cytometry (Figure 25B).

Since glucose-mediated changes in the Ca^{2+} homeostasis seemed to occur at the level of the ER (4.2.4), the induction of Ca^{2+} influx into the cytosol by glucose was further assessed in the absence of extracellular Ca^{2+}. Similarly, the addition of glucose resulted in an increase of the cytosolic Ca^{2+} concentrations due to Ca^{2+} release from the ER (Figure 25C), further supporting that glucose modulates the Ca^{2+} homeostasis at the level of the ER.

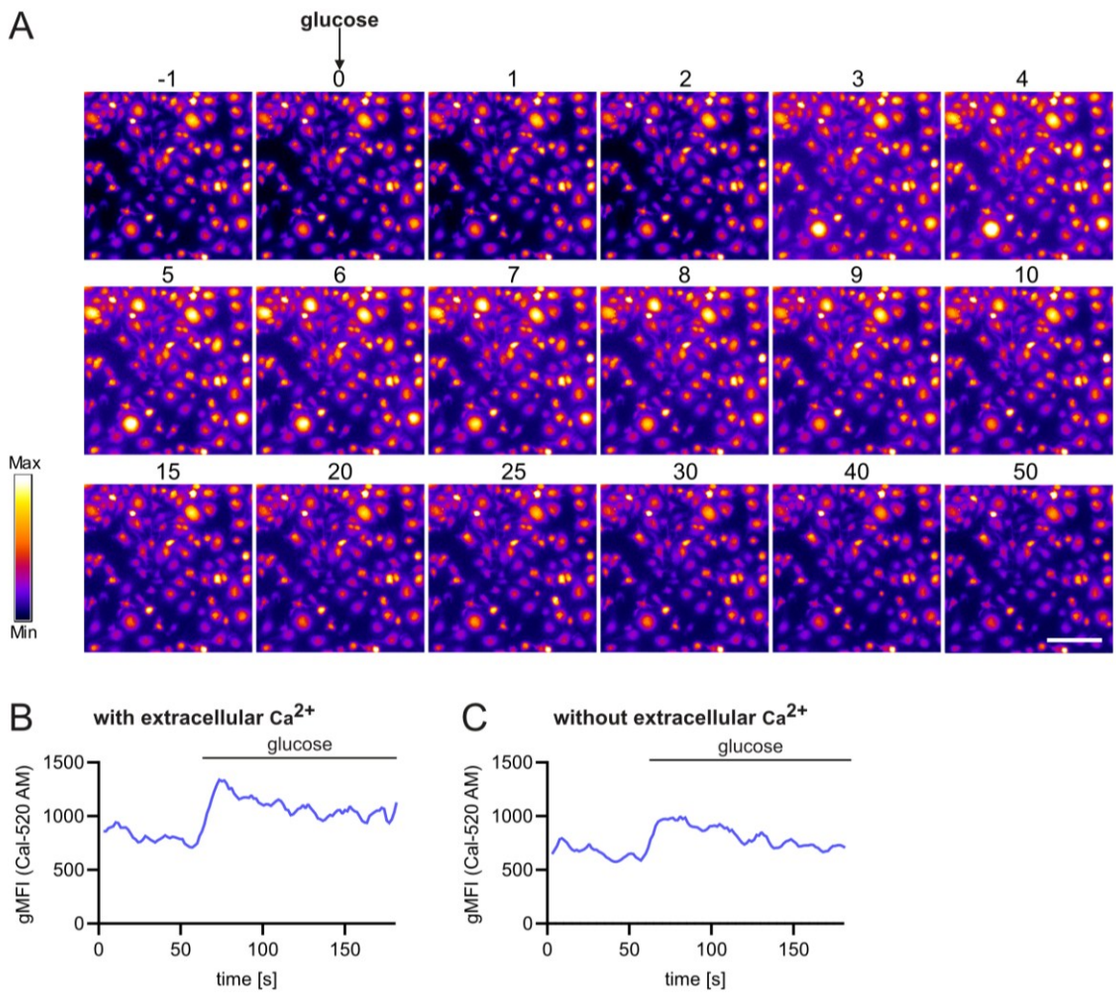

Figure 25 – Glucose mediates Ca^{2+} influx into the cytosol
BMDMs were stained with Cal-520 AM and Ca^{2+} concentrations were monitored over time (resolution in seconds) by live cell imaging (**A**) or flow cytometry (**B** and **C**). Glucose (22 mM) was added at indicated time points in the presence (**A, B**) or absence (**C**) of extracellular Ca^{2+} (1.26 mM). (**A**) Representative microscopy images from one out of three independent experiments. The scale bar is equivalent to 100 µM. (**B** and **C**) Ca^{2+} signaling curves are represented as pooled data from independent experiments (n = 6). *Abbreviations: BMDMs, bone marrow-derived macrophages; gMFI, geometric Mean Fluorescence Intensity.*

The addition of glucose alters the cellular osmolarity by increasing the concentration of osmotically active molecules in the solution. To exclude the possibility that the observed Ca^{2+} response is attributable to osmotic changes, mannitol, which exhibits osmotic properties similar to those of glucose, was added instead of glucose [208]. Strikingly, in contrast to glucose, the addition of mannitol did not result in an increase of cytosolic Ca^{2+} concentrations (Figure 26A and B), thereby excluding that osmotic changes mediate the Ca^{2+} release induced by glucose. Since glucose is metabolized within the cell, Ca^{2+} signaling in response to pyruvate, the end product of glycolysis, was further

assessed. As shown in Figure 26C, pyruvate did not induce an increase in cytosolic Ca^{2+} concentrations, indicating that either a metabolite upstream in glycolysis or glucose itself is responsible for the release of Ca^{2+} from the ER.

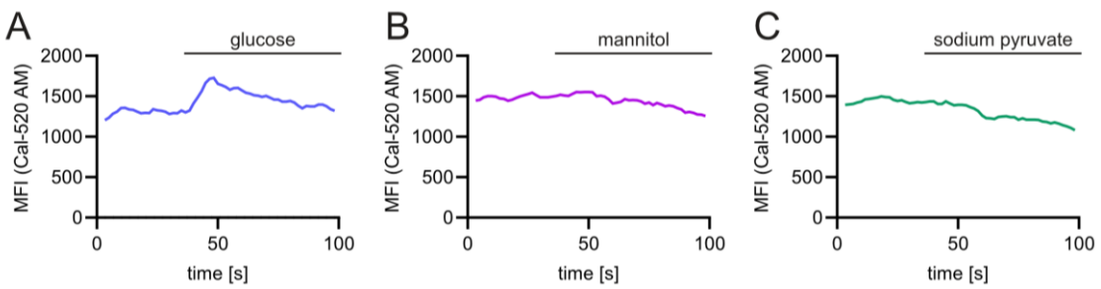

Figure 26 – Glucose but not pyruvate and mannitol induce cellular Ca^{2+} mobilization
BMDMs were stained with Cal-520 AM. Changes in cytosolic Ca^{2+} concentrations in response to 22 mM glucose (**A**), 22 mM mannitol (**B**) or 22 mM sodium pyruvate (**C**) were analyzed by flow cytometry. Depicted are Ca^{2+} signaling curves over time pooled from six independent experiments. *Abbreviations: BMDMs, bone marrow-derived macrophages; gMFI, Mean Fluorescence Intensity.*

To distinguish between these two possibilities, 2-deoxyglucose (2-DG), a glucose analog that cannot be further metabolized, was added to the cells. Strikingly, addition of 2-DG resulted in a Ca^{2+} influx similar to that of glucose in both murine BMDMs (Figure 27A) as well as human $CD14^+$ monocytes (Figure 27B). These data indicate that glucose itself mediates a Ca^{2+} release from the ER into the cytosol.

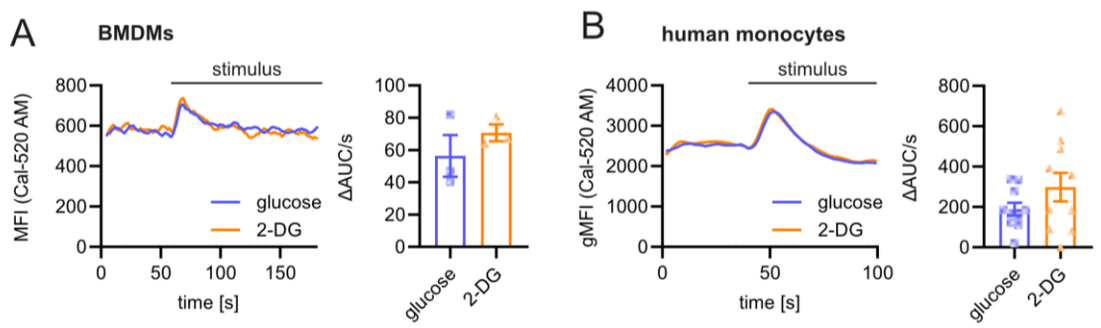

Figure 27 – Glucose itself mediates a Ca^{2+} influx into the cytosol
BMDMs (**A**) or human $CD14^+$ monocytes (**B**) were stained with Cal-520 AM. Cellular Ca^{2+} concentrations after addition of 22 mM glucose or its analog 2-DG were monitored by flow cytometry. Intensity of Ca^{2+} signaling was calculated as the difference of the area under the curve normalized to one second before and after addition of the stimulus. Ca^{2+} signaling curves are represented as pooled data from the same independent experiments as depicted in the bar graph (n = 3 for A, n = 10 for B). Data are shown as mean ± SEM. *Abbreviations: AUC, area under the curve; BMDMs, bone marrow-derived macrophages; Δ, difference; Glu, glucose; gMFI, geometric Mean Fluorescence Intensity; 2-DG, 2-deoxyglucose.*

4.3.2. Glucose induces Ca^{2+} signaling by activation of Tas1R3

The previous data clearly indicated that glucose disrupts cellular Ca^{2+} homeostasis and directly induces a Ca^{2+} release from the ER. However, the precise molecular mechanisms underlying these changes remain elusive. Since glucose directly mediates a Ca^{2+} influx into the cytosol, it is possible that glucose itself might function as a signaling molecule. Commonly, Ca^{2+} release from the ER results from the activation of G protein-coupled receptors (GPCRs) signaling. One such GPCR activated by glucose is the taste receptor 1 member 3 (Tas1R3) [209,210], which is not only present in taste buds but also expressed throughout the entire body [211]. Expression of Tas1R3 mRNA has also been observed in murine peritoneal as well as bone marrow-derived macrophages [212,213]. To further confirm the expression of the receptor in macrophages, we stained cells from different sources with a Tas1R3-specific antibody. Consistent with the literature, Tas1R3 expression was observed in murine peritoneal macrophages, murine BMDMs and human $CD14^+$ monocytes derived from whole blood (Figure 28).

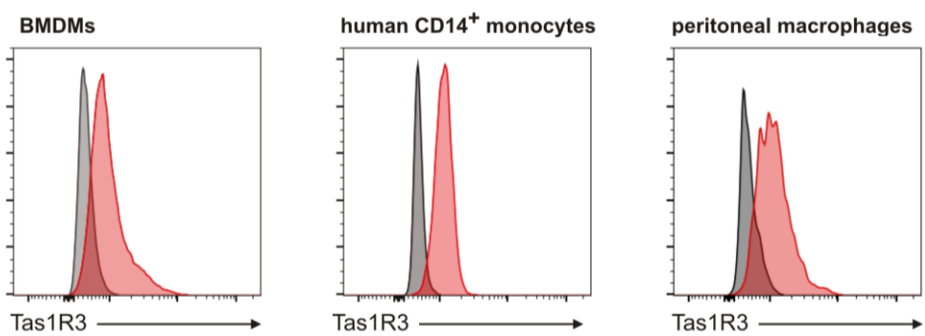

Figure 28 – Tas1R3 expression in macrophages and monocytes
Human PBMCs derived from whole blood, murine BMDMs, and murine cells isolated by a peritoneal lavage were stained with a fluorescently-labeled antibody against the taste receptor Tas1R3 and antibodies to allow discrimination of cell subsets. Expression of Tas1R3 was analyzed by flow cytometry in classical monocytes ($CD14^+$), BMDMs as well as peritoneal macrophages ($CD11b^+$). Representative histograms, $n \geq 3$. *Abbreviations: BMDMs, bone marrow-derived macrophages; PBMCs, peripheral blood mononuclear cells.*

In humans, lactisole has been described as Tas1R3 antagonist, thus inhibiting activation of downstream signaling and, consequently, the perception of sweet taste [214,215]. When human CD14$^+$ monocytes were pretreated with lactisole, the induction of Ca^{2+} signaling by glucose was prevented (Figure 29A), suggesting a putative role of Tas1R3. Accordingly, sucralose, which belongs to the group of artificial sweeteners designed to specifically bind and activate Tas1R3 [216,217], induces a Ca^{2+} influx into the cytosol with an intensity comparable to that mediated by glucose (22 mM) even at lower concentrations (Figure 29B). In contrast to sucralose, the sweetener erythritol induces a clear but weaker influx of Ca^{2+} into the cytosol in BMDMs, as erythritol is a less potent Tas1R3 ligand [218] (Figure 29C). Together these data suggest that glucose might influence the cellular Ca^{2+} homeostasis through activation of Tas1R3.

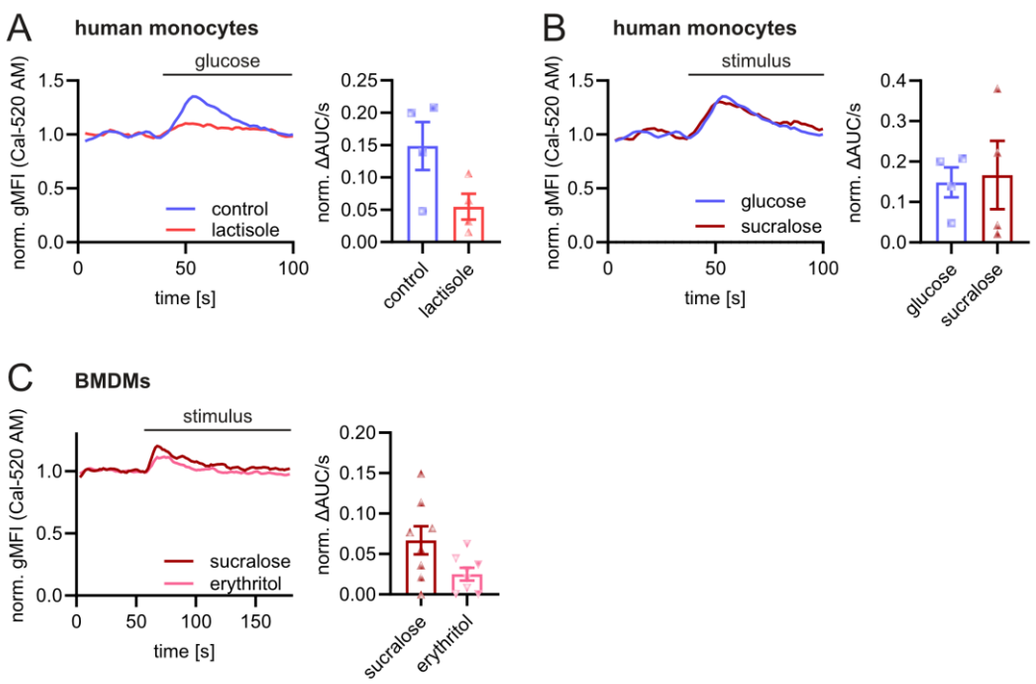

Figure 29 – Lactisole prevents Ca^{2+} signaling induced by glucose and other taste receptor ligands
Human CD14$^+$ classical monocytes (**A, B**) and BMDMs (**C**) were stained with Cal-520 AM, and Ca^{2+} signaling in response to glucose (22 m), sucralose (5 mM) and erythritol (5 mM) was monitored by flow cytometry. For (**A**) Pretreatment of cells with the taste receptor antagonist lactisole (5 mM) for 10 min. The intensity of Ca^{2+} signaling was calculated as the difference of the area under the curve normalized to one second before and after addition of the stimulus. Ca^{2+} signaling curves are represented as pooled data from the same independent experiments as depicted in the bar graph and data were normalized to the mean of each baseline (n = 4 for A and B, n = 7 for C). Data are shown as mean ± SEM. *Abbreviations: AUC, area under the curve; BMDMs, bone marrow-derived macrophages; Δ, difference; gMFI, geometric Mean Fluorescence Intensity; norm., normalized.*

In order to further examine the role of Tas1R3 in glucose-induced changes in Ca^{2+} signaling, cellular Ca^{2+} response to glucose was investigated in BMDMs, in which the taste receptor was downregulated by siRNA. The expression of Tas1R3 was reduced by 54% to 73% using three different siRNAs (Figure 30A). In contrast to glucose-mediated reduction of overall cellular Ca^{2+} levels, the downregulation of Tas1R3 resulted in increased cellular Ca^{2+} concentrations (Figure 30B). Furthermore, the glucose-mediated Ca^{2+} influx into the cytosol was almost completely abolished after siRNA-mediated downregulation of Tas1R3 (Figure 30C).

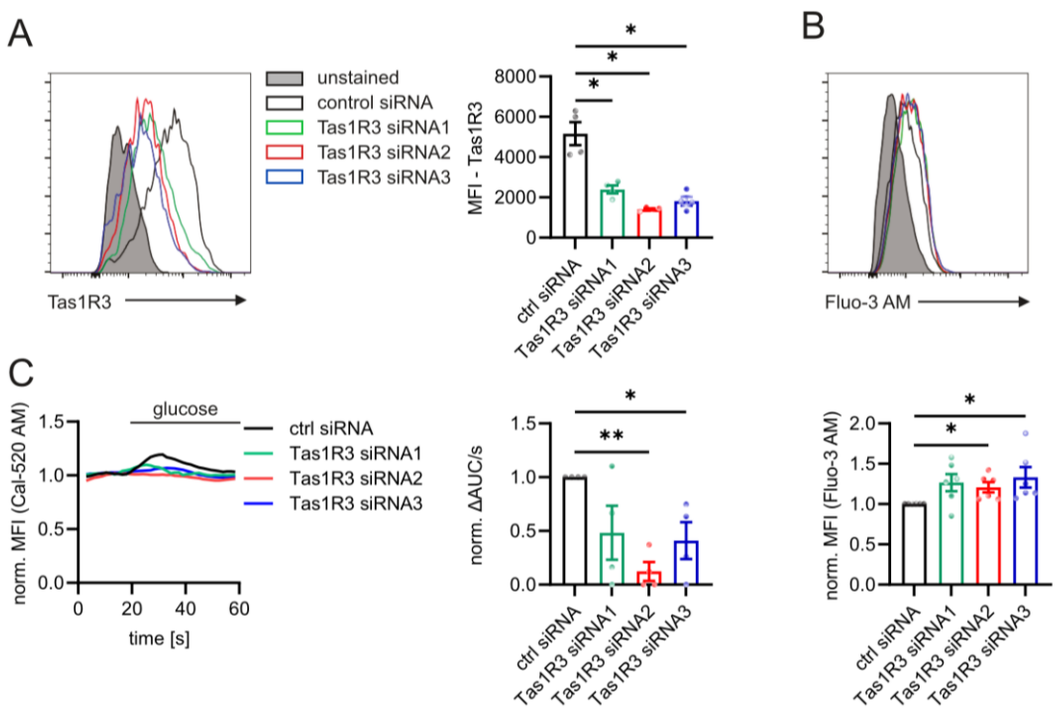

Figure 30 – Glucose-mediated Ca^{2+} signaling is abolished after downregulation of Tas1R3
Downregulation of the taste receptor Tas1R3 in BMDMs by siRNA and flow cytometric analysis after two days. (**A**) Expression of Tas1R3 was determined using a fluorescently-labeled antibody. Exemplary histogram and resulting MFI (n = 4). (**B**) Overall Ca^{2+} concentrations by staining with Fluo-3 AM; MFI was normalized to the respective control siRNA (n = 6). (**C**) Ca^{2+} concentrations in response to glucose (22 mM) were monitored in Cal-520 AM-stained cells. The intensity of Ca^{2+} signaling was calculated as the difference of the area under the curve normalized to one second before and after addition of the stimulus. Ca^{2+} signaling curves are represented as pooled data from the same independent experiments as depicted in the bar graph (n = 4) and data were normalized to the mean of each baseline. Data are shown as mean ± SEM; significance was determined by One-Way ANOVA corrected for multiple comparisons by the Dunnett method (A) or by calculation of confidence intervals (B, C) (* $p<0.05$, ** $p<0.01$). *Abbreviations: AUC, area under the curve; BMDMs, bone marrow-derived macrophages; Δ, difference; MFI, Mean Fluorescence Intensity; norm., normalized.*

Similar to glucose, treatment of BMDMs with the Tas1R3 ligand sucralose for 48 h resulted in a reduction in Ca^{2+} signaling induced by either ATP or thapsigargin (Figure 31). Finally, BMDMs from Tas1R3$^{-/-}$ mice were treated with elevated glucose concentrations and Ca^{2+} signaling in response to ionomycin, ATP and thapsigargin was investigated. In the Tas1R3$^{-/-}$ BMDMs, glucose treatment did not have any effect on the Ca^{2+} response (Figure 32).

These data univocally demonstrate that Tas1R3 is involved in the dysregulation of cellular Ca^{2+} homeostasis caused by elevated glucose concentrations.

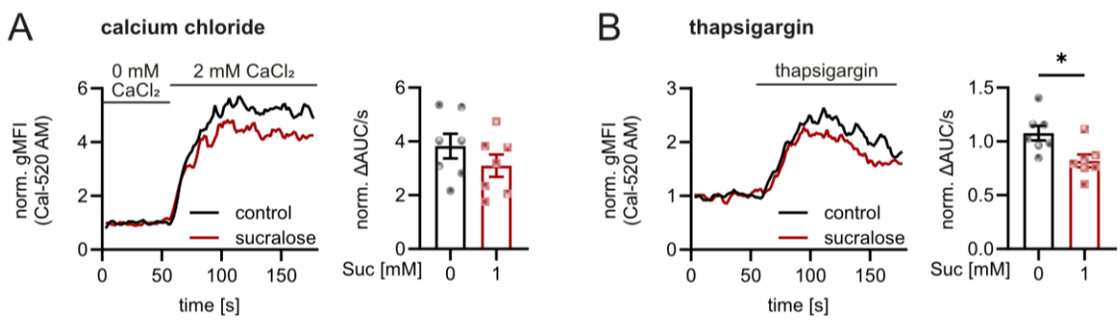

Figure 31 – Sucralose impairs cellular Ca^{2+} signaling
Sucralose-treated (48 h) BMDMs were stained with Cal-520 AM in the absence of extracellular Ca^{2} and Ca^{2+} concentrations were monitored by flow cytometry. Induction of Ca^{2+} signaling by addition of 2 mM extracellular $CaCl_2$ (**A**) or 1 µM thapsigargin (**B**). Intensity of Ca^{2+} signaling was calculated as the difference of the area under the curve normalized to one second before and after addition of the stimulus. Ca^{2+} signaling curves are presented as pooled data from the same independent experiments as depicted in the bar graph (n = 7); data were normalized to the baseline in each experiment. Data are shown as mean ± SEM; significance was determined by paired Student's t-test (* $p<0.05$). *Abbreviations: AUC, area under the curve; BMDMs, bone marrow-derived macrophages; Δ, difference; MFI, Mean Fluorescence Intensity; norm., normalized.*

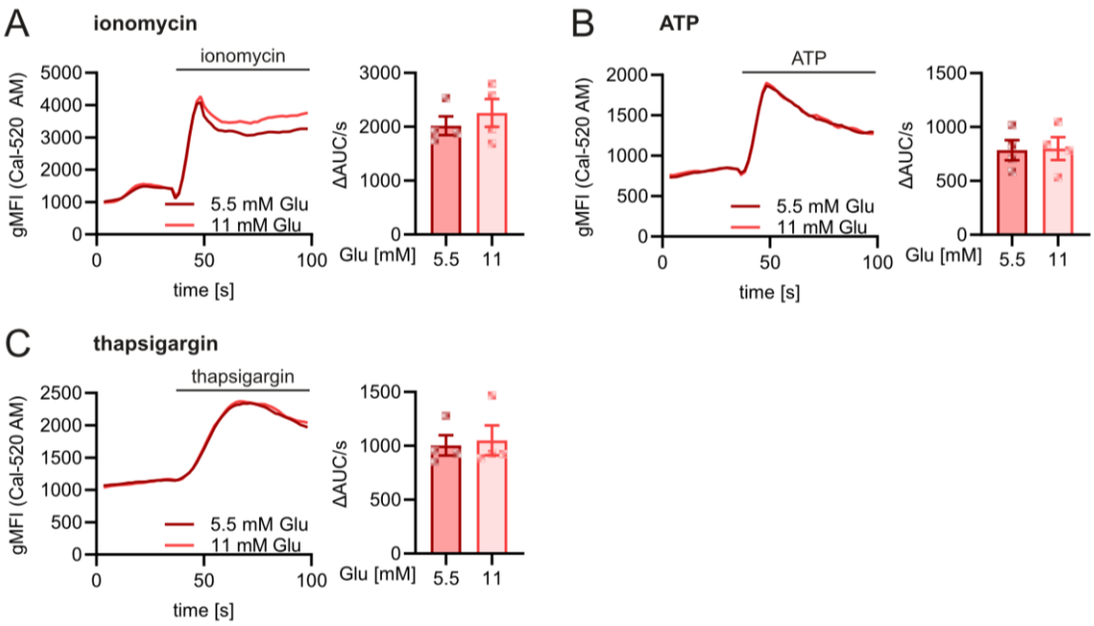

Figure 32 – Glucose treatment has no influence on Ca^{2+} signaling in Tas1R3$^{-/-}$ macrophages
BMDMs from Tas1R3$^{-/-}$ mice were treated with glucose for 48 h and stained with Cal-520 AM. Ca^{2+} signaling in response to 1 µg/mL ionomycin (**A**), 100 µM ATP (**B**) or 1 µM thapsigargin (**C**) was monitored by flow cytometry. The intensity of Ca^{2+} signaling was calculated as the difference of the area under the curve normalized to one second before and after addition of the stimulus. Ca^{2+} signaling curves are represented as pooled data from the same independent experiments as depicted in the bar graph (n = 4). Data are shown as mean ± SEM. *Abbreviations: AUC, area under the curve; BMDMs, bone marrow-derived macrophages; Glu, glucose; Δ, difference; MFI, Mean Fluorescence Intensity; norm., normalized.*

4.3.3. Investigation of signaling induced by glucose-mediated activation of Tas1R3

4.3.3.1. Glucose-induced activation of Tas1R3 promotes IP_3-mediated Ca^{2+} release from the ER

The activation of GPCRs, including Tas1R3, leads to the generation of DAG and IP_3 through the activation of PLC. IP_3, in turn, mediates the release of Ca^{2+} from the ER by activating its respective ligand-gated receptor. If glucose-induced activation of Tas1R3 and subsequent Ca^{2+} release is mediated by signaling involving IP_3, inhibition of the IP_3R or PLC should prevent the induction of a Ca^{2+} influx. Indeed, when BMDMs as well as human $CD14^+$ monocytes were preincubated with the IP_3 receptor inhibitor 2-APB (Figure 33A) or the PLC inhibitor U73122 (Figure 33B), the glucose-mediated release of Ca^{2+} was prevented.

The sensitivity of the IP_3R to its ligand is modulated by phosphorylation [219]. The phosphorylation of IP_3R by PKA has been described to increase the sensitivity of the receptor to IP_3 [102,220], potentially amplifying the glucose-induced Ca^{2+} release and cellular Ca^{2+} loss from the ER. Accordingly, the phosphorylation of Ser1756, which is known to modulate IP_3R activity and consequently Ca^{2+} mobilization via the IP_3R [221], was investigated in glucose-treated BMDMs. Incubation of BMDMs with elevated glucose concentrations increased phosphorylation of the IP_3R in a dose-dependent manner (Figure 33C). These data indicate that PLC and subsequent activation of the IP_3R are induced

downstream of glucose-mediated activation of Tas1R3 and are involved in glucose-mediated Ca^{2+} release from the ER.

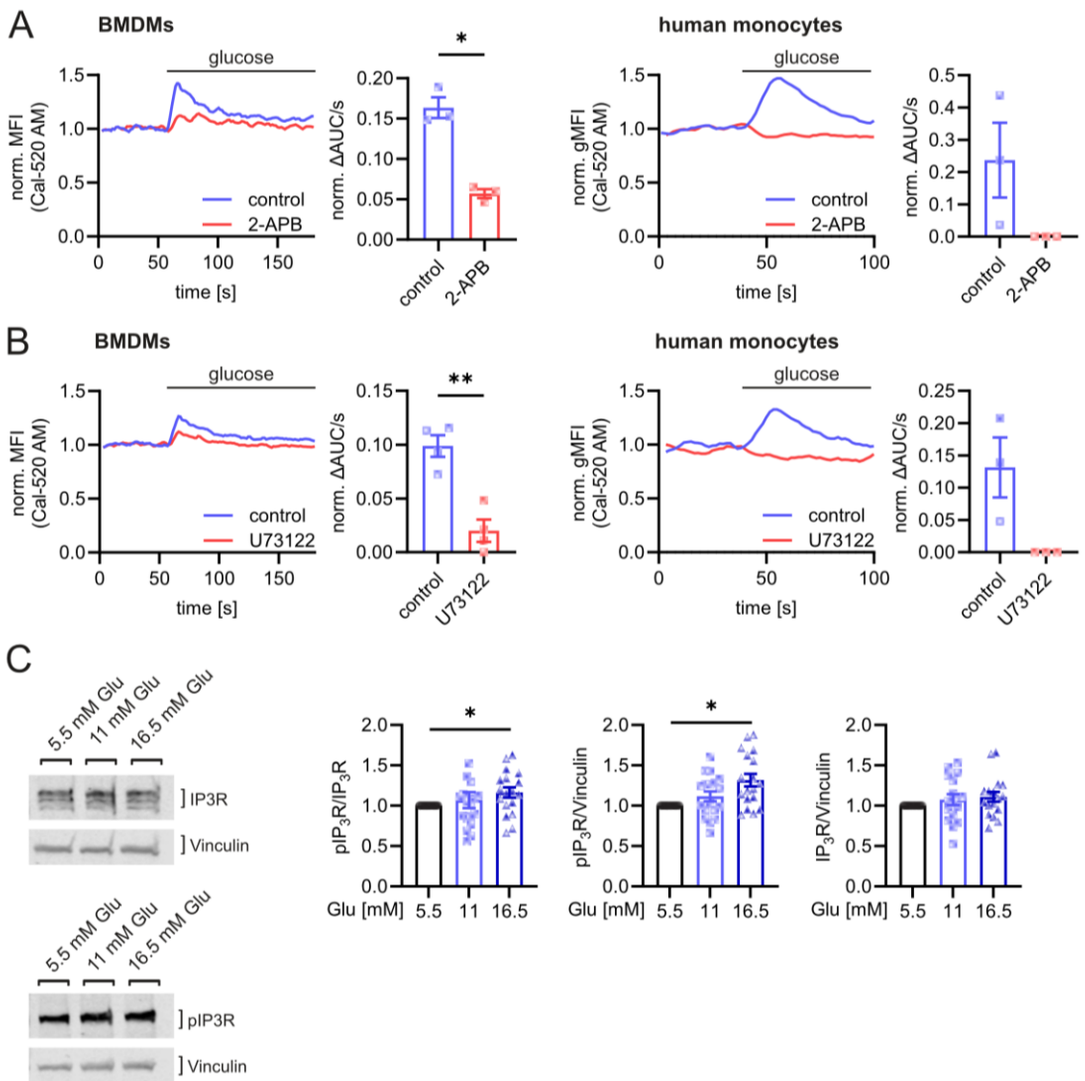

Figure 33 – Taste receptor-mediated Ca^{2+} release by glucose involves PLC-dependent activation of the IP_3 receptor

(**A** and **B**) Flow cytometric analysis of Ca^{2+} response to glucose (22 mM) in Cal-520 AM-stained BMDMs and human $CD14^+$ monocytes. Cells were incubated with the IP_3 receptor inhibitor 2-APB (100 µM, **A**) or the PLC inhibitor U73122 (5 µM, **B**) 10 min prior to the addition of glucose. The intensity of Ca^{2+} signaling was calculated as the difference of the area under the curve normalized to one second before and after addition of the stimulus. Ca^{2+} signaling curves are depicted as pooled data from the same independent experiments as depicted in the bar graph and Ca^{2+} signaling curves were normalized to each baseline before addition of glucose (n = 3-4). (**C**) Western blot analysis of the expression and phosphorylation of the IP_3R in glucose-treated BMDMs (48 h). Relative levels normalized to samples with 5.5 mM glucose; Vinculin was used as a loading control (n = 13). Data are shown as mean ± SEM; significance was determined by paired Student's t-test (A, B) or calculation of confidence intervals (C) (* $p<0.05$, ** $p<0.01$). *Abbreviations: 2-APB, 2-aminoethoxy-diphenyl borate; AUC, area under the curve; BMDMs, bone marrow-derived macrophages; Glu, glucose; Δ, difference; (g)MFI, (geometric) Mean Fluorescence Intensity; IP_3, inositol triphosphate; norm., normalized; PLC, phospholipase C; R, receptor.*

4.3.3.2. Glucose-mediated activation of Tas1R3 leads to inhibition of SERCA

At steady state, the maintenance of the Ca^{2+} homeostasis at the ER is tightly regulated. Ca^{2+} leakage from the ER through various channels, including the IP_3 and ryanodine receptors, is counteracted by continuous pumping of Ca^{2+} back to the ER by SERCA. Inhibiting this ATPase by thapsigargin prevents the replenishment of the Ca^{2+} store, leading to increased cytosolic Ca^{2+} concentrations. Over time, the disruption of the balance of Ca^{2+} leakage from and uptake to the ER leads to a loss of Ca^{2+} from the ER [100,175]. To investigate whether glucose-mediated depletion of Ca^{2+} from the ER involves changes in SERCA activity in addition to activation of the IP_3 receptor, SERCA activity was assessed using an enzyme-coupled spectrophotometric assay [192]. Treatment of BMDMs with elevated glucose concentrations resulted in a reduced SERCA activity, determined as the difference between a sample with and without addition of thapsigargin (Figure 34A). The decrease in SERCA activity was not attributable to altered expression levels of SERCA, as protein levels remained unchanged (Figure 34B). A similar reduction in SERCA activity was also observed in sucralose-treated BMDMs (Figure 34C) indicating that the inhibition is mediated by signaling via Tas1R3.

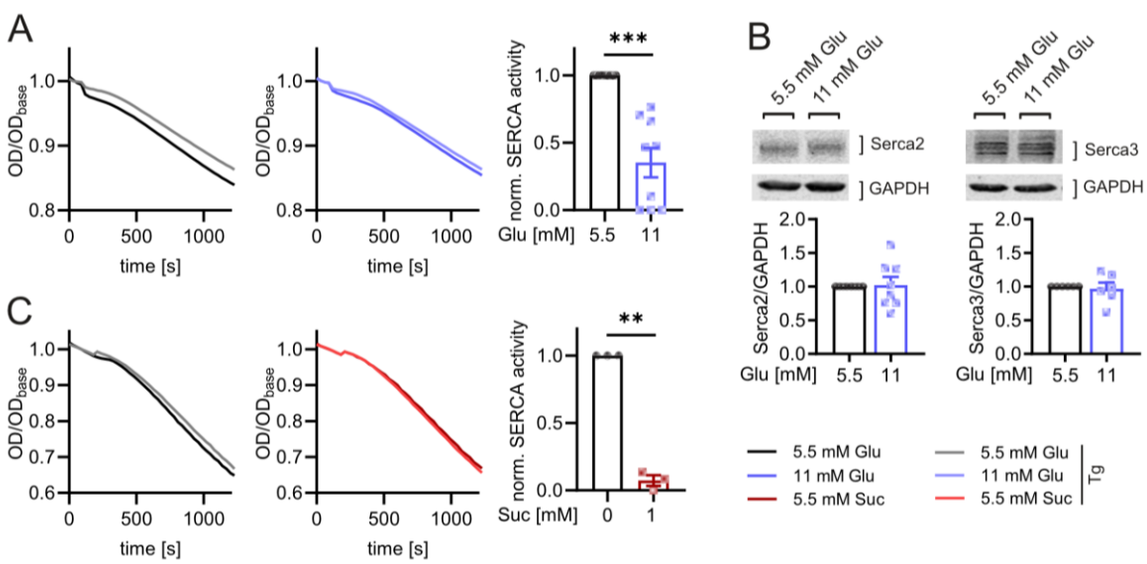

Figure 34 – SERCA activity is reduced in macrophages treated with glucose and sucralose
(**A**) Treatment of BMDMs with glucose for 48 h. SERCA activity was determined via an indirect enzyme-coupled spectrophotometric assay from the oxidation of NADH, measured as a decrease in OD at 340 nm after addition of 5 mM ATP. The SERCA activity was determined as the difference between the curves in the absence or presence of 10 µM thapsigargin and normalized to each control (n = 9). (**B**) Western blot analysis of SERCA2/3 levels in glucose-treated BMDMs (48 h); relative values normalized to the control. GAPDH was used as a loading control (n = 8). (**C**) SERCA activity as described in (A). Treatment of BMDMs with sucralose for 48 h (n = 3). Data are shown as mean ± SEM; significance was determined by calculation of confidence intervals (** $p<0.01$, *** $p<0.001$). *Abbreviations: BMDMs, bone marrow-derived macrophages; Glu, glucose; norm., normalized; OD, optical density; Suc, sucralose; Tg, thapsigargin.*

It has been shown that the SERCA activity in a cellular context is modulated by various micropeptides. The micropeptide phospholamban (PLN), which diminishes the SERCA activity in its dephosphorylated state, has been primarily studied in the context of regulating smooth muscle contractions [141,222]. To explore a putative role of PLN in regulating glucose-mediated inhibition of SERCA, it is first necessary to determine whether PLN is present in macrophages. Therefore, murine PLN, amplified from cDNA of BMDMs, was cloned into a plasmid containing a Flag-Tag and expressed in HEK293T cells. Western blot analysis using antibodies against PLN or Flag revealed bands of the same size, confirming PLN antibody specificity (Figure 35A). A moderate expression of PLN was found in BMDMs at both mRNA and protein levels (Figure 35B) confirming that PLN is expressed in macrophages.

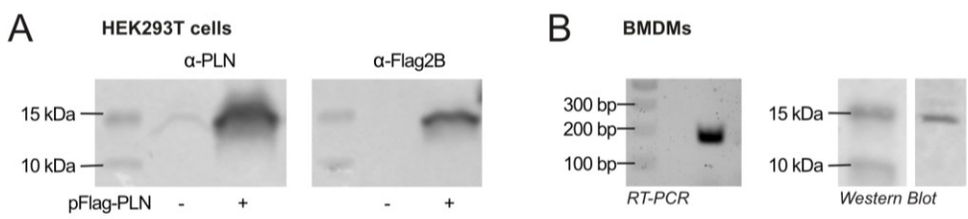

Figure 35 – Expression of phospholamban by macrophages
(**A**) PLN cDNA amplified from BMDMs was cloned into a pCMV-Tag2B plasmid and expressed in HEK293T cells. Expression of the PLN-Flag fusion protein was assessed by Western blot. (**B**) Analysis of PLN protein and mRNA expression by RT-PCR and Western blot in BMDMs. *Abbreviations: BMDMs, bone marrow-derived macrophages; bp, base pairs; PLN, phospholamban; RT-PCR, reverse transcriptase polymerase chain reaction.*

Finally, PLN phosphorylation was determined in BMDMs treated with 2-DG or glucose using Western blot analysis. In line with the inhibitory function of dephosphorylated PLN on SERCA and the reduced SERCA activity observed in glucose-treated cells (see Figure 34), PLN phosphorylation was significantly reduced in BMDMs treated with 2-DG or glucose (Figure 36). Together, these data suggest that glucose-induced activation of Tas1R3 and subsequent release of Ca^{2+} from the ER does not only result from activation of the IP_3 receptor but also results from the inhibition of SERCA activity via dephosphorylation of PLN.

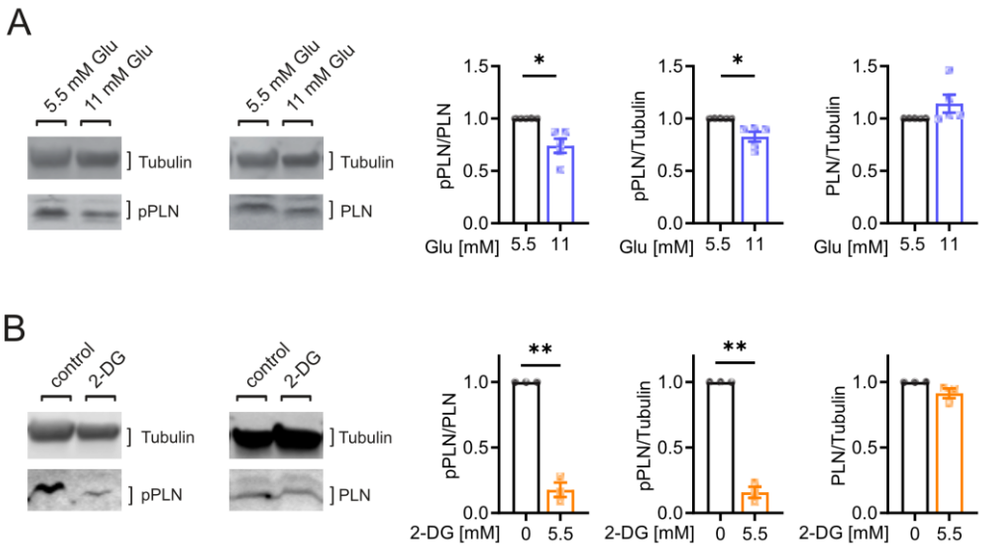

Figure 36 – Glucose and 2-DG mediate the dephosphorylation of phospholamban
BMDMs were treated with glucose (**A**) or its analog 2-DG (**B**) for 4 h. Phosphorylation and expression of PLN was determined via Western blot in whole cell lysates. Tubulin was used as a loading control. Samples were normalized to each control (n = 5 for A, n = 3 for B). Data are shown as mean ± SEM; significance was determined by calculation of confidence intervals (* $p<0.05$, ** $p<0.01$). *Abbreviations: BMDMs, bone marrow-derived macrophages; Glu, glucose; PLN, phospholamban; 2-DG, 2-deoxyglucose.*

4.3.3.3. The activation of Tas1R3 reduces SERCA activity through modulation of PLN by protein phosphatase 1

It has been described that the activation of Tas1R3 and the signal transduction of the GPCR involves the activation of PLC resulting in the generation of DAG and IP_3 [211]. DAG is known to mediate the activation of PKC resulting in the stimulation of PP1, which mediates the dephosphorylation of PLN [141,142]. The involvement of PLC-PKC-PP1 signaling in the reduction of SERCA activity by glucose, and especially the dephosphorylation of PLN by PP1, was investigated using various inhibitors and activators interfering with the signaling cascade.

Therefore, the SERCA activity was assessed in BMDMs that have been stimulated with PMA, a potent activator of the protein kinase C. Similar to glucose, treatment with PMA strongly reduced SERCA activity (Figure 37A). In addition, blockade of PKC with the cell-permeable and highly-selective PKC inhibitor bisindolylmaleimide (BIM) prevented Ca^{2+} signaling in response to glucose in BMDMs and human $CD14^+$ monocytes (Figure 37B and C). These data indicate that PKC is indeed involved in Tas1R3-mediated inhibition of SERCA and induction of Ca^{2+} release from the ER.

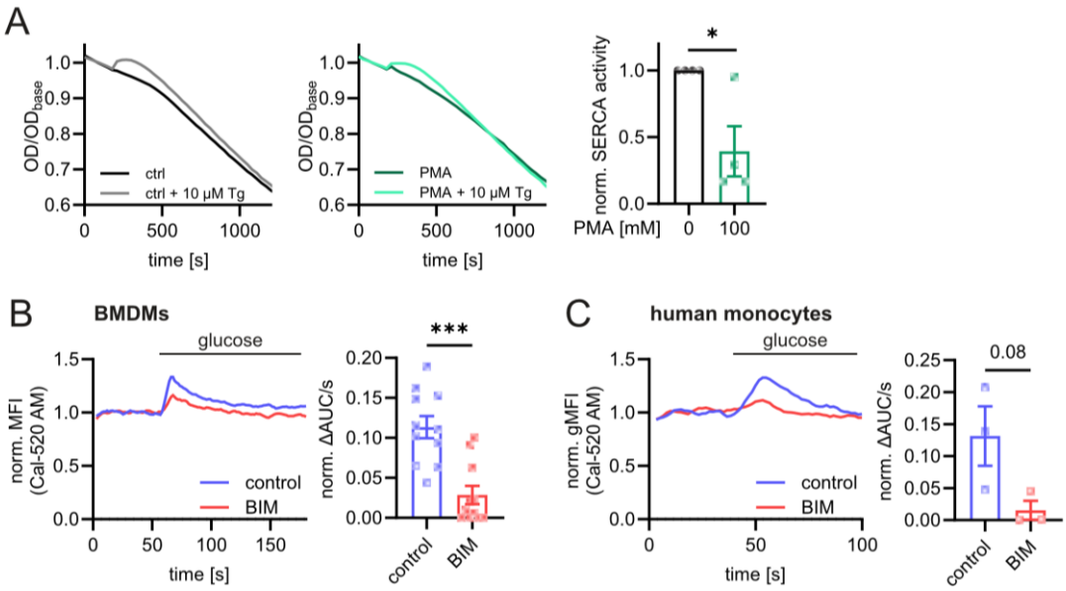

Figure 37 – Glucose-mediated inhibition of SERCA and Ca^{2+} release is mediated via activation of PKC
(**A**) BMDMs were treated with the PKC activator PMA (100 nM) for 24 h. SERCA activity was determined by an enzyme-coupled spectrophotometric assay measuring NADH oxidation as decrease in OD at 340 nm over time. OD was normalized to the baseline before addition of 5 mM ATP. The specific SERCA activity was determined as the difference between the curves without and with addition of 10 µM thapsigargin and normalized to the control (n = 4). (**B** and **C**) Cal-520 AM-stained BMDMs (**B**) and human $CD14^+$ monocytes (**C**) were treated with the PKC inhibitor BIM (5 µM) for 10 min. Ca^{2+} concentrations in response to 22 mM glucose were monitored by flow cytometry. Ca^{2+} signaling curves were normalized to each baseline and intensity of Ca^{2+} signaling was calculated as the difference of the area under the curve normalized to one second before and after addition of the stimulus. Ca^{2+} signaling curves are represented as pooled data from the same independent experiments as depicted in the bar graph (n = 11 for B, n = 3 for C). Data are shown as mean ± SEM; significance was determined by calculation of confidence intervals (A) or paired Student's t-test (B, C) (* $p<0.05$, ** $p<0.01$, *** $p<0.001$). *Abbreviations: BIM, bisindolylmaleimide; BMDMs, bone marrow-derived macrophages; gMFI, geometric Mean Fluorescence Intensity; norm., normalized; OD, optical density; PKC, protein kinase C; PMA, phorbol 12-myristate 13-acetate; Tg, thapsigargin.*

The phosphorylation of protein phosphatase 1 at Thr320 inhibits its function [223]. This phosphorylation process is regulated by inhibitors, including inhibitor I-1, whose activity is modulated by PKC [141,224]. If dephosphorylation of PLN by glucose-induced activation of Tas1R3 is mediated via PKC-dependent modulation of PP1, the phosphorylation of PP1 should be reduced in response to glucose. Indeed, treatment with glucose and its analog 2-DG resulted in reduced levels of phosphorylated PP1 (Figure 38), indicating increased phosphatase activity.

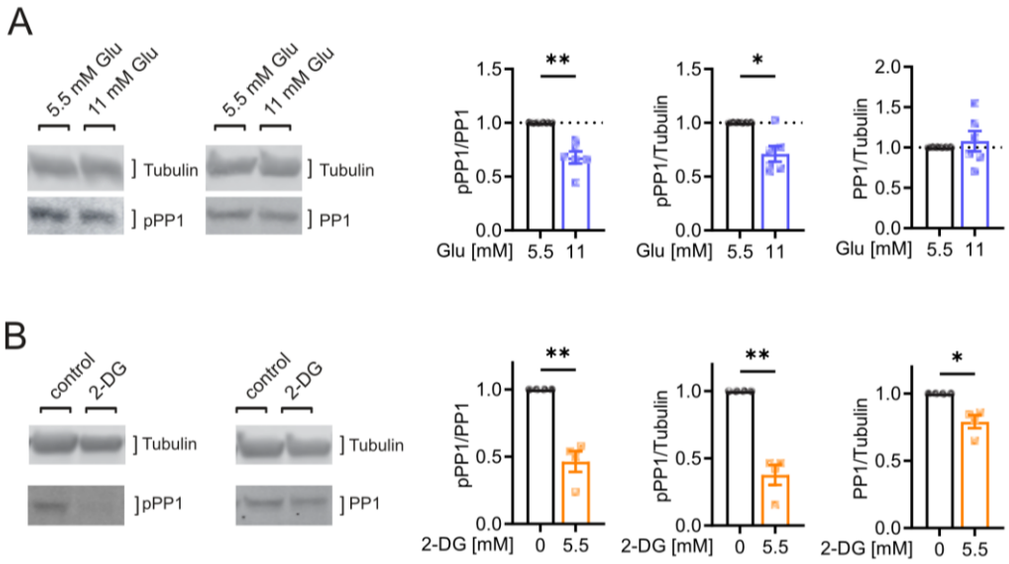

Figure 38 – Glucose and 2-DG mediate the dephosphorylation of protein phosphatase 1
BMDMs were treated with glucose (**A**) or 2-DG (**B**) for 4 h. Phosphorylation and expression of PP1 was determined via Western blot in whole cell lysates. Tubulin was used as a loading control. Samples were normalized to each control (n = 6 for A, n = 4 for B). Data are shown as mean ± SEM; significance was determined by calculation of confidence intervals (* $p<0.05$, ** $p<0.01$). *Abbreviations: BMDMs, bone marrow-derived macrophages; Glu, glucose; PP1, protein phosphatase 1; 2-DG, 2-deoxyglucose.*

Incubation with the PKC inhibitor BIM prevented the dephosphorylation of PP1 following Tas1R3 activation by glucose or 2-DG (Figure 39), supporting the hypothesis that PP1 is modulated by activation of PKC.

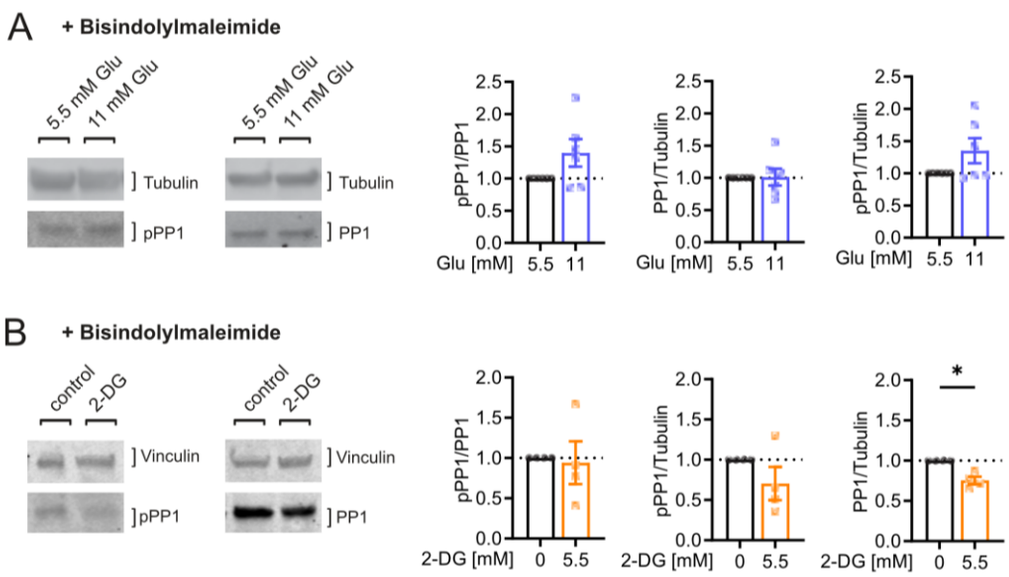

Figure 39 – Dephosphorylation of protein phosphatase 1 by glucose or 2-DG is mediated via PKC
BMDMs were treated with glucose (**A**) or 2-DG (**B**) and the PKC inhibitor bisindolylmaleimide (5 µM) for 4 h. Phosphorylation and expression of protein phosphatase 1 was determined via Western blot in whole cell lysates. Tubulin was used as a loading control (n = 6 for A, n = 4 for B). Samples were normalized to each control. Data are shown as mean ± SEM; significance was determined by calculation of confidence intervals (* $p<0.05$). *Abbreviations: BIM, bisindolylmaleimide; BMDMs, bone marrow-derived macrophages; Glu, glucose; PP1, protein phosphatase 1; 2-DG, 2-deoxyglucose.*

To univocally test the hypothesis that glucose-mediated Ca^{2+} release involves PP1-mediated dephosphorylation of PLN, PP1 activity was inhibited by Calyculin A. Preincubation of BMDMs as well as human $CD14^+$ monocytes with Calyculin A prevented the Ca^{2+} influx into the cytosol in response to glucose (Figure 40A and B). Moreover, the decreased phosphorylation of PLN mediated by glucose or 2-DG (as shown in Figure 36) was abolished by simultaneous incubation with Calyculin A (Figure 40C and D). Taken together, these data show that glucose-mediated activation of Tas1R3 and subsequent Ca^{2+} release from the ER involves PLC-mediated activation of IP_3R and inhibition of SERCA by PLN, which is mediated via PLC-PKC-PP1 signaling.

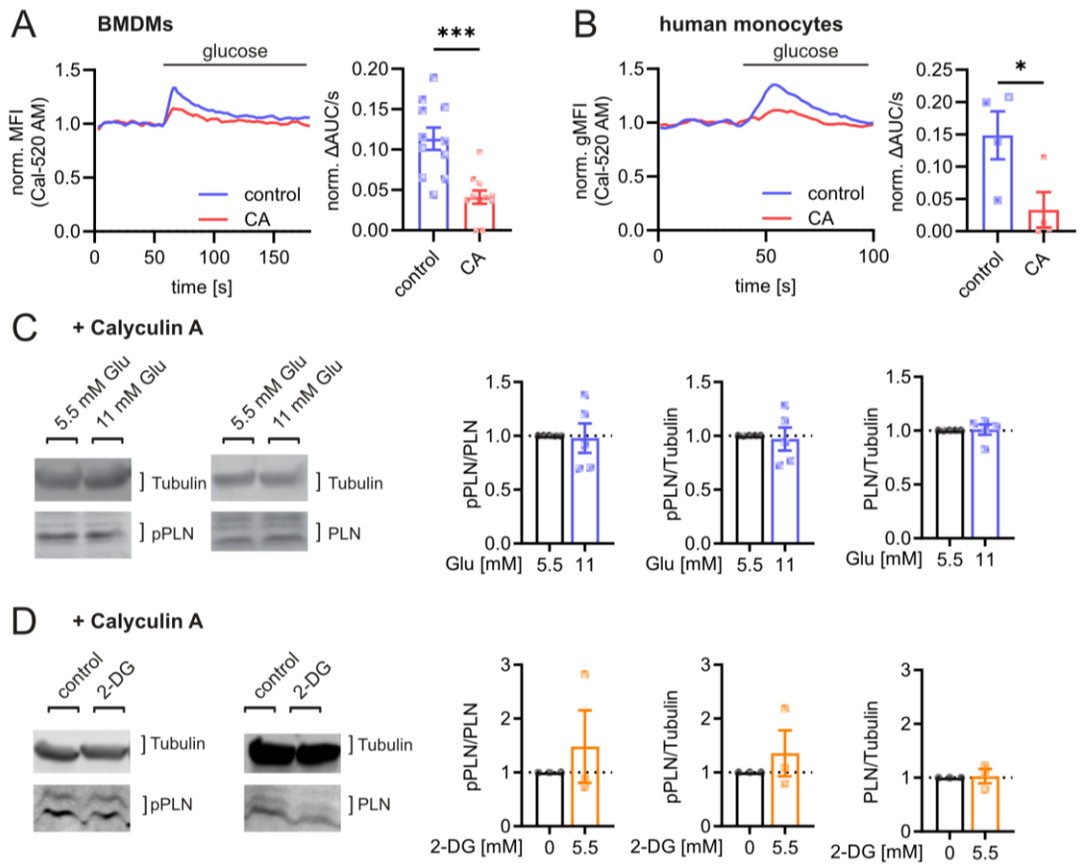

Figure 40 – Tas1R3-mediated modulation of PLN and induction of Ca^{2+} release are mediated via activation of protein phosphatase 1
(**A** and **B**) Cal-520 AM-stained BMDMs (**A**) and human $CD14^+$ monocytes (**B**) were treated with the PP1 inhibitor Calyculin A (100 nM) for 10 min. Ca^{2+} concentrations in response to 22 mM glucose were monitored by flow cytometry. Ca^{2+} signaling curves were normalized to each baseline and intensity of Ca^{2+} signaling was calculated as the difference of the area under the curve normalized to one second before and after addition of the stimulus. Ca^{2+} signaling curves are represented as pooled data from the same independent experiments as depicted in the bar graph (n = 11 for A, n = 4 for B). (**C** and **D**) BMDMs were treated with glucose (**C**) or 2-DG (**D**) and the PP1 inhibitor Calyculin A (100 nM) for 4 h. Phosphorylation and expression of phospholamban was determined via Western blot in whole cell lysates; Tubulin was used as a loading control; samples were normalized to each control (n = 5 for C, n = 3 for D). Data are shown as mean ± SEM; significance was determined by paired Student's t-test (A, B) or calculation of confidence intervals (C, D) (* $p<0.05$, ** $p<0.01$, *** $p<0.001$). *Abbreviations: CA, Calyculin A; BMDMs, bone marrow-derived macrophages; Glu, glucose; gMFI, geometric Mean Fluorescence Intensity; PLN, phospholamban; 2-DG, 2-deoxyglucose.*

4.4. Intensity of Ca^{2+} signaling in murine and human macrophages negatively correlates with blood glucose concentrations

4.4.1. *Ex vivo* analysis of Ca^{2+} signaling in freshly-isolated peritoneal macrophages

The previously described *in vitro* data of BMDMs, cultivated peritoneal macrophages as well as human monocyte-derived macrophages clearly showed that elevated glucose concentrations disrupt Ca^{2+} homeostasis and Ca^{2+} signaling. This disruption of the Ca^{2+} response has been attributed to glucose-mediated activation of Tas1R3 and subsequent depletion of Ca^{2+} from the ER. To further investigate the impact of hyperglycemia on macrophages in a physiological context, Ca^{2+} signaling was investigated in macrophages obtained from a murine and human cohort.

4.4.1.1. The correlation between Ca^{2+} signaling and blood glucose concentrations depends on Tas1R3 expression levels in peritoneal macrophage subsets

Cells from the peritoneal cavity were isolated from up to 18-month-old mice and Ca^{2+} signaling in response to extracellular $CaCl_2$ was investigated by flow cytometry. Further, the blood glucose levels were measured in blood samples taken from the tail vein.

Peritoneal macrophages were identified using the gating strategy depicted in Figure 41 as described previously [225–227]. In brief, peritoneal macrophages were selected by first gating for alive $CD45^+$ immune cells followed by gating based on the expression of CD11b. Small (SPMs) and large peritoneal macrophages (LPMs) were further discriminated based on their expression of MHC II and F4/80, respectively.

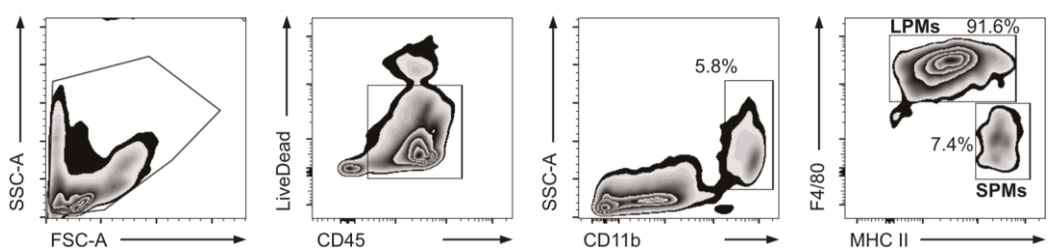

Figure 41 – Gating strategy to identify peritoneal macrophage populations
Cells isolated from the peritoneal cavity were gated based on their FSC-A and SSC-A profile. Alive immune cells were identified by expression of CD45 and using a viability dye (LiveDead) to exclude dead cells. CD11b was used as a marker for peritoneal macrophages. The $CD11b^+$ cells were separated into small ($CD11b^+$ MHC II^+ $F4/80^{int}$, SPMs) and large ($CD11b^+$ MHC II^- $F4/80^+$, LPMs) peritoneal macrophages.

The intensity of Ca^{2+} signaling in all peritoneal macrophages exhibited a weak negative correlation with the blood glucose levels of the mice (Figure 42A). Strikingly, when distinguishing between LPMs and SPMs, it was found that while LPMS displayed a weak negative correlation of Ca^{2+} signaling and blood glucose concentrations, a strong negative correlation could be observed in SPMs (Figure 42A).

Additionally, different levels of Tas1R3 were observed in the subsets of mouse peritoneal macrophages. Both subsets (LPMs and SPMs) expressed Tas1R3, however, the expression was significantly higher in MHC II^+ SPMs (Figure 42B) supporting the relevance of Tas1R3 expression in glucose-mediated changes in Ca^{2+} signaling.

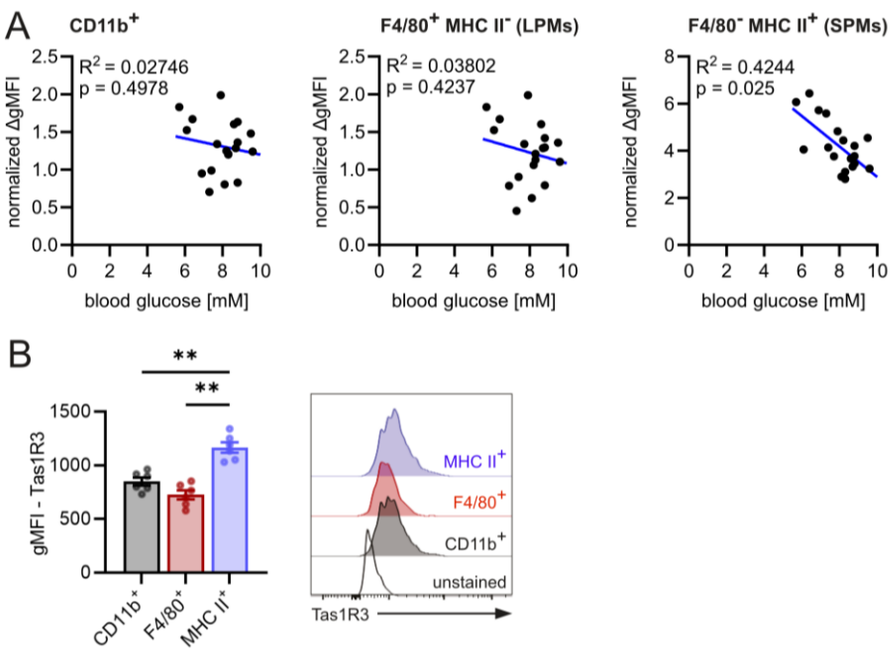

Figure 42 – Ca^{2+} signaling negatively correlates to blood glucose concentrations, especially in Tas1R3^{high} small peritoneal macrophages
(**A**) Cells from the peritoneal cavity were stained with various antibodies and Cal-520 AM. Peritoneal macrophage subsets were gated as described in Figure 41. Correlation analysis of intensity of Ca^{2+} signaling in response to extracellular $CaCl_2$ (2 mM) and blood glucose levels. Ca^{2+} signaling intensities are depicted as differences in the gMFI from before and after stimulation; data were normalized to the gMFI of each baseline beforehand (n = 19). (**B**) Expression of the taste receptor Tas1R3 was determined in peritoneal macrophage subsets by flow cytometry (n = 6). Data are shown as mean ± SEM; significance was determined by linear regression analysis (A) as well as One-Way ANOVA corrected for multiple comparisons by the Tukey method (B). *Abbreviations: gMFI, geometric Mean Fluorescence Intensity; LPMs, large peritoneal macrophages; R^2, coefficient of determination for linear regression; SPMs, small peritoneal macrophages.*

4.4.1.2. Long term high fat diet impairs Ca^{2+} signaling in peritoneal macrophages

Ca^{2+} signaling in response to extracellular $CaCl_2$ was further monitored in SPMs isolated from mice that were fed with a control diet (CD) or high fat diet (HFD) for one year. HFD-treated mice exhibited significantly elevated blood glucose levels (Figure 43A) and Ca^{2+} signaling was reduced in SPMs from these mice (Figure 43B).

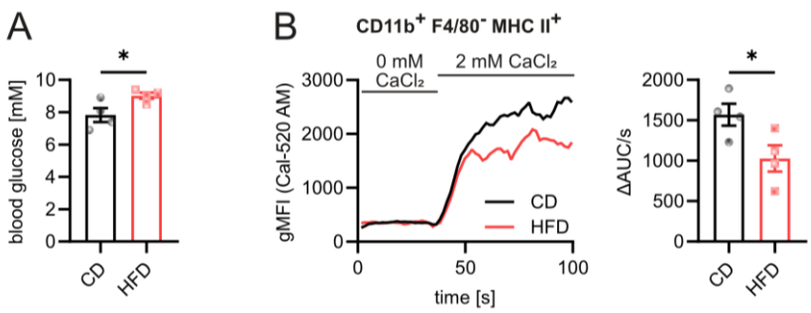

Figure 43 – Ca^{2+} signaling is reduced in peritoneal macrophages from HFD-treated mice
(**A**) Blood glucose was determined in blood from the tail vein of mice fed with a HFD or CD for one year (n = 4). (**B**) The intensity of Ca^{2+} signaling in response to extracellular $CaCl_2$ (2 mM) was determined in Cal-520 AM-stained small peritoneal macrophages ($CD11b^+$ $F4/80^-$ MHC II^+) isolated from the HFD- and CD-treated mice. The intensity of Ca^{2+} signaling was calculated as the difference of the area under the curve normalized to one second before and after addition of the stimulus. Ca^{2+} signaling curves are represented as pooled data from the same independent experiments as depicted in the bar graph (n = 4 per condition). Data are shown as mean ± SEM; significance was determined by Student's t-test (* $p<0.05$). *Abbreviations: CD, control diet; gMFI, geometric Mean Fluorescence Intensity; HFD, high fat diet.*

4.4.2. Analysis of Ca^{2+} signaling in immune cell subsets from human PBMCs

4.4.2.1. The Ca^{2+} response to glucose positively correlates to the expression of Tas1R3 in various human immune cells subsets

Since mouse physiology cannot be completely translated to human physiology, various parameters were further assessed in PBMC subsets isolated from whole blood of a human cohort.

A gating strategy, which has been developed based on previous investigations [228–230], was applied to identify immune cell subsets based on their expression of surface markers (Figure 44). The first steps of the gating were used to exclude doublets and remove dead cells. Next, monocytes were separated from other PBMCs based on the expression of CD14 and CD16. Monocytes were further divided into $CD14^+$ classical as well as $CD16^+$ non-classical monocytes. Within the $CD14^-$ $CD16^-$ PBMC population, the expression of CD19 and CD3 facilitated the identification of B cells and T cells, respectively.

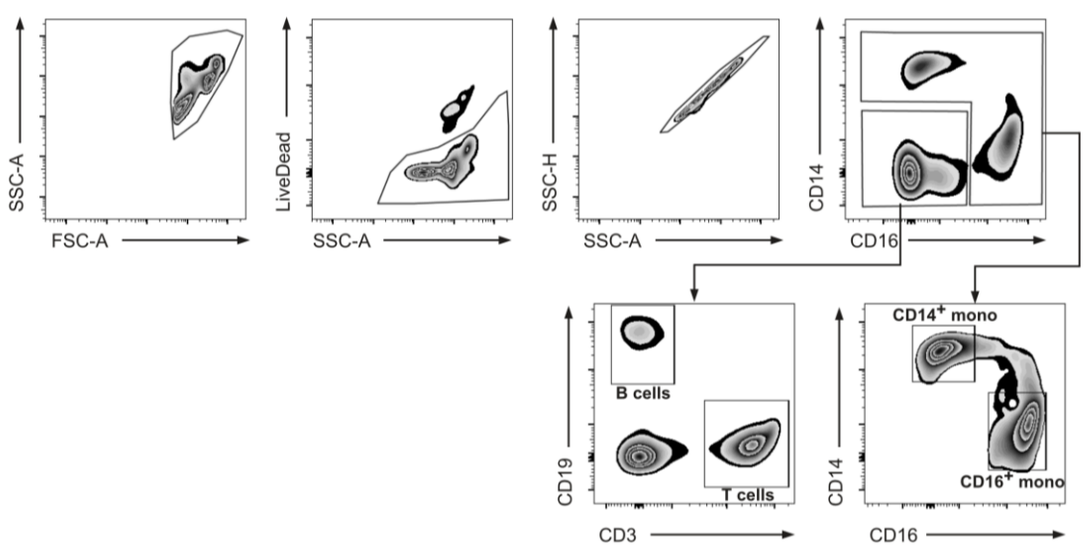

Figure 44 – Gating strategy to identify immune cell subsets from human PBMCs
Alive singlet PBMCs were identified using a LiveDead stain and characteristics in Forward and Sideward Scatter; separation of monocytes and other immune cells based on the expression of CD14 and CD16. Monocytes subsets were further separated into $CD14^+$ classical as well as $CD16^+$ non-classical monocytes. $CD19^+$ B cells and $CD3^+$ T cells were gated within the $CD14^-$ $CD16^-$ non-monocytic subset. *Abbreviations: mono, monocyte; PBMCs, peripheral blood mononuclear cells.*

The changes in Ca^{2+} concentrations in response to addition of glucose were monitored in the described PBMC populations (Figure 45A). A clear Ca^{2+} influx into the cytosol was observed in $CD14^+$ classical monocytes upon addition of glucose. In $CD16^+$ classical monocytes, addition of glucose only led to a slight increase in Ca^{2+} concentrations. In contrast, the addition of glucose did not lead to any changes in cytosolic Ca^{2+} concentrations in T and B cells.

Flow cytometric analysis of Tas1R3 expression in the PBMC populations revealed that T and B cells do not express Tas1R3, whereas significantly higher levels were detected in monocytes (Figure 45B). Similar to the observations in peritoneal macrophages, higher expression levels of Tas1R3 were detected in $CD14^+$ classical monocytes compared to $CD16^+$ non-classical monocytes. Accordingly, the levels of Tas1R3 correlated with the intensity of glucose-mediated Ca^{2+} signaling, highlighting a crucial role of the taste receptor in glucose-mediated release of Ca^{2+} in macrophages and monocytes.

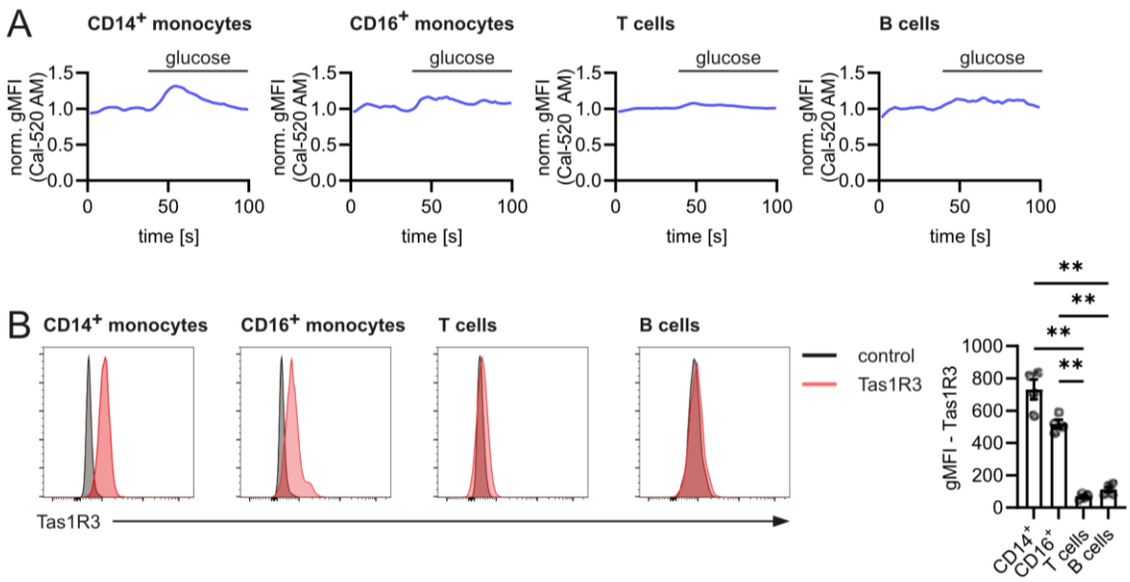

Figure 45 – Ca^{2+} signaling in response to glucose is dependent on Tas1R3 expression of PBMC subsets
(**A**) Cytosolic Ca^{2+} concentrations were monitored in Cal-520 AM-stained human PBMCs after addition of 22 mM glucose. PBMC populations were gated as shown in Figure 44. Ca^{2+} curves are depicted as pooled data from four independent experiments and normalized to each baseline before addition of glucose. (**B**) Flow cytometric analysis of the expression of the taste receptor Tas1R3 in PBMC populations (n = 4). Data are shown as mean ± SEM; significance was determined by One-Way ANOVA corrected for multiple comparisons by the Tukey method (** $p<0.01$). *Abbreviations: gMFI, geometric Mean Fluorescence Intensity; norm., normalized.*

4.4.2.2. Analysis of correlations between Ca^{2+} signaling in classical monocytes and various blood and somatic parameters in a human cohort

The influence of hyperglycemia on Ca^{2+} signaling was further assessed in PBMCs derived from whole blood from a human cohort analyzing a total of 46 individuals. The participants were separated into two groups based on their fasting blood glucose levels. Individuals with fasting blood glucose levels below or equal to 5.5 mM were classified as healthy, whereas donors with fasting blood glucose levels above 5.5 mM were considered prediabetic (Table 3, Figure 46A). Along with the blood glucose levels, several other metabolic biomarkers were employed to evaluate glucose homeostasis and insulin sensitivity in the individuals. HbA1c, known as glycosylated hemoglobin, serves as an indicator for the average blood glucose concentration over the past three months. In addition to fasting blood glucose levels, HbA1c is used as a diagnostic criterion for diabetes and individuals with an HbA1c value above 5.7% are classified as prediabetic. [10] The HOMA (homeostasis model assessment) index, which is based on the fasting insulin and fasting blood glucose levels, is used as an indicator for insulin resistance and accordingly to determine type 2 diabetes [231]. Both HbA1c as well as HOMA index were significantly increased in individuals with prediabetes (Table 3). All other parameters, including anthropometric measurements and blood lipid profiles, were similar in both groups from the human cohort (Table 3).

Table 3 – Metadata and clinical parameters derived from a human cohort study
All data are mean values ± SEM; significance between both groups was determined by unpaired Student's t-test (* $p<0.05$, ** $p<0.01$, *** $p<0.001$).

	≤ 5.5 mM	**> 5.5 mM**
Participant	N = 32	N = 14
Sex	F = 20, M = 12	F = 6, M = 8
Age	63.65 ± 0.61	65.86 ± 1.44
BMI [kg/m²]	27.37 ± 0.92	28.91 ± 0.76
Blood glucose [mM]	4.96 ± 0.08	6.02 ± 0.14 ***
HbA1c [%]	5.46 ± 0.03	5.82 ± 0.08 ***
Waist circumference [cm]	92.48 ± 2.43	98.96 ± 2.59
Non-HDL cholesterol [mg/dL]	153.75 ± 5.77	154.64 ± 13.41
Triglycerides [mg/dL]	116.06 ± 7.44	140.86 ± 13.8
HOMA	2.06 ± 0.14	3.5 ± 0.50 *
Cholesterol [mg/dL]	221.84 ± 5.49	211.43 ± 13.76

Since glucose-mediated Ca^{2+} signaling was mainly observed in $CD14^{+}$ classical monocytes with high expression of Tas1R3 (Figure 45), investigations of Ca^{2+} signaling in the human cohort particularly focused on this PBMC subset. A strong positive correlation was observed between the intensities of thapsigargin- and ionomycin-induced Ca^{2+} signaling in $CD14^{+}$ monocytes of the whole cohort (Figure 46B), suggesting that the Ca^{2+} response is shaped by the metabolic environment, regardless of the applied stimulus. Consistent with the glucose-mediated disturbances of Ca^{2+} signaling in response to various stimuli observed *in vitro*, the intensity of both thapsigargin- and ionomycin-induced Ca^{2+} signaling was significantly reduced in classical monocytes from individuals with prediabetes (Figure 46C). In contrast, blood glucose levels did not affect thapsigargin- and ionomycin-induced Ca^{2+} signaling in non-classical monocytes, T cells and B cells (Figure 46D). To exclude a bias due to uneven sex distribution within the two cohorts, the intensity of Ca^{2+} signaling in both groups was further compared after separating the data by gender. Ca^{2+} signaling was reduced in classical monocytes from individuals with prediabetes in both females and males indicating that the observed changes are independent of the gender of the participants (Figure 46E).

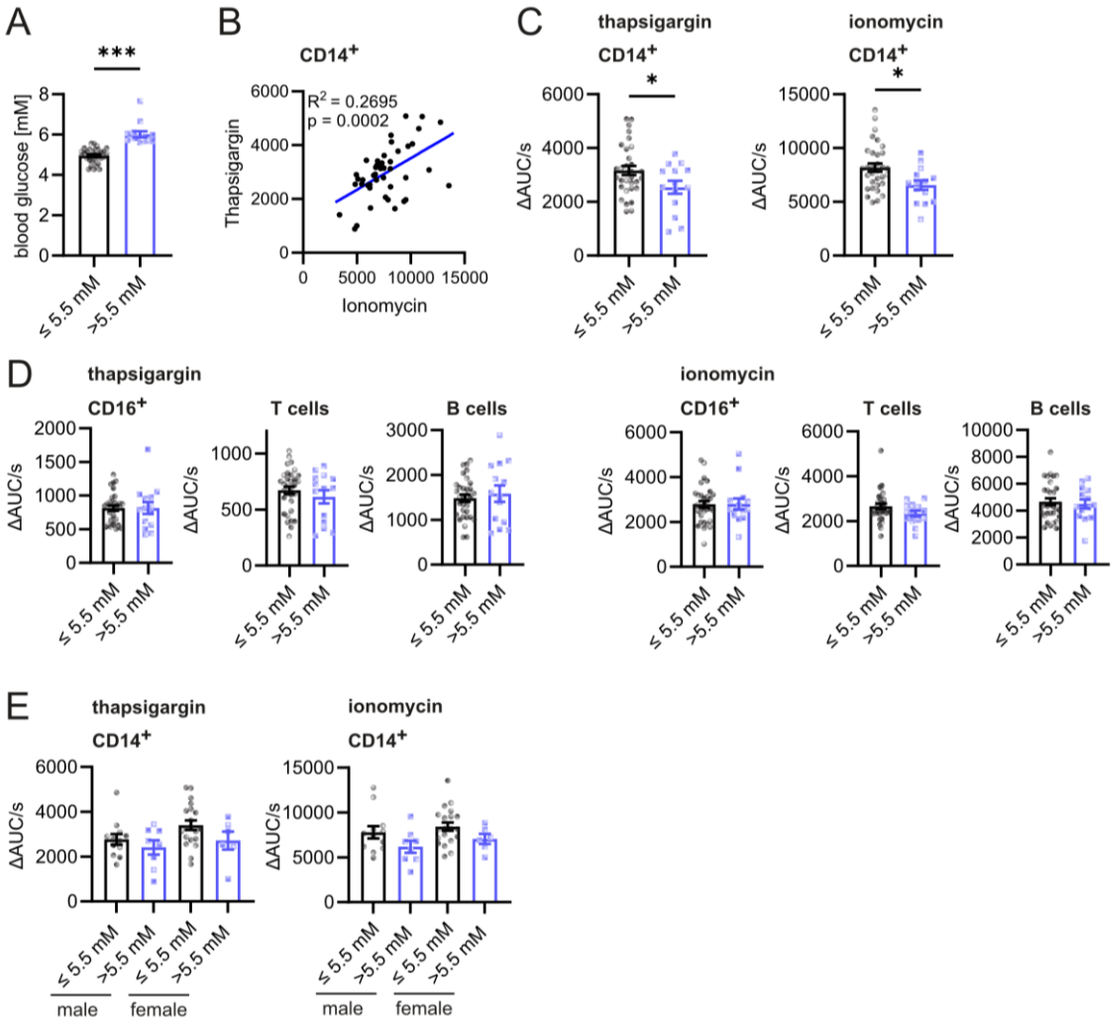

Figure 46 – Ca^{2+} signaling is reduced in classical monocytes from individuals with prediabetes
(**A**) Separation of participants from a human cohort study (n = 46) based on their fasting blood glucose levels; healthy group (blood glucose ≤ 5.5 mM) with 32 and prediabetic group (blood glucose > 5.5 mM) with 14 individuals. (**B** to **E**) The intensity of Ca^{2+} signaling induced by thapsigargin (1 µM) or ionomycin (1 µg/mL) was monitored in PBMC populations isolated from whole blood of participants from the human cohort. PBMCs were gated as shown in Figure 44 and stained with Cal-520 AM. Intensity of Ca^{2+} signaling was calculated as the difference of the area under the curve normalized to one second before and after addition of the stimulus. (**B**) Linear regression analysis of intensities of thapsigargin- and ionomycin-induced Ca^{2+} signaling in $CD14^+$ classical monocytes of all participants. (**C**) Ca^{2+} signaling intensity in $CD14^+$ classical monocytes. (**D**) Ca^{2+} signaling intensity in various PBMC populations. (**E**) Ca^{2+} signaling intensity in $CD14^+$ classical monocytes, groups were separated based on sex in addition to blood glucose levels. Data are shown as mean ± SEM; significance was determined by linear regression analysis or unpaired Student's t-test (* $p<0.01$). *Abbreviations: Δ, difference; AUC, Area under the curve.*

The intensity of thapsigargin- and ionomycin-induced Ca^{2+} signaling in classical monocytes was further correlated to parameters collected from the whole cohort. The correlation analysis revealed a strong negative correlation between Ca^{2+} signaling intensity and blood glucose levels (Figure 47, Figure 48). In addition, Ca^{2+} signaling intensity was negatively correlated to other glucose-related parameters, including HbA1c, insulin levels and HOMA, as well as BMI and waist circumference. In contrast, no correlation was observed between Ca^{2+} signaling intensity and lipid levels in the blood, such as cholesterol and non-HDL cholesterol (Figure 47, Figure 48).

In summary, the data clearly show that glucose-mediated Ca^{2+} release relies on the Tas1R3 expression level in the analyzed immune cell subsets. Accordingly, blood glucose concentrations only negatively correlate to Ca^{2+} signaling in Tas1R3-expressing murine SPMs and human classical, underscoring the critical role of Tas1R3 in glucose-induced Ca^{2+} responses.

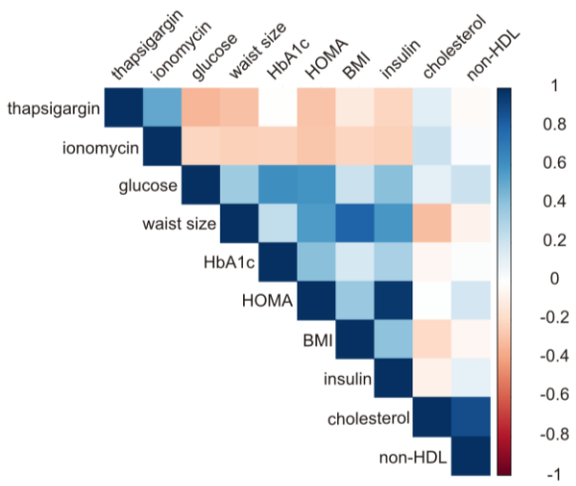

Figure 47 – Correlation analysis of the intensity of Ca^{2+} signaling and various body parameters derived from a human cohort study
Pearson's correlation between the intensities of ionomycin (1 µg/mL)- and thapsigargin (1 µM)-induced Ca^{2+} signaling in $CD14^+$ classical monocytes and various anthropometric and laboratory parameters derived from a human cohort (n = 46).

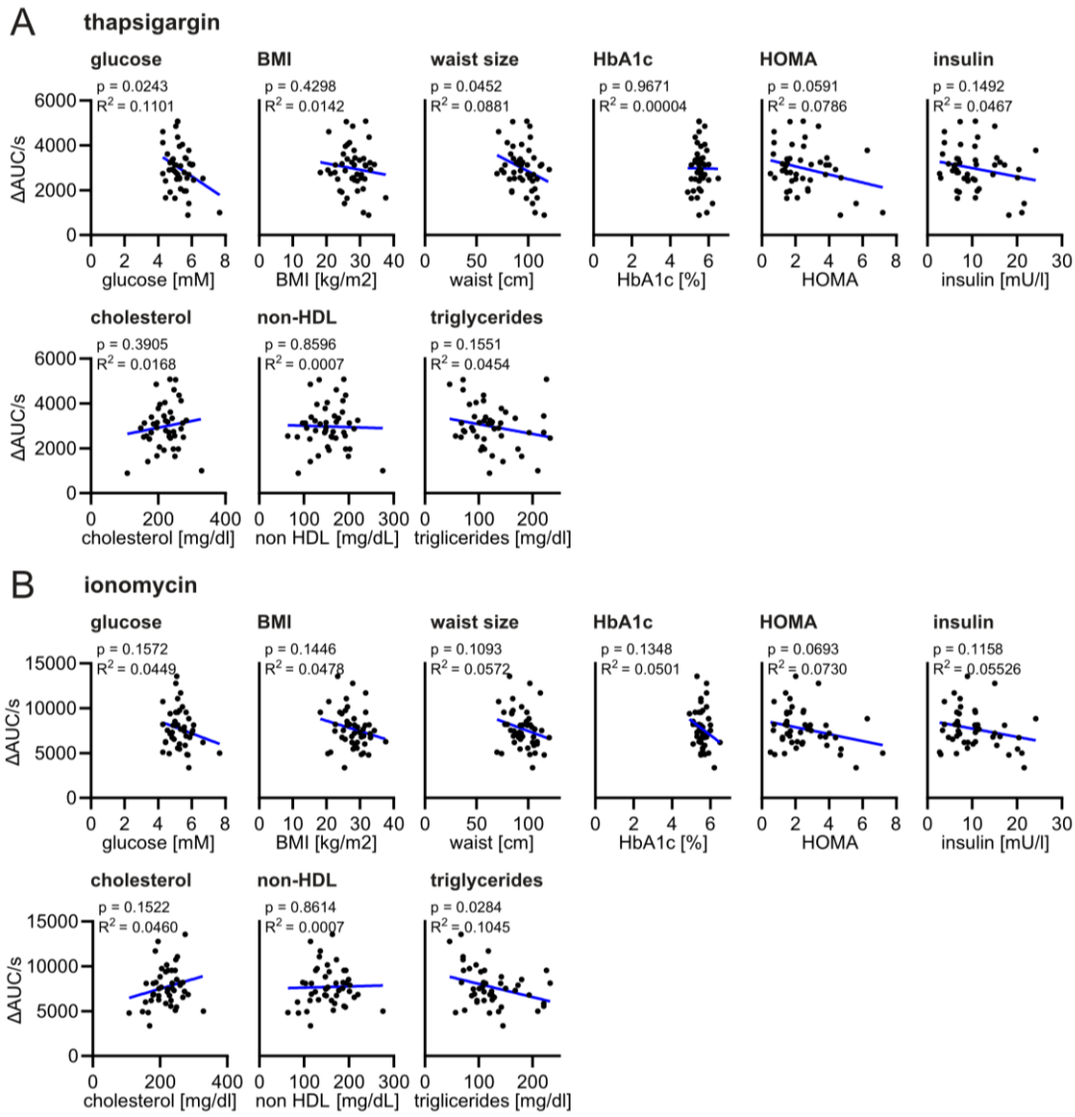

Figure 48 – Linear regression analysis of Ca^{2+} signaling and various body parameters derived from a human cohort study

Ca^{2+} signaling in response to 1 µM thapsigargin (**A**) or 1 µg/mL ionomycin (**B**) was monitored in Cal-520 AM-stained $CD14^{+}$ classical monocytes by flow cytometry. Intensity of Ca^{2+} signaling was calculated as the difference of the area under the curve normalized to one second before and after addition of the stimulus. Linear regression analysis was performed of the Ca^{2+} signaling intensity and various anthropometric and laboratory parameters. All data were obtained from 46 participants of a human cohort. *Abbreviations: Δ, difference; AUC, Area under the Curve, R^2, coefficient of determination.*

4.5. Functional consequences of glucose-mediated disruption of Ca^{2+} signaling

4.5.1. Elevated glucose concentrations result in increased ER stress

As a second messenger, Ca^{2+} plays a pivotal role in numerous signaling pathways and is of vital relevance for cellular functionality. Within macrophages, Ca^{2+} is essential for several cellular processes including chemokine-mediated migration, immune cell activation and protein folding (see 2.3.2) [37,173]. Since glucose mediates the disruption of Ca^{2+} homeostasis and depletion of Ca^{2+} from the ER, our further objective was to investigate the influence of hyperglycemia on Ca^{2+}-related cellular processes.

The accumulation of misfolded proteins, caused by impaired functionality of Ca^{2+}-dependent chaperones, leads to induction of the UPR response and ER stress [173]. As a consequence, the release of BiP from the ER stress sensors, including IRE1α, results in their activation mediating gene transcriptions involved in the degradation of misfolded proteins. Upon activation, IRE1α undergoes auto-phosphorylation, leading to the activation of its RNase domain, which promotes the splicing of XBP1 mRNA. As shown in Figure 49A and B, IRE1α phosphorylation was increased in BMDMs treated with elevated glucose concentrations or 2-DG. Moreover, treatment with 2-DG resulted in increased levels of the spliced form of XBP1 mRNA, as demonstrated by determining spliced and unspliced mRNA levels by RT-PCR (Figure 49C) as well as using a specific antibody in Western blot (Figure 49D). Given that the depletion of Ca^{2+} from the ER and, consequently, ER stress can be experimentally achieved by the inhibition of SERCA, the specific SERCA inhibitor thapsigargin was used here as positive control.

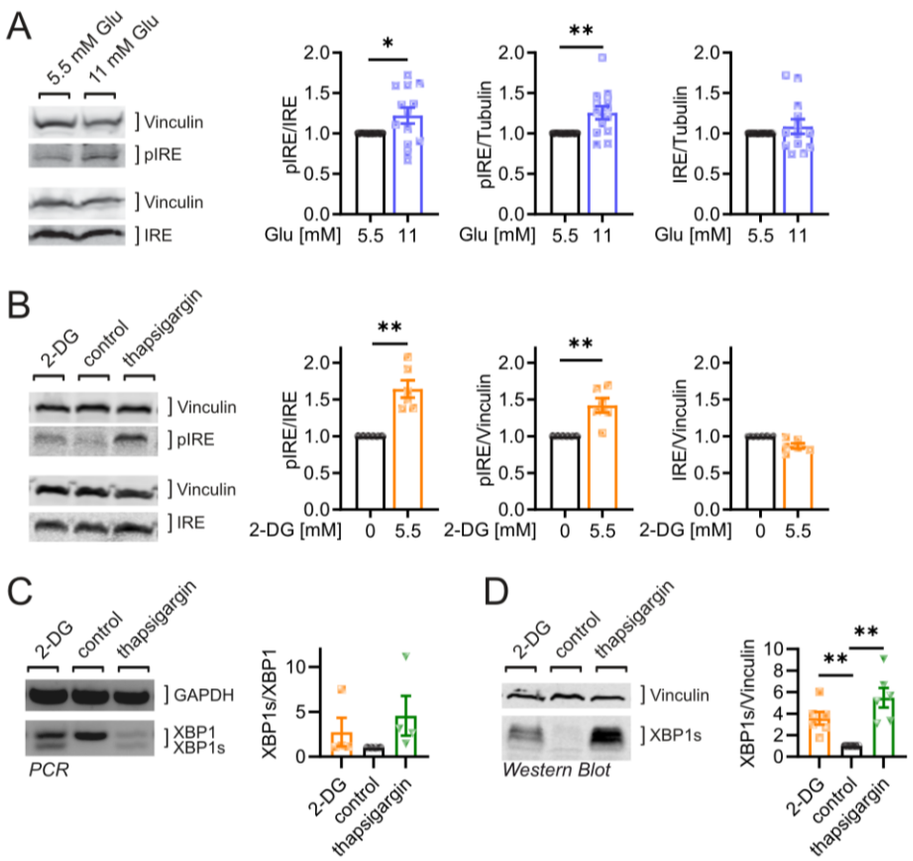

Figure 49 – Hyperglycemia results in activation of the ER stress sensor IRE1α and subsequent splicing of XBP1 mRNA
(**A** and **B**) Phosphorylation and expression of IRE1α were determined by Western blot in whole cell lysates. BMDMs were previously treated with additional glucose for 48 h (**A**) or 5.5 mM 2-DG for 4h (**B**) (n = 13 for A, n = 6 for B). (**C** and **D**) Splicing of XBP1 mRNA was monitored by RT-PCR (**C**) and Western blot (**D**) in BMDMs stimulated with 5.5 mM 2-DG or 500 nM thapsigargsin for 4 h. Tubulin or Vinculin were used as a loading control in Western blot analysis; GAPDH was used as a reference in RT-PCR; samples were normalized to each control (n = 4 for C, n = 6 for D). Data are shown as mean ± SEM; significance was determined by calculation of confidence intervals (* $p<0.05$, ** $p<0.01$, *** $p<0.001$). *Abbreviations: BMDMs, bone marrow-derived macrophages; Glu, glucose; IRE1, inositol-requiring enzyme 1; XBP1; X-box binding protein 1; XBP1s, spliced version of XBP1; 2-DG, 2-deoxyglucose.*

IRE1α activation has been shown to promote the translocation of STIM1 to ER-plasma membrane contact sites in T cells [177]. To investigate, whether STIM1 translocation also occurs in hyperglycemic macrophages, STIM1 expression was examined in membrane sheets using STED microscopy, as described previously by Merklinger *et al.* [232]. The analysis of membrane sheets provides a unique method to monitor contact sites between ER and plasma membrane because these contact sites remain intact upon generation of the sheets by sonication. After identifying the membrane sheets through F-actin staining using confocal microscopy, STED microscopy was used to determine STIM1 expression with high resolution (Figure 50A). Even in unstimulated cells, a few clusters of STIM1 at ER-plasma membrane contact sites were observed. Notably, the amount of STIM1 clusters near the plasma membrane significantly increased upon treatment with glucose, 2-DG or thapsigargin (Figure 50).

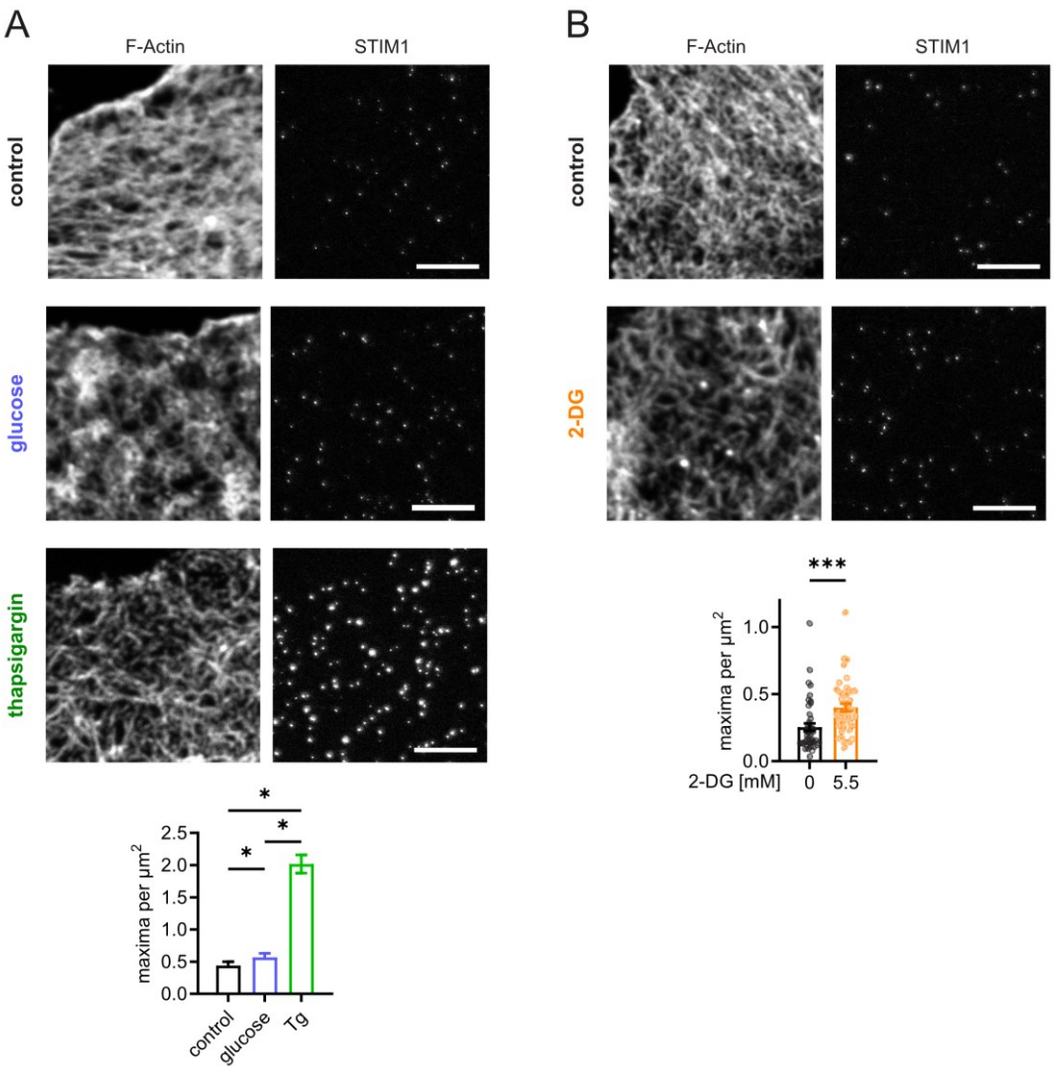

Figure 50 – Glucose increases STIM1 clusters near the plasma membrane
Membrane sheets were generated from BMDMs treated with elevated glucose concentrations (11 mM, **A**), 3 µM thapsigargin (**A**) or 2-DG (5.5 mM, **B**) for 3 h. Sheets were fixed and stained with an antibody against STIM1 as well as Phalloidin-488 to mark F-Actin. Membrane sheets were identified by confocal microscopy of F-Actin (left), STIM1 was monitored by STED microscopy (right). The density of STIM1 clusters was determined with ImageJ. Pooled data from three individual experiments with 15 membrane sheets analyzed per condition. Data are shown as mean ± SEM; significance was determined by one-way ANOVA corrected for multiple comparisons by the Tukey method (A) or unpaired Student's t-test (B). *Abbreviations: BMDMs, bone marrow-derived macrophages; Glu, glucose; 2-DG, 2-deoxyglucose; Tg, thapsigargin.* These experiments were mainly performed by Daniel Burgdorf in cooperation with Thorsten Lang.

Finally, the response to UPR, as well as the disruption of the ER Ca^{2+} homeostasis and resulting ER stress, have been described to influence MHC I peptide presentation [233]. Accordingly, MHC I surface expression, determined by flow cytometry, was reduced in glucose-treated BMDMs (Figure 51).

Together, these findings substantiate the hypothesis that the glucose-mediated depletion of Ca^{2+} from the ER results in ER stress. The presence of ER stress within hyperglycemic macrophages was indicated by an increase in XBP1 splicing following the activation of the ER stress sensor IRE1α. Furthermore, IRE1α activation, in turn, resulted in STIM1 translocation near the plasma membrane and a reduction in MHC I presentation.

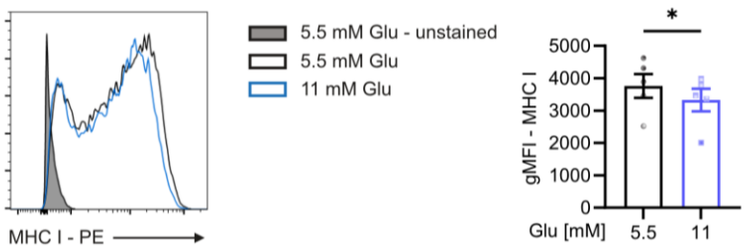

Figure 51 – MHC I expression is reduced in hyperglycemic macrophages
BMDMs were treated with elevated glucose concentrations for 48 h and stained with an antibody against MHC I. Exemplary histogram (left) and MHC I expression levels depicted as fluorescence intensities determined by flow cytometry (right) (n = 5). Data are shown as mean ± SEM; significance was determined by paired Student's t-test (* $p<0.05$). *Abbreviations: BMDMs, bone marrow-derived macrophages; Glu, glucose; gMFI, geometric Mean Fluorescence Intensity.*

4.5.2. Disruption of Ca^{2+} homeostasis by glucose leads to cell migration defects

In addition to the relevance of Ca^{2+} for cellular processes in the ER, Ca^{2+} is indispensable for cellular migration. During chemotactic migration, the binding of chemokines to their receptors triggers Ca^{2+} signaling, which is essential for migration-associated cytoskeletal rearrangements and for maintaining the leading edge, the front portion of the cell driving directional movement through actin polymerization [37,76].

To investigate how glucose influences chemokine-mediated Ca^{2+} signaling and cellular migration, changes in Ca^{2+} concentrations in response to the chemokines CCL2 and CCL19 and levels of the respective chemokine receptors were monitored in BMDMs treated with elevated glucose concentrations. Strikingly, the expression of CCR2, the receptor for CCL2, was found to be upregulated in glucose-treated cells (Figure 52A). Nevertheless, in line with the previously described impaired Ca^{2+} signaling in hyperglycemic macrophages, CCL2-induced Ca^{2+} signaling was significantly reduced in BMDMs treated with elevated glucose concentrations (Figure 52B) despite increased CCR2 levels. The expression of CCR7 remained unchanged in glucose-treated LPS-matured cells (Figure 52C). Consistent with the previous data, CCL19-induced Ca^{2+} signaling was reduced in glucose-treated immature and LPS-matured cells (Figure 52D and E), suggesting that glucose also impairs chemokine-induced Ca^{2+} signaling and, thus may potentially influence cellular migration.

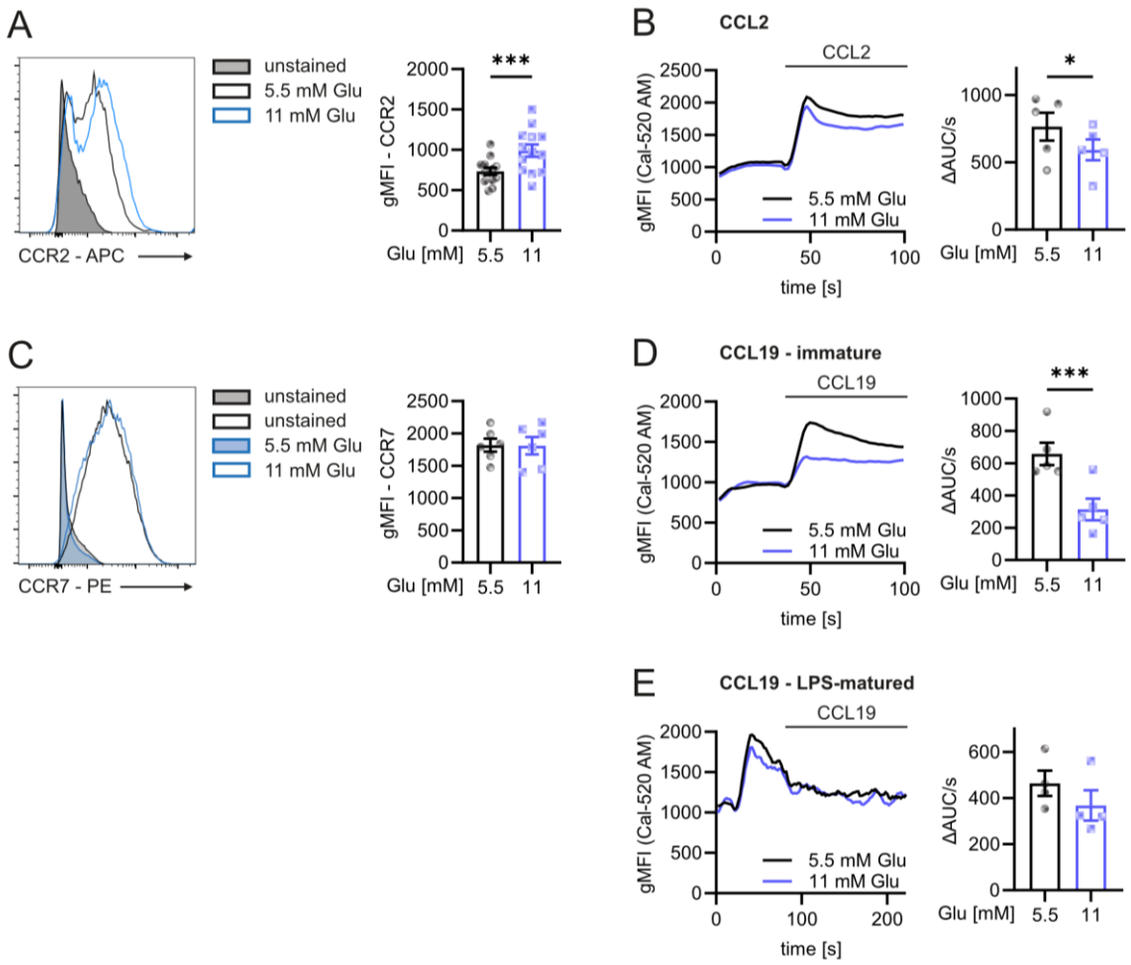

Figure 52 – Chemokine-induced Ca^{2+} signaling is reduced in hyperglycemic macrophages
BMDMs were treated with elevated glucose concentrations for 48 h. For (C and E) BMDMs were matured with LPS for an additional 18 h. (**A**) Cells were stained with an antibody against CCR2. Exemplary histogram (left) and CCR2 expression levels (right) depicted as fluorescence intensities determined by flow cytometry (n = 13). (**B**) Changes in Ca^{2+} concentrations were monitored after addition of 14.5 nM CCL2 in Cal-520 AM-stained BMDMs. The intensity of Ca^{2+} signaling was calculated as difference of the area under the curve normalized to one second before and after addition of the stimulus. Ca^{2+} signaling curves are represented as pooled data from the same independent experiments as depicted in the bar graph (n = 5). (**C**) As in (A) but stained with an antibody against CCR7 (n = 6). (**D** and **E**) As in (B) but Ca^{2+} signaling in response to 500 ng/mL CCL19 (n = 5 for D, n = 4 for E). Data are shown as mean ± SEM; significance was determined by Student's t-test (* $p<0.05$). *Abbreviations: AUC, Area under the Curve; Δ, difference; BMDMs, bone marrow-derived macrophages; gMFI, geometric Mean Fluorescence Intensity.*

A direct influence on cellular migration was first investigated *in vitro* using a transwell migration assay as well as a 3D migration assay with collagen matrices (Figure 53A). In both assays, the migration towards the chemokine CCL19 was assessed in BMDMs that had been matured with LPS overnight. Only minimal cellular migration was observed in all conditions without the addition of the chemokine (Figure 53). BMDMs subjected to CCL19 responded with increased migratory activity, determined in the transwell assay by increased numbers of transmigrated cells (Figure 53B). In addition, in the 3D collagen assay, velocity, accumulated distance and particularly the Forward Migration Index towards CCL19 (yFMI) increased in BMDMs exposed to a CCL19 gradient (Figure 53C to F). Strikingly, migration towards CCL19 was significantly reduced in glucose-treated cells (Figure 53) in both assays.

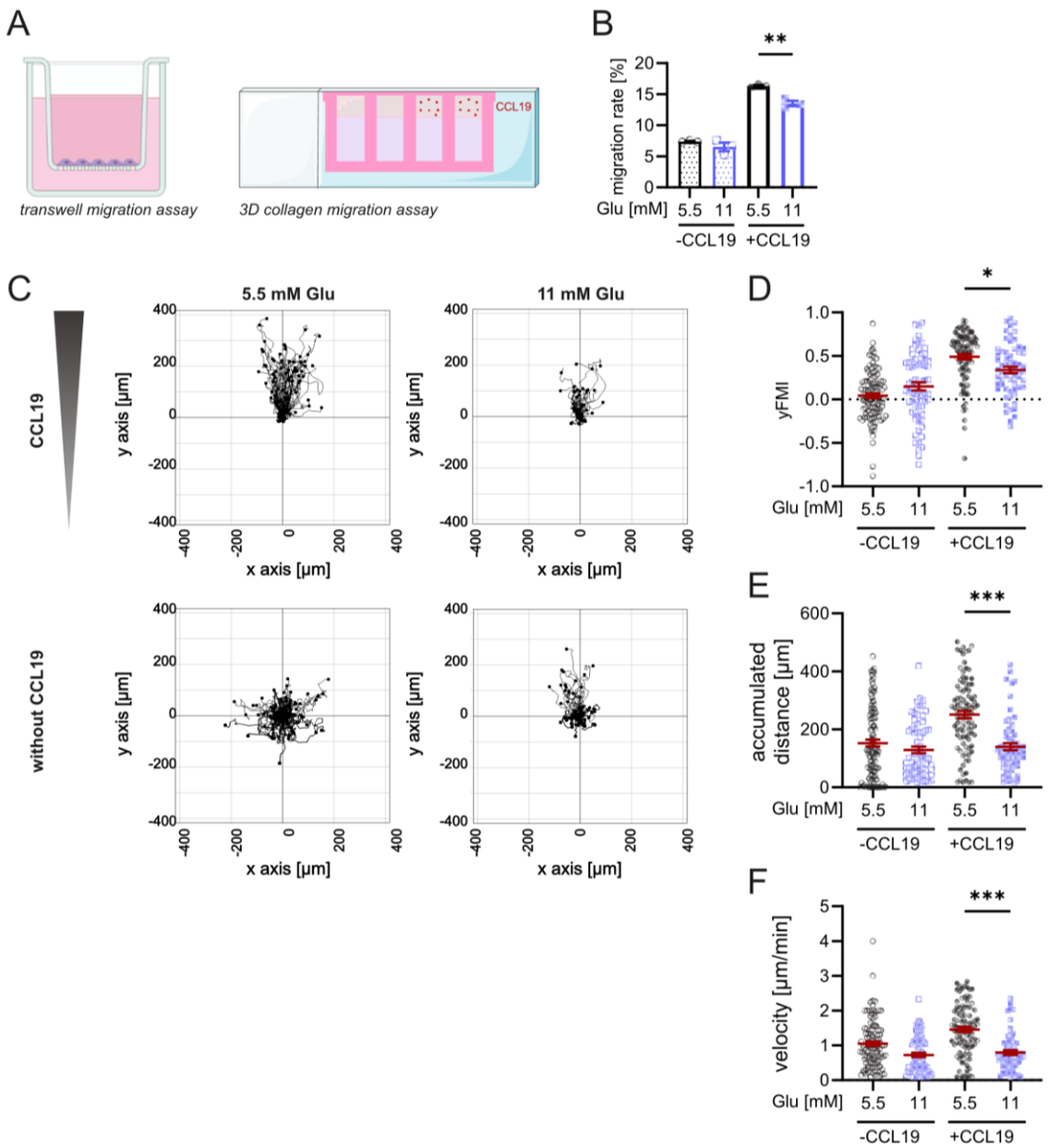

Figure 53 – CCL19-mediated migration is reduced in hyperglycemic macrophages
BMDMs were treated with elevated glucose concentrations for 48 h, followed by maturation with 200 ng/mL LPS for an additional 18 h. (**A**) Experimental set-up of transwell and 3D collagen migration assays. (**B**) Migration towards 200 ng/mL CCL19 was assessed in a transwell migration assay by analyzing the proportion of transmigrated cells (n = 3). (**C** to **F**) Cellular migration towards 1000 ng/mL CCL19 within a 3D collagen matrix was monitored by live cell imaging. Forward migration index towards CCL19 (D), the accumulated distance (E) and the velocity (F) was determined by tracking the cells using ImageJ. Exemplary tracking paths are shown in (C). Graphs depict pooled data from three independent experiments with 80 tracked cells per experiment and condition; a velocity threshold was set at ≥ 0.1 µm/min. Data are shown as mean ± SEM; significance was determined by one-way ANOVA corrected for multiple comparisons by the Tukey method. *Abbreviations: BMDMs, bone marrow-derived macrophages; Glu, glucose; yFMI, Forward Migration index parallel to the chemokine gradient.*

Finally, *in situ* migration assays were performed to investigate cellular migration in a more physiological environment. For this purpose, cellular migration was determined in explanted ear sheets as described by Weier et al [190]. During the splitting of ears into ventral and dorsal sides, mechanical rupture activates the immune cells, leading to their migration towards the lymphatic

vessels [234]. Here, ventral sheets were incubated for 24 h or 48 h in medium containing physiological (5.5 mM) or elevated (11 mM) glucose concentrations and cellular migration towards lymphatic vessels was assessed by microscopy (Figure 54A). Remarkably, ratios of MHC II$^+$ cells between inside and outside lymphatic vessels were reduced in ear sheets cultured in medium containing elevated glucose concentrations (Figure 54B and C). Accordingly, the average distance of MHC II$^+$ cells to the lymphatic vessels was increased after incubation with elevated glucose concentrations (Figure 54B and C). Together, these data show that hyperglycemia impairs chemokine-directed Ca^{2+} signaling and strongly reduces cellular migration both *in vitro* and *in situ*.

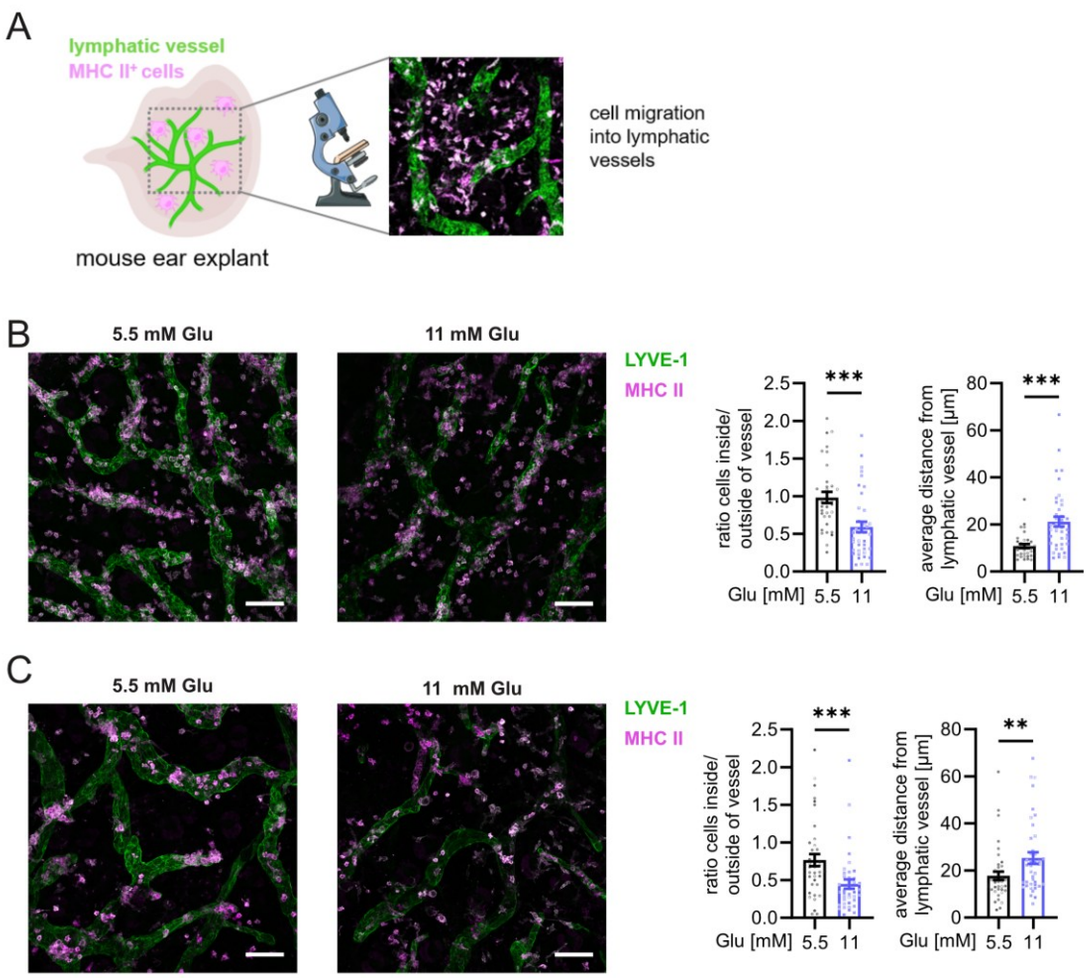

Figure 54 – Hyperglycemia impairs cellular migration in explanted ear sheets
In situ migration was determined in explanted ear sheets from 4-week-old mice by microscopy. Staining of fixed ears with antibodies against LYVE-1 and MHC II to mark lymphatic vessels and migratory cells, respectively. (**A**) Experimental set-up. (**B** and **C**) Ventral ear sheets were incubated with medium containing physiological (5.5 mM) or elevated glucose concentrations (11 mM) for 24 h (B) or 48 h (C). Exemplary Z projections (left) are shown. Migration towards lymphatic vessels is depicted as the ratio of cells inside and outside of the lymphatic vessels as well as the average distance to the closest lymphatic vessel (right). Each data point represents one field of view pooled from ear sheets from 4 different mice. The scale bar is equivalent to 100 µM. Data are shown as mean ± SEM; significance was determined by Mann-Whitney test. *Abbreviations: Glu, glucose.* These experiments were performed in cooperation with Eva Kiermaier and Shaunak Ghosh.

5. Discussion

In recent decades, the prevalence of diabetes has increased at an alarming rate. This increase has been primarily attributed to modern lifestyle, which is associated with growing rates of obesity, a lack of exercise, and unhealthy dietary habits, particularly high sugar consumption [235]. The increase in the prevalence of diabetes has been accompanied by a notable rise in diabetes-related mortality rates, accounting for 21% of deaths in Germany [1,236]. Individuals with diabetes typically die as a result of complications related to the disease, such as heart attack, kidney failure and stroke, rather than from the disease itself [14,236]. For decades, the majority of deaths associated with diabetes were attributed to cardiovascular complications. However, recent findings suggest that, presumably due to improved treatments for cardiovascular diseases, the leading cause of premature deaths of diabetic patients results from cancer, which is considered a long-term consequence of diabetes [237].

Macrophages, which play a pivotal role in maintaining the balance between tissue homeostasis and inflammation, have been identified as key contributors to the onset and progression of diabetes as well as to the development of diabetes-associated secondary diseases. Despite extensive research on the contribution of macrophages to various complications, the phenotypic characteristics and inflammatory responses observed in diabetic macrophages remain inadequately characterized [59,60,238]. Furthermore, the precise mechanisms by which macrophages contribute to the development and exacerbation of diabetic complications are not fully understood.

Accordingly, further research is required to elucidate the impact of hyperglycemia on macrophage phenotype and function, and consequently the subsequent influence of hyperglycemic macrophages on the progression of diabetes and diabetes-related complications. A deeper understanding of the molecular mechanisms underlying macrophage dysfunction is crucial for advancing our knowledge of disease processes and facilitating the development of more targeted therapeutics. One chapter of this thesis examined the inflammatory phenotype of hyperglycemic macrophages. Ca^{2+} serves as a critical second messenger playing a pivotal role in regulating macrophage functionality and various cellular processes. Therefore, the central focus of this thesis was to explore the influence of hyperglycemia on Ca^{2+} homeostasis and the subsequent effects on Ca^{2+}-dependent functions in macrophages.

We demonstrated that hyperglycemic macrophages exhibit enhanced priming towards inflammatory cytokines. Additionally, we showed that elevated glucose concentrations lead to the depletion of Ca^{2+} from cellular stores, which in turn impairs Ca^{2+} signaling and consequently disrupts Ca^{2+}-related processes. We identified a negative correlation between blood glucose concentrations and Ca^{2+} signaling in both murine peritoneal macrophages and human monocytes. Moreover, we elucidated the mechanism by which glucose mediates the release of Ca^{2+} from the ER, resulting in impaired Ca^{2+} homeostasis. The potential implications of the observed effects of hyperglycemia on macrophage activation and function for the understanding of immunological phenotypes in diabetic

patients will be discussed in the following sections. Furthermore, a molecular mechanism through which glucose disrupts Ca^{2+} signaling will be proposed and further experiments will be suggested.

5.1. Hyperglycemia enhances pro-inflammatory cytokine secretion in macrophages

Macrophages secrete pro-inflammatory cytokines in response to a variety of immune triggers, including the bacterial cell wall components LPS. It has been shown that the levels of TNF and IL-1β are elevated in whole blood, PBMCs, and also isolated monocytes in individuals with diabetes even in the absence of stimulation [239–241]. Similarly, it was demonstrated that cytokine production (TNF, IL-6 and IL-1β) is exacerbated in THP-1 macrophages and RAW264.7 cells exposed to hyperglycemia, both at steady state and following stimulation with LPS [242,243]. Furthermore, various *in vitro* studies, analyzing human monocytes and monocyte-derived macrophages, demonstrated that the secretion of TNF is elevated in hyperglycemic cells in response to LPS, but also IFN-γ, IL-4, lysates of *Mycobacterium tuberculosis* and hemoglobin-haptoglobin complexes [244–247].

In line with the literature, we also observed an increased secretion of inflammatory cytokines (TNF, IL-6 and IL-1β) in hyperglycemic macrophages after stimulation with LPS. Notably, no cytokine production was detected under conditions without immune stimulation. The heightened cytokine production in the context of hyperglycemia is driven by the transcription factor NF-κB, which plays a crucial role in mediating the induction of pro-inflammatory genes. Previous studies have already demonstrated that the activation of NF-κB and its subsequent translocation into the nucleus is increased in hyperglycemic macrophages [248,249]. In this thesis, we also measured an increased phosphorylation of the NF-κB subunit p65 in macrophages exposed to elevated glucose concentrations. Given that phosphorylation of p65 promotes its translocation to the nucleus, where it subsequently activates the transcription of the aforementioned pro-inflammatory genes [46], the observed increase in NF-κB activation provides a potential link between hyperglycemia and the amplification of inflammatory responses.

A decisive role in the regulation of NF-κB has been attributed to the mTOR complex 1 (mTORC1) [196]. Dai *et al.* revealed that the inhibition of mTOR results in the attenuation of NF-κB activation and subsequent inflammasome induction in THP-1-derived macrophages treated with high glucose concentrations [195]. Consistent with these findings, we observed that treatment with the mTOR inhibitor Rapamycin reverted both the elevated activation of NF-κB and the associated increase in TNF secretion under hyperglycemic conditions. This further substantiates the hypothesis that the glucose-mediated priming of macrophages towards elevated secretion of pro-inflammatory cytokines is driven by mTOR-dependent activation of NF-κB. The activation of mTORC1 can be modulated through the phosphorylation of its inhibitory complex by protein kinases, including p38 and Akt [250,251]. In diabetic mice, it has been demonstrated that Akt signaling as well as p38 activity are increased in brain macrophages and peritoneal macrophages, respectively [252,253]. On the other hand,

glucose availability has been shown to result in the inactivation of AMPK, which is known to inhibit mTORC1 via phosphorylation of raptor, a key regulator of mTORC1 [254]. Whether the high glucose-induced activation of mTOR and subsequent priming of macrophages towards a pro-inflammatory phenotype rather involves modulation of Akt, p38 or AMPK or whether all three play a critical role remains open and might be addressed in future investigations.

5.2. Disruption of cellular Ca^{2+} homeostasis in hyperglycemic macrophages

As a second messenger, Ca^{2+} is involved in various signaling pathways required for cellular function. Accordingly, Ca^{2+} homeostasis is tightly regulated and its disruption has been implicated in a number of pathologies, including cardiovascular diseases, cancer and neurodegenerative diseases. Furthermore, Ca^{2+} plays a decisive role in regulating blood glucose concentrations, as both glucagon and insulin release rely on Ca^{2+}-dependent processes. [101] It has been demonstrated that dysregulated Ca^{2+} homeostasis in diabetes is not only restricted to the pancreas but rather affects the entire body [255]. Individuals with diabetes are characterized by diminished intestinal Ca^{2+} absorption and hypercalciuria, increased urinary excretion of Ca^{2+} [200]. Intriguingly, various studies revealed a correlation between serum Ca^{2+} concentrations and an increased risk of developing diabetes [256–258]. Moreover, dietary intake of Ca^{2+} has been inversely correlated with the risk of diabetes [259,260]. In addition to Ca^{2+}-dependent disturbances of pancreatic insulin secretion [261], reduced Ca^{2+} levels in skeletal muscles and neurons during diabetes contribute to impaired contractility and diabetic neuropathy [262,263].

Given the association between diabetes and the development of metaflammation as well as several secondary diseases, in which macrophages play an important role, it is of particular interest to understand whether deranging of Ca^{2+} signaling contributes to immune cell dysfunction and increased inflammatory activity. It has previously been proposed that metabolic disorders may influence the release of Ca^{2+} from the ER, thereby affecting cellular Ca^{2+} homeostasis in macrophages [101]. Here, we showed that Ca^{2+} stores are depleted in hyperglycemic macrophages. Furthermore, Ca^{2+} signaling is strongly impaired in hyperglycemic macrophages and monocytes derived from patients with pre-diabetes. The loss of Ca^{2+} from the ER is mediated by high glucose-mediated modulation of the IP_3R and SERCA. On the one hand, hyperglycemia results in the activation and opening of the IP_3R, which releases Ca^{2+} from the ER. Furthermore, analogous to the observations in livers from diabetic mice (*db/db* and *ob/ob* mice) [264], we demonstrated that prolonged exposure of macrophages to elevated glucose concentrations results in augmented PKA-phosphorylated IP_3R, which has been shown to increase its opening probability by enhancing the receptor's sensitivity to IP_3 [102,265]. On the other hand, we showed that prolonged treatment of macrophages with elevated glucose concentrations leads to a reduction in SERCA activity. In contrast to previous observations in macrophages from insulin-resistant and obese mice, we did not observe that reduced SERCA activity and subsequent depletion of ER Ca^{2+} were linked to changes in SERCA expression [199]. Instead, our results suggested that the observed reduction in cellular

SERCA activity is primarily due to the modulation of the enzyme's activity itself, via micropeptides including PLN.

A connection between both mTOR/NF-κB and Ca^{2+} signaling mainly relies on the role of Ca^{2+} as a second messenger involved in the signaling cascade resulting in the activation of both proteins. The binding of Ca^{2+} to calmodulin is an essential step during the activation of both mTOR as well as NF-κB [266,267]. Moreover, TRPC1-mediated Ca^{2+} influx has been implicated in the activation of NF-κB during IFN-γ-induced polarization of inflammatory macrophages [147]. In contrast, the relationship between the mTOR/NF-κB signaling cascade and the regulation of Ca^{2+} signaling remains insufficiently understood and has been inadequately explored. However, it has been shown that activated mTOR, which can also be activated by glucose [254], results in the phosphorylation of the IP_3R at a side that enhances its Ca^{2+} release activity [268], indicating that mTOR may play a role in altered Ca^{2+} signaling observed in hyperglycemic macrophages. In contrast to the cytokine secretion, however, the glucose-mediated reduction in Ca^{2+} signaling appears to be independent of mTOR and NF-κB, as evidenced by the persistence of the glucose-mediated effects after the inhibition of signaling of these molecules. These data clearly suggest that distinct signaling pathways are responsible for the observed changes in cytokine secretion and Ca^{2+} signaling in macrophages after treatment with elevated glucose concentrations. Accordingly, further investigations in this thesis focused on clarifying how glucose disturbs cellular Ca^{2+} homeostasis.

5.3. Macrophages sense glucose via the taste receptor Tas1R3

In macrophages, glucose is primarily taken up through glucose transporters (GLUT1 and GLUT3) as well as Na^+/glucose cotransporters, where it serves as a source for carbons and energy production [269,270]. Instead of glucose being taken up, glucose can also bind receptors on the cell surface, thereby triggering the activation of downstream signaling cascades. One of the few receptors, which can be activated by glucose itself and which mediates Ca^{2+} signaling via the activation of PLC is the receptor for sweet taste [211].

Generally, taste receptors, which belong to the family of GPCRs, are mainly known for their involvement in sensing different tastes, including sweet, umami, and bitter tastes [271]. The sweet taste receptor is composed of a Tas1R2 and a Tas1R3 subunit and exhibits a response to the binding of sweet-tasting compounds, including glucose, but also other natural sugars as well as artificial sweeteners [211,272]. Various studies have shown that sweet taste receptors are not only expressed in taste buds but throughout the whole body [272,273]. It has been previously demonstrated that expression of Tas1R3 can be detected in macrophages, a finding that was further corroborated in this thesis [212,213].

We further demonstrated that the addition of glucose results in a release of Ca^{2+} from the ER, which was prevented by the inhibition or downregulation of Tas1R3. Strikingly, we were able to correlate the glucose-induced effects on Ca^{2+} homeostasis to Tas1R3 expression in these cells. A strong

negative correlation between blood glucose concentrations and intensity of Ca^{2+} signaling was predominantly observed in murine SPMs and human $CD14^+$ classical monocytes, which express high levels of Tas1R3. In these cells, the addition of glucose directly induced a clear Ca^{2+} signaling. In contrast, only a minor correlation and a reduced capacity of glucose to induce Ca^{2+} signaling were observed in murine LPMs and human $CD16^+$ non-classical monocytes, expressing only moderate levels of Tas1R3. We did not detect remarkable levels of Tas1R3 in human B and T cells derived from whole blood, which is consistent with the inability to detect any glucose-mediated Ca^{2+} signaling. Finally, the molecular mechanisms by which the activation of Tas1R3 by glucose results in Ca^{2+} release from the ER were identified. The proposed mechanism will be thoroughly discussed in chapter 5.3.1.

Since Tas1R3 is widely expressed in extraoral tissues, ongoing research aims to understand its involvement in sugar sensing and tissue-specific alterations associated with changes in sugar concentrations. It has been reported that Tas1R3 plays a crucial role in the control of glucose homeostasis in extraoral tissues, as deletion of Tas1R3 leads to reduced insulin sensitivity, impairs glucose tolerance and further induces dystrophic islet tissue [274,275]. In the context of diabetes or hyperglycemia, Tas1R3 expression has been demonstrated to be upregulated in various tissues, including the intestine, lung epithelium, and testes [276–278]. Recent research linked western diet-induced impairment of the male reproductive system, as well as diabetes-related exacerbation of inflammation during lung infection, to Tas1R3 [277,278]. This further emphasizes the importance of elucidating the manner by which Tas1R3-mediated sugar sensing regulates cellular responses, particularly concerning the understanding of the dysfunctions observed in the context of diabetes.

Strikingly, the expression of Tas1R3 does not always correlate with a corresponding expression of Tas1R2. Kojima *et al.* discovered that glucose metabolism and subsequent insulin secretion by pancreatic beta cells might involve the activation of a glucose-sensing receptor, composed of a Tas1R3 and the Ca^{2+}-sensing CaSR subunit rather than a heterodimer of Tas1R2/Tas1R3 [279]. Similar to the observations regarding the expression of Tas1R3 in various organs (see above), an increased expression of CaSR has been detected in diabetic PBMCs [280]. However, data on changes in Tas1R3 expression in macrophages and monocytes as well as on the potential formation of Tas1R3/CaSR heterodimers are missing. In addition to CaSR, it has been demonstrated that Tas1R3 can form a heterodimer with the metabotropic glutamate receptor in human leukocytes [281] as well as low-affinity homodimers that only exhibit a response at high sugar concentrations [282]. Expression data obtained through RNA sequencing (derived from the Immunological Genome Project [283], the Human Protein Atlas [284,285] and BMDM sequencing in our group [286]) revealed striking differences in the levels of Tas1R2 and Tas1R3 across various monocyte and macrophage populations. While a profound Tas1R3 expression was observed, Tas1R2 levels were considerably lower or even below the detection limit, indicating that glucose sensing in macrophages might indeed involve a receptor other than the classical taste receptor, composed of Tas1R3 and a so far unidentified receptor molecule.

Excessive sugar consumption is one of the main lifestyle factors contributing to increased risk for non-communicable diseases, most notably diabetes. Thus, with the aim to control body weight and reduce calorie intake and sugar consumption, the consumption of low-caloric or non-caloric sweeteners has risen immensely over the past two decades. These sweeteners are distinguished by a high relative sweetness as they are designed to bind to the taste receptors with particular high affinity [216,287]. They comprise synthetic, artificial sweeteners, such as acesulfame K, aspartame, saccharin and sucralose, as well as natural sweeteners, such as erythritol or stevia. [288,289] The largest proportion of most sweeteners is absorbed in the small intestine and subsequently transported via the circulatory system and then excreted in the urine. Furthermore, some sweeteners are metabolized by gut microbiota or are directly excreted into feces without being absorbed. [288,290] Despite the beneficial impact of sweeteners on energy intake, their utilization and their influence on health and metabolism have been controversially discussed. Several studies found that sweetener consumption is associated with impaired glucose tolerance, weight gain as well as an increased risk of developing metabolic disorders, including diabetes, metabolic syndrome, and cardiovascular disease. [291,292] Furthermore, sweetener consumption has been shown to increase the risk of developing breast and colorectal cancer and to cause dysbiosis, an imbalance of the gut microbiota, known to influence the body's glucose homeostasis [293,294]. Notably, recent research has also highlighted an association between maternal sweetener consumption and an increased risk for obesity in their children. This association has been attributed to the transplacental transport and the presence of sweeteners in breast milk leading to intergenerational changes in the microbiome [295–297]. Although concentrations of artificial sweeteners are rather low in the blood, these molecules result in a more pronounced activation of taste receptors. Consequently, we observed that even low concentrations of sucralose and erythritol induced a Ca^{2+} signaling response in macrophages that was comparable to that triggered by glucose. Accordingly, the data presented here question the substitution of sugars with sweeteners, particularly concerning the observed effects of Tas1R3 activation on the Ca^{2+} homeostasis and functionality of macrophages. To ascertain the safety of long-term moderate consumption of artificial sweeteners, further investigations are required that focus on the connections between sweetener consumption and human health and particularly analyze the impact of sweetener consumption on macrophage functionality and their contribution to pathologies.

5.3.1. Proposed mechanism by which glucose-mediated activation of Tas1R3 induces Ca^{2+} release from the ER

In the taste buds, Tas1R3 signaling results in the activation of a heterotrimeric G protein, comprising the Gαi-related $G\alpha_{gustducin}$ and a $G\beta_3\gamma_{13}$ subunit. In extraoral tissues, Tas1R3 typically couples to a G protein containing a Gαi subunit. Ubiquitously, Tas1R3 activation results in the induction of PLCβ2 mediated by Gβγ. [272,289] In the present study, we further validated that glucose-induced activation of Tas1R3 mediates the activation of PLC in macrophages and monocytes. By interfering with the signaling cascade at various stages, we investigated the molecular mechanism downstream of glucose-mediated activation of Tas1R3.

In line with previous studies, which established a connection between individual signaling steps and enzymes involved in the signaling cascade downstream of PLC [142,211,298,299], we now propose a mechanism by which Tas1R3 activation by glucose results in the release of Ca^{2+} from the ER (as shown in Figure 55). We demonstrated that the release of Ca^{2+} from the ER, which occurs downstream of PLC activation following hyperglycemia-induced activation of Tas1R3, is mediated by both the modulation of Ca^{2+} release from the ER and the regulation of Ca^{2+} uptake into the ER.

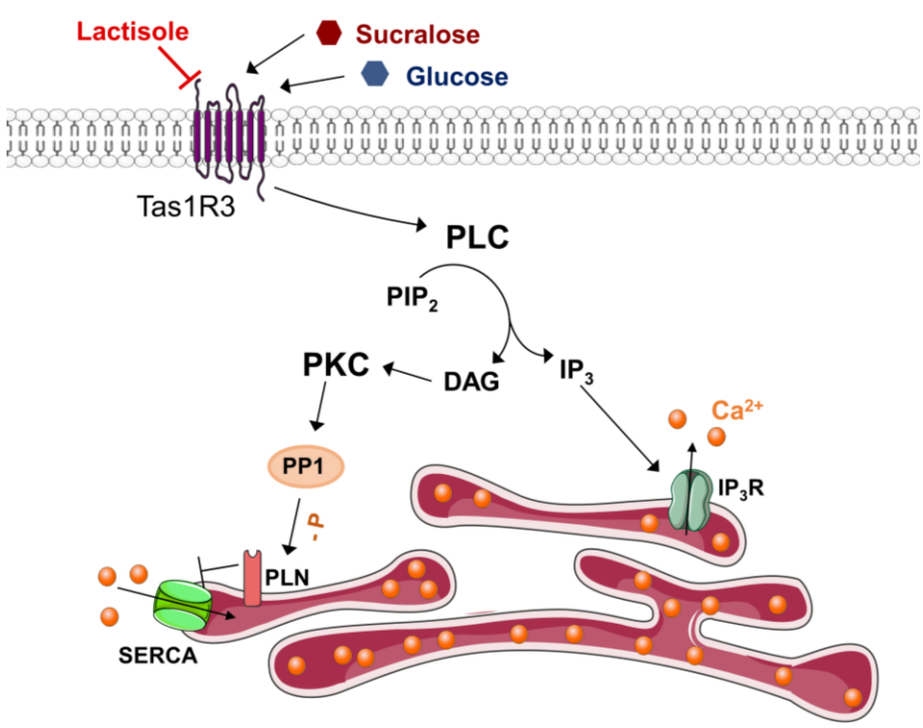

Figure 55 - Proposed model of glucose-induced Tas1R3 signaling cascade
Glucose results in the depletion of Ca^{2+} from the ER by inhibiting the SERCA activity and activating the IP_3 receptor. Tas1R3 activation by glucose or artificial sweeteners results in the activation of PLC, which mediates the dephosphorylation of PLN via PKC-PP1 signaling and the generation of IP_3. Created using Servier Medical Arts [74].

Our findings demonstrated that Ca^{2+} release from the ER is mediated through the opening of the IP_3R by IP_3, which is generated from PIP_2 by PLC. The activity of the IP_3R is regulated by various proteins that form complexes with the IP_3R. The activity of IP_3R can be enhanced by elevating the effective delivery of IP_3, modulating the receptor's sensitivity to Ca^{2+} or IP_3, and even by proteins that directly activate IP_3Rs. Conversely, several proteins inhibit the activity by binding to the receptor, thus disrupting the ability of IP_3 to bind, or by modifying the IP_3R post-transcriptionally [103]. The position of the serine and threonine residues determines whether phosphorylation possesses an inhibitory or activating effect. For instance, PKA-mediated phosphorylation at Serine (Ser)1589 and Ser1755 is known to enhance the Ca^{2+} release by increasing the sensitivity to IP_3 [102,300], which we also observed after treatment with elevated glucose concentrations.

In addition to the opening of the IP_3R, glucose-mediated Tas1R3 and subsequent PLC activation results in the inhibition of SERCA, thereby reducing the Ca^{2+} transport to the ER. We demonstrated that PKC, which can be activated by PLC-induced generation of DAG [298,301], results in the modulation of PP1 activity. PKC modulates PP1 activity by phosphorylating its inhibitor I-1 at Ser67, thereby releasing its inhibitory function [141,143,299]. Subsequently, PP1 leads to the dephosphorylation of PLN, which we have shown to be moderately expressed also in macrophages and which increases its inhibitory function on SERCA [108]. In addition to PLN, various other micropeptides modulating SERCA activity, including ALN, have been identified. ALN, supposed to bind to the same region as PLN, is the most ubiquitously expressed known micropeptide and is also present in various immune cell subsets including macrophages and monocytes [107,108,284,285]. Accordingly, based on its published expression in macrophages and homology to PLN, it is likely that ALN may also play a decisive role in the glucose-mediated inhibition of SERCA, which is involved in the depletion of Ca^{2+} from the ER. Previous investigations already revealed that murine ALN can be phosphorylated at Ser19, whereas human ALN is phosphorylated at Ser21 [302,303]. However, the lack of commercially available antibodies that can stain both phosphorylated and total ALN presents a significant challenge for analyzing the potential role of ALN in glucose-induced inhibition of SERCA. Recently, Hassel *et al.* connected PKC to the regulation of ALN phosphorylation as well as the ALN phosphorylation to the modulation of its inhibitory function on SERCA [303]. They generated expression constructs of murine ALN, as well as mutated ALN-S19A and ALN-S19D with an HA tag. The introduction of the mutations enabled the analysis of the different phosphorylation statuses on SERCA activity, as mutation of Ser19 to Alanine (A) prevents its phosphorylation, whereas the mutation of Ser19 to Aspartate (D) serves as a phosphomimetic for phospho-serine. Accordingly, the findings by Hassel *et al.* strongly support the hypothesis that, in addition to PLN, ALN might play an additional role in altered SERCA activity upon hyperglycemia, which might be a focus of prospective investigations. It also needs to be investigated whether ALN is dephosphorylated by PP1.

5.4. Implications of hyperglycemia for macrophage function

Patients with diabetes are characterized by an increased risk of developing a variety of secondary diseases, alongside a generalized immune dysfunction. This immune dysfunction in patients with diabetes, which diminishes the ability to combat pathogens and infectious stimuli effectively, is associated with increased infection rates, increased rates of hospitalization, and infection-related mortality. Especially, individuals with diabetes exhibit an impaired susceptibility to respiratory and urinary infections and are more prone to develop sepsis. [304,305]

Given their role in maintaining the balance between homeostasis and inflammation, macrophages have been the focus of numerous previous studies investigating the mechanisms underlying immune dysfunction in diabetes. It has been demonstrated that macrophage dysregulation contributes to several diabetes-related complications, including atherosclerosis and nephropathy. Delayed and impaired wound healing in patients with diabetes has been attributed to increased infiltration of pro-inflammatory macrophages, combined with a defective phagocytic capacity, which impairs the removal of pathogens and debris, as well as an impaired transition to pro-healing macrophages. Together, this results in an impaired healing process, thereby promoting the development of chronic, inflamed wounds. [70,71,306] Similarly, the lack of pro-regenerating macrophages contributes to impaired osteogenesis and bone regeneration in diabetic patients [307]. Recent research has demonstrated that the process of osseointegration in diabetic patients can be enhanced by the use of titania nanotubes, which mitigate the inflammatory phenotype of diabetic macrophages through the reduction of ER stress [308]. Moreover, the heightened inflammatory response of hyperglycemic or diabetic macrophages has been linked to increased susceptibility to develop periodontitis as well as defective skin self-renewal, which can result in the formation of diabetic wounds [309,310]. Macrophages also play a pivotal role in the induction of beta cell dysfunction and the exacerbation of insulin resistance. Ying *et al.* established a correlation between the number of intra-islet macrophages and the degree of beta cell dysfunction and attributed the corresponding dysfunction in glucose-stimulated insulin secretion to macrophage-derived cytokines and direct cell-cell interactions [62,67]. Furthermore, increased islet macrophage-derived miR-155 has been shown to contribute to the disruption of beta cell function in diabetic mice [68].

Interestingly, it has been demonstrated that the pro-inflammatory phenotype of macrophages persists even after normalization of glucose levels, which has been ascribed to epigenetic reprogramming and induction of trained immunity in these macrophages [311,312]. The induction of epigenetic changes upon treatment with elevated glucose concentrations was further supported by the observations presented in this thesis, which demonstrate that Ca^{2+} dysregulation remains over one week after glucose normalization. These data may also explain, why the short-term normalization of blood glucose levels in diabetic patients does not always reduce the risk of diabetes-related secondary diseases [312].

Calcium is involved in a huge range of cellular signaling pathways and macrophage-specific functions, thereby playing a crucial role in both physiological and pathophysiological processes. Given this pivotal role of Ca^{2+} and the dysregulation of Ca^{2+} homeostasis as well as the loss of ER Ca^{2+} in hyperglycemic macrophages demonstrated in this thesis, we hypothesized that Ca^{2+}-dependent functions might be consequently impaired, as well. In order to investigate the influence of impaired Ca^{2+} signaling on macrophage functionality in hyperglycemia, we focused on two key Ca^{2+}-dependent cellular processes. Accordingly, the following sections will discuss the impact of hyperglycemia on ER stress as well as cellular migration. The results will be evaluated and classified in the context of known immune dysregulations associated with diabetes.

5.4.1. Hyperglycemia-mediated depletion of Ca^{2+} induces ER stress

The process of protein folding is highly dependent on the proper functionality of various protein-folding enzymes, many of which require high local Ca^{2+} concentrations for their activity. Accordingly, the depletion of ER Ca^{2+} and subsequent dysfunction of chaperone proteins have been associated with elevated levels of misfolded proteins, triggering the UPR and ER stress. [173,313,314] It has recently been demonstrated that the induction of the UPR is a highly dynamic process, with distinct kinetic profiles for its different sensors. The activation of all three ER stress sensors occurs within one hour of Ca^{2+} depletion and replenishment of ER Ca^{2+} results in the reversion of IRE1 and PERK activation within 15 min. [313] Accordingly, in addition to ER stress inducers that directly interfere with the protein folding process, such as tunicamycin or Brefeldin A, thapsigargin – an experimental ER stressor that depletes Ca^{2+} by inhibiting SERCA – is widely used to study ER stress [315,316]. Consistent with the observations made regarding thapsigargin, we observed that hyperglycemia-mediated depletion of ER Ca^{2+} results in increased ER stress. This was evidenced by the elevated activation of IRE1 and subsequent splicing of XBP1 in macrophages treated with elevated glucose concentrations or the glucose analog 2-DG. Similarly, previous investigations revealed that hyperglycemia results in the depletion of ER Ca^{2+} and increased ER stress in rat mesangial cells and cardiomyocytes, which can be reversed using the ER stress inhibitor 4-phenyl butyric acid [317,318]. Furthermore, an elevated ER stress response has been observed in insulin-resistant macrophages [319]. Notably, Komura *et al.* demonstrated that, in comparison to all PBMCs, the subset of $CD14^+$ monocytes derived from diabetic patients exhibits an increased susceptibility to apoptosis due to increased ER stress [72]. This finding is consistent with our observations, as we only observed a Ca^{2+} release induced by glucose in $CD14^+$ monocytes, which we were able to link to their higher expression levels of Tas1R3 compared to other PBMC subsets (T cells, B cells, $CD16^+$ monocytes).

In addition to the observations that diabetes or hyperglycemia results in the depletion of ER Ca^{2+} and increased ER stress, a mutual influence has also been proposed, suggesting that ER stress may contribute to progression of diabetes and alterations of cellular Ca^{2+} homeostasis. Particularly, mediators of the XBP1s/IRE1 pathway have been described to contribute to the onset and progression of several diseases, including type 2 diabetes, obesity as well as the associated complications. IRE1

activation has been shown to mediate activation of JNK, which in turn results in increased serine and decreased tyrosine phosphorylation of IRS1 and accordingly insulin resistance [320]. The essential role of ER function in regulating metabolic pathways is further highlighted by studies showing that the downregulation of ER chaperones (e.g. ORP150) impairs glucose tolerance [321,322]. Conversely, the overexpression of ER chaperones, such as Grp78 or ORP150, or the induction of SERCA has been observed to improve glycemic control in obese mice [322,323]. Accordingly, mutations disrupting UPR signaling and protein folding are implicated in the pathogenesis of genetic syndromes of diabetes, such as the Wolcott-Rallison syndrome, in which patients suffer from juvenile diabetes due to a mutation in PERK [324,325]. Increased ER stress in macrophages from obese mice has been described to result in increased levels of the oxidoreductase ERO1, which can induce the release of Ca^{2+} from the ER by binding to the IP_3R, thereby aggravating the depletion of ER Ca^{2+} [326].
Moreover, increased ER stress observed in obese or diabetic macrophages has been implicated in the pathogenesis of atherosclerosis. ER stressors, particularly XBP1s and PERK, have been shown to promote cholesterol accumulation and foam cell formation from macrophages, critical events during the development of atherosclerotic plaques [327,328].

Beyond these metabolic implications, the induction of ER stress in hyperglycemic macrophages has further consequences on cellular processes and immune cell function. In our study, we observed that MHC I surface expression was reduced in hyperglycemic macrophages, a phenomenon that has been previously monitored in the context of ER stress [233]. Accordingly, since MHC I-restricted antigen presentation plays an indispensable role during immunity to viral infection and immune tolerance, these data provide a potential link between hyperglycemia and altered immune responses in diabetic patients. Additionally, treatment with glucose or 2-DG, as well as the ER stressor thapsigargin resulted in an increased translocation of STIM1 aggregates in the vicinity of the plasma membrane. STIM1 aggregates were monitored by STED microscopy of membrane sheets generated by sonication, in which the contact sites between ER and plasma membrane remain intact. These findings are consistent with previous observations that IRE1 interacts with STIM1, promoting ER-plasma membrane contact sites and SOCE, a mechanism that helps to restore Ca^{2+} homeostasis and preserve immune cell function [177]. Strikingly, prolonged treatment of macrophages with ER stressors (12 h) has been shown to result in a reduction of proteins involved in SOCE (STIM1, ORAI1), and the inhibition of Ca^{2+} entry via ORAI1 and TRPC1 also increases ER stress. Moreover, it has been demonstrated that ER stress increases the secretion of pro-inflammatory cytokines, highlighting a relevant connection between ER stress, regulation of Ca^{2+} levels and immune cell activation. [329]
Together, the data from the previously referenced studies, along with our observations, strongly suggest that targeting ER stress could represent a promising therapeutic approach for preventing or reducing the risk of diabetes-related secondary complications and aggravation of the disease itself.

5.4.2. Glucose-induced depletion of Ca^{2+} stores disrupts chemokine-mediated Ca^{2+} signaling and impairs cellular migration

Cellular migration is a key feature of numerous immune cells, indispensable for the fulfillment of their functions at designated locations and for the contribution to immune surveillance, tissue homeostasis and repair. Under steady-state conditions, macrophages patrol the tissue to maintain its integrity and respond to physiological changes and immune signals. During infection, macrophages, in concert with other immune cells, are recruited to sites of inflammation, where they engage pathogens and contribute to the initiation of the immune response. Furthermore, upon stimulation by immune mediators, macrophages migrate into the lymphatic vessels, which is a crucial step for the transport of antigens to regional lymph nodes. Accordingly, this migratory process represents a key step in facilitating the communication between adaptive and innate immunity, thereby promoting the activation of T cells and enhancing the overall immune response. Given their central roles in both health and disease, dysregulation of macrophage migration can contribute to pathological conditions, including those associated with diabetes. [33,34]

Various studies have identified defects in the migration of macrophages, monocytes and neutrophils in individuals with diabetes [240,330,331]. Accordingly, the recruitment of macrophages to the lung during infections with *Klebsiella pneumoniae* and *Mycobacterium tuberculosis* was shown to be impaired in diabetic or HFD-treated mice, respectively [73,332]. Furthermore, Liu *et al.* demonstrated that diabetic peritoneal macrophages exhibit a reduced adhesion capacity along with an impaired migration towards the chemotactic peptide fMLP [330]. Consistent with these findings, we observed a reduced migratory response of LPS-matured hyperglycemic BMDMs towards the chemokine CCL19, as assessed by both a transwell migration assay and 3D collagen assay.

In addition to assessing cellular migration *in vitro,* we further investigated cellular migration in a more physiologically relevant environment. For this purpose, we used a model system adapted from Holzmann *et al.* [234], in which a mild skin inflammation and the subsequent emigration of Langerhans cells and dermal DCs to the lymphatics is induced by the mechanical separation of the ventral and dorsal sides of a mouse ear. We then mimicked hyperglycemia in the tissue by incubating the ear sheets with physiological or elevated glucose concentrations. In contrast to the performed *in vitro* migration assays, the cells were only exposed to elevated glucose concentrations after their activation by mechanical rupture. However, similar to the *in vitro* finding, the *in situ* assay demonstrated that fewer MHC II^+ cells migrated to the lymphatic vessels when ear sheets were incubated with elevated glucose concentrations. Correspondingly, another *in vitro* analysis revealed that high glucose concentrations impaired the chemotactic ability of RAW264.7 macrophages [333]. Moreover, reduced recruitment of inflammatory macrophages and monocytes has been observed in diabetic mice following infection with the Middle East respiratory syndrome coronavirus, which was attributed to a diminished expression of *Ccl2* in the lung [334]. Our observations indicate that the impaired

recruitment of macrophages and monocytes in hyperglycemic conditions may be further exacerbated by a defective Ca^{2+} response to CCL2 in hyperglycemic macrophages.

During cellular migration, Ca^{2+} plays a critical role in regulating cellular contractility and orchestrating key processes, including cytoskeletal rearrangement, the formation of adhesion contacts, and integrin activation [335]. Accordingly, the dysregulation of cellular migration observed under hyperglycemic conditions in this thesis is consistent with our findings related to Ca^{2+} signaling, which was impaired in hyperglycemic macrophages in response to the chemokines CCL2 and CCL19. Taken together, the dysregulation of Ca^{2+} signaling, which is associated with functional impairments, such as defective migration and ER stress, in combination with a pro-inflammatory cytokine profile observed in hyperglycemic macrophages, may significantly contribute to the chronic inflammation and immune dysfunction observed in patients with diabetes. It is conceivable that restoring the cellular Ca^{2+} homeostasis could alleviate ER stress and improve migratory behavior. Therefore, targeting the cellular Ca^{2+} homeostasis may represent a promising approach for the development of new therapeutics to improve immune pathologies in diabetic patients.

5.5. Concluding remarks and Outlook

The data presented in this thesis demonstrate that hyperglycemia, as observed in the blood of patients with diabetes, exerts a considerable influence on macrophage activation and functionality. The results particularly highlight the glucose-mediated disruption of the cellular Ca^{2+} homeostasis, the depletion of Ca^{2+} stores and subsequent impairment of Ca^{2+}-related processes in macrophages.

Cell culture media are typically modified to provide sufficient energy, act as a major carbon source and support cell proliferation. Consequently, the media usually contain excessive amounts of nutrients, including glutamine, glucose and pyruvate and are supplemented with amino acids and vitamins. [336] Strikingly, various studies already revealed that the composition of culture media, including varying formulations, such as RPMI, DMEM and IMDM, affects the differentiation and phenotype of both murine and human macrophages [337,338]. Accordingly, the observed alterations raise the question of whether the results obtained from *in vitro* studies utilizing nutrient-rich media are transferable to murine and human physiology, and whether these cultured cells resemble the immunological phenotypes they are intended to model. To more closely mimic a physiological metabolic environment while supporting cellular differentiation and growth, the media used for experiments in the present study contained standard concentrations of amino acids and vitamins, but reduced levels of glutamine, pyruvate and glucose.

The present study exclusively focused on the influence of hyperglycemia on differentiated macrophages, whereas the impact of hyperglycemia on macrophage differentiation itself remains to be explored. Consequently, another compelling aspect for future investigations may involve examining the impact of excessive amounts of glucose on macrophage differentiation, particularly in relation to the epigenetic alterations observed in monocytes from individuals with diabetes [311].

The present work identified the taste receptor Tas1R3 as the primary receptor through which macrophages sense elevated glucose concentrations. The activation of Tas1R3 by glucose or other sweet-tasting agents results in the initiation of a signaling cascade via PLC, leading to the depletion of Ca^{2+} from the ER through the inhibition of SERCA and the activation of the IP_3R. Accordingly, our data emphasize a decisive role of Tas1R3 in extraoral tissues and provide insight into how elevated glucose concentrations impair Ca^{2+} signaling in Tas1R3-expressing macrophages and monocytes. These findings further offer a significant advancement in our understanding of the molecular mechanisms through which glucose modulates macrophage function in the context of diabetes. The data highlight the importance of investigating the relationship between macrophage functionality and hyperglycemia and its contribution to the progression of diabetes and the development of secondary diseases.

To more precisely decipher the role of glucose-mediated activation of Tas1R3 in shaping macrophage phenotype and function in a physiological setting and its subsequent contribution to the onset of diabetes and diabetes-related complications, further *in vivo* investigations are required. However, thus far, only mice with a global deletion of Tas1R3 are available. These mice have been shown to exhibit a reduced overall glucose tolerance, however, an improved western diet-induced anxiety as well as reduced high-fat diet-induced development of atherosclerotic plaques [339–341]. The specific role of Tas1R3 on macrophage functionality in the context of diabetes can only be elucidated by the generation of a new mouse line. Specifically, the crossing of a $Tas1R3^{fl/fl}$ mouse, in which the Tas1R3 gene has been flanked by loxP sites, with a mouse expressing a Cre recombinase under the control of a macrophage-specific promoter, such as the lysozyme M promoter (LysM), would generate a mouse model with macrophage-, monocyte- and neutrophil-specific deletion of Tas1R3. Further delineation of the influence of Tas1R3 deletion in macrophages of distinct origins on the development and progression of diabetes could be achieved by employing alternative Cre models, such as the $Cx3cr1^{Cre}$ or $Ms4a3^{Cre}$ mice, which selectively target embryonically-derived and hematopoietic stem cell-derived macrophages, respectively. [342,343] To obtain a comprehensive understanding of the complex development, progression and pathologies of diabetes, it is essential to investigate the role of Tas1R3-deficient macrophages across multiple animal models of diabetes. Each model captures distinct aspects of the disease, thereby enriching the understanding of the multifactorial nature of diabetes. For instance, insulin deficiency in the context of type 1 diabetes can be explored through either immune-mediated or chemically-induced destruction of beta cells, using models, such as non-obese diabetic mice or streptozotocin treatment, respectively. Conversely, insulin resistance, as a hallmark of type 2 diabetes, is most commonly studied in obesity models, which can be induced by feeding a high-fat diet or genetic modifications. [344,345]

In summary, the data presented in this thesis revealed that hyperglycemia induces a pro-inflammatory cytokine profile in macrophages via the mTOR/NF-κB pathway. Furthermore, glucose-mediated activation of Tas1R3 leads to the depletion of Ca^{2+} from its stores, thereby disrupting Ca^{2+}-dependent processes, such as cellular migration and protein folding. Accordingly, these findings propose a novel mechanism by which glucose sensing by macrophages modulates their phenotype. This mechanism is not only relevant in terms of understanding the immunological phenotypes observed in diabetes but also holds potential for the development of new therapeutic approaches aimed at mitigating the immune dysfunctions and complications associated with diabetes.

6. Appendix

6.1. Bibliography

1. Magliano, D. & Boyko, E. J. *IDF diabetes atlas.* 10th ed. (International Diabetes Federation, Brussels, 2021).
2. *Noncommunicable Diseases Progress Monitor 2020.* 1st ed. (World Health Organization, Geneva, 2020).
3. Non communicable diseases. Available at https://www.who.int/news-room/fact-sheets/detail/noncommunicable-diseases (2024).
4. Roden, M. & Shulman, G. I. The integrative biology of type 2 diabetes. *Nature* **576,** 51–60; 10.1038/s41586-019-1797-8 (2019).
5. German, M. S. Glucose sensing in pancreatic islet beta cells: the key role of glucokinase and the glycolytic intermediates. *Proceedings of the National Academy of Sciences of the United States of America* **90,** 1781–1785; 10.1073/pnas.90.5.1781 (1993).
6. Zakaria, N. F., Hamid, M. & Khayat, M. E. Amino Acid-Induced Impairment of Insulin Signaling and Involvement of G-Protein Coupling Receptor. *Nutrients* **13,** 2229; 10.3390/nu13072229 (2021).
7. Roden, M. & Shulman, G. I. The integrative biology of type 2 diabetes. *Nature* **576,** 51–60; 10.1038/s41586-019-1797-8 (2019).
8. Galicia-Garcia, U. *et al.* Pathophysiology of Type 2 Diabetes Mellitus. *International Journal of Molecular Sciences* **21**; 10.3390/ijms21176275 (2020).
9. Ahrén, B. Glucose: Glucose Tolerance. In *Caballero (Hg.) – Encyclopedia of human nutrition [electronic,* pp. 381–386.
10. 2. Diagnosis and Classification of Diabetes: Standards of Care in Diabetes-2024. *Diabetes care* **47,** S20-S42; 10.2337/dc24-S002 (2024).
11. Classification of diabetes mellitus.
12. Management-Screening, D. & Treatment. Classification of diabetes mellitus. *World Health Organization* (2019).
13. Kuryłowicz, A. & Koźniewski, K. Anti-Inflammatory Strategies Targeting Metaflammation in Type 2 Diabetes. *Molecules* **25,** 2224; 10.3390/molecules25092224 (2020).
14. Zhao, L. *et al.* Inflammation in diabetes complications: molecular mechanisms and therapeutic interventions. *MedComm* **5,** e516; 10.1002/mco2.516 (2024).

15. Berbudi, A., Rahmadika, N., Tjahjadi, A. I. & Ruslami, R. Type 2 Diabetes and its Impact on the Immune System. *Current Diabetes Reviews* **16,** 442–449; 10.2174/1573399815666191024085838 (2020).

16. Prattichizzo, F. *et al.* Inflammageing and metaflammation: The yin and yang of type 2 diabetes. *Ageing research reviews* **41,** 1–17; 10.1016/j.arr.2017.10.003 (2018).

17. Banu, S. & Sur, D. Role of Macrophage in Type 2 Diabetes Mellitus: Macrophage Polarization a New Paradigm for Treatment of Type 2 Diabetes Mellitus. *Endocrine, metabolic & immune disorders drug targets* **23,** 2–11; 10.2174/1871530322666220630093359 (2023).

18. Li, H. *et al.* Macrophages, Chronic Inflammation, and Insulin Resistance. *Cells* **11**; 10.3390/cells11193001 (2022).

19. Orliaguet, L., Dalmas, E., Drareni, K., Venteclef, N. & Alzaid, F. Mechanisms of Macrophage Polarization in Insulin Signaling and Sensitivity. *Frontiers in endocrinology* **11,** 62; 10.3389/fendo.2020.00062 (2020).

20. Röder, P. V., Wu, B., Liu, Y. & Han, W. Pancreatic regulation of glucose homeostasis. *Exp Mol Med* **48,** e219; 10.1038/emm.2016.6 (2016).

21. Aronoff, S. L., Berkowitz, K., Shreiner, B. & Want, L. Glucose Metabolism and Regulation: Beyond Insulin and Glucagon. *Diabetes Spectrum* **17,** 183–190; 10.2337/diaspect.17.3.183 (2004).

22. Marchetti, P., Bugliani, M., Tata, V. de, Suleiman, M. & Marselli, L. Pancreatic Beta Cell Identity in Humans and the Role of Type 2 Diabetes. *Frontiers in cell and developmental biology* **5,** 55; 10.3389/fcell.2017.00055 (2017).

23. Boucher, J., Kleinridders, A. & Kahn, C. R. Insulin receptor signaling in normal and insulin-resistant states. *Cold Spring Harbor Perspectives in Biology* **6**; 10.1101/cshperspect.a009191 (2014).

24. Olivares-Reyes, J. A., Arellano-Plancarte, A. & Castillo-Hernandez, J. R. Angiotensin II and the development of insulin resistance: implications for diabetes. *Molecular and cellular endocrinology* **302,** 128–139; 10.1016/j.mce.2008.12.011 (2009).

25. Hopkins, B. D., Goncalves, M. D. & Cantley, L. C. Insulin-PI3K signalling: an evolutionarily insulated metabolic driver of cancer. *Nature reviews. Endocrinology* **16,** 276–283; 10.1038/s41574-020-0329-9 (2020).

26. Gabbouj, S. *et al.* Altered Insulin Signaling in Alzheimer's Disease Brain - Special Emphasis on PI3K-Akt Pathway. *Frontiers in neuroscience* **13,** 629; 10.3389/fnins.2019.00629 (2019).

27. Abbas, A. K., Lichtman, A. H. & Pillai, S. *Basic immunology. Functions and disorders of the immune system* (Elsevier, Philadelphia, PA, 2024).

28. Franken, L., Schiwon, M. & Kurts, C. Macrophages: sentinels and regulators of the immune system. *Cellular microbiology* **18,** 475–487; 10.1111/cmi.12580 (2016).

29. Watanabe, S., Alexander, M., Misharin, A. V. & Budinger, G. R. S. The role of macrophages in the resolution of inflammation. *J Clin Invest* **129,** 2619–2628; 10.1172/JCI124615 (2019).

30. Ginhoux, F. & Jung, S. Monocytes and macrophages: developmental pathways and tissue homeostasis. *Nat Rev Immunol* **14,** 392–404; 10.1038/nri3671 (2014).

31. Rodríguez-Morales, P. & Franklin, R. A. Macrophage phenotypes and functions: resolving inflammation and restoring homeostasis. *Trends in immunology* **44,** 986–998; 10.1016/j.it.2023.10.004 (2023).

32. Gordon, S. & Plüddemann, A. Tissue macrophages: heterogeneity and functions. *BMC Biol* **15,** 53; 10.1186/s12915-017-0392-4 (2017).

33. Park, M. D., Silvin, A., Ginhoux, F. & Merad, M. Macrophages in health and disease. *Cell* **185,** 4259–4279; 10.1016/j.cell.2022.10.007 (2022).

34. Gao, W.-J. *et al.* Macrophage 3D migration: A potential therapeutic target for inflammation and deleterious progression in diseases. *Pharmacological research* **167,** 105563; 10.1016/j.phrs.2021.105563 (2021).

35. Pixley, F. J. Macrophage Migration and Its Regulation by CSF-1. *International journal of cell biology* **2012,** 501962; 10.1155/2012/501962 (2012).

36. Da Nascimento Conceicao, V. *et al.* Resolving macrophage polarization through distinct Ca2+ entry channel that maintains intracellular signaling and mitochondrial bioenergetics. *iScience* **24,** 103339; 10.1016/j.isci.2021.103339 (2021).

37. Desai, B. N. & Leitinger, N. Purinergic and calcium signaling in macrophage function and plasticity. *Frontiers in immunology* **5,** 580; 10.3389/fimmu.2014.00580 (2014).

38. Hamilton, T. A., Zhao, C., Pavicic, P. G. & Datta, S. Myeloid colony-stimulating factors as regulators of macrophage polarization. *Frontiers in immunology* **5,** 554; 10.3389/fimmu.2014.00554 (2014).

39. Sander, J. *et al.* Cellular Differentiation of Human Monocytes Is Regulated by Time-Dependent Interleukin-4 Signaling and the Transcriptional Regulator NCOR2. *Immunity* **47,** 1051-1066.e12; 10.1016/j.immuni.2017.11.024 (2017).

40. Marrocco, A. & Ortiz, L. A. Role of metabolic reprogramming in pro-inflammatory cytokine secretion from LPS or silica-activated macrophages. *Frontiers in immunology* **13,** 936167; 10.3389/fimmu.2022.936167 (2022).

41. Xue, J. *et al.* Transcriptome-based network analysis reveals a spectrum model of human macrophage activation. *Immunity* **40,** 274–288; 10.1016/j.immuni.2014.01.006 (2014).

42. Mosser, D. M. & Edwards, J. P. Exploring the full spectrum of macrophage activation. *Nat Rev Immunol* **8,** 958–969; 10.1038/nri2448 (2008).

43. Kadomoto, S., Izumi, K. & Mizokami, A. Macrophage Polarity and Disease Control. *International Journal of Molecular Sciences* **23**; 10.3390/ijms23010144 (2021).

44. Kelly, B. & O'Neill, L. A. J. Metabolic reprogramming in macrophages and dendritic cells in innate immunity. *Cell research* **25,** 771–784; 10.1038/cr.2015.68 (2015).

45. Jost, P. J. & Ruland, J. Aberrant NF-kappaB signaling in lymphoma: mechanisms, consequences, and therapeutic implications. *Blood* **109,** 2700–2707; 10.1182/blood-2006-07-025809 (2007).

46. Akira, S., Uematsu, S. & Takeuchi, O. Pathogen recognition and innate immunity. *Cell* **124,** 783–801; 10.1016/j.cell.2006.02.015 (2006).

47. Charlotte R. Kleiveland. Peripheral Blood Mononuclear Cells. In *The Impact of Food Bioactives on Health: in vitro and ex vivo models [Internet],* edited by C. R. Kleiveland (Springer2015).

48. Yang, J., Zhang, L., Yu, C., Yang, X.-F. & Wang, H. Monocyte and macrophage differentiation: circulation inflammatory monocyte as biomarker for inflammatory diseases. *Biomark Res* **2,** 1; 10.1186/2050-7771-2-1 (2014).

49. Cassado, A. D. A., D'Império Lima, M. R. & Bortoluci, K. R. Revisiting mouse peritoneal macrophages: heterogeneity, development, and function. *Frontiers in immunology* **6,** 225; 10.3389/fimmu.2015.00225 (2015).

50. Ghosn, E. E. B. *et al.* Two physically, functionally, and developmentally distinct peritoneal macrophage subsets. *Proceedings of the National Academy of Sciences of the United States of America* **107,** 2568–2573; 10.1073/pnas.0915000107 (2010).

51. Wang, J. & Kubes, P. A Reservoir of Mature Cavity Macrophages that Can Rapidly Invade Visceral Organs to Affect Tissue Repair. *Cell* **165,** 668–678; 10.1016/j.cell.2016.03.009 (2016).

52. Takenaka, E., van Vo, A., Yamashita-Kanemaru, Y., Shibuya, A. & Shibuya, K. Selective DNAM-1 expression on small peritoneal macrophages contributes to CD4+ T cell costimulation. *Sci Rep* **8,** 15180; 10.1038/s41598-018-33437-4 (2018).

53. Zhang, X., Goncalves, R. & Mosser, D. M. The isolation and characterization of murine macrophages. *Current protocols in immunology* **Chapter 14,** 14.1.1-14.1.14; 10.1002/0471142735.im1401s83 (2008).

54. Jesus, A. de *et al.* Optimized protocol to isolate primary mouse peritoneal macrophage metabolites. *STAR protocols* **3,** 101668; 10.1016/j.xpro.2022.101668 (2022).

55. Pavlou, S., Wang, L., Xu, H. & Chen, M. Higher phagocytic activity of thioglycollate-elicited peritoneal macrophages is related to metabolic status of the cells. *Journal of inflammation (London, England)* **14,** 4; 10.1186/s12950-017-0151-x (2017).

56. Ruiz-Alcaraz, A. J. *et al.* Characterization of human peritoneal monocyte/macrophage subsets in homeostasis: Phenotype, GATA6, phagocytic/oxidative activities and cytokines expression. *Sci Rep* **8,** 12794; 10.1038/s41598-018-30787-x (2018).

57. García-Peñarrubia, P., Ruiz-Alcaraz, A. J., Ruiz-Ballester, M., Ramírez-Pávez, T. N. & Martínez-Esparza, M. Recent insights into the characteristics and role of peritoneal macrophages from ascites of cirrhotic patients. *World journal of gastroenterology* **27,** 7014–7024; 10.3748/wjg.v27.i41.7014 (2021).

58. Lauterbach, M. A. R. & Wunderlich, F. T. Macrophage function in obesity-induced inflammation and insulin resistance. *Pflugers Archiv : European journal of physiology* **469,** 385–396; 10.1007/s00424-017-1955-5 (2017).

59. Meshkani, R. & Vakili, S. Tissue resident macrophages: Key players in the pathogenesis of type 2 diabetes and its complications. *Clinica chimica acta; international journal of clinical chemistry* **462,** 77–89; 10.1016/j.cca.2016.08.015 (2016).

60. Tesch, G. H. Role of macrophages in complications of type 2 diabetes. *Clinical and experimental pharmacology & physiology* **34,** 1016–1019; 10.1111/j.1440-1681.2007.04729.x (2007).

61. Zhang, S. *et al.* The role and therapeutic potential of macrophages in the pathogenesis of diabetic cardiomyopathy. *Frontiers in immunology* **15,** 1393392; 10.3389/fimmu.2024.1393392 (2024).

62. Ying, W., Fu, W., Lee, Y. S. & Olefsky, J. M. The role of macrophages in obesity-associated islet inflammation and β-cell abnormalities. *Nature reviews. Endocrinology* **16,** 81–90; 10.1038/s41574-019-0286-3 (2020).

63. Hotamisligil, G. S., Shargill, N. S. & Spiegelman, B. M. Adipose expression of tumor necrosis factor-alpha: direct role in obesity-linked insulin resistance. *Science (New York, N.Y.)* **259,** 87–91; 10.1126/science.7678183 (1993).

64. Kim, J.-H., Bachmann, R. A. & Chen, J. Interleukin-6 and insulin resistance. *Vitamins and hormones* **80,** 613–633; 10.1016/S0083-6729(08)00621-3 (2009).

65. Lee, B.-C. & Lee, J. Cellular and molecular players in adipose tissue inflammation in the development of obesity-induced insulin resistance. *Biochimica et biophysica acta* **1842,** 446–462; 10.1016/j.bbadis.2013.05.017 (2014).

66. Cucak, H., Grunnet, L. G. & Rosendahl, A. Accumulation of M1-like macrophages in type 2 diabetic islets is followed by a systemic shift in macrophage polarization. *Journal of leukocyte biology* **95,** 149–160; 10.1189/jlb.0213075 (2014).

67. Ying, W. *et al.* Expansion of Islet-Resident Macrophages Leads to Inflammation Affecting β Cell Proliferation and Function in Obesity. *Cell Metabolism* **29,** 457-474.e5; 10.1016/j.cmet.2018.12.003 (2019).

68. Zhang, Y. *et al.* Islet-resident macrophage-derived miR-155 promotes β cell decompensation via targeting PDX1. *iScience* **27,** 109540; 10.1016/j.isci.2024.109540 (2024).

69. Pavlou, S., Lindsay, J., Ingram, R., Xu, H. & Chen, M. Sustained high glucose exposure sensitizes macrophage responses to cytokine stimuli but reduces their phagocytic activity. *BMC Immunol* **19,** 24; 10.1186/s12865-018-0261-0 (2018).

70. Sharifiaghdam, M. *et al.* Macrophages as a therapeutic target to promote diabetic wound healing. *Molecular therapy : the journal of the American Society of Gene Therapy* **30,** 2891–2908; 10.1016/j.ymthe.2022.07.016 (2022).

71. Barman, P. K. & Koh, T. J. Macrophage Dysregulation and Impaired Skin Wound Healing in Diabetes. *Frontiers in cell and developmental biology* **8,** 528; 10.3389/fcell.2020.00528 (2020).

72. Komura, T. *et al.* CD14+ monocytes are vulnerable and functionally impaired under endoplasmic reticulum stress in patients with type 2 diabetes. *Diabetes* **59,** 634–643; 10.2337/db09-0659 (2010).

73. Martinez, N. *et al.* Defects in early cell recruitment contribute to the increased susceptibility to respiratory Klebsiella pneumoniae infection in diabetic mice. *Microbes and Infection* **18,** 649–655; 10.1016/j.micinf.2016.05.007 (2016).

74. Servier Medical Art. SMART - Servier Medical ART. licensed under CC BY 4.0. Available at https://smart.servier.com/ (2024).

75. Rossi, A., Pizzo, P. & Filadi, R. Calcium, mitochondria and cell metabolism: A functional triangle in bioenergetics. *Biochimica et biophysica acta. Molecular cell research* **1866,** 1068–1078; 10.1016/j.bbamcr.2018.10.016 (2019).

76. Tsai, F.-C., Kuo, G.-H., Chang, S.-W. & Tsai, P.-J. Ca2+ signaling in cytoskeletal reorganization, cell migration, and cancer metastasis. *BioMed Research International* **2015,** 409245; 10.1155/2015/409245 (2015).

77. Berridge, M. J., Lipp, P. & Bootman, M. D. The versatility and universality of calcium signalling. *Nature reviews. Molecular cell biology* **1,** 11–21; 10.1038/35036035 (2000).

78. Berridge, M. J., Bootman, M. D. & Roderick, H. L. Calcium signalling: dynamics, homeostasis and remodelling. *Nature reviews. Molecular cell biology* **4,** 517–529; 10.1038/nrm1155 (2003).

79. Carafoli, E. Special issue: calcium signaling and disease. *Biochemical and Biophysical Research Communications* **322,** 1097; 10.1016/j.bbrc.2004.08.049 (2004).

80. Pchitskaya, E., Popugaeva, E. & Bezprozvanny, I. Calcium signaling and molecular mechanisms underlying neurodegenerative diseases. *Cell Calcium* **70,** 87–94; 10.1016/j.ceca.2017.06.008 (2018).

81. Chen, C.-C. *et al.* Emerging Roles of Calcium Signaling in the Development of Non-Alcoholic Fatty Liver Disease. *International Journal of Molecular Sciences* **23**; 10.3390/ijms23010256 (2021).

82. Guerrero-Hernandez, A. & Verkhratsky, A. Calcium signalling in diabetes. *Cell Calcium* **56,** 297–301; 10.1016/j.ceca.2014.08.009 (2014).

83. Wu, L., Lian, W. & Zhao, L. Calcium signaling in cancer progression and therapy. *The FEBS journal* **288,** 6187–6205; 10.1111/febs.16133 (2021).

84. Feske, S., Wulff, H. & Skolnik, E. Y. Ion channels in innate and adaptive immunity. *Annual review of immunology* **33,** 291–353; 10.1146/annurev-immunol-032414-112212 (2015).

85. Shumilina, E., Huber, S. M. & Lang, F. Ca2+ signaling in the regulation of dendritic cell functions. *American journal of physiology. Cell physiology* **300,** C1205-14; 10.1152/ajpcell.00039.2011 (2011).

86. Selezneva, A., Gibb, A. J. & Willis, D. The contribution of ion channels to shaping macrophage behaviour. *Frontiers in Pharmacology* **13,** 970234; 10.3389/fphar.2022.970234 (2022).

87. Putney, J. W. Capacitative calcium entry: sensing the calcium stores. *J Cell Biol* **169,** 381–382; 10.1083/jcb.200503161 (2005).

88. Hosoi, E. *et al.* Expression of the ryanodine receptor isoforms in immune cells. *J Immunol* **167,** 4887–4894; 10.4049/jimmunol.167.9.4887 (2001).

89. Zhu, L., Jones, C. & Zhang, G. The Role of Phospholipase C Signaling in Macrophage-Mediated Inflammatory Response. *Journal of immunology research* **2018,** 5201759; 10.1155/2018/5201759 (2018).

90. Rhee, S. G. Regulation of phosphoinositide-specific phospholipase C. *Annual review of biochemistry* **70,** 281–312; 10.1146/annurev.biochem.70.1.281 (2001).

91. Nunes, P. & Demaurex, N. The role of calcium signaling in phagocytosis. *Journal of leukocyte biology* **88,** 57–68; 10.1189/jlb.0110028 (2010).

92. Liu, J. *et al.* ATP ion channel P2X purinergic receptors in inflammation response. *Biomedicine & pharmacotherapy = Biomedecine & pharmacotherapie* **158,** 114205; 10.1016/j.biopha.2022.114205 (2023).

93. Ren, W., Rubini, P., Tang, Y., Engel, T. & Illes, P. Inherent P2X7 Receptors Regulate Macrophage Functions during Inflammatory Diseases. *International Journal of Molecular Sciences* **23**; 10.3390/ijms23010232 (2021).

94. Wu, J. *et al.* Function of TRP channels in monocytes/macrophages. *Frontiers in immunology* **14,** 1187890; 10.3389/fimmu.2023.1187890 (2023).

95. Ramsey, I. S., Delling, M. & Clapham, D. E. An introduction to TRP channels. *Annual review of physiology* **68,** 619–647; 10.1146/annurev.physiol.68.040204.100431 (2006).

96. Rohacs, T. Regulation of transient receptor potential channels by the phospholipase C pathway. *Advances in biological regulation* **53,** 341–355; 10.1016/j.jbior.2013.07.004 (2013).

97. Clapham, D. E. Calcium signaling. *Cell* **131,** 1047–1058; 10.1016/j.cell.2007.11.028 (2007).

98. Raffaello, A. *et al.* The mitochondrial calcium uniporter is a multimer that can include a dominant-negative pore-forming subunit. *The EMBO journal* **32,** 2362–2376; 10.1038/emboj.2013.157 (2013).

99. Ramos, V. M. *et al.* Mitochondrial sodium/calcium exchanger (NCLX) regulates basal and starvation-induced autophagy through calcium signaling. *The FASEB Journal* **38,** e23454; 10.1096/fj.202301368RR (2024).

100. Lemos, F. O., Bultynck, G. & Parys, J. B. A comprehensive overview of the complex world of the endo- and sarcoplasmic reticulum Ca2+-leak channels. *Biochimica et biophysica acta. Molecular cell research* **1868,** 119020; 10.1016/j.bbamcr.2021.119020 (2021).

101. Arruda, A. P. & Hotamisligil, G. S. Calcium Homeostasis and Organelle Function in the Pathogenesis of Obesity and Diabetes. *Cell Metabolism* **22,** 381–397; 10.1016/j.cmet.2015.06.010 (2015).

102. Taylor, C. W. Regulation of IP3 receptors by cyclic AMP. *Cell Calcium* **63,** 48–52; 10.1016/j.ceca.2016.10.005 (2017).

103. Prole, D. L. & Taylor, C. W. Inositol 1,4,5-trisphosphate receptors and their protein partners as signalling hubs. *The Journal of physiology* **594,** 2849–2866; 10.1113/JP271139 (2016).

104. Zeng, W. *et al.* A new mode of Ca2+ signaling by G protein-coupled receptors: gating of IP3 receptor Ca2+ release channels by Gbetagamma. *Current biology : CB* **13,** 872–876; 10.1016/s0960-9822(03)00330-0 (2003).

105. Camors, E. & Valdivia, H. H. CaMKII regulation of cardiac ryanodine receptors and inositol triphosphate receptors. *Frontiers in Pharmacology* **5,** 101; 10.3389/fphar.2014.00101 (2014).

106. Pick, T., Gamayun, I., Tinschert, R. & Cavalié, A. Kinetics of the thapsigargin-induced Ca2+ mobilisation: A quantitative analysis in the HEK-293 cell line. *Frontiers in physiology* **14,** 1127545; 10.3389/fphys.2023.1127545 (2023).

107. Anderson, D. M. *et al.* Widespread control of calcium signaling by a family of SERCA-inhibiting micropeptides. *Science signaling* **9,** ra119; 10.1126/scisignal.aaj1460 (2016).

108. Rathod, N. *et al.* Nothing Regular about the Regulins: Distinct Functional Properties of SERCA Transmembrane Peptide Regulatory Subunits. *International Journal of Molecular Sciences* **22**; 10.3390/ijms22168891 (2021).

109. Cleary, S. R. *et al.* Inhibitory and stimulatory micropeptides preferentially bind to different conformations of the cardiac calcium pump. *The Journal of biological chemistry* **298,** 102060; 10.1016/j.jbc.2022.102060 (2022).

110. Shaikh, S. A., Sahoo, S. K. & Periasamy, M. Phospholamban and sarcolipin: Are they functionally redundant or distinct regulators of the Sarco(Endo)Plasmic Reticulum Calcium ATPase? *Journal of molecular and cellular cardiology* **91,** 81–91; 10.1016/j.yjmcc.2015.12.030 (2016).

111. Cleary, S. R. *et al.* Phospholamban inhibits the cardiac calcium pump by interrupting an allosteric activation pathway. *Journal of Biological Chemistry* **300,** 107267; 10.1016/j.jbc.2024.107267 (2024).

112. Bidwell, P., Blackwell, D. J., Hou, Z., Zima, A. V. & Robia, S. L. Phospholamban binds with differential affinity to calcium pump conformers. *Journal of Biological Chemistry* **286,** 35044–35050; 10.1074/jbc.M111.266759 (2011).

113. Fisher, M. E. *et al.* Dwarf open reading frame (DWORF) is a direct activator of the sarcoplasmic reticulum calcium pump SERCA. *eLife* **10**; 10.7554/eLife.65545 (2021).

114. Andersen, L. L. *et al.* Systematic P2Y receptor survey identifies P2Y11 as modulator of immune responses and virus replication in macrophages. *The EMBO journal* **42,** e113279; 10.15252/embj.2022113279 (2023).

115. Klaver, D. & Thurnher, M. Control of Macrophage Inflammation by P2Y Purinergic Receptors. *Cells* **10**; 10.3390/cells10051098 (2021).

116. Kronlage, M. *et al.* Autocrine purinergic receptor signaling is essential for macrophage chemotaxis. *Science signaling* **3,** ra55; 10.1126/scisignal.2000588 (2010).

117. Hofer, A. M. & Brown, E. M. Extracellular calcium sensing and signalling. *Nature reviews. Molecular cell biology* **4,** 530–538; 10.1038/nrm1154 (2003).

118. Chen, X. *et al.* The CaSR/TRPV4 coupling mediates pro-inflammatory macrophage function. *Acta Physiologica* **237,** e13926; 10.1111/apha.13926 (2023).

119. Wu, K.-C., Leong, I.-L. & Leung, Y.-M. Ca2+-sensing receptor-TRP channel-mediated Ca2+ signaling: Functional diversity and pharmacological complexity. *European journal of pharmacology* **977,** 176717; 10.1016/j.ejphar.2024.176717 (2024).

120. Olszak, I. T. *et al.* Extracellular calcium elicits a chemokinetic response from monocytes in vitro and in vivo. *J Clin Invest* **105,** 1299–1305; 10.1172/JCI9799 (2000).

121. Ruytinx, P., Proost, P., van Damme, J. & Struyf, S. Chemokine-Induced Macrophage Polarization in Inflammatory Conditions. *Frontiers in immunology* **9,** 1930; 10.3389/fimmu.2018.01930 (2018).

122. Xuan, W., Qu, Q., Zheng, B., Xiong, S. & Fan, G.-H. The chemotaxis of M1 and M2 macrophages is regulated by different chemokines. *Journal of leukocyte biology* **97,** 61–69; 10.1189/jlb.1A0314-170R (2015).

123. Dorsam, R. T. & Gutkind, J. S. G-protein-coupled receptors and cancer. *Nature reviews. Cancer* **7,** 79–94; 10.1038/nrc2069 (2007).

124. Kee, T. R. *et al.* The multifaceted functions of β-arrestins and their therapeutic potential in neurodegenerative diseases. *Exp Mol Med* **56,** 129–141; 10.1038/s12276-023-01144-4 (2024).

125. Tripathi, D. K. & Poluri, K. M. Molecular insights into kinase mediated signaling pathways of chemokines and their cognate G protein coupled receptors. *Frontiers in bioscience (Landmark edition)* **25,** 1361–1385; 10.2741/4860 (2020).

126. Senarath, K. *et al.* Gγ identity dictates efficacy of Gβγ signaling and macrophage migration. *Journal of Biological Chemistry* **293,** 2974–2989; 10.1074/jbc.RA117.000872 (2018).

127. Tennakoon, M. *et al.* Subtype-dependent regulation of Gβγ signalling. *Cellular signalling* **82,** 109947; 10.1016/j.cellsig.2021.109947 (2021).

128. Villaseca, S. *et al.* Gαi protein subunit: A step toward understanding its non-canonical mechanisms. *Frontiers in cell and developmental biology* **10,** 941870; 10.3389/fcell.2022.941870 (2022).

129. Pablo Gainza & Bruno E. Correia. *Code for Rules and mechanisms governing G protein coupling selectivity of GPCRs* (Zenodo, 2023).

130. Okashah, N. *et al.* Variable G protein determinants of GPCR coupling selectivity. *Proceedings of the National Academy of Sciences of the United States of America* **116,** 12054–12059; 10.1073/pnas.1905993116 (2019).

131. Rodríguez-Fernández, J. L. & Criado-García, O. The Chemokine Receptor CCR7 Uses Distinct Signaling Modules With Biased Functionality to Regulate Dendritic Cells. *Frontiers in immunology* **11,** 528; 10.3389/fimmu.2020.00528 (2020).

132. Corbisier, J., Galès, C., Huszagh, A., Parmentier, M. & Springael, J.-Y. Biased signaling at chemokine receptors. *Journal of Biological Chemistry* **290,** 9542–9554; 10.1074/jbc.M114.596098 (2015).

133. Hannan, F. M., Kallay, E., Chang, W., Brandi, M. L. & Thakker, R. V. The calcium-sensing receptor in physiology and in calcitropic and noncalcitropic diseases. *Nature reviews. Endocrinology* **15,** 33–51; 10.1038/s41574-018-0115-0 (2018).

134. Erb, L. & Weisman, G. A. Coupling of P2Y receptors to G proteins and other signaling pathways. *Wiley interdisciplinary reviews. Membrane transport and signaling* **1,** 789–803; 10.1002/wmts.62 (2012).

135. Wu, H.-Y., Tang, X.-Q., Liu, H., Mao, X.-F. & Wang, Y.-X. Both classic Gs-cAMP/PKA/CREB and alternative Gs-cAMP/PKA/p38β/CREB signal pathways mediate exenatide-stimulated expression of M2 microglial markers. *Journal of neuroimmunology* **316,** 17–22; 10.1016/j.jneuroim.2017.12.005 (2018).

136. Worzfeld, T., Wettschureck, N. & Offermanns, S. G(12)/G(13)-mediated signalling in mammalian physiology and disease. *Trends in pharmacological sciences* **29,** 582–589; 10.1016/j.tips.2008.08.002 (2008).

137. Wu, V. *et al.* Illuminating the Onco-GPCRome: Novel G protein-coupled receptor-driven oncocrine networks and targets for cancer immunotherapy. *Journal of Biological Chemistry* **294,** 11062–11086; 10.1074/jbc.REV119.005601 (2019).

138. Marinissen, M. J. & Gutkind, J. S. G-protein-coupled receptors and signaling networks: emerging paradigms. *Trends in pharmacological sciences* **22,** 368–376; 10.1016/S0165-6147(00)01678-3 (2001).

139. Naor, Z., Benard, O. & Seger, R. Activation of MAPK cascades by G-protein-coupled receptors: the case of gonadotropin-releasing hormone receptor. *Trends in Endocrinology & Metabolism* **11,** 91–99; 10.1016/S1043-2760(99)00232-5 (2000).

140. Zhao, M. *et al.* The Roles of Orphan G Protein-Coupled Receptors in Autoimmune Diseases. *Clinical reviews in allergy & immunology* **60,** 220–243; 10.1007/s12016-020-08829-y (2021).

141. Champion, H. C. Targeting protein phosphatase 1 in heart failure. *Circulation research* **96,** 708–710; 10.1161/01.RES.0000164359.95588.25 (2005).

142. Zarain-Herzberg, A. Regulation of the sarcoplasmic reticulum Ca2+-ATPase expression in the hypertrophic and failing heart. *Canadian journal of physiology and pharmacology* **84,** 509–521; 10.1139/y06-023 (2006).

143. Sahin, B. *et al.* Phosphorylation of protein phosphatase inhibitor-1 by protein kinase C. *Journal of Biological Chemistry* **281,** 24322–24335; 10.1074/jbc.M603282200 (2006).

144. Nicolaou, P., Hajjar, R. J. & Kranias, E. G. Role of protein phosphatase-1 inhibitor-1 in cardiac physiology and pathophysiology. *Journal of molecular and cellular cardiology* **47,** 365–371; 10.1016/j.yjmcc.2009.05.010 (2009).

145. Yano, M., Ikeda, Y. & Matsuzaki, M. Altered intracellular Ca2+ handling in heart failure. *J Clin Invest* **115,** 556–564; 10.1172/JCI24159 (2005).

146. Zumerle, S. *et al.* Intercellular Calcium Signaling Induced by ATP Potentiates Macrophage Phagocytosis. *Cell reports* **27,** 1-10.e4; 10.1016/j.celrep.2019.03.011 (2019).

147. Chauhan, A. *et al.* M1 Macrophage Polarization Is Dependent on TRPC1-Mediated Calcium Entry. *iScience* **8,** 85–102; 10.1016/j.isci.2018.09.014 (2018).

148. Vaeth, M. *et al.* Ca2+ Signaling but Not Store-Operated Ca2+ Entry Is Required for the Function of Macrophages and Dendritic Cells. *Journal of immunology (Baltimore, Md. : 1950)* **195,** 1202–1217; 10.4049/jimmunol.1403013 (2015).

149. Tsai, F.-C. *et al.* A polarized Ca2+, diacylglycerol and STIM1 signalling system regulates directed cell migration. *Nat Cell Biol* **16,** 133–144; 10.1038/ncb2906 (2014).

150. Zanoni, I. & Granucci, F. Differences in lipopolysaccharide-induced signaling between conventional dendritic cells and macrophages. *Immunobiology* **215,** 709–712; 10.1016/j.imbio.2010.05.026 (2010).

151. Aki, D. *et al.* Peptidoglycan and lipopolysaccharide activate PLCgamma2, leading to enhanced cytokine production in macrophages and dendritic cells. *Genes to Cells* **13,** 199–208; 10.1111/j.1365-2443.2007.01159.x (2008).

152. Becker, S. M., Delamarre, L., Mellman, I. & Andrews, N. W. Differential role of the Ca(2+) sensor synaptotagmin VII in macrophages and dendritic cells. *Immunobiology* **214,** 495–505; 10.1016/j.imbio.2008.11.006 (2009).

153. Matzner, N. *et al.* Ion channels modulating mouse dendritic cell functions. *J Immunol* **181,** 6803–6809; 10.4049/jimmunol.181.10.6803 (2008).

154. Kutschat, A. P., Johnsen, S. A. & Hamdan, F. H. Store-Operated Calcium Entry: Shaping the Transcriptional and Epigenetic Landscape in Pancreatic Cancer. *Cells* **10**; 10.3390/cells10050966 (2021).

155. Thiel, G., Schmidt, T. & Rössler, O. G. Ca2+ Microdomains, Calcineurin and the Regulation of Gene Transcription. *Cells* **10**; 10.3390/cells10040875 (2021).

156. Tano, J.-Y., Lee, R. H. & Vazquez, G. Involvement of calmodulin and calmodulin kinase II in tumor necrosis factor alpha-induced survival of bone marrow derived macrophages. *Biochemical and Biophysical Research Communications* **427,** 178–184; 10.1016/j.bbrc.2012.09.038 (2012).

157. Wiesner, C., Le-Cabec, V., El Azzouzi, K., Maridonneau-Parini, I. & Linder, S. Podosomes in space: macrophage migration and matrix degradation in 2D and 3D settings. *Cell adhesion & migration* **8,** 179–191; 10.4161/cam.28116 (2014).

158. Schenkel, A. R., Mamdouh, Z. & Muller, W. A. Locomotion of monocytes on endothelium is a critical step during extravasation. *Nat Immunol* **5,** 393–400; 10.1038/ni1051 (2004).

159. Bear, J. E. & Haugh, J. M. Directed migration of mesenchymal cells: where signaling and the cytoskeleton meet. *Current Opinion in Cell Biology* **30,** 74–82; 10.1016/j.ceb.2014.06.005 (2014).

160. Dixit, N. & Simon, S. I. Chemokines, selectins and intracellular calcium flux: temporal and spatial cues for leukocyte arrest. *Frontiers in immunology* **3,** 188; 10.3389/fimmu.2012.00188 (2012).

161. Deshmane, S. L., Kremlev, S., Amini, S. & Sawaya, B. E. Monocyte chemoattractant protein-1 (MCP-1): an overview. *Journal of interferon & cytokine research : the official journal of the International Society for Interferon and Cytokine Research* **29,** 313–326; 10.1089/jir.2008.0027 (2009).

162. Lin, Z. *et al.* CCL2: An important cytokine in normal and pathological pregnancies: A review. *Frontiers in immunology* **13,** 1053457; 10.3389/fimmu.2022.1053457 (2022).

163. Gschwandtner, M., Derler, R. & Midwood, K. S. More Than Just Attractive: How CCL2 Influences Myeloid Cell Behavior Beyond Chemotaxis. *Frontiers in immunology* **10,** 2759; 10.3389/fimmu.2019.02759 (2019).

164. Tanaka, T., Terada, M., Ariyoshi, K. & Morimoto, K. Monocyte chemoattractant protein-1/CC chemokine ligand 2 enhances apoptotic cell removal by macrophages through Rac1 activation. *Biochemical and Biophysical Research Communications* **399,** 677–682; 10.1016/j.bbrc.2010.07.141 (2010).

165. Tsaur, I. *et al.* CCL2 promotes integrin-mediated adhesion of prostate cancer cells in vitro. *World journal of urology* **33,** 1051–1056; 10.1007/s00345-014-1389-z (2015).

166. Yan, Y. *et al.* CCL19 and CCR7 Expression, Signaling Pathways, and Adjuvant Functions in Viral Infection and Prevention. *Frontiers in cell and developmental biology* **7,** 212; 10.3389/fcell.2019.00212 (2019).

167. Hong, W., Yang, B., He, Q., Wang, J. & Weng, Q. New Insights of CCR7 Signaling in Dendritic Cell Migration and Inflammatory Diseases. *Frontiers in Pharmacology* **13,** 841687; 10.3389/fphar.2022.841687 (2022).

168. Hammad, A. S. & Machaca, K. Store Operated Calcium Entry in Cell Migration and Cancer Metastasis. *Cells* **10**; 10.3390/cells10051246 (2021).

169. White, C. & Fresquez, A. M. Store-Operated Calcium Entry Regulates Macrophage Chemotaxis. *The FASEB Journal* **34,** 1; 10.1096/fasebj.2020.34.s1.06014 (2020).

170. Fresquez, A. M. *et al.* STIM1-dependent store-operated calcium entry mediates sex differences in macrophage chemotaxis and monocyte recruitment. *Journal of Biological Chemistry* **300,** 107422; 10.1016/j.jbc.2024.107422 (2024).

171. Basu, S. & Srivastava, P. Immunological role of neuronal receptor vanilloid receptor 1 expressed on dendritic cells. *Proceedings of the National Academy of Sciences of the United States of America* **102,** 5120–5125; 10.1073/pnas.0407780102 (2005).

172. Howe, A. K. Cross-talk between calcium and protein kinase A in the regulation of cell migration. *Current Opinion in Cell Biology* **23,** 554–561; 10.1016/j.ceb.2011.05.006 (2011).

173. Carreras-Sureda, A., Pihán, P. & Hetz, C. Calcium signaling at the endoplasmic reticulum: fine-tuning stress responses. *Cell Calcium* **70,** 24–31; 10.1016/j.ceca.2017.08.004 (2018).

174. Eizirik, D. L., Cardozo, A. K. & Cnop, M. The role for endoplasmic reticulum stress in diabetes mellitus. *Endocr Rev* **29,** 42–61; 10.1210/er.2007-0015 (2008).

175. Daverkausen-Fischer, L. & Pröls, F. Regulation of calcium homeostasis and flux between the endoplasmic reticulum and the cytosol. *The Journal of biological chemistry* **298,** 102061; 10.1016/j.jbc.2022.102061 (2022).

176. Kiviluoto, S. *et al.* Regulation of inositol 1,4,5-trisphosphate receptors during endoplasmic reticulum stress. *Biochimica et biophysica acta* **1833,** 1612–1624; 10.1016/j.bbamcr.2013.01.026 (2013).

177. Carreras-Sureda, A. *et al.* The ER stress sensor IRE1 interacts with STIM1 to promote store-operated calcium entry, T cell activation, and muscular differentiation. *Cell reports* **42,** 113540; 10.1016/j.celrep.2023.113540 (2023).

178. Guha, P., Kaptan, E., Gade, P., Kalvakolanu, D. V. & Ahmed, H. Tunicamycin induced endoplasmic reticulum stress promotes apoptosis of prostate cancer cells by activating mTORC1. *Oncotarget* **8,** 68191–68207; 10.18632/oncotarget.19277 (2017).

179. Qin, L., Wang, Z., Tao, L. & Wang, Y. ER stress negatively regulates AKT/TSC/mTOR pathway to enhance autophagy. *Autophagy* **6,** 239–247; 10.4161/auto.6.2.11062 (2010).

180. Lindner, P., Christensen, S. B., Nissen, P., Møller, J. V. & Engedal, N. Cell death induced by the ER stressor thapsigargin involves death receptor 5, a non-autophagic function of MAP1LC3B, and distinct contributions from unfolded protein response components. *Cell Commun Signal* **18,** 12; 10.1186/s12964-019-0499-z (2020).

181. Diabetes. Available at https://www.who.int/news-room/fact-sheets/detail/diabetes (2024).

182. Yoon, S.-B. *et al.* Real-time PCR quantification of spliced X-box binding protein 1 (XBP1) using a universal primer method. *PLoS ONE* **14,** e0219978; 10.1371/journal.pone.0219978 (2019).

183. Mass, E. *et al.* Developmental programming of Kupffer cells by maternal obesity causes fatty liver disease in the offspring; 10.21203/rs.3.rs-3242837/v1 (2023).

184. Lamamy, J. *et al.* The neonatal Fc receptor expression during macrophage differentiation is related to autophagy. *Frontiers in immunology* **13,** 1054425; 10.3389/fimmu.2022.1054425 (2022).

185. Neu, C. *et al.* CD14-dependent monocyte isolation enhances phagocytosis of listeria monocytogenes by proinflammatory, GM-CSF-derived macrophages. *PLoS ONE* **8,** e66898; 10.1371/journal.pone.0066898 (2013).

186. Porcheray, F. *et al.* Macrophage activation switching: an asset for the resolution of inflammation. *Clin Exp Immunol* **142,** 481–489; 10.1111/j.1365-2249.2005.02934.x (2005).

187. Schmidt, S. C., Massenberg, A., Homsi, Y., Sons, D. & Lang, T. Microscopic clusters feature the composition of biochemical tetraspanin-assemblies and constitute building-blocks of tetraspanin enriched domains. *Sci Rep* **14,** 2093; 10.1038/s41598-024-52615-1 (2024).

188. Quast, T. *et al.* Cytohesin-1 controls the activation of RhoA and modulates integrin-dependent adhesion and migration of dendritic cells. *Blood* **113,** 5801–5810; 10.1182/blood-2008-08-176123 (2009).

189. Foxman, E. F., Kunkel, E. J. & Butcher, E. C. Integrating conflicting chemotactic signals. The role of memory in leukocyte navigation. *J Cell Biol* **147,** 577–588; 10.1083/jcb.147.3.577 (1999).

190. Weier, A.-K. *et al.* Multiple centrosomes enhance migration and immune cell effector functions of mature dendritic cells. *The Journal of cell biology* **221**; 10.1083/jcb.202107134 (2022).

191. Kopf, A. *et al.* Microtubules control cellular shape and coherence in amoeboid migrating cells. *J Cell Biol* **219**; 10.1083/jcb.201907154 (2020).

192. Gehrig, S. M. *et al.* Hsp72 preserves muscle function and slows progression of severe muscular dystrophy. *Nature* **484,** 394–398; 10.1038/nature10980 (2012).

193. Ruyck, J. de *et al.* Towards the understanding of the absorption spectra of NAD(P)H/NAD(P)+ as a common indicator of dehydrogenase enzymatic activity. *Chemical Physics Letters* **450,** 119–122; 10.1016/j.cplett.2007.10.092 (2007).

194. Zheng, D., Liwinski, T. & Elinav, E. Inflammasome activation and regulation: toward a better understanding of complex mechanisms. *Cell discovery* **6,** 36; 10.1038/s41421-020-0167-x (2020).

195. Dai, J., Jiang, C., Chen, H. & Chai, Y. Rapamycin Attenuates High Glucose-Induced Inflammation Through Modulation of mTOR/NF-κB Pathways in Macrophages. *Frontiers in Pharmacology* **10,** 1292; 10.3389/fphar.2019.01292 (2019).

196. Dan, H. C. *et al.* Akt-dependent regulation of NF-{kappa}B is controlled by mTOR and Raptor in association with IKK. *Genes & development* **22,** 1490–1500; 10.1101/gad.1662308 (2008).

197. Ahn, C., Kang, J.-H. & Jeung, E.-B. Calcium homeostasis in diabetes mellitus. *Journal of Veterinary Science* **18,** 261–266; 10.4142/jvs.2017.18.3.261 (2017).

198. Kaur, K., Gill, G. K. & Dhawan, R. K. Effect of Hyperglycemia on Impairment of Calcium Metabolism in T2DM. *Int J Health Sci Res* **12,** 86–93; 10.52403/ijhsr.20221113 (2022).

199. Liang, C.-P., Han, S., Li, G., Tabas, I. & Tall, A. R. Impaired MEK signaling and SERCA expression promote ER stress and apoptosis in insulin-resistant macrophages and are reversed by exenatide treatment. *Diabetes* **61,** 2609–2620; 10.2337/db11-1415 (2012).

200. Wongdee, K., Krishnamra, N. & Charoenphandhu, N. Derangement of calcium metabolism in diabetes mellitus: negative outcome from the synergy between impaired bone turnover and intestinal calcium absorption. *The journal of physiological sciences : JPS* **67,** 71–81; 10.1007/s12576-016-0487-7 (2017).

201. Grynkiewicz, G., Poenie, M. & Tsien, R. Y. A new generation of Ca2+ indicators with greatly improved fluorescence properties. *Journal of Biological Chemistry* **260,** 3440–3450; 10.1016/S0021-9258(19)83641-4 (1985).

202. Thomas, D. *et al.* A comparison of fluorescent Ca2+ indicator properties and their use in measuring elementary and global Ca2+ signals. *Cell Calcium* **28,** 213–223; 10.1054/ceca.2000.0152 (2000).

203. Tada, M., Takeuchi, A., Hashizume, M., Kitamura, K. & Kano, M. A highly sensitive fluorescent indicator dye for calcium imaging of neural activity in vitro and in vivo. *The European Journal of Neuroscience* **39,** 1720–1728; 10.1111/ejn.12476 (2014).

204. Liao, J. *et al.* A novel Ca2+ indicator for long-term tracking of intracellular calcium flux. *BioTechniques* **70,** 271–277; 10.2144/btn-2020-0161 (2021).

205. Morgan, A. J. & Jacob, R. Ionomycin enhances Ca2+ influx by stimulating store-regulated cation entry and not by a direct action at the plasma membrane. *Biochem J* **300 (Pt 3),** 665–672; 10.1042/bj3000665 (1994).

206. Pierce, J. W. *et al.* Novel inhibitors of cytokine-induced IkappaBalpha phosphorylation and endothelial cell adhesion molecule expression show anti-inflammatory effects in vivo. *Journal of Biological Chemistry* **272,** 21096–21103; 10.1074/jbc.272.34.21096 (1997).

207. Waldron, R. T., Short, A. D. & Gill, D. L. Store-operated Ca2+ entry and coupling to Ca2+ pool depletion in thapsigargin-resistant cells. *Journal of Biological Chemistry* **272,** 6440–6447; 10.1074/jbc.272.10.6440 (1997).

208. Schmidt, P. *et al.* Tas1R3 Dependent and Independent Recognition of Sugars in the Urethra and the Role of Tuft Cells in this Process. *Advanced Biology* **8,** e2400117; 10.1002/adbi.202400117 (2024).

209. Nie, Y., Vigues, S., Hobbs, J. R., Conn, G. L. & Munger, S. D. Distinct contributions of T1R2 and T1R3 taste receptor subunits to the detection of sweet stimuli. *Current biology : CB* **15,** 1948–1952; 10.1016/j.cub.2005.09.037 (2005).

210. Dubovski, N., Ben Shoshan-Galeczki, Y., Malach, E. & Niv, M. Y. Taste and chirality: l-glucose sweetness is mediated by TAS1R2/TAS2R3 receptor. *Food Chemistry* **373,** 131393; 10.1016/j.foodchem.2021.131393 (2022).

211. Sukumaran, S. K. & Palayyan, S. R. Sweet Taste Signaling: The Core Pathways and Regulatory Mechanisms. *International Journal of Molecular Sciences* **23**; 10.3390/ijms23158225 (2022).

212. Lee, J. *et al.* Sweet taste receptor agonists attenuate macrophage IL-1β expression and eosinophilic inflammation linked to autophagy deficiency in myeloid cells. *Clinical and Translational Medicine* **12,** e1021; 10.1002/ctm2.1021 (2022).

213. Taya, K., Hirose, K. & Hamada, S. Trehalose inhibits inflammatory cytokine production by protecting IkappaB-alpha reduction in mouse peritoneal macrophages. *Archives of Oral Biology* **54,** 749–756; 10.1016/j.archoralbio.2009.05.003 (2009).

214. Jiang, P. *et al.* Lactisole interacts with the transmembrane domains of human T1R3 to inhibit sweet taste. *Journal of Biological Chemistry* **280,** 15238–15246; 10.1074/jbc.M414287200 (2005).

215. McMahon, D. B. *et al.* Utilizing the Off-Target Effects of T1R3 Antagonist Lactisole to Enhance Nitric Oxide Production in Basal Airway Epithelial Cells. *Nutrients* **15**; 10.3390/nu15030517 (2023).

216. Li, X. *et al.* Human receptors for sweet and umami taste. *Proceedings of the National Academy of Sciences of the United States of America* **99,** 4692–4696; 10.1073/pnas.072090199 (2002).

217. Laffitte, A., Belloir, C., Neiers, F. & Briand, L. Functional Characterization of the Venus Flytrap Domain of the Human TAS1R2 Sweet Taste Receptor. *International Journal of Molecular Sciences* **23**; 10.3390/ijms23169216 (2022).

218. Inoue, M. *et al.* Allelic variation of the Tas1r3 taste receptor gene selectively affects taste responses to sweeteners: evidence from 129.B6-Tas1r3 congenic mice. *Physiological genomics* **32,** 82–94; 10.1152/physiolgenomics.00161.2007 (2007).

219. Zhang, S., Fritz, N., Ibarra, C. & Uhlén, P. Inositol 1,4,5-trisphosphate receptor subtype-specific regulation of calcium oscillations. *Neurochemical Research* **36,** 1175–1185; 10.1007/s11064-011-0457-7 (2011).

220. Ferris, C. D., Huganir, R. L., Bredt, D. S., Cameron, A. M. & Snyder, S. H. Inositol trisphosphate receptor: phosphorylation by protein kinase C and calcium calmodulin-dependent protein kinases in reconstituted lipid vesicles. *Proceedings of the National Academy of Sciences of the United States of America* **88,** 2232–2235; 10.1073/pnas.88.6.2232 (1991).

221. Soulsby, M. D. & Wojcikiewicz, R. J. H. Calcium mobilization via type III inositol 1,4,5-trisphosphate receptors is not altered by PKA-mediated phosphorylation of serines 916, 934, and 1832. *Cell Calcium* **42,** 261–270; 10.1016/j.ceca.2006.12.002 (2007).

222. MacLennan, D. H. & Kranias, E. G. Phospholamban: a crucial regulator of cardiac contractility. *Nature reviews. Molecular cell biology* **4,** 566–577; 10.1038/nrm1151 (2003).

223. Salvi, F. *et al.* Towards Dissecting the Mechanism of Protein Phosphatase-1 Inhibition by Its C-Terminal Phosphorylation. *Chembiochem : a European journal of chemical biology* **22,** 834–838; 10.1002/cbic.202000669 (2021).

224. Braz, J. C. *et al.* PKC-alpha regulates cardiac contractility and propensity toward heart failure. *Nat Med* **10,** 248–254; 10.1038/nm1000 (2004).

225. Takenaka, E., van Vo, A., Yamashita-Kanemaru, Y., Shibuya, A. & Shibuya, K. Selective DNAM-1 expression on small peritoneal macrophages contributes to CD4+ T cell costimulation. *Sci Rep* **8,** 15180; 10.1038/s41598-018-33437-4 (2018).

226. Skuljec, J. *et al.* Absence of Regulatory T Cells Causes Phenotypic and Functional Switch in Murine Peritoneal Macrophages. *Frontiers in immunology* **9,** 2458; 10.3389/fimmu.2018.02458 (2018).

227. Bai, W.-J. *et al.* Prolonged Deleterious Influences of Chemotherapeutic Agent CPT-11 on Resident Peritoneal Macrophages and B1 Cells. *Frontiers in immunology* **8,** 1919; 10.3389/fimmu.2017.01919 (2017).

228. Lee, J. *et al.* The MHC class II antigen presentation pathway in human monocytes differs by subset and is regulated by cytokines. *PLoS ONE* **12,** e0183594; 10.1371/journal.pone.0183594 (2017).

229. Li, C. *et al.* Comprehensive analysis of human monocyte subsets using full-spectrum flow cytometry and hierarchical marker clustering. *Frontiers in immunology* **15,** 1405249; 10.3389/fimmu.2024.1405249 (2024).

230. Groen, B. *et al.* Immunological Adaptations to Pregnancy in Women with Type 1 Diabetes. *Sci Rep* **5,** 13618; 10.1038/srep13618 (2015).

231. Matthews, D. R. *et al.* Homeostasis model assessment: insulin resistance and beta-cell function from fasting plasma glucose and insulin concentrations in man. *Diabetologia* **28,** 412–419; 10.1007/BF00280883 (1985).

232. Merklinger, E., Schloetel, J.-G., Spitta, L., Thiele, C. & Lang, T. No Evidence for Spontaneous Lipid Transfer at ER-PM Membrane Contact Sites. *The Journal of membrane biology* **249,** 41–56; 10.1007/s00232-015-9845-2 (2016).

233. Granados, D. P. *et al.* ER stress affects processing of MHC class I-associated peptides. *BMC Immunol* **10,** 10; 10.1186/1471-2172-10-10 (2009).

234. Holzmann, S. *et al.* A model system using tape stripping for characterization of Langerhans cell-precursors in vivo. *The Journal of investigative dermatology* **122,** 1165–1174; 10.1111/j.0022-202X.2004.22520.x (2004).

235. Lancet, T. Diabetes: a defining disease of the 21st century. *The Lancet* **401,** 2087; 10.1016/S0140-6736(23)01296-5 (2023).

236. Kulzer, B. Körperliche und psychische Folgeerkrankungen bei Diabetes mellitus. *Bundesgesundheitsblatt, Gesundheitsforschung, Gesundheitsschutz* **65,** 503–510; 10.1007/s00103-022-03517-y (2022).

237. Wang, M., Sperrin, M., Rutter, M. K. & Renehan, A. G. Cancer is becoming the leading cause of death in diabetes. *The Lancet* **401,** 1849; 10.1016/S0140-6736(23)00445-2 (2023).

238. Kanter, J. E., Hsu, C.-C. & Bornfeldt, K. E. Monocytes and Macrophages as Protagonists in Vascular Complications of Diabetes. *Frontiers in cardiovascular medicine* **7,** 10; 10.3389/fcvm.2020.00010 (2020).

239. Bories, G. *et al.* Impaired alternative macrophage differentiation of peripheral blood mononuclear cells from obese subjects. *Diabetes & vascular disease research* **9,** 189–195; 10.1177/1479164111430242 (2012).

240. Geerlings, S. E. & Hoepelman, A. I. Immune dysfunction in patients with diabetes mellitus (DM). *FEMS immunology and medical microbiology* **26,** 259–265; 10.1111/j.1574-695X.1999.tb01397.x (1999).

241. van Loo, G. & Bertrand, M. J. M. Death by TNF: a road to inflammation. *Nat Rev Immunol* **23,** 289–303; 10.1038/s41577-022-00792-3 (2023).

242. Grosick, R., Alvarado-Vazquez, P. A., Messersmith, A. & Romero-Sandoval, E. A. High glucose induces a priming effect in macrophages and exacerbates the production of pro-inflammatory cytokines after a challenge. *JPR* **Volume 11,** 1769–1778; 10.2147/JPR.S164493 (2018).

243. Suzuki, T., Yamashita, S., Hattori, K., Matsuda, N. & Hattori, Y. Impact of a long-term high-glucose environment on pro-inflammatory responses in macrophages stimulated with lipopolysaccharide. *Naunyn-Schmiedeberg's archives of pharmacology* **394,** 2129–2139; 10.1007/s00210-021-02137-8 (2021).

244. Moganti, K. *et al.* Hyperglycemia induces mixed M1/M2 cytokine profile in primary human monocyte-derived macrophages. *Immunobiology* **222,** 952–959; 10.1016/j.imbio.2016.07.006 (2017).

245. Lachmandas, E. *et al.* The Effect of Hyperglycaemia on In Vitro Cytokine Production and Macrophage Infection with Mycobacterium tuberculosis. *PLoS ONE* **10,** e0117941; 10.1371/journal.pone.0117941 (2015).

246. Megawati, E. R., Meutia, N. & Lubis, L. D. The effect of hyperglycaemia on the macrophages in the cell culture. *Folia morphologica* **81,** 387–393; 10.5603/FM.a2021.0017 (2022).

247. Matuschik, L. *et al.* Hyperglycemia Induces Inflammatory Response of Human Macrophages to CD163-Mediated Scavenging of Hemoglobin-Haptoglobin Complexes. *International Journal of Molecular Sciences* **23,** 1385; 10.3390/ijms23031385 (2022).

248. Shanmugam, N., Reddy, M. A., Guha, M. & Natarajan, R. High Glucose-Induced Expression of Proinflammatory Cytokine and Chemokine Genes in Monocytic Cells. *Diabetes* **52,** 1256–1264; 10.2337/diabetes.52.5.1256 (2003).

249. Zgheib, C., Hodges, M. M., Hu, J., Liechty, K. W. & Xu, J. Long non-coding RNA Lethe regulates hyperglycemia-induced reactive oxygen species production in macrophages. *PLoS ONE* **12,** e0177453; 10.1371/journal.pone.0177453 (2017).

250. Weichhart, T., Hengstschläger, M. & Linke, M. Regulation of innate immune cell function by mTOR. *Nat Rev Immunol* **15,** 599–614; 10.1038/nri3901 (2015).

251. Katholnig, K., Linke, M., Pham, H., Hengstschläger, M. & Weichhart, T. Immune responses of macrophages and dendritic cells regulated by mTOR signalling. *Biochemical Society Transactions* **41,** 927–933; 10.1042/BST20130032 (2013).

252. Sherry, C. L., O'Connor, J. C., Kramer, J. M. & Freund, G. G. Augmented Lipopolysaccharide-Induced TNF-α Production by Peritoneal Macrophages in Type 2 Diabetic Mice Is Dependent on Elevated Glucose and Requires p38 MAPK. *Journal of immunology (Baltimore, Md. : 1950)* **178,** 663–670; 10.4049/jimmunol.178.2.663 (2007).

253. Wang, B., Zhong, Y., Li, Q., Cui, L. & Huang, G. Autophagy of macrophages is regulated by PI3k/Akt/mTOR signalling in the development of diabetic encephalopathy. *Aging* **10,** 2772–2782; 10.18632/aging.101586 (2018).

254. Leprivier, G. & Rotblat, B. How does mTOR sense glucose starvation? AMPK is the usual suspect. *Cell death discovery* **6,** 27; 10.1038/s41420-020-0260-9 (2020).

255. Mekahli, D., Bultynck, G., Parys, J. B., Smedt, H. de & Missiaen, L. Endoplasmic-reticulum calcium depletion and disease. *Cold Spring Harbor Perspectives in Biology* **3**; 10.1101/cshperspect.a004317 (2011).

256. Zhai, Z. *et al.* Association between serum calcium level and type 2 diabetes: An NHANES analysis and Mendelian randomization study. *Diabetic medicine : a journal of the British Diabetic Association* **40,** e15080; 10.1111/dme.15080 (2023).

257. Zhu, J. *et al.* Circulating calcium levels and the risk of type 2 diabetes: a systematic review and meta-analysis. *The British journal of nutrition* **122,** 376–387; 10.1017/S0007114519001430 (2019).

258. Yamaguchi, T., Kanazawa, I., Takaoka, S. & Sugimoto, T. Serum calcium is positively correlated with fasting plasma glucose and insulin resistance, independent of parathyroid hormone, in male patients with type 2 diabetes mellitus. *Metabolism: clinical and experimental* **60,** 1334–1339; 10.1016/j.metabol.2011.02.003 (2011).

259. Hajhashemy, Z., Rouhani, P. & Saneei, P. Dietary calcium intake in relation to type-2 diabetes and hyperglycemia in adults: A systematic review and dose-response meta-analysis of epidemiologic studies. *Sci Rep* **12,** 1050; 10.1038/s41598-022-05144-8 (2022).

260. Shah, I. U. *et al.* Association of dietary calcium, magnesium, and vitamin D with type 2 diabetes among US adults: National health and nutrition examination survey 2007-2014-A cross-sectional study. *Food science & nutrition* **9,** 1480–1490; 10.1002/fsn3.2118 (2021).

261. Kono, T. *et al.* Impaired Store-Operated Calcium Entry and STIM1 Loss Lead to Reduced Insulin Secretion and Increased Endoplasmic Reticulum Stress in the Diabetic β-Cell. *Diabetes* **67,** 2293–2304; 10.2337/db17-1351 (2018).

262. Verkhratsky, A. & Fernyhough, P. Mitochondrial malfunction and Ca2+ dyshomeostasis drive neuronal pathology in diabetes. *Cell Calcium* **44,** 112–122; 10.1016/j.ceca.2007.11.010 (2008).

263. Eshima, H. Influence of Obesity and Type 2 Diabetes on Calcium Handling by Skeletal Muscle: Spotlight on the Sarcoplasmic Reticulum and Mitochondria. *Frontiers in physiology* **12,** 758316; 10.3389/fphys.2021.758316 (2021).

264. Wang, Y. *et al.* Inositol-1,4,5-trisphosphate receptor regulates hepatic gluconeogenesis in fasting and diabetes. *Nature* **485,** 128–132; 10.1038/nature10988 (2012).

265. Vanderheyden, V. *et al.* Regulation of inositol 1,4,5-trisphosphate-induced Ca2+ release by reversible phosphorylation and dephosphorylation. *Biochimica et biophysica acta* **1793,** 959–970; 10.1016/j.bbamcr.2008.12.003 (2009).

266. Amemiya, Y., Maki, M., Shibata, H. & Takahara, T. New Insights into the Regulation of mTOR Signaling via Ca2+-Binding Proteins. *International Journal of Molecular Sciences* **24**; 10.3390/ijms24043923 (2023).

267. Hughes, K., Antonsson, A. & Grundstrøm, T. Calmodulin dependence of NFkappaB activation. *FEBS letters* **441,** 132–136; 10.1016/s0014-5793(98)01537-3 (1998).

268. Régimbald-Dumas, Y., Frégeau, M.-O. & Guillemette, G. Mammalian target of rapamycin (mTOR) phosphorylates inositol 1,4,5-trisphosphate receptor type 2 and increases its Ca(2+) release activity. *Cellular signalling* **23,** 71–79; 10.1016/j.cellsig.2010.08.005 (2011).

269. Fu, Y. Facilitative glucose transporter gene expression in human lymphocytes, monocytes, and macrophages: a role for GLUT isoforms 1, 3, and 5 in the immune response and foam cell formation. *Blood Cells, Molecules, and Diseases* **32,** 182–190; 10.1016/j.bcmd.2003.09.002 (2004).

270. Semo, D. *et al.* The Sodium-Glucose Co-Transporter 2 (SGLT2) Inhibitor Empagliflozin Reverses Hyperglycemia-Induced Monocyte and Endothelial Dysfunction Primarily through Glucose Transport-Independent but Redox-Dependent Mechanisms. *JCM* **12,** 1356; 10.3390/jcm12041356 (2023).

271. Chaudhari, N. & Roper, S. D. The cell biology of taste. *J Cell Biol* **190,** 285–296; 10.1083/jcb.201003144 (2010).

272. Laffitte, A., Neiers, F. & Briand, L. Functional roles of the sweet taste receptor in oral and extraoral tissues. *Current opinion in clinical nutrition and metabolic care* **17,** 379–385; 10.1097/MCO.0000000000000058 (2014).

273. Nelson, G. *et al.* Mammalian Sweet Taste Receptors. *Cell* **106,** 381–390; 10.1016/S0092-8674(01)00451-2 (2001).

274. Murovets, V. O., Bachmanov, A. A. & Zolotarev, V. A. Impaired Glucose Metabolism in Mice Lacking the Tas1r3 Taste Receptor Gene. *PLoS ONE* **10,** e0130997; 10.1371/journal.pone.0130997 (2015).

275. Murovets, V. O., Sozontov, E. A. & Zachepilo, T. G. The Effect of the Taste Receptor Protein T1R3 on the Development of Islet Tissue of the Murine Pancreas. *Dokl Biol Sci* **484,** 1–4; 10.1134/S0012496619010010 (2019).

276. Ercin, M., Gezginci-Oktayoglu, S. & Bolkent, S. Exendin-4 inhibits small intestinal glucose sensing and absorption through repression of T1R2/T1R3 sweet taste receptor signalling in streptozotocin diabetic mice. *Translational research : the journal of laboratory and clinical medicine* **246,** 87–101; 10.1016/j.trsl.2022.03.012 (2022).

277. Yu, S. *et al.* Exendin-4 blockade of T1R2/T1R3 activation improves Pseudomonas aeruginosa-related pneumonia in an animal model of chemically induced diabetes. *Inflammation research : official journal of the European Histamine Research Society ... [et al.]* **73,** 1185–1201; 10.1007/s00011-024-01891-8 (2024).

278. Seong, H. *et al.* Taste receptor type 1 member 3 regulates Western diet-induced male infertility. *Biochimica et biophysica acta. Molecular and cell biology of lipids* **1869,** 159433; 10.1016/j.bbalip.2023.159433 (2024).

279. Kojima, I., Medina, J. & Nakagawa, Y. Role of the glucose-sensing receptor in insulin secretion. *Diabetes, obesity & metabolism* **19 Suppl 1,** 54–62; 10.1111/dom.13013 (2017).

280. Malecki, R., Fiodorenko-Dumas, Z., Jakobsche-Policht, U., Malodobra, M. & Adamiec, R. Altered monocyte calcium-sensing receptor expression in patients with type 2 diabetes mellitus and atherosclerosis. *Journal of physiology and pharmacology : an official journal of the Polish Physiological Society* **64,** 521–527 (2013).

281. Ball, L., Bauer, J. & Krautwurst, D. Heterodimerization of Chemoreceptors TAS1R3 and mGlu2 in Human Blood Leukocytes. *International Journal of Molecular Sciences* **24**; 10.3390/ijms241612942 (2023).

282. Mafi, A., Kim, S.-K., Chou, K. C., Güthrie, B. & Goddard, W. A. Predicted Structure of Fully Activated Tas1R3/1R3' Homodimer Bound to G Protein and Natural Sugars: Structural Insights into G Protein Activation by a Class C Sweet Taste Homodimer with Natural Sugars. *Journal of the American Chemical Society* **143,** 16824–16838; 10.1021/jacs.1c08839 (2021).

283. Heng, T. S. P. & Painter, M. W. The Immunological Genome Project: networks of gene expression in immune cells. *Nat Immunol* **9,** 1091–1094; 10.1038/ni1008-1091 (2008).

284. Uhlen, M. *et al.* A genome-wide transcriptomic analysis of protein-coding genes in human blood cells. *Science (New York, N.Y.)* **366**; 10.1126/science.aax9198 (2019).

285. The Human Protein Atlas. Available at https://www.proteinatlas.org/ (2024).

286. Embgenbroich, M. *et al.* Soluble mannose receptor induces proinflammatory macrophage activation and metaflammation. *Proceedings of the National Academy of Sciences of the United States of America* **118**; 10.1073/pnas.2103304118 (2021).

287. Moran, A. W. *et al.* Sweet taste receptor expression in ruminant intestine and its activation by artificial sweeteners to regulate glucose absorption. *Journal of Dairy Science* **97,** 4955–4972; 10.3168/jds.2014-8004 (2014).

288. Gómez-Fernández, A. R., Santacruz, A. & Jacobo-Velázquez, D. A. The complex relationship between metabolic syndrome and sweeteners. *Journal of food science* **86,** 1511–1531; 10.1111/1750-3841.15709 (2021).

289. Molitor, E. von *et al.* Sweet Taste Is Complex: Signaling Cascades and Circuits Involved in Sweet Sensation. *Frontiers in human neuroscience* **15,** 667709; 10.3389/fnhum.2021.667709 (2021).

290. Pang, M. D., Goossens, G. H. & Blaak, E. E. The Impact of Artificial Sweeteners on Body Weight Control and Glucose Homeostasis. *Frontiers in nutrition* **7,** 598340; 10.3389/fnut.2020.598340 (2020).

291. Escobedo, G., Egea, M. B., Roldan-Valadez, E., Peter-Corpe, C. & Bueno-Hernández, N. Editorial: Noncaloric artificial sweeteners and their impact on human health. *Frontiers in nutrition* **11,** 1461624; 10.3389/fnut.2024.1461624 (2024).

292. Schiano, C. *et al.* Soft drinks and sweeteners intake: Possible contribution to the development of metabolic syndrome and cardiovascular diseases. Beneficial or detrimental action of alternative sweeteners? *Food research international (Ottawa, Ont.)* **142,** 110220; 10.1016/j.foodres.2021.110220 (2021).

293. Jin, X., Wu, M., Dong, S., Liu, H. & Ma, H. Artificially sweetened beverages consumption and risk of obesity-related cancers: a wide-angled Mendelian randomization study. *Frontiers in nutrition* **11,** 1347724; 10.3389/fnut.2024.1347724 (2024).

294. Basson, A. R., Rodriguez-Palacios, A. & Cominelli, F. Artificial Sweeteners: History and New Concepts on Inflammation. *Frontiers in nutrition* **8,** 746247; 10.3389/fnut.2021.746247 (2021).

295. Leth-Møller, M. *et al.* Transplacental Transport of Artificial Sweeteners. *Nutrients* **15**; 10.3390/nu15092063 (2023).

296. Stampe, S. *et al.* Artificial Sweeteners in Breast Milk: A Clinical Investigation with a Kinetic Perspective. *Nutrients* **14**; 10.3390/nu14132635 (2022).

297. Wang, W., Nettleton, J. E., Gänzle, M. G. & Reimer, R. A. A Metagenomics Investigation of Intergenerational Effects of Non-nutritive Sweeteners on Gut Microbiome. *Frontiers in nutrition* **8,** 795848; 10.3389/fnut.2021.795848 (2021).

298. Spitaler, M. & Cantrell, D. A. Protein kinase C and beyond. *Nat Immunol* **5,** 785–790; 10.1038/ni1097 (2004).

299. Nicolaou, P. & Kranias, E. G. Role of PP1 in the regulation of Ca cycling in cardiac physiology and pathophysiology. *Frontiers in bioscience (Landmark edition)* **14,** 3571–3585; 10.2741/3472 (2009).

300. Vervloessem, T., Yule, D. I., Bultynck, G. & Parys, J. B. The type 2 inositol 1,4,5-trisphosphate receptor, emerging functions for an intriguing Ca^{2+}-release channel. *Biochimica et biophysica acta* **1853,** 1992–2005; 10.1016/j.bbamcr.2014.12.006 (2015).

301. Kolczynska, K., Loza-Valdes, A., Hawro, I. & Sumara, G. Diacylglycerol-evoked activation of PKC and PKD isoforms in regulation of glucose and lipid metabolism: a review. *Lipids in health and disease* **19,** 113; 10.1186/s12944-020-01286-8 (2020).

302. Qin, J. *et al.* Structures of PKA-phospholamban complexes reveal a mechanism of familial dilated cardiomyopathy. *eLife* **11**; 10.7554/elife.75346 (2022).

303. Hassel, K. R. *et al.* Another-regulin regulates cardiomyocyte calcium handling via integration of neuroendocrine signaling with SERCA2a activity. *Journal of molecular and cellular cardiology*; 10.1016/j.yjmcc.2024.10.008 (2024).

304. Carey, I. M. *et al.* Risk of Infection in Type 1 and Type 2 Diabetes Compared With the General Population: A Matched Cohort Study. *Diabetes care* **41,** 513–521; 10.2337/dc17-2131 (2018).

305. Zhou, Z., Wang, H., Tan, S., Zhang, H. & Zhu, Y. The alterations of innate immunity and enhanced severity of infections in diabetes mellitus. *Immunology* **171,** 313–323; 10.1111/imm.13706 (2024).

306. Wu, X. *et al.* Macrophage polarization in diabetic wound healing. *Burns & trauma* **10,** tkac051; 10.1093/burnst/tkac051 (2022).

307. Shen, Y. *et al.* Dysfunction of macrophages leads to diabetic bone regeneration deficiency. *Frontiers in immunology* **13,** 990457; 10.3389/fimmu.2022.990457 (2022).

308. Yu, X. *et al.* Size-Dependent Effect of Titania Nanotubes on Endoplasmic Reticulum Stress to Re-establish Diabetic Macrophages Homeostasis. *ACS biomaterials science & engineering* **10,** 4323–4335; 10.1021/acsbiomaterials.4c00549 (2024).

309. Song, Y. *et al.* High glucose condition aggravates inflammatory response induced by Porphyromonas gingivalis in THP-1 macrophages via autophagy inhibition. *BMC Immunol* **25,** 69; 10.1186/s12865-024-00655-7 (2024).

310. Wang, M. *et al.* Diabetes Mellitus Inhibits Hair Follicle Regeneration by Inducing Macrophage Reprogramming-Mediated Pyroptosis. *Journal of inflammation research* **17,** 6781–6796; 10.2147/JIR.S469239 (2024).

311. Yaseen, H. & Khamaisi, M. Skin well-being in diabetes: Role of macrophages. *Cellular immunology* **356,** 104154; 10.1016/j.cellimm.2020.104154 (2020).

312. Edgar, L. *et al.* Hyperglycemia Induces Trained Immunity in Macrophages and Their Precursors and Promotes Atherosclerosis. *Circulation* **144,** 961–982; 10.1161/CIRCULATIONAHA.120.046464 (2021).

313. Pontisso, I., Ornelas-Guevara, R., Chevet, E., Combettes, L. & Dupont, G. Gradual ER calcium depletion induces a progressive and reversible UPR signaling. *PNAS nexus* **3,** pgae229; 10.1093/pnasnexus/pgae229 (2024).

314. Eizirik, D. L. & Cnop, M. ER stress in pancreatic beta cells: the thin red line between adaptation and failure. *Science signaling* **3,** pe7; 10.1126/scisignal.3110pe7 (2010).

315. Abdullahi, A., Stanojcic, M., Parousis, A., Patsouris, D. & Jeschke, M. G. Modeling Acute ER Stress in Vivo and in Vitro. *Shock (Augusta, Ga.)* **47,** 506–513; 10.1097/SHK.0000000000000759 (2017).

316. Moon, J. L., Kim, S. Y., Shin, S. W. & Park, J.-W. Regulation of brefeldin A-induced ER stress and apoptosis by mitochondrial $NADP^+$-dependent isocitrate dehydrogenase. *Biochemical and Biophysical Research Communications* **417,** 760–764; 10.1016/j.bbrc.2011.12.030 (2012).

317. Menè, P. *et al.* High glucose inhibits cytosolic calcium signaling in cultured rat mesangial cells. *Kidney international* **43,** 585–591; 10.1038/ki.1993.86 (1993).

318. Yuan, M. *et al.* Hyperglycemia Induces Endoplasmic Reticulum Stress in Atrial Cardiomyocytes, and Mitofusin-2 Downregulation Prevents Mitochondrial Dysfunction and

Subsequent Cell Death. *Oxidative medicine and cellular longevity* **2020,** 6569728; 10.1155/2020/6569728 (2020).

319. Han, S. *et al.* Macrophage insulin receptor deficiency increases ER stress-induced apoptosis and necrotic core formation in advanced atherosclerotic lesions. *Cell Metabolism* **3,** 257–266; 10.1016/j.cmet.2006.02.008 (2006).

320. Sha, H., He, Y., Yang, L. & Qi, L. Stressed out about obesity: IRE1α-XBP1 in metabolic disorders. *Trends in endocrinology and metabolism: TEM* **22,** 374–381; 10.1016/j.tem.2011.05.002 (2011).

321. Zhao, L. & Ackerman, S. L. Endoplasmic reticulum stress in health and disease. *Current Opinion in Cell Biology* **18,** 444–452; 10.1016/j.ceb.2006.06.005 (2006).

322. Hotamisligil, G. S. Endoplasmic reticulum stress and the inflammatory basis of metabolic disease. *Cell* **140,** 900–917; 10.1016/j.cell.2010.02.034 (2010).

323. Park, S. W., Zhou, Y., Lee, J., Lee, J. & Ozcan, U. Sarco(endo)plasmic reticulum Ca2+-ATPase 2b is a major regulator of endoplasmic reticulum stress and glucose homeostasis in obesity. *Proceedings of the National Academy of Sciences of the United States of America* **107,** 19320–19325; 10.1073/pnas.1012044107 (2010).

324. Stone, S. I., Abreu, D., McGill, J. B. & Urano, F. Monogenic and syndromic diabetes due to endoplasmic reticulum stress. *Journal of diabetes and its complications* **35,** 107618; 10.1016/j.jdiacomp.2020.107618 (2021).

325. Delépine, M. *et al.* EIF2AK3, encoding translation initiation factor 2-alpha kinase 3, is mutated in patients with Wolcott-Rallison syndrome. *Nature genetics* **25,** 406–409; 10.1038/78085 (2000).

326. Li, G. *et al.* Role of ERO1-alpha-mediated stimulation of inositol 1,4,5-triphosphate receptor activity in endoplasmic reticulum stress-induced apoptosis. *The Journal of cell biology* **186,** 783–792; 10.1083/jcb.200904060 (2009).

327. Wu, R., Zhang, Q.-H., Lu, Y.-J., Ren, K. & Yi, G.-H. Involvement of the IRE1α-XBP1 pathway and XBP1s-dependent transcriptional reprogramming in metabolic diseases. *DNA and cell biology* **34,** 6–18; 10.1089/dna.2014.2552 (2015).

328. Oh, J. *et al.* Endoplasmic reticulum stress controls M2 macrophage differentiation and foam cell formation. *Journal of Biological Chemistry* **287,** 11629–11641; 10.1074/jbc.M111.338673 (2012).

329. Da Nascimento Conceicao, V., Sun, Y., Zboril, E. K., La Chapa, J. J. de & Singh, B. B. Loss of Ca2+ entry via Orai-TRPC1 induces ER stress, initiating immune activation in macrophages. *J Cell Sci* **133**; 10.1242/jcs.237610 (2019).

330. Liu, H.-F. *et al.* Altered polarization, morphology, and impaired innate immunity germane to resident peritoneal macrophages in mice with long-term type 2 diabetes. *Journal of biomedicine & biotechnology* **2012,** 867023; 10.1155/2012/867023 (2012).

331. Delamaire, M. *et al.* Impaired Leucocyte Functions in Diabetic Patients. *Diabet. Med.* **14,** 29–34; 10.1002/(SICI)1096-9136(199701)14:1<29::AID-DIA300>3.0.CO;2-V (1997).

332. Ngo, M. D. *et al.* A Blunted GPR183/Oxysterol Axis During Dysglycemia Results in Delayed Recruitment of Macrophages to the Lung During Mycobacterium tuberculosis Infection. *The Journal of infectious diseases* **225,** 2219–2228; 10.1093/infdis/jiac102 (2022).

333. Nie, L. *et al.* Diabetes induces macrophage dysfunction through cytoplasmic dsDNA/AIM2 associated pyroptosis. *Journal of leukocyte biology* **110,** 497–510; 10.1002/JLB.3MA0321-745R (2021).

334. Kulcsar, K. A., Coleman, C. M., Beck, S. E. & Frieman, M. B. Comorbid diabetes results in immune dysregulation and enhanced disease severity following MERS-CoV infection. *JCI insight* **4**; 10.1172/jci.insight.131774 (2019).

335. Sáez, P. J., Sáez, J. C., Lennon-Duménil, A.-M. & Vargas, P. Role of calcium permeable channels in dendritic cell migration. *Current opinion in immunology* **52,** 74–80; 10.1016/j.coi.2018.04.005 (2018).

336. Ackermann, T. & Tardito, S. Cell Culture Medium Formulation and Its Implications in Cancer Metabolism. *Trends in cancer* **5,** 329–332; 10.1016/j.trecan.2019.05.004 (2019).

337. Antonsen, K. W. *et al.* Comparison of culture media reveals that non-essential amino acids strongly affect the phenotype of human monocyte-derived macrophages. *Immunology* **170,** 344–358; 10.1111/imm.13670 (2023).

338. Kawakami, T., Koike, A. & Amano, F. Induction of different activated phenotypes of mouse peritoneal macrophages grown in different tissue culture media. *Cytotechnology* **69,** 631–642; 10.1007/s10616-017-0073-8 (2017).

339. Murovets, V. O. *et al.* Allelic variation of the Tas1r3 taste receptor gene affects sweet taste responsiveness and metabolism of glucose in F1 mouse hybrids. *PLoS ONE* **15,** e0235913; 10.1371/journal.pone.0235913 (2020).

340. Song, J. W., Lee, K.-H., Seong, H., Shin, D.-M. & Shon, W.-J. Taste receptor type 1 member 3 enables western diet-induced anxiety in mice. *BMC Biol* **21,** 243; 10.1186/s12915-023-01723-x (2023).

341. Shojaat, S. S., Engman, S., Hofferber, J., Keomanivong, F. & Wauson, E. M. Loss of the nutrient receptor Tas1R3 reduces atherosclerotic plaque accumulation and hepatic steatosis in ApoE-/- mice. *Journal of physiology and biochemistry* **76,** 623–636; 10.1007/s13105-020-00768-8 (2020).

342. Shi, J., Hua, L., Harmer, D., Li, P. & Ren, G. Cre Driver Mice Targeting Macrophages. *Methods in molecular biology (Clifton, N.J.)* **1784,** 263–275; 10.1007/978-1-4939-7837-3_24 (2018).

343. Mass, E. *Tissue-Resident Macrophages* (Springer US, New York, NY, 2024).

344. Singh, R., Gholipourmalekabadi, M. & Shafikhani, S. H. Animal models for type 1 and type 2 diabetes: advantages and limitations. *Frontiers in endocrinology* **15,** 1359685; 10.3389/fendo.2024.1359685 (2024).

345. Al-Awar, A. *et al.* Experimental Diabetes Mellitus in Different Animal Models. *Journal of diabetes research* **2016,** 9051426; 10.1155/2016/9051426 (2016).

6.2. Acknowledgements

First of all, I would like to express my gratitude to Prof. Dr. Sven Burgdorf for providing me with the opportunity to conduct my research in his laboratory. I am thankful for your unwavering support, insightful guidance and the freedom to explore my own ideas. Thank you for the opportunity to approach you with my questions at any time. Not only have I grown as a researcher, but I also had the chance to acquire invaluable experiences in teaching and lab management.

Furthermore, I would like to thank Prof. Dr. Irmgard Förster for being my second examiner and for her advice and support during my doctoral time. I would also like to thank Prof. Dr. Waldemar Kolanus and Prof. Dr. Valentin Stein as members of my examination committee.

A big thank you goes to all current and former lab members for their support and invaluable discussions. I am especially very grateful to Julia Bremser, Isabel Stötzel and Daniel Burgdorf, who supported me and my work as student assistants in our laboratory. Both the time with you and your contributions were essential to the success of this project.
In addition, I would extend my gratitude to Thomas Quast and Heike Weighardt, whose continuous support and scientific expertise have been indispensable throughout my work. I would like to thank Shaunak Ghosh and Eva Kiermaier for conducting the *in situ* migration assays. Furthermore, I wish to thank Alina Schieren, Linda Klümpen and Marie-Christine Simon for their help and support with the human cohort study as well as Thorsten Lang for mentoring Daniel how to perform and analyze the STED experiments. Without all of your work and dedication, the project would have not reached its current stage.

Last but certainly not least, I would like to thank all my friends and my family for their help and guidance whenever I needed it. A special gratitude and appreciation go to my parents and my sister Sarah. Your unending love, belief in me and constant encouragement have been and always will be the foundation of my success and perseverance.
Many thanks to all my friends inside and outside of my science bubble: Thank you for listening to any frustrations, uncertainties or dissatisfaction – even if it was the same thing a hundred times over. Your support, love and patience have carried me through this journey. A special thanks to Lasse, Jonas and Kerstin for providing balance, fun and much-needed relief during the countless game afternoons and evenings, as well as for being my social contact during the corona period. A heartfelt thank you to Fabi, whose friendship has been a constant throughout many stages of my life, and who, despite the distance, is always there for me.
Without all of you, I would not have been able to overcome the challenges, failures and setbacks that arose and get through difficult times.